

Vibrational Predissociation Spectroscopy of Ionic Complexes and Clusters

Inauguraldissertation

zur

Erlangung der Würde eines Doktors der Philosophie
vorgelegt der
Philosophisch-Naturwissenschaftlichen Fakultät
der Universität Basel

von

S.A. Nizkorodov
aus Novosibirsk (Russland)

Basel, 1997

Genehmigt von der Philosophisch-Naturwissenschaftlichen Fakultät

auf Antrag der

Herren Professoren J.P. Maier und H. Huber

Basel, den 29. April 1997

Prof. Dr. S.C. Stearns
Dekan

Acknowledgments

I would like to thank all my colleagues working in the group of John Maier in the period from 1993 till 1997 for sharing their knowledge, experimental skills and experience with me. Special thanks are given to John Maier, who gave me a chance of doing Ph.D. in Basle, and to Evan Bieske, the most enthusiastic and motivated scientist I ever met, for raising my interest in spectroscopy of ionic complexes by many orders of magnitude. Prof. Hanspeter Huber is thanked for acting as co-examinator for my thesis. The work presented here would not be possible without constant support from my wife Elena. The Swiss National Science Foundation and the City of Basle are thanked for the financial support in the past four years.

Contents

1. Structure of the thesis	1
2. Introduction	1
2.1. Ionic complexes and clusters. Definition and motivations.....	1
2.2. Indirect absorption methods. Photodissociation.....	3
2.3. Spectroscopy of ionic complexes and clusters.....	7
3. Objective of the thesis	19
4. Information pertaining to data analysis	20
4.1. Spectroscopy of chromophore ions.....	20
4.1.1. General.....	20
4.1.2. The HN_2^+ ion.....	20
4.1.3. The HCO^+ and HOC^+ ions.....	22
4.1.4. The NH_4^+ ion.....	23
4.2. Analysis of the observed spectra.....	25
4.3. Approximate 1D potentials for $\text{Rg}\dots\text{HX}^+$ complexes.....	30
5. Experimental	31
5.1. General.....	31
5.2. Gas mixer.....	31
5.3. Ion source.....	32
5.4. Quadrupoles.....	34
5.5. Octopole ion guide.....	35
5.6. Second quadrupole and Daly detector.....	36
5.7. OPO laser system.....	36
5.8. Optoacoustic calibration cell.....	38
5.9. Measurement of the Nd: YAG fundamental frequency.....	39
5.10. Experiment timing and data acquisition.....	39
5.11. Calibration of spectra.....	40
6. H_2 vibrations in $\text{H}_2\text{-HX}^+$ complexes	42
6.1. General.....	42
6.2. The $\text{H}_2\text{-HCO}^+$ complex.....	42
6.2.1. Motivations for the study and associated chemistry.....	42
6.2.2. Ab initio structure predictions.....	43
6.2.3. Observed spectra and assignment.....	47
6.2.4. Discussion.....	50
6.3. The $\text{H}_2\text{-HN}_2^+$ complex.....	52
6.3.1. General.....	52
6.3.2. Ab initio calculations.....	52
6.3.3. Results and assignments.....	54
6.4. The $\text{H}_2\text{-NH}_4^+$, $\text{H}_2\text{-H}_3\text{O}^+$, XeH_3^+ , and ArH_3^+ complexes.....	57

- Table of contents -

7. HM vibrations in Rg-HM+ complexes.....	58
7.1. The He-HCO ⁺ complex.....	58
7.1.1. Spectrum	58
7.1.2. Perturbations.....	60
7.2. The Ne-HCO ⁺ complex.....	62
7.3. The Ar-HCO ⁺ complex.....	66
7.3.1. Experimental Details	66
7.3.2. Overview	67
7.3.3. The ν_1 band.....	67
7.3.4. The $\nu_1 + \nu_2$ band.....	70
7.3.5. The $2\nu_1$ band.....	72
7.3.6. The $\nu_1 + \nu_3 - \nu_3$ band.....	74
7.3.7. Rotational energy distribution in the $\nu_1 + \nu_3 - \nu_3$ band.....	75
7.3.8. The 2955 cm ⁻¹ band.....	77
7.3.9. The 2961 ($\nu_1 + \nu_s$), 3068, and 3125 cm ⁻¹ bands.....	79
7.3.10. The $\nu_1 + \nu_s - \nu_s$ band.....	83
7.3.11. Discussion.....	84
7.4. The He-HN ₂ ⁺ complex.....	86
7.4.1. Spectrum	86
7.4.2. One-dimensional RKR potential.....	89
7.4.3. Vibrational predissociation.....	90
7.5. The Ne-HN ₂ ⁺ complex.....	92
7.5.1. Spectrum	92
7.5.2. Ground state rotational constants.....	94
7.5.3. Vibrational assignment.....	95
7.5.4. Rotational fits.....	99
7.5.5. Discussion.....	100
7.6. The Ar-HN ₂ ⁺ complex.....	102
7.6.1. Expectations.....	102
7.6.2. Spectrum	102
7.6.3. Ground state rotational constants.....	105
7.6.4. Rotational fits and vibrational origins.....	105
7.6.5. Intermolecular binding energy of the complex.....	107
7.6.6. Vibrational assignment.....	110
7.6.7. Conclusions.....	113
8. The Rg-NH₄⁺ complexes.....	114
8.1. Overview	114
8.2. The He-NH ₄ ⁺ complex.....	115
8.3. The Ar-NH ₄ ⁺ complex.....	118
8.3.1. Spectrum	118

- Table of contents -

8.3.2. Assignment.....	119
8.4. Conclusion	120
9. Larger complexes	122
9.1. Complexes $Rg_n\text{-HCO}^+/\text{HN}_2^+$. General remarks	122
9.2. $Ar_n\text{-HCO}^+$ complexes.....	122
9.2.1. Some experimental details.....	122
9.2.2. Results and analysis. The ν_1 band shifts.....	124
9.2.3. ν_1 band profiles	127
9.2.4. Combination bands.....	128
9.2.5. Structure modeling	129
9.2.6. Discussion.....	131
9.3. The $Ne_2\text{-HCO}^+$, $He_2\text{-HN}_2^+$ and $Ne_n\text{-HN}_2^+$ clusters.....	132
9.4. Conclusions for the $Rg_n\text{-HCO}^+/\text{HN}_2^+$ complexes	135
9.5. Complexes $Ar_n\text{-NH}_4^+$	136
9.5.1. Preview.....	136
9.5.2. Ab initio calculations.....	136
9.5.3. Spectra.....	137
9.5.4. Vibrational analysis	139
9.5.5. Summary	141
10. Discussion	142
10.1. H_2 stretching vibrations in $H_2\text{-M}^+$ complexes	142
10.2. HM stretching vibrations in $Rg\text{-HM}^+$ complexes.....	147
11. Outlook.....	150
12. Appendix.....	151
13. List of tables.....	162
14. List of figures	164
15. List of the author's publications.....	166
16. References	167
17. Curriculum Vitae of the author	182

1. Structure of the thesis

The manuscript is organized in the following way. First, there is a short introductory chapter intended to make the reader familiar with the definitions of ionic complexes and clusters, and with the basics of indirect absorption methods. The next section is devoted to the review of today's state of research in the field of spectroscopy of ionic complexes. The objective of the thesis is formulated at the end of this chapter. Further, the topics essential for the analysis and discussion of the results obtained in this work are discussed. This includes spectroscopy of the chromophore ions and approaches to the analysis of vibrational-rotational spectra of stable and weakly bound species. After the chapter that describes the experimental setup, the results of the study are presented. The complexes are grouped according to their chromophores and sizes. Analysis of the spectra of the dimer complexes of H₂, He, Ne, and Ar with HCO⁺, HN₂⁺, and of He and Ar with NH₄⁺ is followed by the description of larger aggregates formed on solvation of HCO⁺, HN₂⁺, and NH₄⁺ by rare gas atoms. The final chapter discusses the trends in the derived spectroscopic parameters and gives an outlook for the possible future studies.

2. Introduction

2.1. Ionic complexes and clusters. Definition and motivations

Labeling the charged species as ionic complexes is usually done for a very specific class of composite ions. An ionic complex, as it would probably be defined by most of the workers in this field, consists of a stable atomic or molecular ion bound to a neutral particle by some sort of an interaction which is not strong enough to greatly distort the individual properties of the constituents. Ionic complexes can be represented by a simplified generic formula $I^{\pm}\cdot L$ where I^{\pm} is a positive or negative ion and L is a neutral ligand. For certain ionic complexes the electrostatic interactions provide the largest contribution to the binding energy. However there are complexes in which the interactions can be considered as half-chemical and where the binding energies comparable to those of weak covalent chemical bonds are not inconceivable. These include for example most of the hydrogen bonded species that are probably among the most strongly bound ionic complexes. Other systems with high binding energies include metal cations solvated by polar solvents (e.g. Na⁺(H₂O)). A good example of a complex bound primarily by electrostatic forces is N₂⁺-He with calculated binding energy of only 100 cm⁻¹ [1, 2]. On contrary in the complex of H₃O⁺ with H₂O a much stronger hydrogen bond with binding energy of ≈ 12600 cm⁻¹ [3] is formed.

Complexes of the type $I^{\pm}\cdot L_n$, consisting of an ion and several ligands (e.g. NH₄⁺(NH₃)_{n \geq 2}) are somewhat arbitrary called ionic clusters [4]. With this definition, a

complex is a cluster with $n=1$ and both names are frequently used in the literature. If the ligands are not identical one talks of a mixed cluster. A large compilation of thermodynamic properties of ionic clusters was made by Keesee and Castleman [5] in form of the tables listing ΔH^0 and ΔS^0 for the respective step-by-step clustering reactions. Thermochemical data have provided a wealth of valuable information allowing the evaluation of useful trends in the strength of bonding for different classes of ionic clusters. In favorable cases perception of the structures of ionic clusters can be obtained by connecting the discontinuities in the cluster size dependence of ΔH^0 with the change in the differential binding energy of the ligands to the rest of the cluster due to filling of the successive solvation shells. Similar discontinuities are observed in intensity distributions of ionic clusters in mass spectra, which usually reflect chemistry taken place in an ion source, or different rates of ligand evaporation on the way from the source to the ion detector. Other properties of ionic clusters such as electron detachment energies, metastable fractions, reactivities and collision induced dissociation cross sections can feature discontinuities as well. "Magic numbers" obtained from the size dependence of cluster properties are usually linked with particularly regular structures. For example, it has been observed that, when clusters are composed mainly of atoms that interact more or less isotropically with one another (e.g., Ar_n^+ [6]), certain sizes where monomer coordination is optimized are particularly abundant, and that these correspond to the icosohedral structures. Another good example is the ammoniated ammonium series $\text{NH}_4^+(\text{NH}_3)_n$ where a strong discontinuity is observed between $n=4$ and 5 in both the $\Delta H^0(n)$ dependence [5], and in the unimolecular decomposition kinetic energy release spectra [7] indicating the formation of the first solvation shell at $n=4$.

The importance of ionic complexes and clusters in chemistry is indisputable [8-11]. This is particularly true for the hydrogen bonded species [4] since the hydrogen bond is probably one of the most ubiquitous in nature. Molecules in a variety of solids and liquids including common ice and water organize themselves in such way as to maximize the number of hydrogen interactions. Even in the gas phase vaporized molecules of such compounds aggregate in hydrogen-bonded polymers. A celebrated example among proton-bound ionic complexes is the $\text{H}_3\text{O}^+(\text{H}_2\text{O})_n$ ion which is found mass-spectroscopically to be quite abundant in the upper layer of the earth's atmosphere. Hydrogen bonding is responsible for the secondary structure of DNA and proteins. A huge class of proton transfer reactions proceeds via hydrogen-bonded intermediates.

Investigations of small binary ionic complexes provide scientists with the fundamental aspects of non-chemical bonding interactions, required to model the behaviour and properties of more complicated systems. Since the ionic complexes have in general intermediate binding energies compared to the stable covalent and extremely fragile van der Waals compounds, their study is believed to establish a bridge between these two interesting

classes. Studies of the intermediate sized clusters should allow to approach the as yet poorly understood problem of many-body interactions [12]. Finally, investigation of the development of larger clusters' properties as their size progressively increases provides valuable information about solvation phenomena. Diluted solutions containing ionic species can in fact be viewed as a collection of infinitely large clusters. These few important examples nicely illustrate the fundamental importance of the ionic cluster's science.

For stable molecules and ions a variety of spectroscopic methods has been developed that are capable of providing extremely useful information complementary to the data obtained from the thermochemical, reactive, and theoretical research. However, in spite of the importance of the ionic clusters and complexes their gas-phase spectroscopic studies have been scarce because of the difficulties associated with handling these fragile systems. Apart from the general space charge limitations preventing accumulation of a sufficient density of the ionic species in a reaction volume the concentration of clusters compared to that of stable ions is further suppressed by their low binding energies and respective equilibrium constants. The formation of ionic complexes typically proceeds via three-body association reactions and is therefore favored by an increased partial pressure of both ligand vapor and a buffer gas and by reduced temperature of the reaction mixture. The conditions are almost never met in most of the known ionic sources and discharge cells. For the reason of low density, the spectroscopic investigations of ionic complexes had been accomplished for the most part by means of "consequence" or "action" techniques, of which photodissociation has become the most popular. By now only few complex ions could be generated in sufficient quantities to allow observation of their gas phase spectra by the direct absorption methods. They include historically significant infrared studies of $\text{H}_3\text{O}^+(\text{H}_2\text{O})_n$ [13] and $\text{NH}_4^+(\text{NH}_3)_n$ [14] complexes in a pulsed radiolysis cell and microwave studies of ArH_3^+ [15-17] and Ar-HCO^+ [18] complexes. Most significant spectroscopic works on *positive* ionic complexes in the microwave, IR, visible, and UV frequency ranges will be reviewed in section 2.3.

2.2. Indirect absorption methods. Photodissociation

In a typical direct absorption experiment one monitors the reduction in the intensity of a light beam passing through a sample with a photosensitive detector. If the transition intensity is small or the concentration of the absorbing molecules in the sample is very low, the number of photons that are absorbed can easily be few orders of magnitude smaller than their total number. In this case, the separation of the changes in the photon flux due to the light source instabilities from the changes arising from the absorption by sample molecules can be quite problematic and is generally the main factor that limits the sensitivity of direct absorption experiments.

- Introduction -

Usually the energy delivered in the absorber by photoexcitation is quickly dissipated into heat in collisions with nearby background molecules. Fortunately for spectroscopists, certain absorbers can get rid of the excess energy in more specific ways, leading to certain kinds of experimentally observable effects (consequences), particularly if the absorbing species are placed in a collision free environment. Changes in the magnitude of these effects with the excitation frequency provides a spectrum which is a convolution of the absorption cross section and the state dependent effect probability. If the latter varies in a smooth way with respect to the excitation frequency (state dependence is weak) such consequence spectrum will be similar to the one obtained by the direct absorption methods. The consequence spectroscopy is advantageous if such effects do not occur spontaneously, i.e. without photoexcitation, since in this case one will have a background free technique. The performance of the background free methods is not so dramatically sensitive to the variations in the light source stability, and more important, the large concentrations of the absorbing species are no longer required.

There are quite a few examples of practical realizations of the consequence spectroscopic experiments, with the simplest one being fluorescence. In a fluorescence event the excess energy leaves the photoexcited molecule in form of a photon which is emitted in a fairly random direction (polarization and alignment effects are neglected). The detector is usually placed in a direction perpendicular to that of the excitation beam and the only interfering signal in this case comes from the weak scattering of the excitation light on the windows and the walls of the sample container. A monochromator can be inserted before the detector to allow spectral resolution of the fluorescent emission. Fluorescence is not quite suitable for the IR studies because of the very long lifetimes associated with the low frequency emissions, but it is invaluable in the UV and visible electronic spectroscopy. Ionic clusters of $C_6F_6^+$ with rare gases have been studied by the LIF method [19, 20].

Another possibility to generate a photoinduced consequence is to open a reaction channel which is forbidden for the lower state absorbers. The consequence in this case is the presence of the reaction products after the excitation. This can be either a bimolecular reaction with a background gas or an unimolecular decomposition. A good example of the former kind of the photoinduced reactions is provided by N_2^+ ion which is known to exchange charge with Ar atoms efficiently only when it is vibrationally excited. Following the excitation of the (cold) N_2^+ ($B \leftarrow X$) electronic transition the fluorescence takes the ions back into vibrationally excited levels of the ground electronic state which are capable of quick charge exchange with Ar atoms. The spectrum is obtained by monitoring the number of observed Ar^+ ions as a function of excitation frequency. Though the methods involving bimolecular reactions are quite elegant, they are of rather limited applicability because one almost never knows what sort of reaction may turn out to be specific for the excited molecules or ions and not for the ground state ones. However, it is by this method that the

- Introduction -

first spectral lines of H_2D^+ [21], HD^+ [22], and HeH^+ [23] ions were observed (reaction = charge exchange). For weakly bound ionic clusters the method is inapplicable since for them the most probable bimolecular reaction at any degree of internal excitation is the collision induced fragmentation.

The process of unimolecular decomposition that follows photoexcitation, or simply speaking *photodissociation*, has turned out to be much more productive for the spectroscopy of ionic clusters than the photoinduced bimolecular reactions. Indeed any isolated polyatomic molecule excited above one of its dissociation thresholds has a certain probability to break apart. There is a weak limitation in that the lifetime of the excited state can in certain cases be very much longer than the timescale on which the molecule can be kept isolated. (Or on contrary it can be extremely short as in the process of a direct photodissociation which occurs on a timescale of a single vibrational period upon an electronic transition from a bound state to a repulsive one. Direct dissociation is not considered here since it usually bears a very limited information content for spectroscopy). For example, a collision with another molecule can prevent dissociation by taking away some portion of the internal energy of the photoexcited species. Or there is a possibility of importance for weakly bound ionic complexes and clusters that they can be efficiently destroyed by collisions irrespectively of their internal energy and therefore the consequence technique will not work. Fortunately, most of the indirect photodissociation processes occur in the experimentally convenient picosecond to microsecond time window and can be utilized for spectroscopy. The experiments of this sort are performed under vacuum conditions which minimize the unwanted collisional interference.

Indirect dissociation can proceed via different mechanisms. When the absorbed photon is in the infrared, vibrational predissociation is typical [4, 24]. Excitation in the visible or UV range often takes a molecule in a bound electronic state that interacts in an adiabatic way with a repulsive state. Dissociation is particularly efficient in the regions of intersystem crossing. One example is electronic predissociation of N_2O^+ from vibrationally excited levels of the $\text{A}^2\Sigma^+$ electronic state [25, 26].

To use consequence techniques based on photodissociation most effectively one has to find means for selective detection of the photofragments. For ionic species this problem can be solved in an elegant way by the use of tandem mass spectrometry [27]. A typical tandem machine consists of an ion source, at least two mass filters capable of separating ions with a given charge/mass ratio, a reaction volume between the two mass spectrometers where photodissociation or an ion-molecule reaction can take place, and an ion detector. The first mass filter serves to pick up the ion of interest from the rest of the ions produced in the ion source and the second one lets only the (charged) fragments of the reaction/photodissociation proceed to the detector. The photodissociation spectrum is

obtained by monitoring the intensity of the fragment ion current vs. excitation frequency. Coupling the mass selection and photodissociation turns this consequence technique in a really powerful spectroscopic tool suited particularly well for the investigation of ionic clusters [4, 24, 28]. The main advantages of the method can be summarized as follows. (1) The identification of the spectrum carrier is in most cases unambiguous because the masses of the absorbing ion and of the fragment in which it falls apart are known. On contrary in a discharge cell a number of ionic and neutral species may happen to absorb at similar frequency range and identification of lines as belonging to one or the other species can be quite complicated. For example in the spectra of chromophore ions surrounded by weakly polarizable ligands (rare gases) the positions of the transition maxima for different sized clusters often changes very little with size and measuring the peak positions without prior mass selection is virtually impossible. (2) The high sensitivity of the modern ion detectors allows very weak transitions and the transitions of complexes with low binding energies to be studied with a good signal to noise ratio. (3) Apart from obtaining purely spectroscopic information, the dynamics of the photodissociation processes can itself be investigated from the observation of thresholds, linewidths, and integrated intensities in the spectra. Of course there are certain limitations and disadvantages of the method that have to be mentioned as well. (1) Only the energy levels lying above the dissociation threshold can be studied by this method. In studies of electronic spectra of ionic clusters this is usually not a problem since the energy required for the excitation of a typical electronic transition is much higher than binding energies in most of the clusters. However in the IR range the chromophore fundamentals ($\leq 4000 \text{ cm}^{-1}$) will only be observable for weakly bound complexes. Complexes with higher binding energies can be studied by looking at their combination, overtone, or sequence bands or alternatively by using multiphoton dissociation (2) By their virtue the upper state levels are metastable and for moderately large systems dissociation can proceed on a smaller timescale than the characteristic period of rotation of the ion. Rotational structure of the transition will thus be resolved only in favorable cases. But the electronic and vibrational energies of the clusters often remain well defined.

Of course the examples given above are not the only consequence schemes that have been realized experimentally. Zero kinetic energy (ZEKE) photoelectron spectroscopy is a rapidly developing method allowing to obtain spectroscopic information on stable and complex ions with a moderate resolution [29, 30]. Conventional photoelectron spectroscopy can be utilized to probe the properties of neutral and charged clusters [8]. Photodetachment is another useful method for spectroscopic investigation of negatively charged ions [31-34].

All the spectra reported in this work have been recorded in a tandem mass spectrometer apparatus with use of the IR photodissociation consequence spectroscopy.

2.3. Spectroscopy of ionic complexes and clusters

This section gives a review of spectroscopic studies of ionic complexes and clusters. The review is by no means complete, only the most relevant works are cited here. The main stress is placed on the infrared vibrational predissociation studies and some representative works in the area of visible/UV photodissociation spectroscopy, where at least vibrational resolution is attained. Negative cluster ions are not reviewed here, an interested reader is referred to refs. [24, 29]. A bibliography containing references to high resolution experimental studies of all weakly bound complexes, including the charged ones is available from ref. [35].

Though discovered by mere luck in a search for a CH_2D^+ microwave spectrum in a $\text{CH}_4/\text{D}_2/\text{Ar}$ discharge [17] the ArD_3^+ ion became the first ionic complex for which a high-resolution microwave spectrum was observed. From a preliminary study of ArH_3^+ and ArD_3^+ isotopomers [15] firm evidence was obtained that ArH_3^+ is planar with the Ar atom situated on a vertex of the H_3^+ equilateral triangle. Splitting of some rotational lines was interpreted as a result of an in-plane tunneling motion of the H_3^+ unit which leads to an exchange of the bound H atom. Later different H/D isotopomers of ArH_3^+ were studied as well [16]. A model with a usual cosine potential to imitate the internal rotation of H_3^+ could satisfactorily explain the magnitude and the pattern of the observed line splitting with a 1700 cm^{-1} barrier for the tunneling motion. The fact that the precise quantitative agreement was not obtained was attributed to the neglect of the out-of-plane motions predicted to have barriers that are not so much higher than the one for the in-plane jumps [36].

Just before the completion of this thesis another microwave study of an ionic complex between Ar and HCO^+ has appeared [18]. The spectroscopic search of the complex was guided by preliminary report of the photodissociation spectrum of Ar-HCO^+ from our group [37]. The microwave study has substantially narrowed the error limits for the rotational constants and rigorously proven the ordering of the atoms in the complex. Intermolecular stretching and bending frequencies were estimated as 130 and 110 cm^{-1} in fair agreement with present data. Unfortunately the paper appeared too late to take an advantage of the improved rotational constants in this thesis.

Microwave transitions between high-lying energy levels of ions have been extensively studied by Carrington and co-workers [38, 39]. The ions selected for the investigation (H_2^+ , H_3^+ , HeAr^+ , etc.) are relatively stable in their ground states, but when they are excited to the energy levels lying within a few wavenumbers from the dissociation threshold they spend most of the time on the long-range part of the potential energy surface. The microwave transitions between such levels provide a direct probe of the long-range interactions in ions. The transitions are followed by the field dissociation and the fragments

are detected as a function of the microwave frequency, so the method is a variation of photodissociation spectroscopy. Recently the method has been applied to a "true" ionic complex He-H₂⁺ [38, 40].

The only ionic complex observed by direct absorption in the IR range is N₄⁺ [41]. The species is so stable (≈ 1 eV) that it is often not considered as a complex. Thanks to its stability it is relatively easy to generate the ion in sufficient quantities in a supersonic expansion of N₂, coupled to a discharge. Both N₂ and N₂⁺ are IR inactive making the spectral assignment fairly unambiguous. In the work of Ruchti et al [41], the antisymmetric stretching vibration of N₄⁺ was observed and analyzed. The authors could prove that the complex possesses a linear ground state structure in agreement with previous *ab initio* and matrix isolation studies [41].

The discovery of the H₃⁺ ν_2 infrared transition in 1980 [42] is considered as the initiation of high-resolution infrared spectroscopy of molecular ions [43]. Similarly, weakly bound hydrogen clusters H₃⁺·(H₂)_n played an important historical role in the development of vibrational predissociation spectroscopy, being the first ionic clusters investigated by this method [44]. The spectra of the hydrogen clusters for n \leq 6 recorded near 4000 cm⁻¹ in the region of the H₂ stretching vibration [44, 45] illustrated many aspects of the behaviour common for the infrared spectra of other ionic clusters. Firstly, a very interesting cluster size dependence of the H₂ stretching vibration frequency was found. While the addition of the first H₂ ligand to H₃⁺ resulted in a shift of 250 cm⁻¹ of the complexed H₂ frequency compared to that of the free molecular hydrogen (4160 cm⁻¹), the transition center moved monotonically back towards higher frequencies as the size of the clusters progressively increased. The dependence seemed to level off at a value (≈ 4050 -4080 cm⁻¹) that is significantly lower than the free H₂ stretch frequency. This behavior was explained in terms of the structure and nature of binding in the clusters predicted from theory. Both *ab-initio* studies existing at that stage [46-49] as well as later studies [50-52] agreed that the H₂ molecules bind first to the vertices of the H₃⁺ triangle. In these corner positions the H₂ units are strongly perturbed and their vibrations become IR active. Though it is not yet quite clear what sort of structure (if there is any) is adopted by the hydrogen clusters larger than H₃⁺·(H₂)₃ [50, 53, 54], the next hydrogen molecules are believed to be situated somewhere outside the H₃⁺ plane and be less influenced by the charge. It is the corner ligands that absorb the IR radiation and dictate the magnitude of the shift, with the outer H₂ molecules playing a passive role of weak perturbors of the corner ones. The decrease in the shift observed from H₅⁺ to H₉⁺ is explained by a size dependent redistribution of the charge within the cluster. Though the H₅⁺ global minimum is predicted to have C_{2v} symmetry, the D_{2h} transition state lies less than 4 kJ/mol higher in energy, and the charge in the system is highly delocalized leading to a large distortion of H₂ ligand properties [51]. Charge distributions in the clusters H₇⁺ and H₉⁺ approach the picture of H₂ units weakly interacting

with an undistorted H_3^+ much more closely. In them the ligands are less influenced by the core and the shifts are respectively smaller [46]. The second important and somewhat disappointing observation was that the spectra were not rotationally resolved. In spite of the expected rotational line spacing of 6 cm^{-1} for H_5^+ the search for individual rotational lines in the spectrum with a high resolution laser failed. Apparently the predissociation of the complexes is quite efficient, occurring on less than a picosecond timescale. And finally, with the $\text{H}_3^+(\text{H}_2)_n$ example the sensitivity of the vibrational predissociation method was clearly demonstrated. Obviously the spectra of this quality could be obtained by no other spectroscopic method. To add to this, Bae [55] succeeded in recording weaker overtone transitions of H_5^+ between 5400 and 10000 cm^{-1} and in combination with the data from ref. [44, 45] derived harmonic frequencies and anharmonicities for the H_2 stretch and H_3^+ symmetric stretch vibrations of H_5^+ .

Inspired with their success with hydrogen clusters Lee's group proceeded to study protonated water clusters $\text{H}_3\text{O}^+(\text{H}_2\text{O})_n$. But here, because the hydrogen bonds in the hydrated hydronium ions are too strong to fragment the clusters by an excitation of the OH fundamental vibrations the authors adopted an approach referred by them as "messenger" detection [56]. The idea was to investigate water clusters with an H_2 molecule attached in a hope that in the weakly-bound complex with H_2 the properties of the hydrated hydronium ions are not perturbed too greatly. After IR excitation the H_2 "messenger" unit is knocked away from the cluster allowing to use consequence spectroscopic detection. The spectra obtained for $\text{H}_2\text{-H}_7\text{O}_3^+$ and $\text{H}_2\text{-H}_9\text{O}_4^+$ were a clear improvement of Schwarz's low resolution spectra of H_7O_3^+ and H_9O_4^+ obtained by direct absorption in a pressure controlled pulsed radiolysis cell [13]. However the tractability of the measurements still suffered somewhat from the presence of the "messenger", since H_2 is expected to reduce the characteristic frequencies of the OH bonds to which it is attached. These uncertainties were resolved in a benchmark work from the same group that introduced the use of multiphoton IR dissociation for spectroscopic purposes [57]. A tunable IR laser is used to excite the complex vibrations and a fixed frequency CO_2 laser promotes the multiphoton dissociation of the clusters. By a proper choice of the CO_2 frequency and power it is possible to avoid dissociation from the clusters that were not excited by the tunable laser. With this method the spectra of $\text{H}_3\text{O}^+(\text{H}_2\text{O})_n$ ($n=1,2,3$) of impressing quality were recorded between 3550 to 3800 cm^{-1} [57].

There is a qualitative difference between $\text{H}_3\text{O}^+(\text{H}_2\text{O})_n$ and hydrogen clusters since the water ligands in the former do not need to be perturbed by the charge of the core to have their transitions IR active. Consequently in the $\text{H}_3\text{O}^+(\text{H}_2\text{O})_n$ clusters the vibrations correlating to the H_2O modes can remain strong, irrespectively in which solvation shell the water molecules are situated. For all three studied clusters the vibrations corresponding to the antisymmetric and symmetric OH stretches of the outer H_2O groups were observed.

Besides for H_7O_3^+ the vibration of the unbound OH bond of the H_3O^+ core was seen, though rather weakly. The antisymmetric H_2O vibration in H_5O_2^+ displayed rotationally resolved substructure ($\Delta K=\pm 1$ transitions). Comparison of the spectra recorded with "messenger" technique and by multiphoton dissociation revealed that the spectra are drastically different for H_5O_2^+ and $\text{H}_2\text{-H}_5\text{O}_2^+$. The distortion for the larger clusters also existed but it was not so dramatic. One suggested possibility to explain the large disparity between the H_5O_2^+ and $\text{H}_2\text{-H}_5\text{O}_2^+$ spectra was that the H_2 ligand manages to stabilize H_5O_2^+ in the C_s structure. The global minimum for free H_5O_2^+ corresponds to a C_2 structure [58-60] that has completely different vibrational frequencies from the C_s one. The authors concluded that the "messenger" technique certainly has a potential for obtaining low-resolution spectra of the ions which are not possible to study otherwise, however the "messenger" for such experiments should be selected with caution, the smaller is the binding energy of the "messenger" to the rest of the cluster the better. For example the spectra of the $\text{H}_3\text{O}^+(\text{H}_2\text{O})_n\text{-Ne}$ clusters (recorded in the channel corresponding to the loss of the Ne atom) looked more similar to those of $\text{H}_3\text{O}^+(\text{H}_2\text{O})_n$ [57].

An extension of the two aforementioned studies of hydrated hydronium ions complexed with H_2 was published [61] which additionally included clusters of the type $(\text{H}_2)_n\text{-H}_3\text{O}^+$ ($n=1,2,3$). The spectra were readily interpreted in terms of the hypothesized structures wherein H_2 molecules form T-shaped hydrogen bonds with the hydronium ion. Observed transitions corresponded to the excitation of stretching vibrations of H_2 and bound and free OH bonds. The red shifts in the H_2 absorptions in $(\text{H}_2)_n\text{-H}_3\text{O}^+$ ($\approx 100\text{ cm}^{-1}$) were substantially smaller than the respective values for the hydrogen cluster series indicating that the H_2 's are bound less strongly to the H_3O^+ ion. The OH stretches were found to shift by as much as $200\text{-}400\text{ cm}^{-1}$ upon the hydrogen bond formation (here the "messenger" technique is absolutely inappropriate). The most exciting result of this study was the partial resolution in the H_2 and free OH bands. In the former P, Q, and R branches of a parallel type band were half resolved, with the rotational spacings being in rough agreement with theoretical predictions. In the latter numerous Q branch looking features characteristic of a perpendicular vibrations were observed. Though the low resolution of the laser (0.75 cm^{-1}) used in that study prevented the derivation of reliable structural information, it was demonstrated that vibrational predissociation in ionic complexes can be slow enough to render the absorption bands rotationally resolved. From doubling of the PR branch lines of the H_2 band and irregular distribution of the Q branches in the free OH band, the authors speculated that the complex experiences tunneling motion of the H_2 subunit as well as the umbrella motion of H_3O^+ . In the spectra of the $(\text{H}_2)_2\text{-H}_3\text{O}^+$ and $(\text{H}_2)_2\text{-H}_3\text{O}^+$ clusters no individual rotational lines were resolvable. From the observed fragmentation patterns an average binding energy between H_2 and H_3O^+ of $13\text{-}16\text{ kJ/mol}$ was estimated.

- Introduction -

Recently an attempt was made to reinvestigate the H_5O_2^+ and H_9O_4^+ clusters under higher resolution ($3 \times 10^{-5} \text{ cm}^{-1}$) [62]. For H_5O_2^+ in the antisymmetric stretching region many more lines than expected for a single vibration-rotation band of rigid molecule were observed. Though the signal-to-noise ratio in the spectrum was quite low and there were unfilled gaps due to the atmospheric water absorptions all the observed spectral features could be grouped in branches with line spacing only 14 % less than the *ab initio* B+C value. The complication in the infrared spectrum were attributed to splitting caused by tunneling between equivalent structures. In the spectrum of H_9O_4^+ individual rotational lines were not resolved. However the incompletely resolved features in the P and R branches were spaced by the expected order of magnitude.

Another important system studied with use of multiphoton dissociation spectroscopy is the ammoniated ammonium cluster series $\text{NH}_4^+(\text{NH}_3)_n$ ($n=1-10$) [63, 64]. From theoretical calculations [65] as well as on the basis of comparison with related systems it is expected that for the smaller clusters strong hydrogen bonds will be formed between the nitrogen atoms of the ammonia molecules and hydrogen atoms of the NH_4^+ core. For larger clusters secondary solvation shells will be formed and interactions between the solvent molecules will become important. There are many parallels in the spectra of $\text{NH}_4^+(\text{NH}_3)_n$ and $\text{H}_3\text{O}^+(\text{H}_2\text{O})_n$ clusters [4]. As in the case with the hydrated hydronium clusters, in the $\text{NH}_4^+(\text{NH}_3)_n$ spectra both absorptions due to the NH_4^+ core and weaker ones due to the ammonia molecules are observed. Apart from this there is a fairly distinct grouping of the vibrations reflecting solvation of the core in a shell-like order. The vibrational bands associated with the core vibrations involved in the hydrogen bonds are significantly shifted from the respective ammonium frequencies. On the other hand the transitions involving NH_3 molecules in the first solvation shell, which becomes fully completed at $n=4$, are less influenced unless they are themselves involved in the hydrogen bonding with the second shell ligands. For the smaller clusters the strongest feature in the spectrum arises from an antisymmetric stretching mode involving the core NH oscillators bonded to the first shell ligands only. This feature gets smaller as the size of the clusters progressively increases since the number of the core NH bonds not influenced directly by the second shell ligands drops, and at $n=8$ the band fades completely. Instead starting at $n=5$ and becoming dominant at $n \geq 7$ there appears another vibration assigned as the NH stretching modes of the core involved in hydrogen bonding to both the first and the second shell ligands. It is really astonishing how large can be the influence of the second shell ligands on the core frequencies in the hydrogen bonded systems. Another strong series of transitions also apparent in the larger clusters corresponds to the vibrations of the NH bonds of the first shell ammonia molecules connected to the second shell ones. Vibrations of the bonds *not involved* in the hydrogen bonding appear to be considerably weaker in intensity. The most interesting of them is the vibration of the first solvation shell molecules correlating to the doubly degenerate antisymmetric stretch of the free ammonia (ν_3), since it provides a

compelling evidence that the ammonia molecules are capable of free internal rotation about the N-H...N axes. Such a vibration, if considered for a single NH₃ molecule, generates an oscillating dipole moment in the direction perpendicular to the N-H...N axis. The corresponding band is composed of a number of resolved subbands interpreted as $\Delta K = \pm 1$ transitions between the internal rotational states of the NH₃ ligand. For larger clusters the internal rotational substructure starts to wash out and disappears for $n \geq 7$ because the second shell ligands tend to restrain this degree of freedom. Well-defined trends exist for the measured vibrational frequencies for both core and solvent vibrations in the ammoniated ammonium clusters. The vibrations of the bonds involved in extensive hydrogen bonding show a gradual blue shift which converge at large n ($n \approx 9, 10$). Overall, the main conclusion of this study is that there is a well-defined shell structure in NH₄⁺(NH₃)_n in agreement with both theoretical [65] and thermochemical data [66]. The first solvent shell is completed by four ligands, and the main step towards the second shell formation ends at $n = 8$. Though it is not clear yet what binding sites are occupied by the next ligands most probably they will try to connect to the free NH bonds of the first shell ammonia molecules. For further discussion of NH₄⁺(NH₃)_n, H₃O⁺(H₂O)_n, and mixed NH₄⁺(NH₃)_n(H₂O)_m clusters see ref. [4].

Several vibrational predissociation spectroscopy papers appeared in press recently addressing the question of nonclassical bonding. Nonclassical bonding involves a two-electron three-center bond and can occur for certain carbonium ions such as protonated acetylene C₂H₃⁺, protonated ethylene C₂H₅⁺, protonated ethane C₂H₇⁺, etc. The common feature of nonclassical ions is that they include pentacoordinated carbon atoms. Recent calculations generally conclude that bridged (nonclassical) structures are more stable than the classical ones for the three carbonium ions mentioned above (see [67] for references). For C₂H₃⁺ the preference for the bridged structure has been proven spectroscopically [68-70] though it was found that the three hydrogen atoms in the ion participate in a continuous pseudorotational exchange. Classical and bridged structures of C₂H₇⁺ can be considered as two stable intermediates of the reaction



The classical form of C₂H₇⁺ can be thought of as a complex between C₂H₅⁺ and molecular hydrogen. Yeh et al [67] conducted vibrational predissociation experiments on C₂H₇⁺, producing it by an electron impact on hydrogen supersonic expansion doped with C₂H₆. The photodissociation spectrum (C₂H₇⁺ → C₂H₅⁺ + H₂) that they observed showed a strong dependence on the ratio of ethane to hydrogen and on the backing pressure. By systematically varying the experimental conditions the authors were able to separate the observed vibrational transitions into two connected groups which they attributed to the absorptions of the co-existing classical and bridged forms of C₂H₇⁺. Again the H₂ stretching vibration of the classical form occurring at 3964 cm⁻¹ displayed a partial

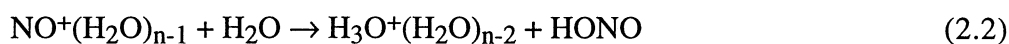
resolution of rotational structure. Agreement between the theoretical and experimental frequencies for the two forms of $C_2H_7^+$ was in some cases rather poor demanding for new theoretical studies.

Further spectroscopic studies of pentacoordinated carbon concentrated on protonated methane, CH_5^+ . There was much debate in the recent literature concerning the position of the global minimum on the CH_5^+ potential energy surface (staggered C_s , eclipsed C_s , or C_{2v}) and the degree of floppiness of the ion. The currently accepted views agree on the fact that the energy differences between the three configurations are extremely small, and as a result CH_5^+ does not have a unique, stable equilibrium structure, with the hydrogen atoms scrambling freely among the multiple equivalent minima [71-73]. Because of the extremely fast hydrogen atom exchange (scrambling) the notion of a localized two-electron three-center bond is not quite applicable to CH_5^+ [72] but traditionally it is considered to be the simplest non-classical ion. The binding energy of CH_5^+ is apparently too high [72] to study it with vibrational predissociation methods even if multiphoton dissociation is utilized. However, Lee and coworkers succeeded in systematic study of CH_5^+ complexed with a variety of neutral ligands including H_2 [74-76] and Ar, N_2 , and CH_4 [77]. For the $(H_2)_n-CH_5^+$ ($n=1-6$) series, the vibrations of the CH_5^+ core as well as H_2 stretches of the ligands were observed in the photodissociation spectra [75]. From the reduction in the widths of the CH_5^+ spectral features with cluster size the authors concluded that the scrambling of the core hydrogen atoms slows down considerably in the clusters. For $n \geq 3$ the core is effectively frozen in an $e-C_s$ structure as follows from comparison between the experimental and predicted vibrational frequencies [75]. The intensity and red shift of the H_2 stretching vibration both decrease with cluster size indicating a gradual delocalization of positive charge of the CH_5^+ core. A linear correlation was found between the H_2 stretching frequencies and the values of $-\Delta H^0$ for the clustering reactions $(H_2)_{n-1}-CH_5^+ + H_2 = (H_2)_n-CH_5^+$ available for ref. [78]. This correlation suggested that the H_2 frequency shift can be used as a convenient measure of the electrostatic interaction between a solvent H_2 molecule and the rest of the cluster. As for quite a few of H_2 containing complexes the H_2 stretching bands of $H_2-CH_5^+$ and even $(H_2)_2-CH_5^+$ had the traces of rotational resolution.

Similar conclusion concerning the degree of CH_5^+ hydrogen atom scrambling were reached from the spectra of $CH_5^+(A)_x(B)_y$ ($A, B = Ar, N_2, CH_4$; $x, y = 0-5$) [77]. The strength of the ligand-core interactions and consequently the steadiness of the core decreased in the row $CH_4 > N_2 > Ar$. The CH_5^+ core of the $CH_5^+(CH_4)_{n \geq 3}$ was regarded as rigid. For complexes stabilized by the N_2 and CH_4 ligands the HH stretching band of the CH_5^+ core was found in the $2500-2700\text{ cm}^{-1}$ region proving that two-electron three-center bond exists in these clusters.

In contrast to the extremely stable CH_5^+ ion the minimum energy structures of SiH_5^+ [79] and GeH_5^+ [80] correspond to a complex between SiH_3^+ (or respectively GeH_3^+) and H_2 , with the H_2 unit rotating freely around the symmetry axis of the core. The barriers for the scrambling motion via the C_{2v} transition state were predicted to be quite high, unlike the case of CH_5^+ , leading to completely different spectroscopic properties of the siliconium and carbonium ions. These theoretical predictions were supported by the observation of the vibrational predissociation spectra of the H_2 stretching vibrations of SiH_5^+ [81] and SiH_7^+ [82]. The spectrum of SiH_5^+ centered at 3694 cm^{-1} was rotationally resolved sufficiently well to allow testing the structure predictions of the *ab initio* calculations [79]. However it was found that the intensities of individual rotational lines were affected by the CO_2 multiphoton dissociation because the density of states at the level of the H_2 vibrational energy is not sufficiently high to make them quasicontinuous. Unfortunately, the fine structure of the P and R branch lines was not resolved in the experiment, preventing estimation of the height of the barrier for the H_2 internal rotation. The H_2 stretching vibration of SiH_7^+ was observed at 3866 cm^{-1} , shifted to the blue of the SiH_5^+ band by near 150 cm^{-1} . The band profile contained well developed P, Q, and R branches of the type encountered in parallel transitions of symmetric top molecules. The parallel structure of the band was explained by assuming that the transition corresponds to the out-of-phase vibration of two H_2 oscillators, with the H_2 ligands bound to opposite faces of the SiH_3^+ ion, equidistant from the Si atom. The proposed SiH_7^+ structure is completely different from that assumed for CH_7^+ reflecting differences between SiH_5^+ and CH_5^+ mentioned above.

Vibrational predissociation spectroscopy has found an interesting application for the studies of intracuster hydration reactions within certain cluster ions. Choi et al [83] have measured the spectra of $\text{NO}^+(\text{H}_2\text{O})_n$ clusters, $n=1-5$, between 2700 and 3800 cm^{-1} . They observed that the clusters with $n\leq 3$ could be photodissociated by knocking away one water molecule. For them only symmetric and antisymmetric stretch modes of water ligands were observed in the spectrum. For the $\text{NO}^+(\text{H}_2\text{O})_4$ cluster, the loss of one and also two water molecules was still the major dissociation channel, however some amount of H_7O_3^+ fragment ions corresponding to the loss of HONO was observed as well. The spectrum of $\text{NO}^+(\text{H}_2\text{O})_4$ contained similar water bands and in addition three new very broad bands appeared. For $\text{NO}^+(\text{H}_2\text{O})_5$ the loss of HONO molecule became the dominant photodissociation channel and its spectrum was markedly different from the others. In the spectrum one could identify the bands associated with the vibrations of hydrated H_3O^+ , solvent water molecules, and HONO. From their experimental observations and accompanying *ab initio* calculations the authors [83] concluded that, while the smaller clusters ($n\leq 3$) can be represented by the formula $\text{NO}^+(\text{H}_2\text{O})_n$, the larger ones undergo intracuster rearrangement corresponding to the reaction



Starting from $n=5$, the HONO unit is pushed out in the outer solvation shell and NO^+ stops to be the core of the cluster, which is now represented by the formula $\text{H}_3\text{O}^+(\text{H}_2\text{O})_{n-2}(\text{HONO})$. An onset of this transformation is seen already in the $n=4$ cluster. Studied in a similar spirit was the size dependence of photodissociation pattern of the $\text{NO}_2^+(\text{H}_2\text{O})_n$ ionic clusters [84, 85]. For this cluster series the same behavior was observed, with small clusters having the structure of $\text{NO}_2^+(\text{H}_2\text{O})_n$ and larger clusters ($n \geq 4$) being transformed into $\text{H}_3\text{O}^+(\text{H}_2\text{O})_{n-2}(\text{HNO}_3)$. Such processes have important implications for atmospheric chemistry because they may substantially accelerate the hydration of H_3O^+ . Unfortunately no other vibrational predissociation studies of this sort have so far appeared.

Lisy and co-workers [86] have studied infrared dissociation of relatively large clusters of Cs^+ and Na^+ with methanol, water, and ammonia. Initially the spectra were observed in a depletion mode using a line tunable CO_2 laser for the excitation of CO stretching vibration in CH_3OH or NH bend in NH_3 ligands [87]. After modifications done with the setup it became possible to use the "consequence" photofragment detection, and a LiNO_3 OPO laser extended the range of solvent vibrations that can be probed by this method [88]. Since the clusters that they produce have a significant content of internal energy and their dissociation can occur after absorption of a single infrared photon [86], infrared band centers observed in the spectra may be somewhat different from the frequencies of respective cold clusters. However it is possible to draw certain conclusions about the changes in solvation mechanisms from the consideration of size dependent trends. In this way studies of the $\text{Cs}^+(\text{CH}_3\text{OH})_n$ series ($n=4-25$) [87, 89] have demonstrated the existence of shells in the solvation processes. The first solvation shell is believed to be completed at $n=10$. Methanol molecules in the second shell ($n=11-18$) interact with the first shell ones and have somewhat different CO frequency leading to a new set of bands in the spectrum. Finally for $n \geq 18$ a third feature appeared corresponding to the absorptions of bulk methanol. To get an idea about the role of ion size in the solvation mechanisms of ions, the CO stretching vibrations of $\text{Na}^+(\text{CH}_3\text{OH})_n$ series ($n=3-24$) were studied as well [90]. It was expected that the smaller size of Na^+ will lead to a more compact first solvation shell. Indeed it was found that the first solvation shell in the $\text{Na}^+(\text{CH}_3\text{OH})_n$ clusters is filled already at $n=6$. Besides, the number of distinct methanol environment in the Na^+ based clusters seemed to be larger as well. While Cs^+ has only one on the way from the first solvent shell to the bulk-like environment, Na^+ appears to have two, reflecting stronger influence of smaller ions on the ligands in the outer shells. In a subsequent study of $\text{Na}^+(\text{NH}_3)_n$ ($n=6-12$) clusters [91] it was found that the first solvation shell fully develops at $n=6$ as for the methanol clusters. However the onset of liquid-like behaviour occurs much earlier, already at $n > 9$, implying that the sodium ion has a much larger disruptive effect on the hydrogen bonding between the solvent methanol molecules than for the ammonia ones.

More recent studies from the group were concerned with excitation of OH stretching vibrations in $\text{Cs}^+(\text{CH}_3\text{OH})_{1-6}$ [88], $\text{Na}^+(\text{CH}_3\text{OH})_{2-7}$ [92], and $\text{Cs}^+(\text{H}_2\text{O})_{1-5}$ [93], and also with mixed clusters $\text{Cs}^+(\text{CH}_3\text{OH})_n((\text{CH}_3)_2\text{O})_m$ [94]. For the latter it was found that methanol molecules are always observed in the first solvation shell in spite of larger binding energy between Cs^+ and acetone. Such behavior was attributed to the ability of methanol molecules in the first shell to form hydrogen bonds to the second shell acetone and methanol molecules, which resulted in a better stabilized cluster. From the studies of OH stretches in $\text{Cs}^+(\text{CH}_3\text{OH})_n$, $\text{Na}^+(\text{CH}_3\text{OH})_n$, and $\text{Cs}^+(\text{H}_2\text{O})_n$ the frequencies of which are very sensitive to the degree of hydrogen bonding in the clusters a very surprising result was obtained. It appears that the solvent molecules are able to form hydrogen bonds between each other already before the first solvation shell is completed. For $\text{Na}^+(\text{CH}_3\text{OH})_n$ the onset of hydrogen bonding was observed $n=4$ and the first manifestations of it for $\text{Cs}^+(\text{CH}_3\text{OH})_n$ were evident at $n=3$. For $\text{Cs}^+(\text{CH}_3\text{OH})_6$ all OH bonds are involved in hydrogen bonding [88]. Certain structural features in the spectra could be assigned to the dimer, trimer, and tetramer methanol substructures within the cluster ions. Some structural isomers existed too. Apparently the study of these $\text{M}^+(\text{solvent})_n$ systems is far from completion.

Dietrich et al [95] have studied multiphoton photodesorption of methanol molecules from $\text{Au}_4^+(\text{CH}_3\text{OH})_{1-3}$ initiated with a CO_2 laser. An evidence was obtained that contrary to the complexes of Cs^+ , the methanol molecules in $\text{Au}_4^+(\text{CH}_3\text{OH})_{1-3}$ do not interact. From the power dependence of the fragment ion current the number of photons required to dissociate a particular sized cluster was determined. From this, with help of the classical version of Kassel's theory, the desorption energy was estimated as 0.6 ± 0.1 eV, which is larger than either evaporation enthalpy of liquid methanol (0.37 eV) or desorption energy of CH_3OH from a Au surface (0.52 eV) [95].

In a series of papers a special class of ionic clusters which represent associations of a single IR active neutral chromophore with mass-selected cluster ions was studied by IR photofragmentation spectroscopy. Due to the disparity in ionization potentials the charge in $\text{SF}_6(\text{NO})_n^+$ [96], $\text{SF}_6\cdot\text{Ar}_n^+$ [97, 98], $\text{SF}_6(\text{C}_6\text{H}_6)_n^+$ [99], $\text{C}_2\text{H}_4(\text{NO})_n^+$ [100], $\text{SF}_6(\text{CO}_2)_n^+$ [101] does not reside on the chromophore but rather on the X_n^+ cluster component. Studies of such systems are of interest since they allow direct comparison with the related neutral clusters, like $\text{SF}_6\cdot\text{Ar}_n$, which are subjects of an extensive research [102, 103]. By monitoring the photofragmentation channels and efficiency in conjunction with other aspects of cluster ion behavior it is possible to relate the spectra to the structure and decay dynamics of the cluster. In this way it was found that $n=21$ cluster is particularly stable in the $\text{SF}_6\cdot\text{Ar}_n^+$ series, and that there are structural isomers starting with $n \geq 40$. In $\text{SF}_6(\text{C}_6\text{H}_6)_n^+$ clusters the SF_6 unit resides on the surface of the $(\text{C}_6\text{H}_6)_n^+$ cluster. The clusters $\text{SF}_6(\text{NO})_n^+$ and $\text{C}_2\text{H}_4(\text{NO})_n^+$ preferably dissociate into products containing an odd number of NO's,

which are even electron systems, and are probably more stable due to the effect of pairing of NO electrons. The $(\text{NO})_3^+$ subunit is believed to serve as a core in these clusters.

Ever-growing amount of spectroscopic information about ionic complexes and clusters is obtained with ZEKE and related techniques. For comprehensive reviews on the topic the reader is referred to ref. [29, 104]. The first step in ZEKE spectroscopy corresponds to a laser excitation of a neutral molecule or intermolecular complex to a Rydberg state lying just below one of the neutral's rovibronic ionization thresholds. Then some time is given for the kinetic electrons resulting from the direct ionization to escape the area and after this the Rydberg-states are field ionized. The number of the resulting low kinetic energy electrons is detected as a function of the laser excitation frequency. The positive ions can also be detected in coincidence with ZEKE electrons, such combined experimental method is known under the name MATI (Mass Analyzed Threshold Ionization). ZEKE methods routinely provide 2-3 orders of magnitude better resolution than the conventional photoelectron spectroscopy. Among the systems investigated with the method van der Waals complexes of aromatic molecules (benzene, toluene, etc.) with rare gases and also hydrogen bonded complexes between phenol and simple organic solvents seem to prevail [29]. Information about the strength of the intermolecular interactions is derived from the differences in the ionization potentials of the free and complexed chromophores, and frequencies of the intermolecular vibrations. However some studies of smaller systems like $(\text{NO})_2^+$ [105] and Ar-NO^+ start to appear as well.

Spectroscopic studies utilizing indirect dissociation following visible or UV photoexcitation in a quasibound electronic state are quite numerous, particularly for metal containing species [24]. Because of a strong $2\text{P} \leftarrow 2\text{S}$ atomic transition in Mg^+ lying at the experimentally convenient wavelength of 280 nm, it became one of the most popular metal ion chromophores [106]. Effect of adding a ligand to Mg^+ is different for 2P and 2S atomic states resulting in a shift of the complex's absorption origin from the respective atomic transition. Interaction in the $\text{Mg}^+\text{-L}$ complexes is primarily electrostatic, and for the 2P state its strength depends on the mutual orientation of the singly-populated p-orbital of Mg^+ and the intermolecular axis. When the p-orbital is lying on the axis the positive charge of the Mg^+ core is shielded by the additional axial electron density which lessens the electrostatic interaction. On contrary when the p-orbital is perpendicular to the axis the shielding is smaller and the interaction is stronger. For linear $\text{Mg}^+\text{-L}$ complexes 2P atomic state transforms into 2Π and 2Σ molecular states, with the former lying substantially lower on the absolute energy scale. The complex's transitions $2\Pi \leftarrow 2\Sigma$ and $2\Sigma \leftarrow 2\Sigma$ are respectively red- and blue- shifted with respect to the atomic line. Due to the change in the binding energy between the lower and the upper electronic states, the $2\Pi \leftarrow 2\Sigma$ transitions have enriched vibrational structures. In many cases a sufficient number of vibrational states is observed to allow the determination of binding energy by means of Birge-Sponer extrapolation. For

example for Mg⁺-Ar complex binding energies for the ²Σ⁺ and ²Π_{1/2} states were derived as 1281 and 5554 cm⁻¹ [107, 108]. Respective values for the isoelectronic complex NaAr are 40 and 568 cm⁻¹ reflecting the magnitude of the electrostatic enhancement in the interaction strength. It was possible to record the photodissociation spectrum of Mg⁺-Ar on the level of rotational resolution [109]. It was found that the complex contracts by as much as 0.36 Å upon excitation in agreement with the previous assessment of the large binding energy difference. In other linear complexes of Mg⁺ such as Mg⁺-N₂ [110] and Mg⁺-CO₂ [111] similar trends were observed, though binding energies there are considerably higher. For water solvated ions Mg⁺-OH₂ [106, 112] the obtained binding energies are very high (≈100 and 190 kJ/mol in the lower and in the upper state) demonstrating an onset of chemical bonding in the complex. Ca⁺-Rg [113, 114] and Ca⁺-OH₂ [115] complexes, studied using a similar experimental strategy, are generally less strongly bound than their Mg⁺ brothers because of the reduced strength of the electrostatic interaction.

Photoexcitation in certain metal containing systems may lead to *reactive* dissociation. For example in Mg⁺-CO₂ complex MgO⁺ products are detected following the ²Σ⁻←²Σ electronic transition in addition to the expected Mg⁺ ions [111]. In the Mg₂⁺-(CO₂)_{1,2} complexes [116, 117] Mg₂O⁺ and Mg₂⁺ photofragments are observed in addition to Mg⁺. In free Mg₂⁺, the photodissociation proceeds in a direct way via a bound-repulsive ²Σ_g⁺←²Σ_u⁺ transition. The observation of the Mg₂O⁺ and Mg₂⁺ products is interpreted to result from a "cage effect" of the CO₂ solvents.

Other Metal⁺-Ligand system extensively studied by electronic predissociation spectroscopy methods are complexes of V⁺, Co⁺, Cr⁺, and Ni⁺ with Ar, Kr, H₂O, and N₂ [24]. There too, most of the spectra show a number of resolved vibrational transitions, allowing to obtain harmonic frequencies, anharmonicities, and dissociation energies for the upper and in certain cases the lower electronic states. For example derived adiabatic ground state dissociation energies of Co⁺-Ar and Co⁺-Kr are determined as 4100 and 5400 cm⁻¹. For other complexes in this series comparable values are obtained (Table III of ref. [24]). Some rotationally resolved spectra of these systems appear in press as well. From the Co⁺-Kr spectrum the ground state intermolecular separation of 2.447 Å was derived from the analysis of the rotational structure of the a¹Δ₂ ← X³Δ₃ band [118].

Finally, the studies in the present laboratory also contributed to the body of information on dissociation spectroscopy of ionic complexes [28]. Selected photodissociation studies in the IR range form the subject of this thesis and few examples of electronic photodissociation spectra are briefly reviewed here. The largest amount of attention was devoted to the weakly bound complexes between N₂⁺ ion and either He [119-122] or Ne [123, 124] rare gas atoms. The N₂⁺ molecular ion has a very strong B←X electronic transition at around 391 nm and it is used as a chromophore in the complexes.

The corresponding transition in N_2^+ -He is almost unshifted from that of the monomer implying more or less equal influence of the complexation on the electronic term energies in the X and B states. The transition contains rotational features corresponding to $\Delta J = \pm 1$ transitions in free N_2^+ with intensities obeying even-odd nuclear spin alternation, as proven by $^{15}N/^{14}N$ substitution experiments [122]. The signatures of the free internal rotation persist for complexes as large as N_2^+ -He₆ [120]. The experimental results are in good agreement with existing *ab initio* calculations predicting an unhindered internal rotation of N_2^+ in the He- N_2^+ complex [2]. Through the observation of 1_1^1 sequence band it was possible to estimate the lifetimes of N_2^+ -He_n clusters in the X($v_1=1$) state which for n=1 complex was as large as 220 μ s [121]. For neutral vdW complexes lifetimes of this order of magnitude are difficult to measure experimentally and only the lower bounds for the lifetimes of extremely long-lived species are usually available [125]. The N_2^+ -He is one of the most weakly bound ionic complex studied to date by spectroscopic methods. The complex N_2^+ -Ne was found to be significantly more strongly bound. Only when the internal temperature of the complex was sufficiently large the signatures of free internal rotation of N_2^+ unit became apparent [123, 124]. Cold complexes appeared to possess a well defined linear structure with intermolecular stretching frequency in the B state of at least 100 cm^{-1} . Another interesting system studied in the group is the odd nitrogen cluster series N_{2n+1}^+ . Localized absorptions lying near the N_3^+ $A^3\Pi \leftarrow X^3\Sigma_g^-$ transition [126] observed for the clusters with n=2-7 were interpreted as an evidence that the N_3^+ ion plays a role of the chromophore core in the clusters [127]. This is markedly different from the even-sized series N_{2n}^+ which can be photofragmented in a broad range of the spectrum due to the direct photodissociation of the N_4^+ chromophore [128].

3. Objective of the thesis

As obvious from the discussion above, spectroscopy of ionic complexes and clusters is an exciting and rapidly developing field. Scientists try to approach the problem by various means, including photodissociation, fluorescence, ZEKE, photodetachment, and other techniques, obtaining spectra of the complexes of miscellaneous quality and information content. However the number of rotationally-resolved spectra is still rather low. Three years ago, at the time this project was initiated, there was just one ionic complex, ArH_3^+ , studied in high resolution. Investigation of complexes at the rotationally-resolved level is extremely valuable since it provides much better understanding of their structures, dynamics, and intermolecular forces holding the complexes' constituents together. With this in mind a series of relatively simple complexes with well studied ionic IR chromophores was selected for the present study. To avoid complications related to the ligand absorptions they were confined to inert gases He, Ne, and Ar and to molecular hydrogen. It was hoped that the investigation of systematic trends in the spectroscopic properties of this simple series of complexes would cast light on the fundamental aspects of ion-neutral long-range

interactions. The main objective of this work was the foundation of a firm platform for understanding the spectra of more complicated systems, spectra of which are to be recorded in future.

4. Information pertaining to data analysis

4.1. Spectroscopy of chromophore ions

4.1.1. General

Useful compilation of spectroscopic properties of transient species containing more than 3 atoms including positive and negative ions has been composed by Jacocs [129]. Review of IR and microwave spectroscopic works on ions and radicals prior to 1992 is available from ref. [130]. Here only the spectroscopy of the ions relevant for this study is surveyed. IR active vibrations of HN_2^+ , HCO^+ , and NH_4^+ molecular ions serve as chromophores in their clusters with rare gases and molecular hydrogen $\text{Rg}_n\text{-I}^+$ and $\text{H}_2\text{-I}^+$.

4.1.2. The HN_2^+ ion

An excellent review devoted solely to HN_2^+ is available which encompasses all spectroscopic, chemical, and thermochemical studies of this ion prior to 1992 [131]. The HN_2^+ ion is linear in the ground $^1\Sigma^+$ state and possesses no low lying electronic states. The ground state dissociation energy $D_0(\text{N}_2\text{-H}^+)$ with respect to N_2 and H^+ fragments was estimated theoretically to be around 490 kJ/mol [132]. The enthalpy change of this dissociation reaction measured at 298K is defined as the proton affinity (PA) of N_2 . The currently recommended value for the molecular nitrogen's PA is 494.5 kJ/mol [133]. In the laboratory studies this ion is usually generated by the $\text{H}_3^+\text{+N}_2$ proton transfer reaction in a glow or hollow cathode discharge.

Both HN_2^+ and its isoelectronic brother HCO^+ probably belong to the best characterized molecular ions both chemically and spectroscopically. Much interest in their spectroscopy comes from their apparent importance in chemical processes in hydrogen containing plasmas, flames, and in the interstellar space. Spectral lines of HN_2^+ were first detected by radioastronomy in 1974 [134] in the spectrum of a dense interstellar cloud and shortly after the proposed assignment [135] was confirmed by recording a laboratory microwave spectrum of this ion [136]. Further work in the microwave area of the spectrum allowed to obtain high quality ground state molecular constants [137-140] and the ion's substitution structure [141, 142]. The seven hyperfine components of $J=1\leftarrow 0$ transition arising from non zero nuclear spin on the inner and outer nitrogen atoms were fully resolved by Cazzoli et al [143]. It is probably the highest resolution spectrum available for this ion.

- Introduction -

The first report of an infrared spectrum of HN_2^+ appeared in 1983 when Gudeman et al [144] observed the strongest ν_1 fundamental of the ion. Later Nesbitt et al observed the respective ν_1 band and in addition the $\nu_1+\nu_2-\nu_2$ sequence transition for DN_2^+ [145]. The ν_1 band was also studied by FTIR method [146], with HN_2^+ being one of a few ions for which gas phase FTIR spectra are available. Foster and McKellar [147] detected the NN stretching fundamental (ν_3) of HN_2^+ and of its deuterated isotopomer. Sears studied the ν_2 band of both HN_2^+ [148] and DN_2^+ [149] with a tunable-diode laser spectrometer. Owrutsky et al [150] used a color center laser to extend the observed J range for the HN_2^+ ν_1 transition and detect the $\nu_1+\nu_2-\nu_2$ combination band. They combined their data with the majority of previous infrared and microwave measurements and determined the best available equilibrium structure for this ion and very accurate rotational constants for the ν_1 band [150]. The first overtone of ν_1 was observed by Sasada and Amano with a distributed feedback semiconductor laser [151]. Relatively high intensity of the overtone transition comes from the appreciable anharmonicity of the ν_1 stretching vibration, common for the XH bonds. Ho et al [152] performed an elegant infrared-microwave double resonance experiment on HN_2^+ ion which provided highly accurate rotational and l -doubling constant for the ν_2 vibrational state. Finally, Kabbadj et al [153] in their arduous study investigated the HN_2^+ ion in a white cell under the conditions promoting the formation of vibrationally hot ions. They could observe a number of new sequence bands build on ν_1 originating from the vibrational levels lying as high as 7000 cm^{-1} above the ground state of the ion. Rovibrational constants (harmonic frequencies, anharmonicities, rotational constants, etc.) and rovibrational level energies obtained in this work are probably the most complete and accurate available today. Theoretical force constants for NH and NN stretching and HNN bending vibrations as well as for the stretch-stretch and bend-bend interactions are available from high-quality *ab-initio* calculations [132, 154]. From these, the harmonic stretching frequencies for all chemically significant isotopomers were predicted [132]. No electronic spectrum of HN_2^+ has been observed yet. Calculated vertical excitation energies for transitions into the low-lying electronic states all exceed 7 eV. For more information about the calculated electronic spectrum of HN_2^+ see ref. [131].

In addition to pure spectroscopic studies of HN_2^+ a variety of experiments related or involving spectroscopy have been conducted with this ion. Apart from its chemical importance the reason for the ion's popularity is the ease of its production in a laboratory and the relative strength of its infrared transitions. Pursel et al [155] studied the collision-induced rotational transitions in HN_2^+ as compared to HCN using double resonance spectroscopy and found a modest difference in collisional propensity rules for charged vs. neutral systems. Intensity of the ν_1 band of HN_2^+ as well as that of HCO^+ was measured by direct absorption measurements of integrated band intensities in fast ion beams [156, 157]. A number of studies concerned with observation of HN_2^+ in interstellar space is continuously increasing [158]. And finally, the spectra of this ion are often recorded to test

the performance of newly-designed ion sources [159-161]. In this work high intensity and large number of IR transitions in Ar-HN₂⁺ complex spectrum also served to optimize the conditions for maximum yield of other ionic complexes. Relevant spectroscopic information about the HN₂⁺ ion is collected in table 4.1.

4.1.3. The HCO⁺ and HOC⁺ ions

The HCO⁺ ion is isoelectronic with HN₂⁺ and as a consequence has a number of similar properties. It is linear and it has no electronic states within a few (≥ 9) electron volts from the ¹Σ⁺ ground state [162]. The electronic spectrum of this ion has not been observed yet. The astrophysical importance of this ion is unquestionable, historically it is the first molecular ion discovered in space, and besides, it is one of the most abundant ions in the dense interstellar clouds. Calculated binding energy with respect to H⁺ and CO fragments amounts to 589 kJ/mol [163] and recommended value for CO's proton affinity on carbon end is 594 kJ/mol [164] (it is one of the standards in the ladder of relative proton affinities).

The history of discovery and laboratory investigations of the HCO⁺ ion is in many ways similar to that of HN₂⁺. The rotational spectrum of this species was first observed by radioastronomy in 1970 [165] and the yet unidentified species was named X-ogen by the discoverers. Shortly after, on the grounds of structural considerations Klemperer [166] proposed that X-ogen is most probably HCO⁺ ion. This assignment was confirmed after 5 years by laboratory observation of rotational transitions of HCO⁺ [167]. A number of microwave studies followed aimed on obtaining accurate molecular constants for different isotopomers [168, 169] and deriving a reliable substitution structure [142, 169, 170] for this ion. The first IR observation of HCO⁺ was reported by Gudeman et al [171] in their pioneering paper introducing the technique of velocity modulation, that gave a tremendous impact to the development of molecular ion spectroscopy [172]. They observed 19 lines in the R branch of the ν₁ fundamental and assigned J values to individual lines such that the ground state rotational constant matched the microwave results. Amano [173] extended their studies by observing previously undetected P branch transitions and obtained more reliable rotational constants. The ν₁ transition of the deuterated isotopomer was studied in ref. [174]. The CO stretching fundamental was investigated independently by Davies et al [175] and Foster et al [176]. Respective studies for DCO⁺ were conducted by Foster and McKellar [147]. The bending mode of HCO⁺ was observed by Davies and Rothwell [177] and by Kawagutchi et al [178]. The rotational spectrum of HCO⁺ in ν₂=1 state was observed in ref. [179] They obtained highly accurate rotational and *l*-doubling constants for this vibrational state. Finally Liu et al [180] reported the spectra of the ν₃+ν₂-ν₂ and 2ν₃-ν₃ sequence hot bands. Because of the limited data the complete set of anharmonicities for HCO⁺ is not available as it is in the case of HN₂⁺ [153] and the situation is not likely to change in the near future. The problem may possibly come from the fact that in H₂/CO/He

- Introduction -

discharges typically used for producing HCO⁺ a number of other carbonaceous species is formed, that absorb at similar frequencies, whereas in the case of H₂/N₂/He discharges one can easily obtain conditions for the predominant production of the HN₂⁺ ions.

Table 4.1: Spectroscopic properties of HN₂⁺, HCO⁺, and HOC⁺

Included are the frequencies of fundamental vibrations, ground and v₁ state rotational constants, equilibrium and substitution structures, HX stretch intensity, and proton affinities of respective neutrals.

property of HXY ⁺	HN ₂ ⁺	HCO ⁺	HOC ⁺
v ₁ [cm ⁻¹]	3233.961	3088.740	3268.026
v ₂ [cm ⁻¹]	685.251	829.721	-
v ₃ [cm ⁻¹]	2257.867	2183.950	-
B ₀ [cm ⁻¹]	1.55397	1.48751	1.49250
B ₁ [cm ⁻¹] (for v ₁ =1 state)	1.54136	1.47570	1.48293
R ^e _{HX} [Å]	1.0336	1.0972	-
R ^s _{HX} [Å]	1.0314	1.0923	0.964
R ^e _{XY} [Å]	1.0928	1.1047	-
R ^s _{XY} [Å]	1.0954	1.1072	1.160
v ₁ intensity [cm ⁻² atm ⁻¹]	1880	580	-
-ΔH ²⁹⁸ (YX-H ⁺) [kJ mol ⁻¹]	494.5	594	431

The HOC⁺ isomer (isoformyl cation) has received much less attention than HCO⁺ probably because under typical experimental conditions it is quickly converted in the more stable HCO⁺ in collisions with either H₂ or CO molecules. According to a high quality *ab initio* calculation of Ma et al [163] HOC⁺ is less stable than HCO⁺ by 163 kJ/mol (this value corresponds roughly to the difference in proton affinities of oxygen and carbon ends of CO). The ion is also a linear closed shell species. The structure and ground state constants are available from microwave works [181-183]. From IR transitions only v₁ fundamental has been detected [184]. Relevant HCO⁺, HN₂⁺, and HOC⁺ spectroscopic properties are gathered in table 4.1.

4.1.4. The NH₄⁺ ion

The NH₄⁺ is a stable closed shell spherical top molecule. This ion plays a tremendous role in inorganic chemistry. It is readily formed in acidic aqueous solutions by means of protonation reaction with ammonia from where it can be crystallized in a number of salts. It is believed to be important in the interstellar chemistry [185], however due to the lack of the rotational spectrum there is no way to detect it by radioastronomy. The high stability of this ion is reflected in a very high proton affinity of ammonia measured as 852 kJ/mol [164].

The NH_4^+ ion belongs to the T_d symmetry group and as a consequence it has no dipole microwave transitions. Out of four fundamental vibrations only two are infrared active and both were investigated thoroughly by high resolution IR spectroscopy. The triply degenerate ν_3 fundamental was detected independently by Crofton and Oka [186] and by Schäfer et al [187]. In a later publication [188] more rotational transitions of the ν_3 transition were observed. Because of the nature of the transition in a triply degenerate vibrational state it was not possible to obtain separately the ground and excited state rotational constants, and therefore the structure of NH_4^+ could not be determined precisely from these three studies. However in the last study the positions of *forbidden* rovibrational transitions were predicted from a model Hamiltonian in which part of the parameters was taken from *ab initio* calculations. These weaker lines were subsequently detected [189]. In the same paper the ν_3 transition of the deuterated ammonia, ND_4^+ , was investigated. The obtained data allowed to calculate r_0 value of 1.0287 Å, while r_e was estimated to be 1.021 Å [189]. Another IR active fundamental of NH_4^+ , the triply degenerate ν_4 vibration, was studied in refs. [190, 191]. The ν_4 band was found to be heavily perturbed by the nearby ν_2 state. Measuring the ν_4 spectrum for the monodeuterated isotopomer NH_3D^+ [192] provided an independent estimation of the NH equilibrium bond length in excellent agreement with data from ref. [189]. Experimental values for the ν_1 and ν_2 fundamentals are not available. However there exists an accurate *ab initio* quartic force field [193] that reproduces the other two fundamentals with a very good precision. Table 4.2 provides the calculated NH_4^+ frequencies together with experimental ones and other relevant spectroscopic information.

Table 4.2: Spectroscopic properties of NH_4^+

property	exp.	theory*
ν_1 [cm^{-1}]	-	3236.6
ν_2 [cm^{-1}]	-	1690.1
ν_3 [cm^{-1}]	3343.139	3345.1
ν_4 [cm^{-1}]	1447.216	1447.2
B_0 [cm^{-1}]	5.929	
B_3 [cm^{-1}] ($\nu_3=1$)	5.876	
ξ_3 ($\nu_3=1$)	0.0604	
R_{HN}^e [Å]	1.0208	1.0203
R_{HN}^0 [Å]	1.0287	-
$-\Delta H^{298}(\text{YX-H}^+)$ [kJ mol^{-1}]	852	

* Theoretical predictions were taken from ref. [193]

4.2. Analysis of the observed spectra

For stable molecules, including ionic species, contributions to the total molecular level energies can be approximately separated in electronic, vibrational, and rotational ones, with smaller hyperfine corrections being treated in a perturbative way if they are relevant.

- Introduction -

Such a separation is justified by the disparate characteristic frequencies of the motions of the electrons within the molecule and rotations and vibrations of the nuclei. Electrons are thought to move so fast that they always have time to adjust themselves to any spatial and geometrical configuration adopted by the molecule's nuclei. This principle is widely quoted in spectroscopic and quantum-mechanical literature as Born-Oppenheimer separation. With this approximation a much simpler and more illustrative representation of the molecular wavefunctions and energies can be obtained than from the solution of the full problem. Rotations and vibrations of the nuclei can be separated from each other in a similar way since typical molecules can vibrate hundreds of times during the period of a complete rotation. This again leads to rather simple energy level expressions for the nuclear motion. To account for the actual existence of interactions between the rotations and vibrations special rather insignificant corrections are introduced in the approximate energy expressions. These principles have been used in the spectroscopic analysis of a number of stable molecules. On the whole for the purposes of this thesis, the spectroscopy of stable molecular species can be considered as a well established discipline.

These simple and illustrative views are not fully transferable to weakly bound van der Waals complexes. For them, the Born-Oppenheimer separation is as good (or as bad depending on the experimental precision) as for the stable molecules. However the separation of the vibrational and rotational motion does not always work quite well. Specifically, the motions correlating with the intermolecular bending vibrations can have characteristic frequencies comparable to the rotational ones and in the limit of infinitely small angular anisotropy of the intermolecular interaction they transform into internal rotations of the subunits. In this limit the energy of the system is additive and consists of the internal energies of each constituent and orientation-independent interaction energy. For real weakly bound systems absolutely free internal rotation is an unrealizable idealized limit, some degree of hindrance is always present. The way a real complex is handled depends on the particularities of the system but in general it involves explicit treatment of rotations together with low-frequency librational motions and applying standard methods to high frequency vibrations (monomers usually retain most of their individual properties in the complex). A number of excellent reviews on this topic is available in the literature [194-199]. Some applications of this sort of treatment can be found in the $\text{H}_2\text{-HCO}^+$ and Ar-NH_4^+ sections.

Ionic complexes are on average more strongly bound than comparable neutral species. Though it is not by no means obvious whether the presence of the charge induced interactions makes the ionic complexes more rigid in the angular sense, the currently available spectroscopic information indicates that it is indeed the case. However, it is not quite correct to generalize this statement since among ionic complexes one can find systems ranging from near-free internal rotators, such as $\text{N}_2^+\text{-He}$ [2, 122], to the systems with stabilities and rigidity approaching stable molecules, for example N_4^+ [41].

With the exception of He-NH₄⁺ most of the systems studied in this work are closer in behaviour to stable molecules than to the floppy van der Waals aggregates. Therefore the expressions used for describing their energy levels and IR rovibrational transitions are taken initially as they are for the stable molecules. Yet interpreting the spectroscopic constants obtained from fitting observed line positions to these expressions may be somewhat different than it is done for molecular systems. To make the situation simpler the complexes studied here are either linear or so close to prolate symmetric tops (e.g. Ar-NH₄⁺) that the asymmetry doubling is not resolvable in the spectra. Consequently the rotational energy expressions are uncomplicated. For a **linear molecule**, the rotational energy levels for a given vibrational state can be expressed with help of a pseudodiatomic expression

$$E_{\text{rot}} = B[J(J+1) - K^2] - D[J(J+1) - K^2]^2 \quad (4.1)$$

where B is rotational constant, J is angular momentum of the system, K the is projection of the total angular moment onto the molecular axis, and D is centrifugal distortion constant related to the radial strength of the intermolecular bond. Sometimes higher order terms of the form $K_n[J(J+1) - K^2]^n$ ($K_{3,4,5}=H, K, L$, etc.) are added to the expansion to improve the convergence. The degeneracy of levels with $K \neq 0$ is actually removed by vibration-rotation interactions. For $K=1$ a somewhat more precise expression for the energies of rotational levels is given by

$$E_{\text{rot}} = (B \pm \frac{1}{2}q)[J(J+1) - 1] - D[J(J+1) - 1]^2 \quad (4.2)$$

where q is a small (compared to B) *l*-doubling constant. In these doublets the levels corresponding to the positive and negative sign have different symmetry properties. Upper and lower sets of the levels are labeled as either *e* or *f* manifolds according to the currently adopted parity conventions [200]. In electric dipole approximation the only allowed rovibrational transitions correspond to $\Delta J = J' - J'' = -1, 0, 1$, which form P, Q, and R branches, plus there are additional restrictions on parity changes. The latter make the Q branches of the $\Sigma \leftarrow \Sigma$ transitions forbidden. Another important consequence of the parity restrictions is that for $\Pi \leftarrow \Sigma$ transitions each given manifold (*e* or *f*) cannot be accessed by P/R and Q branch transitions at the same time. The transitions are typically labeled in terms of the lower state J quantum number, e.g. P(J''), but in some special cases of perturbed bands numbering in terms of J' may be more appropriate. Frequencies of the transitions between the rotational energy levels of two different vibrational states are expressed as

$$\begin{aligned} \nu_{\text{obs}} = \nu_0 + E_{\text{rot}}(J', K', B', D', \dots) - E_{\text{rot}}(J'', K'', B'', D'', \dots) = \\ \nu_0 + B' [m(m+1) - K^2] - D' [m(m+1) - K^2]^2 - B'' [m(m-1) - K^2] + D'' [m(m-1) - K^2]^2 \end{aligned} \quad (4.3)$$

- Introduction -

The example given in equation (4.3) describes P and R branch transitions of a linear molecule, neglecting the l -doubling effect ($m=J''+1$ for R branch and $m=-J''$ for P branch). As usual, the primed and double primed quantities refer to the state lying respectively higher and lower in energy. The constant ν_0 is the vibrational origin of the transition in question. The vibrational transitions observed in this work are of either $\Sigma \leftarrow \Sigma$ ($K'=K''=0$), or $\Pi \leftarrow \Sigma$ ($K'=1; K''=0$), or $\Pi \leftarrow \Pi$ ($K'=K''=1$) type. Formula for the Q branch transitions is easily derivable from equation (4.3) if one sets $J'=J''$.

Evaluation and comparison of combination differences (CD's) played an invaluable role in the assignment of the spectra presented in this thesis. So called second combination differences are defined as

$$\Delta_2 F(J) = E_{rot}(J+1) - E_{rot}(J-1) \quad (4.4)$$

From a given transition CD's for the lower and upper vibrational states can be obtained via the relationships

$$\Delta_2 F'(J) = R(J) - P(J) \quad (4.5)$$

$$\Delta_2 F''(J) = R(J-1) - P(J+1) \quad (4.6)$$

Note that CD's for a Π state when derived from the line positions of a $\Pi \leftarrow \Sigma$ transition can only be obtained for the rotational manifold accessed in P/R branch transitions. The convenience of combination differences hides in the fact that they separate the upper and lower vibrational states. This provides an extremely valuable check for the correctness of the vibrational assignment. Vibrational transitions originating from a common vibrational state should have identical lower state CD's. Besides for the bands in which one of the states is perturbed CD's help to evaluate reliable rotational constants for the other unperturbed state. To do this experimental CD's are fitted against expression easily derivable from equations (4.4) and (4.1) (Σ state)

$$\Delta_2 F(J) = (4B - 6D) \left(J + \frac{1}{2} \right) - 8D \left(J + \frac{1}{2} \right)^3 \quad (4.7)$$

For a **near prolate symmetric top** the rotational energy level expression

$$E_{rot} = \bar{B}x + (A - \bar{B})K^2 - D_{JJ}x^2 - D_{JK}xK^2 - D_{KK}K^4 \quad (4.8)$$

$$x = J(J+1) - K^2$$

will be very similar to that for the linear molecules (4.1) if $A \gg \bar{B}$ and only very few K levels are observed. In this case D_{JK} and D_{KK} can be neglected and each K level can be

considered separately, with the $(A - \bar{B})K^2$ related terms being contained in the transition origin. This was done for the H_2-HCO^+ and $Ar-NH_4^+$ complexes.

The rotational constant is inversely proportional to the molecule's moment of inertia averaged over the vibrational motion of the nuclei. For diatomic molecules the equilibrium interatomic separation can be obtained relatively easily if the rotational constants are known for a couple of low-lying vibrational states. For polyatomic molecules structural information can be obtained if the spectra of a sufficient number of isotopically substituted molecules are known. For complexes, it is assumed that the weak intermolecular interaction does not appreciably distort the geometric properties of the individual constituents of the complex. Under this assumption, the estimation of intermolecular structural parameters is relatively straightforward, unless the effects of radial angular coupling are large (see below). For example, if a linear complex is formed from a linear molecule and an atom, then the separation between the latter and the center of mass of the former is given by

$$r_{cm} = \sqrt{F \cdot (1/B_{\text{complex}} - 1/B_{HCO^+}) / \mu_{\text{complex}}}, \quad (4.9)$$

where $F=16.85763$ is the conversion factor between the moment of inertia (in $u \cdot \text{\AA}^2$) and the rotational constant (in cm^{-1}), and μ_{complex} is the reduced mass of the complex. This formula is applied to estimate geometrical parameters of the intermolecular bond in linear complexes of Rg and HCO^+ and HN_2^+ later on. From the r_{cm} value the Rg -proton separation can be obtained since structures of both ions are known very well [142].

The size of the centrifugal distortion constant can also be connected to the properties of the intermolecular bond. For diatomic molecules there are well-known expressions relating the magnitude of D to the strength of interatomic interaction. Similar expressions have been developed for complexes [201], with the effect of the extended size of the complex's constituents being explicitly taken into account. For an atom-linear molecule complex, the perturbation expressions for the intermolecular stretching frequency and the harmonic force constant are

$$\nu_s = \sqrt{\frac{4B_{\text{complex}}^3}{D_{\text{complex}}} \left(1 - \frac{B_{\text{complex}}}{B_{\text{monomer}}}\right)} \quad (4.10)$$

$$k_s = 16\pi^2 \mu c^2 B_{\text{complex}}^3 (1 - B_{\text{complex}} / B_{\text{monomer}}) / D_{\text{complex}} \quad (4.11)$$

However in certain cases, particularly in the complexes consisting of an atom bound to an extended rod-like molecule, relating the B and D values to radial intermolecular properties can be quite misleading. This point has been emphasized in studies on the

Ar-HCN van der Waals molecule [202]. While the potential energy surface for this neutral complex has a linear minimum, there is little encumbrance to the Ar moving about the core into a T-shaped configuration and zero point bending excursions are substantial. As the radial equilibrium distance between the constituents' centres of mass is significantly less in the T-shaped configuration than in the linear one, and as rotation tends to bring the intermolecular bond into alignment with the HCN axis, there is a marked rotational dependence of the effective rotational constant, manifesting itself as an anomalously large centrifugal distortion constant [202, 203]. For such complexes the formulae (4.10) and (4.11) are not applicable.

Vibrations of complexes can be subdivided in two main categories. First, there are high frequency modes that can be readily correlated to the vibrations of the isolated monomers. The influence of complexation on these *intramolecular* vibrations is usually not large particularly if the vibrating bond is not directly involved in the intermolecular connection (e.g. CH vibration of HCN-HF). If it is, however, the effect may be quite prominent, in the same HCN-HF complex the bonded hydrogen HF stretch frequency is reduced by as much as 245 cm^{-1} [196]. In the $\text{H}_2/\text{Ar}/\text{Ne}/\text{He} - \text{HCO}^+/\text{HN}_2^+$ complexes the CH and NH stretches are the ones that are influenced most. Second, in any binary complex up to six new motions appear pertaining solely to the radial and angular deformations of the intermolecular bond (three for an atom-polyatom complex). If the molecule is not too flexible down to the point of being a free rotor these motions can be considered as vibrations characterized typically by low frequencies, large amplitude motions, and extreme "anharmonicities". Normal coordinate representation for these *intermolecular* vibrations is relatively useless and models seriously different from the standard harmonic expansion have to be employed. In Rg-HCO^+ and Rg-HN_2^+ complexes the 3 new modes correspond to the intermolecular stretch and doubly degenerate intermolecular bend. In these complexes the intermolecular modes are denoted as respectively ν_s and ν_b . Intramolecular vibrations are labeled by the corresponding monomer vibrations (ν_1, ν_2, ν_3). Composite vibrational transitions are denoted as it is done for stable molecules, e.g. $\nu_1+\nu_s$ correspond to a transition from the ground state of the complex to the state where intermolecular stretch is excited on top of the intramolecular XH vibration. For the He-NH_4^+ and Ar-NH_4^+ complexes, all transitions observed in the spectrum correspond to the intramolecular vibrations of the NH_4^+ core and they are labeled accordingly, using the quantum numbers appropriate for free NH_4^+ . Only for $\text{H}_2\text{-HCO}^+$ and $\text{H}_2\text{-HN}_2^+$ the vibrations were labeled in a proper way according to the currently adopted rules [204].

4.3. Approximate 1D potentials for $\text{Rg}\cdots\text{HX}^+$ complexes

Spectroscopic data obtained in this work can be used for deriving approximate radial potentials appropriate for the interaction of Rg with HN_2^+ and HCO^+ in its ($\nu_1=0$) and

- Introduction -

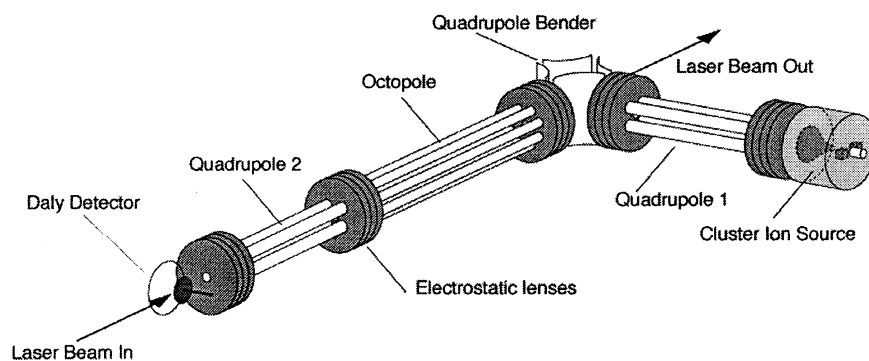
($v_1=1$) vibrational states, proceeding in the fashion developed for constructing spectroscopically based radial potentials for neutral van der Waals complexes. The 1-D potentials enable one to estimate properties of the complexes that have not yet been measured, including their dissociation energies and frequencies for higher intermolecular stretching states. The procedure has been thoroughly described in the Ph.D. thesis of M. Meuwly [205] who was actively pursuing these studies in parallel with the experimental work presented here. Briefly, the utilized approach involves combining the rotational RKR potential obtained from inversion of the spectroscopic data for the v_1 (and if available v_1+v_s) bands with a theoretical long range potential appropriate for the interaction between a set of multipoles distributed over the nuclei of the $\text{HCO}^+/\text{HN}_2^+$ ions and the polarizable Rg atom. Some parameters of the potentials derived in ref. [205] will be used in section 10.2 that compares the properties of the complexes in the Rg- $\text{HCO}^+/\text{HN}_2^+$ series.

5. Experimental

5.1. General

This part is devoted to the description of the experimental setup [28]. As outlined in the introduction the experiment is aimed at the investigation of photodissociation of mass selected ions, and in particular cluster ions. The setup comprises a tandem mass spectrometer machine (called QOQ for Quadrupole-Octopole-Quadrupole), a tunable mid-infrared OPO laser system, and data acquisition and processing hardware and software. Diagrams of the ion source, gas inlet system, and QOQ apparatus can be found in figures 5.1-5.3. All essential pieces of equipment and experimental techniques are described in turn below.

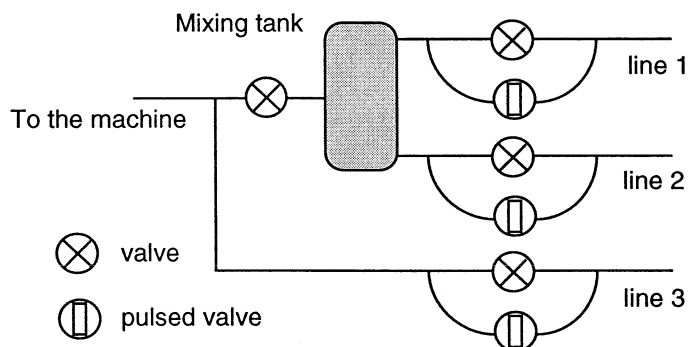
Figure 5.1: QOQ tandem mass-spectrometer apparatus



5.2. Gas mixer

The preparation of the gas mixtures is facilitated by a home build gas mixer (figure 5.2). Two gases are admitted in a mixing tank of ca. 0.5 l in volume through two identical pulsed valves. The pressure in the tank is controlled on-line by a microcomputer. Whenever the pressure drops below a specified level one of the valves opens for a short period of time and admits a portion of gas in the tank. The number of times, the first valve is triggered compared to that for the second valve, controls the gas composition. Mixing ratios of up to 20 are easily possible. Higher ratios lead to instabilities in mixing, since the time for filling the mixing tank becomes comparable to the period of one complete mixing cycle.

Figure 5.2: Inlet gas -mixing system

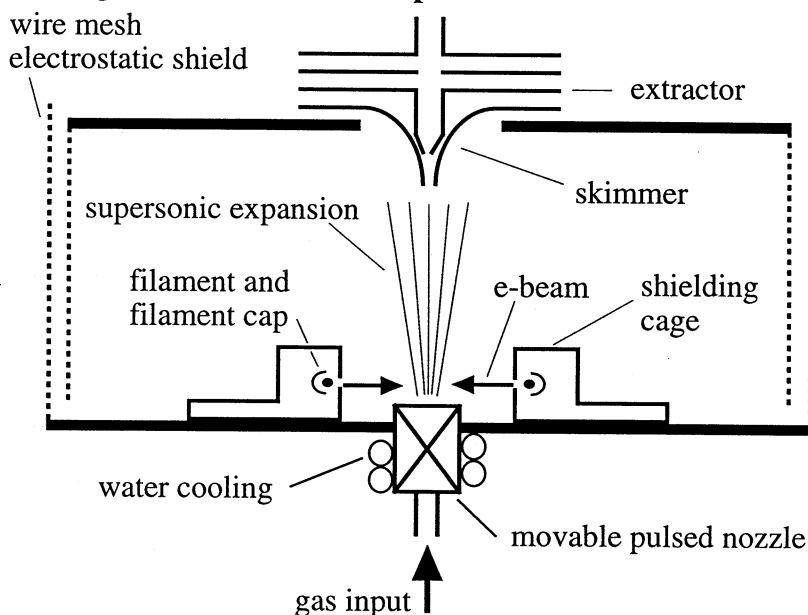


The way the gas mixer was used can be illustrated by the following example. To produce complexes of HCO^+ with rare gases He, Ne and Ar one and the same mixture containing 2% CO and 3% H_2 in He was mixed with respective rare gas at a ratio of about 1 to 1-10. In this way compositions presented in table 5.1 were achieved.

5.3. Ion source

A schematic diagram of the ion source is shown in figure 5.3. The source is axially symmetric and consists of the following major parts, source body with a wire-mesh shield, a pair of heated tungsten filaments, a movable pulsed nozzle, a group of extracting electrostatic lenses, and a water cooling circuit. The ion source is placed inside a chamber differentially pumped by a 2000 l/s diffusion pump. Typical operating pressures in the source chamber range from 10^{-5} to 10^{-4} torr. The source body is kept at an arbitrarily chosen DC level of 40 V which defines initial potential energy at which the ions are synthesized within the source.

Figure 5.3: Electron impact cluster ion source



The main feature of this ion source is a supersonic expansion of the ionized media. A gas mixture prepared by the gas mixer expands through a small (ca. 0.5 mm in diameter) conical orifice in a pulsed nozzle. An electromagnetic valve opens the nozzle for a period of 50-300 μ s with frequencies up to 100 Hz. Typically, the valve is driven with a frequency of 40Hz to meet the requirements of the laser system. Usual backing pressures range from 0.5 to 15 bar. The supersonic expansion leads to a reasonably efficient cooling of internal and translational degrees of freedom of ions formed in the source. Besides, due to an increased density of molecules and large number of three body collisions behind the nozzle it stimulates the formation of weakly bound aggregates of ions with neutral species.

Ionization of molecules in this ion source is accomplished by means of electron impact. Electrons accelerated to ca. 50-150 eV impinge on the expanding molecules and atoms just behind the nozzle and either lead to a direct emission of a secondary electron by the system or leave it in a highly electronically excited state which can subsequently ionize other molecules with lower ionization potentials in collisions. One example of the latter process is Penning ionization where metastable rare gas atoms play an important role in ionization. For most of the molecules, the electron impact ionization cross section as a function of electron energy increases quite rapidly above the ionization potential and subsequently reaches the maximum at $E = 50-90$ eV after which it starts to decrease slowly. It has been found that for most of the gas mixtures used, the highest possible electron energy (≈ 150 eV) is preferred for optimum ion production, and only for a few systems a reduction in electron energy would favor larger ion currents. For polyatomic molecules some degree of fragmentation accompanying ionization is common. However, since ionization is followed by a series of ion-molecule reaction in the molecular beam, the final ion composition may differ very much from what was created by the electron impact.

- Experiment -

Electrons are supplied by two thin tungsten filaments (\varnothing 0.2 mm) placed perpendicular to the source axis and parallel to each other. The filaments are fed with 20-30 W of dc power. The current flowing through the filaments is kept fixed at ≈ 7 A which is optimal for ion production. A rectangular electrical pulse (50-150 eV) is applied to the filaments synchronized in time with the pulse driving the nozzle valve. Specially constructed filament caps direct the ionizing electrons towards the expansion axis through narrow slits. Filaments wear out reasonably quickly and have to be replaced after every ≈ 50 hours of use.

Table 5.1: Experimental conditions used for preparing ionic complexes

Complex	Mixture components	Ratio	Pressure [bar]
He-HCO ⁺	He H ₂ CO	100:1:1	6
Ne-HCO ⁺	Ne He H ₂ CO	600:50:8:1	6
Ar-HCO ⁺	Ar He H ₂ CO	100:50:2:1	4
H ₂ -HCO ⁺	H ₂ He CO	200:100:1	4-5
He-HN ₂ ⁺	He H ₂ N ₂	100:1:1	6
Ne-HN ₂ ⁺	Ne He H ₂ N ₂	600:50:8:1	6-8
Ar-HN ₂ ⁺	Ar H ₂ CO	100:20:1	3-5
H ₂ -HN ₂ ⁺	H ₂ N ₂	15:1	4-5
He-NH ₄ ⁺	He H ₂ NH ₃	1000:1:1	4-6
Ar-NH ₄ ⁺	Ar H ₂ NH ₃	60:4:1	5
H ₂ -NH ₄ ⁺	H ₂ NH ₃	100:1	5
Ar-H ₃ O ⁺	Ar He H ₂ O ₂	360:100:30:1	3
H ₂ -H ₃ O ⁺	H ₂ He O ₂	100:100:1	6
He-OH ⁺	He O ₂ H ₂	120:1:1	6
Ne-OH ⁺	Ne He O ₂ H ₂	100:100:1:1	6
Ar-CH ₃ ⁺	Ar He CH ₄	500:100:1	5
Ar-H ₃ ⁺	Ar H ₂	5:1	5

The composition of ions that are formed in the expansion in the process of electron impact ionization may be very different depending on the gas mixture used, backing pressure, timing, kinetic energy of the ionizing electrons and the distance between the nozzle and the plane where the electrons cross the expansion. Typically higher backing pressures and smaller nozzle-filament separation promote formation of ionic complexes while reversed conditions lead to simpler ions. For example if pure Ar is ionized very late in the expansion (> 5 cm away from the nozzle) one observes that Ar⁺ and Ar²⁺ are the predominantly formed ions. Early ionization (< 1 mm from the nozzle) produces mainly clusters Ar_n⁺, with the average n value increasing with backing pressure.

Species studied in this work represent weakly bound complexes between stable molecular ions and either rare gas atoms or molecular hydrogen. The choice of the gas mixture to synthesize the complexes is usually very simple. Commonly the rare gas (or respectively hydrogen) is seeded with traces of molecules necessary to build the stable ion of interest. Table 5.1 provides information about typical mixtures and experimental conditions aimed to prepare a specific complex.

Ions are extracted from the source with help of four electrostatic lenses. The first one, the skimmer, is biased at -5 V with respect to the source body. It produces a weak extracting field for positive ions and, besides, due to its shape it lets only the central coldest

part of the expansion pass through. The next lens, called extractor, is much more negative than the skimmer and it serves to produce a strong field gradient near the tip of the skimmer to accelerate the ions into the first quadrupole. The remaining two lenses serve for better coupling between the ion source and the first quadrupole. All four lenses, as well as certain parts of the source body, are covered with a layer of graphite to avoid accumulation of surface charges and to simplify cleaning after using adhesive or reactive substances. All parts are cleaned and re-covered with a fresh graphite every time the filaments are replaced.

5.4. Quadrupoles

There are two quadrupole mass spectrometers in the apparatus, with the first one being placed immediately after the ion source. Principles of quadrupole operation, as well as its advantages and disadvantages as mass filter have been reviewed in [206]. Briefly an ideal quadrupole consists of four identical conducting parallel hyperbolic surfaces. In common commercial quadrupoles those are replaced with cylindrical rods. Opposite rods are short circuited. To one pair of rods a rapidly oscillating potential of the form of $U+V\cdot\sin(\omega\cdot t)$ is applied. The other pair receives the inverse of this potential. The frequency typically lies in the MHz range.

Ions entering the quadrupole parallel to the quadrupole axis follow rather complicated trajectories. Analytical solutions for an ideal quadrupole were obtained which contain either an exponential or an oscillatory factor depending on mass of the ion (more precisely on the q/m ratio). With a proper choice of U , V , and ω , only ions with a given q/m ratio reach the exit of the quadrupole without striking the rods. Resolution of an ideal quadrupole is a function of U/V and theoretically can be infinite. However there are many factors limiting the resolution. First, translational energy of the ions along the mass spectrometer axis should be small enough to allow the complete separation for a quadrupole of a given length. Experimentally the ion energy in the quadrupole region is controlled by applying an offset dc voltage to all four quadrupole rods. The kinetic energy can then be expressed as

$$E_{\text{ion}} = V_{\text{ion source}} - V_{\text{quadrupole offset}} \quad (5.1)$$

Secondly, for a realistic situation of non-ideal injection conditions, i.e. off axis and/or not vanishing transverse initial velocity components, the resolution becomes linked to the quadrupole transmission. This happens, because even the ions with a right q/m ratio have a finite probability of striking the rods if injected improperly, and this probability increases when the resolution is decreased. Thirdly, as mentioned above, quadrupole rods are fabricated in cylindrical and not hyperbolic shapes and are subject to mechanical perturbations like vibrations, etc. For photodissociation experiments described in this work, a resolution $m/\Delta m$ of the order of 200 is sufficient. This level of resolution is easily obtained without much loss in transmission with the employed Extrel quadrupoles from "Extranuclear Laboratories". Resolution in these quadrupole mass spectrometers is controlled in a sophisticated way and the devices can be easily transformed from a constant Δm mode to constant $\Delta m/m$ mode.

The purpose of the first quadrupole is to separate an ion of interest from all others ions generated in the ion source. The upper mass limit for this quadrupole is of the order of 550 u. After mass selection, the ions enter into another kind of quadrupole device, a quadrupole bender, which serves to deflect the ions by 90 degrees. The quadrupole bender similarly consists of four parallel rods kept under static voltage which is again the same for each pair of opposite rods. The ion trajectory is bent in the plane perpendicular to all the rods. The bent arrangement of the QOOQ apparatus as compared to a linear one simplifies the alignment of excitation laser beam with respect to the machine axis. In the linear geometry the laser would not leave the interior of the machine and would scatter off the ion source parts instead. The first quadrupole and the quadrupole bender are linked together with a group of electrostatic lenses. Both are pumped with a 500 l/s turbomolecular pump.

5.5. Octopole ion guide

After leaving the quadrupole bender and passing through a series of electrostatic lenses the ions enter an octopole ion guide. The construction of an octopole is very similar to that of a quadrupole except the number of rods is doubled. Every second rod is connected together and bears a potential $V \cdot \sin(\omega \cdot t)$ without any dc component. Another quartet of rods is biased in the opposite way. All eight rods can be given a constant offset voltage which defines the translational energy of the ions in the octopole according to the formula

$$E_{\text{ion}} = V_{\text{ion source}} - V_{\text{octopole offset}} \quad (5.2)$$

As stated before the ion source body is fixed at a constant voltage of 40 V while octopole offset voltage can be varied. Typically ion energies in the octopole do not exceed 10 eV.

The main difference between a quadrupole mass filter and an octopole ion guide is that basically all ions entering the latter follow non-diverging trajectories irrespective of their masses (there is an upper limit of course). Therefore any ion formed in the octopole region as a result of metastable decay, or photodissociation, or collision induced fragmentation, or chemical reaction will be trapped and subsequently transported to the exit from the octopole together with the parent ions.

The octopole can be used to analyze the translational energy spread of the ions. For this number of ions penetrating through the octopole is observed as a function of octopole offset voltage. When it substantially exceeds $V_{\text{ion source}} = 40$ V no ions come through, and when it is much below 40 volts transmission starts to approach 100%. The sharpness of the transition between these two regimes defines the ion energy spread. Values measured in this way did not exceed 1 eV fwhm even for the lightest ions (hydrogen clusters and helium ion).

Another useful feature of the octopole is its ability to trap ions. For trapping a simple sequence of pulses is applied to the entrance and exit lenses of the octopole. First a high ($\gg 40$ V) positive potential is placed on the exit lens. After all or most of the ions get into the octopole the entrance lens is similarly locked. Ions are released after some time by removing the potential from the exit lens. Depending on the mass of the ions a reasonably efficient trapping on the millisecond to second time scale is possible. This is to be compared with a single traversal through the octopole that happens on the microsecond time scale. Since photodissociation of ions typically proceeds much faster, the trapping has been used only for very specific experiments.

The reasonably high speed of the ions in the octopole produces a measurable Doppler shift in the laser excitation frequency from the point of view of a static observer (calibration cell). In a typical photodissociation experiment (without ion trapping) laser and ion beams propagate in opposite direction. This means that the ions perceive a higher frequency than is detected by the calibration cell. To account for this effect, the Doppler correction

$$\Delta\nu = 4.634 \times 10^{-5} \times \nu \times \sqrt{E_{\text{ion}}/M} \quad (5.3)$$

is always added to the calibrated wavelength. Here ν is excitation frequency, M and E_{ion} are the ion's mass and energy (5.2). This correction can in certain cases be quite large particularly for small molecules. For example for $\text{H}_2\text{-HCO}^+$ complex excited at 4000 cm^{-1} with 10 eV of translational energy it amounts to ca. 0.11 cm^{-1} which is 5 times the laser resolution. The uncertainty in the ion energy carries over into uncertainty in the excitation wavelength according to

$$\Delta(\Delta\nu) = 0.5 \times \Delta\nu \times \Delta E_{\text{ion}}/E_{\text{ion}} \quad (5.4)$$

- Experiment -

Even for the lightest complex He-OH^+ (from those studied in the QOQ machine) this uncertainty calculated at $E_{ion} = 5 \text{ eV}$ and $v = 2800 \text{ cm}^{-1}$ is 0.006 cm^{-1} which is smaller than the excitation laser bandwidth. However at lower energies in the octopole it is possible to achieve less favorable values for the Doppler broadening. For this reason, the octopole voltage is usually set to $V \leq 35$ for lighter molecules, with energies in the range of 5-10 eV being typical. For heavier ions like Ar-HCO^+ energies as low as 3 eV can be used.

The octopole chamber is differentially pumped by a 500 l/s turbomolecular pump. Under normal operating conditions, the pressure in the octopole region is of the order of 10^{-7} torr. Additionally there is a convenient possibility to set the pressure of a buffer gas to any value below $2 \cdot 10^{-5}$ torr (there is an upper limit because of the high peak voltage on the octopole rods) by means of steady gas injection through a needle valve. This allows to monitor the reactions of ions with gaseous neutral molecules as a function of collision energy. For example, the collision induced fragmentation is very helpful for initial optimization of the experimental conditions for the production of weakly-bound complexes, which have very high collisional dissociation cross sections.

5.6. Second quadrupole and Daly detector

Fragment ions that are produced in the octopole as a result of photodissociation, etc., are separated from the parent ions in the second quadrupole mass spectrometer situated after the octopole and separated from it by a group of electrostatic lenses. Probably due to improved injection conditions, the resolution of the second quadrupole is somewhat better than that of the first one at a similar transmission level. Survey mass spectra were therefore always taken with the second quadrupole. The upper mass limit for the second quadrupole is of the order of 400 u.

Ions are sensed with a Daly detector [207] placed after the second quadrupole. It consists of a highly polished pancake-like stainless steel electrode kept at a high negative potential (-20 kV). When an ion crashes onto the surface of the electrode several electrons are emitted. The electrons are absorbed by a nearby scintillator plate, each producing a bunch of photons. Photons are detected by a photomultiplier. In this way single ions can easily be detected. The chamber containing the second quadrupole and Daly detector is differentially pumped by a 300 l/s turbomolecular pump.

5.7. OPO laser system

Tunable IR laser radiation is produced by a commercial OPO laser system "Mirage 3000", from "Continuum". This pulsed system (3-5 ns, 20Hz) is capable of producing IR radiation in the range $2500\text{-}6900 \text{ cm}^{-1}$ with a 0.02 cm^{-1} resolution. Though description of the system can be found in the corresponding manual some relevant details are provided here as well. The laser has three optical stages, with the first one utilizing optical parametric oscillation, and the other two making use of optical parametric amplification. The laser is pumped with the fundamental and the first harmonic of a Nd:YAG laser "Powerlite 8020" from "Continuum". A fraction of the 532 nm light (15%) is used to pump an oscillator cavity. The cavity design is based upon a grazing-incidence grating resonator similar to the well known Littman arrangement widely spread in dye lasers. The cavity is characterized by a very small angle of 1.6-2 degrees between the incoming pump beam and the grating plane and by a reasonably small length, with the path tuning mirror - grating - rear mirror being only about 5 cm long. The shortness of the cavity allows for a large spacing between the cavity's longitudinal modes (3 GHz) which in favorable operating conditions exceeds the cavity gain width. Wavelength tuning is accomplished by rotating the tuning mirror. The cavity contains a non-linear KTP crystal which plays a role of the gain medium. If the crystal is properly phasematched for OPO generation the cavity starts to lase. It is possible to make the cavity lase on only one longitudinal mode by a proper choice of the pump beam power and focusing. Single longitudinal mode (SLM) lasing is actively stabilized by mounting the rear mirror of the cavity on a piezo crystal and generating an error signal from spatial deviations of the laser beam from the center of a distant split photodiode. To change

- Experiment -

the wavelength, both tuning mirror and the crystal have to be rotated synchronously. The cavity is designed to lase in the range of $\lambda_{osc} = 710-840$ nm. However at around 752 nm the crystal phasematching angle becomes very close to zero and optical parametric oscillation starts to interfere with unwanted non-resonant lasing off the crystal surfaces. This interference creates a “dead zone” between 750 and 754 nm where SLM scanning is virtually impossible. In addition it is very difficult to get the cavity lasing below 730 nm because of the decreased conversion efficiency. The laser pump power has to be increased substantially at the lower wavelength end. The cavity does its best in the range of 770 to 840 nm and is used mainly in this range.

The largest portion of the oscillator cavity output is coupled into a fiber optical guide and is transmitted to an etalon. Etalon fringes are projected on a computer monitor with an infrared camera. The fringes are very useful for evaluating the oscillator stability and also for calibration purposes. A smaller portion of the oscillator output (5%) is directed into the first optical amplification stage which contains two KTP crystals identical to the one from the oscillator cavity and phasematched for OPO generation at the oscillator wavelength. The oscillator output is used to seed the nonlinear OPO process in the amplifier. The amplifier is pumped with the rest of the 532 output of the Nd:YAG laser. The amplifier stage is situated in a non-resonant cavity designed in such a way that the signal (amplified oscillator, λ_{osc}) and idler (λ_1) outputs go out of it in opposite directions. The idler output of the first amplification stage (λ_1) is used in turn as seed and becomes signal for the second amplification stage pumped by the Nd:YAG fundamental. The second amplifier crystals are not placed in a cavity and optical parametric amplification occurs on a single pass through. These crystals, too, have to be phasematched for OPO generation at the wavelength coming in from the first amplifier. The amplified signal (λ_1) and newly-born idler (λ_2) waves abandon the second amplification stage together. The amplified oscillator output (λ_{osc}) leaves the laser from the other end of the laser bench. Up to now it has not been used for spectroscopic purposes but it allows to control the performance of the first amplification stage during the scan. The crystals used in the laser survive about 500-1000 hours of operation after which they get either gray tracks or burns in their antireflection coating.

The laser is controlled with a microcomputer which allows to move any of the 5 crystals and the tuning mirror separately as well as in a concerted way when scanning. Besides, the computer takes care of the laser SLM operation and can be used for testing the performance of the oscillator stage. For a scan one routinely phasematches all crystals, establishes SLM operation, and optimizes coupling between the oscillator and the fiber. During the scan the wavelength of the oscillator is estimated all the time from the encoded position of the tuning mirror. Information about optimal speed of crystal tuning as a function of wavelength is stored in the computer in form of pre calibrated polynomials and the crystals are rotated accordingly. Only SLM operation is controlled on-line, all the other tuned elements have a chance of deviation from the correct positions. This procedure works nicely for short and slow scans. A typical SLM scan is ca. 1 nm ($14-19$ cm⁻¹) long and it is taken with a speed of 0.2-1 pm/s (wavelength refers to the oscillator). For longer and faster scans the laser has to be paused from time to time to readjust the crystals. These survey scans taken with a speed of 1-10 pm/s demonstrate relatively poor SLM performance but allow preliminary determination of location and shape of absorption bands in a spectrum.

The wavenumbers for all waves involved in OPO generation are interconnected via the following relationships.

$$\begin{aligned}\omega_0 &= \omega_{\text{YAG fundamental}} = 9394.482 \text{ cm}^{-1} \text{ (measured, see below)} \\ \omega_{osc} &= 11900 - 14100 \text{ cm}^{-1} \text{ (tunable, } 0.02 \text{ cm}^{-1} \text{ resolution, works best below } 13000 \text{ cm}^{-1}) \\ \omega_1 &= 2 \times \omega_0 - \omega_{osc} = 4700 - 6900 \text{ cm}^{-1} \text{ (} 0.02 \text{ cm}^{-1}, \text{ best above } 5800 \text{ cm}^{-1}) \\ \omega_2 &= \omega_0 - \omega_1 = \omega_{osc} - \omega_0 = 2500 - 4700 \text{ cm}^{-1} \text{ (} 0.02 \text{ cm}^{-1}, \text{ best below } 3600 \text{ cm}^{-1})\end{aligned}$$

The wavelengths λ_1 and λ_2 will be referred from here on as the first and second outputs respectively. The proportion of the first output is always larger by a factor of around 2-3. As mentioned above both come out of the laser in the same direction. In addition, there is some amount of admixtures of the YAG fundamental and first harmonic to the combined beam. The second output and most of the 1064 nm impurities can be eliminated easily by blocking the 1064 nm pump beam before the second amplification stage. The combined beam is directed into the QQQ machine with a couple of concave gold-coated mirrors. One of the mirrors is positioned on a piezo controlled plate to simplify the alignment. Visible traces of the green 532 nm light can be used for a preliminary alignment of the laser beam path since all of the component rays are nearly overlapping. Traces of the YAG fundamental can be monitored with an infrared card or infrared viewer. The first output is strong enough to leave burns on photographic paper. Besides, at $\omega_1 > 6000 \text{ cm}^{-1}$ it is possible to see it with the infrared viewer. Unfortunately there is no way to observe visually where the second output goes. However its position can be estimated by using an IR photosensitive device like InSb LN₂ cooled photovoltaic detector. As experience shows the second output beam may diverge slightly from all the other beams (the rest appears to be well collimated) particularly when the oscillator wavelength exceeds 800 nm. By the time the combined laser beam has traveled 4 m between the laser and the octopole the separation between the first and second output rays may become as large as 4-7 mm. On one hand it is convenient since it allows to separate the rays with a diaphragm, but on the other hand it always causes trouble during the alignment of the second output ray through the reference cell and QQQ machine. Usually the alignment is accomplished by maximizing the response of the InSb detector placed behind the machine. The detector window is covered with a Germanium filter with cut-off at 1.65 μm , that efficiently absorbs the first output wavelength corresponding to the master oscillator wavelength range $\lambda_{\text{osc}} > 780 \text{ nm}$.

When a photodissociative transition is detected the alignment can be improved further by maximizing this signal (this method works for any output of the laser and for any wavelength range). To inquire which of the outputs causes the photodissociation the second output is eliminated from the beam. In those rare cases when the first output drives the photodissociation, blocking the second output does not reduce the signal down to zero. The situation, when both first and second output produce photodissociation action of similar magnitude was found only in one complex ArH_3^+ between, 800 and 820 nm, (oscillator). But in this case the solution was quite simple since the first and second output beams could be separated with a diaphragm.

5.8. Optoacoustic calibration cell

There are many available standards in the IR region. Calibration of photodissociation spectra presented in this work was accomplished by means of optoacoustic spectroscopy. Optoacoustic spectroscopy relies on the detection of the acoustic wave produced by dissipation of thermal energy from a locally heated cord of vibrationally excited molecules created by the laser. Two identical cells were employed. The cells have an asymmetric shape to achieve higher sensitivity [208]. Typical vapor pressure of the reference gas in the cell is of the order of 10-20 torr. Depending on the spectral range different reference molecules were used. The list includes fundamentals, overtones and combination bands of HDO, C₂H₂, NH₃, OCS, N₂O, and others. Line positions for these transitions were taken from [209].

Since either first or second output can be used for calibration of a given spectral range one get more flexibility in the choice of reference gases. Unfortunately there are certain wavelengths for which data are either not available or scarce. As will be clear from the discussion of the calibration of spectra the best results are obtained when the density of reference lines exceeds 1-2 per wavenumber. There are certain ranges with poorer density of calibration lines, for example the one between 3650 and 3800 cm^{-1} . All spectra recorded in similar ranges are expected to have somewhat lower calibration accuracy.

5.9. Measurement of the Nd YAG fundamental frequency

Since the first output is often used for calibration purposes while most of photodissociation spectra are due to the second output it is important to know the frequency of the Nd:YAG fundamental for the interconversion. The frequency was measured three times with intervals of half a year by recording optoacoustic spectra of certain gas mixtures. Two components of the mixture should absorb wavelengths from different outputs at the same oscillator frequency. A very convenient combination is OCS (second) and HDO (first output) at around $\lambda_{\text{osc}} = 800\text{-}802$ nm. Two sets of optoacoustic lines were calibrated with respect to each other to provide the YAG frequency. The three measurements gave results $9394.481(5)$, $9394.482(5)$, and $9394.482(4)$ cm^{-1} . The average value of 9394.482 cm^{-1} was adopted.

5.10. Experiment timing and data acquisition

Experimental timing is arranged in the following way. The laser is triggered at 20 Hz, i.e. at half the frequency of the ion source. For every trigger pulse three signals are integrated with three Stanford Research boxcars, namely photodissociation fragment ion current, signal from the optoacoustic cell, and signal from the IR detector. The laser wavelength changes continuously and it assumes a different value every trigger pulse. Since storing data from every trigger pulse would require a lot of memory, some averaging and data reduction takes place already during the scan. For this, information from the boxcars is accumulated by a Stanford Research computer interface SR245 for some even number of triggers ($=2P$). After this the data is logged into the computer (Macintosh II) via a GPIB bus. The computer analyzes the data sequence from the IR detector first to decide whether even or odd triggers correspond to the laser ON state. Then it calculates the difference between the average of data taken with laser ON and that taken with laser OFF for all three channels. As a net result one has three averaged data points for photodissociation, laser power, and optoacoustic signal obtained during $N=2P+K$ triggers, where K triggers were wasted for the mathematical treatment. The change in the laser wavelength which takes place during these N triggers is equal to $\Delta\lambda = \text{speed} \times N/40$ Hz. It can be considered as effective wavelength step for the scan. For a typical scan the step is made of the same order as the scanning speed so N should be around 40. The number of triggers K is estimated as 5, i.e. it takes about 100 ms to read the data from the computer interface, calculate the average, and initiate a new cycle. The laser ON/OFF technique described above helps to compensate for slow drifts in boxcar offset voltages. Additionally, if the photodissociation signal appears on the top of a metastable decay signal, the method eliminates slow drifts in the latter as well.

The fourth signal that is acquired together with the other three comes from the etalon fringes. As mentioned above part of the laser oscillator light is projected onto an etalon inside an IR camera. Fringes are detected by a slow photodiode attached right to the monitor that displays the fringes. Since the monitor frequency is not synchronized with that of the experiment, the laser ON/OFF subtraction is not possible. Instead the output of the photodiode is averaged on-line to provide a slow-varying (quasi DC) signal which is read in directly by the computer interface. The fringes are absolutely essential for the calibration of the spectra (see below).

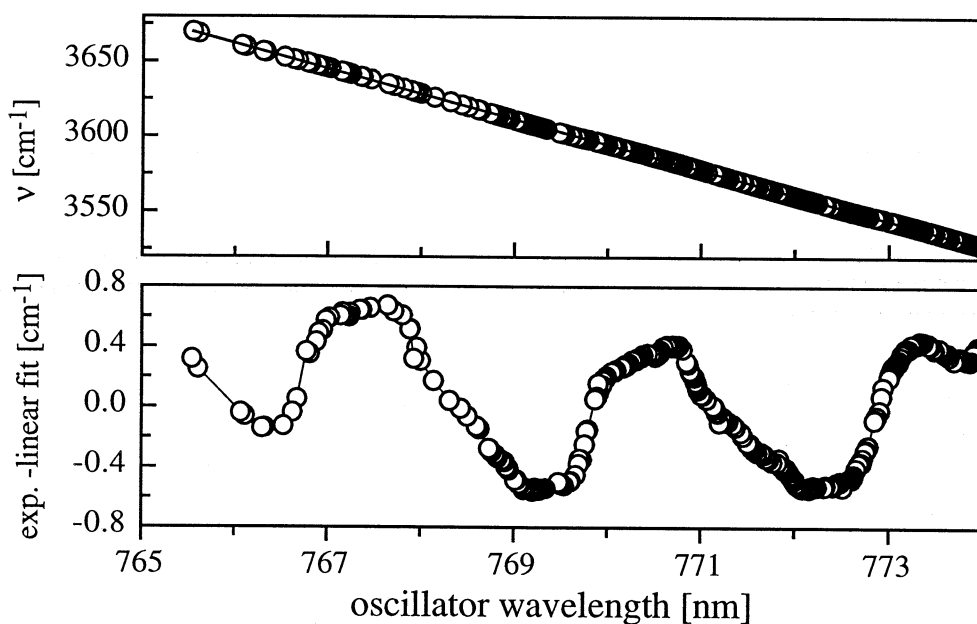
The laser is controlled with a PC compatible computer, while the central computer has a Macintosh platform. To obtain information from as many triggers as possible the wavelength is read out of the laser only twice, at the beginning and at the end of the scan (communication between the two computers is not very fast). Wavelength values for all intermediate points are calculated at the end of the scan under assumption of a uniform speed of scanning and data acquisition. The wavelength obtained in this way provides only a rough idea about the actual wavelength and it has to be calibrated later against the optoacoustic spectrum. As a measure of the photoexcitation energy in a raw uncalibrated scan approximate oscillator wavelength in nanometers is taken (this choice is rather arbitrary).

5.11. Calibration of spectra

As a first step in the calibration the optoacoustic spectrum is assigned. For certain isolated transitions of linear molecules like OCS or C₂H₂ the observation of band gaps or characteristic Q branches assists the assignment of lines. For molecules with more complicated spectra like HDO or NH₃, the assignments are accomplished by visual comparison with reference absorption spectra given in ref. [209]. Though the actual wavelength for a given scan can be estimated from the nanometer scale provided by the computer with an accuracy of only 5-10 cm⁻¹ and intensities in optoacoustic and absorption spectra do not always match, the assignment never caused a serious problem.

Figure 5.4: Non uniform scanning of the "Mirage 3000" OPO laser

Dependence between the master oscillator wavelength reading generated by the tuning mirror decoder and the actual wavenumber of the second output of the laser (top). Though scanning looks faultless at the first glance there are some unwanted systematic variations in the frequency as evident from the bottom trace which shows what is left from the top one after removing the linear component.



After this, the positions of relevant optoacoustic peaks and fringes are determined. The positions are measured in the oscillator nanometers that have only approximate meaning. Both data sets are subjected to a mild Gaussian averaging to get rid of high frequency noise and provide the peaks with better shapes. Peak positions are taken as peak maxima in the averaged spectrum. For closely separated peaks, corrections for mutual penetration are made. As a result two data sets are obtained, positions of etalon fringes as a function of an arbitrarily running integer fringe index, and positions of optoacoustic lines against their actual positions in wavenumbers. To simplify the description of the calibration procedure, the fringes and optoacoustic positions are denoted as λ_i^{fr} , λ_k^{opto} and ω_k^{opto} respectively. Here i is fringe index and k is optoacoustic line index (any number).

If positions ω_k^{opto} are plotted against λ_k^{opto} a roughly linear dependence is obtained (figure 5.4). However a closer look reveals systematic deviations which are reproducible from scan to scan and are sometimes as large as 0.5-1.0 cm⁻¹. In figure 5.4 where such deviations are shown for a reasonably long scan it is seen that the deviations lie on a sort of periodic function of the wavelength. It is suspected that the deviations come from the non-uniform motion of the tuning mirror in the oscillator cavity. Their presence complicates the calibration somewhat since there should be enough calibration pairs to reproduce this behavior correctly. One would be in a much better position if the dependence $\omega_k^{\text{opto}}(\lambda_k^{\text{opto}})$ was represented by a low order polynomial function.

- Experiment -

Fortunately it is possible to use the fringes for filling the gaps between widely separated optoacoustic lines. Real positions of fringe maxima ω_i^{fr} should all lie on a straight line, i.e. the following relationship should be satisfied

$$\omega_i^{\text{fr}} = i \times \text{FSR} + \text{offset} \quad (5.5)$$

where FSR is the free spectral range of the etalon. Values of ω_i^{fr} are initially unknown but can be calculated in the first approximation from λ_i^{fr} using the linear interpolation

$$\omega_i^{\text{fr calibr}} = \omega_b^{\text{opto}} + (\lambda_i^{\text{fr}} - \lambda_b^{\text{opto}}) \times (\omega_a^{\text{opto}} - \omega_b^{\text{opto}}) / (\lambda_a^{\text{opto}} - \lambda_b^{\text{opto}}) \quad (5.6)$$

where λ_a^{opto} and λ_b^{opto} are two closest optoacoustic lines surrounding the fringe λ_i^{fr} . Obtained $\omega_k^{\text{fr calibr}}$ values usually do lie on a straight line with possible exception of fringes falling in wide gaps between optoacoustic pairs. These (hopefully few) poorly calibrated fringes are taken out and the rest is fitted to a linear curve with respect to the fringe index. Pairs $\omega_i^{\text{fr fitted}}$ vs. λ_i^{fr} ($\omega_i^{\text{fr fitted}}$ is calculated for all fringes) are the ones that are used to fill the gaps between the optoacoustic lines. The quality of these pairs can be examined by trying to reproduce the values of ω_k^{opto} from λ_k^{opto} with interpolation similar to the one given above. In most cases the obtained precision is much better than the laser resolution. If the uniformity of the laser scanning is particularly bad at a certain wavelength, for example due to a local mode hop or the FSR of the etalon changes during the scan because of a sudden change in surrounding temperature the scan is split at this particular point and for each piece separate sets of calibration pairs are derived.

Finally, the pairs $\omega_i^{\text{fr fitted}}$ vs. λ_i^{fr} and ω_k^{opto} vs. λ_k^{opto} are combined together and used to recalculate the whole wavelength axis for a given scan from approximate oscillator nanometers to the actual scale. After correcting the wavenumber scale for the Doppler shift, the calibration is completed. Since for every absorption band three to six independent scans are taken the whole procedure can take quite a long time (substantially longer than the time spent for the experiment). Individual scans overlap to a good precision after calibration. They are added together to give one final data set with an increased signal-to-noise ratio. It is used subsequently to measure line positions in the corresponding band.

6. H₂ vibrations in H₂-HX⁺ complexes

6.1. General

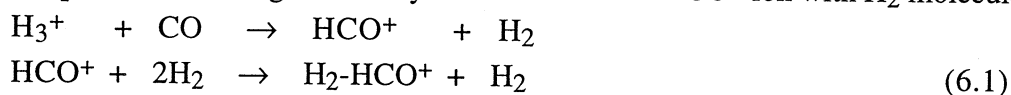
According to a number of *ab-initio* calculations and some available experimental data the complexes between protonated molecular ions and molecular hydrogen tend to have a structure with a triangular arrangement of the hydrogen atoms. Infrared transitions of the free molecular hydrogen are dipole forbidden but the situation in the complexes is markedly different. The magnitude of the intermolecular binding energy depends on the amount of electron density transferred from the H₂ bond onto the proton of HX⁺, which is different for the inner and outer turning points of the H₂ stretching vibration. Thus excitation of the H₂ vibration may lead to the in phase changes of the intermolecular separation and produce a weak oscillating dipole moment in the direction of the intermolecular axis. Respective parallel bands in the spectra of the complexes of H₂ with H₃⁺ [44, 45], H₃O⁺ [61], CH₅⁺ [74-76], and SiH₃⁺ [81, 82] have been observed in the past by vibrational predissociation spectroscopy. Here the number of such systems is extended to include the complexes of molecular hydrogen with HCO⁺, HN₂⁺, NH₄⁺, HAr⁺, and HXe⁺. Beside that, the quality of the H₂-H₃O⁺ spectrum has been substantially improved. Below the most significant studies of H₂-HX⁺ complexes from this laboratory are reviewed.

6.2. The H₂-HCO⁺ complex

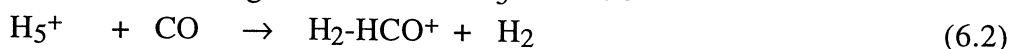
6.2.1. Motivations for the study and associated chemistry

Interest in the isomeric forms of H₃CO⁺ followed the proposal by Herbst and Klemperer in 1973 that formaldehyde may be produced in dark interstellar clouds through a mechanism in which the primary step was the radiative association of H₂ and HCO⁺ [210]. The association product was presumed to be protonated formaldehyde which produced formaldehyde after dissociative recombination with electrons. Fehsenfeld, Dunkin and Ferguson [211] subsequently showed that H₃CO⁺ ions formed in such low energy encounters rapidly exchange H₂ for CO to form (CO)₂H⁺, suggesting that they have an H₂-HCO⁺ form, rather than the more stable protonated formaldehyde structure. This conjecture received a firm foundation from high pressure mass spectrometry measurements which provided an association energy for the complex of ≈ 16 kJ/mol with respect to the H₂+HCO⁺ limit [212]. Corresponding theoretical studies [213-219] have since identified at least three stable isomers of H₃CO⁺, the protonated formaldehyde cation H₂COH⁺ which is in fact the most stable form, and the two proton bound complexes H₂-HCO⁺ and H₂-HOC⁺. Barriers for isomerization between the three forms appear to exceed the H₃⁺+CO and H₂+HCO⁺ dissociation limit making it appropriate to think of them as distinct molecular species. Prior to the present study only the protonated formaldehyde cation had received spectroscopic attention [220].

A 15:1 mixture of H₂ and CO expanded at 4-5 atmospheres was used to prepare the complexes. Several reaction schemes appear capable of producing H₂-HCO⁺ in the supersonic plasma, including three body association of the HCO⁺ ion with H₂ molecules



and direct formation through the reaction of H₅⁺ with CO



Several pieces of evidence encourage the attribution of the spectra recorded in the present work to the H₂⋯HCO⁺ ionic complex.

1. The magnitude of the H₃CO⁺ mass peak was found to be sensitive to the nozzle - filaments separation, being maximized when the filaments were reasonably close to the nozzle orifice, which can be taken as a sign of a weakly bound complex. .
2. Collisional dissociation of the H₃CO⁺ by helium buffer gas in the octopole at 2-5 eV laboratory energy resulted in the appearance of a mass 29 peak, strongly suggesting that a substantial fraction of the parent mass signal is due either to H₂-HCO⁺ or H₂-HOC⁺. Experimental studies indicate that although the protonation of CO by H₃⁺ produces both the isoformyl HOC⁺ and formyl HCO⁺ species [221-223], the former are readily converted to the latter through subsequent collisions with H₂ or CO [224]. Given the large CO and H₂ densities in our ion source, it is likely that practically complete conversion of the isoformyl to the more stable formyl ion should occur. From spectroscopic measurement of relative intensities of HCO⁺ and HOC⁺ rovibrational lines it was found that in a H₂/CO discharge under conditions that are probably similar to those maintained in the present ion source less than 1% of HOC⁺ isomer was formed [43, 221].
3. Finally the rotational constants extracted from the spectral analysis agree with *ab initio* predictions for the H₂-HCO⁺ complex, but not for the other possible isomers.

6.2.2. *Ab initio* structure predictions

The considerably higher proton affinity of CO compared to H₂ means that the H₂-HCO⁺ complex can be considered essentially as an H₂ molecule associated with an HCO⁺ cation. A degree of insight into the nature of intermolecular bonding can be obtained by examining the long range electrostatic and inductive interactions. The chief attractive long range forces arise from the electrostatic interaction between the positive charge on the HCO⁺, which is principally localized on the H and C atoms, and the quadrupole moment of the H₂ molecule, together with the inductive charge-induced dipole interaction

$$V_{lr}(R, \theta) = \frac{Q\Theta}{8\pi\epsilon_0 R^3} \times (3\cos^2 \theta - 1) - \frac{1}{2} \frac{Q^2 (\alpha_{\perp} \cos^2 \theta + \alpha_{\parallel} \sin^2 \theta)}{4\pi\epsilon_0 R^4} \quad (6.3)$$

Here Q is the ion charge, R the distance between the H₂ centre of mass and the ion, α_{\parallel} and α_{\perp} the parallel and perpendicular volume polarizabilities of H₂, and Θ the quadrupole moment of H₂. While the induction contribution is attractive for any geometrical arrangement, the charge-quadrupole interaction may be either attractive or repulsive depending upon the orientation. From expression (6.3) it can be estimated that at intermediate ranges the total interaction is considerably more attractive in the T-shaped than the linear configuration and that there is a substantial barrier to the internal rotation of the H₂ molecule.

In order to guide interpretation of the H₂-HCO⁺ spectrum *ab initio* investigations of the potential hypersurface in regions adjacent to the H₂-HCO⁺ minimum have been carried out using the QCISD(T) approach. Interested reader is referred to ref. [225] for the details of the calculations. The most stable conformer of H₂-HCO⁺ is predicted to have C_{2v} symmetry and has been identified in several previous theoretical studies. The calculations show that the C_{2v} conformer lies 17.3 kJ/mol lower in energy than the separated monomer units, or 10.2 kJ/mol when harmonic, zero point energy corrections are taken into account. Although the H₂-HCO⁺ bond energy has not been reported for low temperatures, the heat of formation at 300K has been determined to be -16 kJ/mol [212]. After standard thermodynamical corrections are made to the theoretical result, the ΔH_{300}^0 for the ion-molecule reaction becomes -13.3 kJ/mol, representing a reasonable agreement with the experimental value.

Harmonic vibrational frequencies and dipole strengths for the 9 normal vibrational modes of the H₂-HCO⁺ complex determined from the *ab initio* calculations, along with symmetries and descriptions are listed in Table 6.1. One expects that in a moderately bound complex such as H₂-HCO⁺ the vibrations should factor into high frequency ones involving

internal deformations of the molecular subunits and ones of lower frequency involving 'intermolecular' motions. Vibrations in the former category should be similar in nature to the ones of the isolated subunits although, depending upon the strength of the intermolecular interactions frequencies will be shifted somewhat. It is easy to identify the ν_1 vibration of H₂-HCO⁺ with the H₂ stretch, ν_2 and ν_3 with the C-H and C-O stretches of HCO⁺, and ν_5 and ν_7 with the HCO⁺ degenerate bend. In order to better predict the intermolecular frequencies of the H₂-HCO⁺ complex, the calculated values were scaled by a factor necessary to bring the corresponding monomer calculated frequencies into line with the experimental ones. These scaled frequencies are also provided in Table 6.1. Normal coordinate for the vibrations are shown in figure 6.1.

Table 6.1: The H₂-HCO⁺ calculated vibrations

Symmetries, vibrational frequencies, and transition dipole strengths for the H₂-HCO⁺ complex. Frequencies and intensities were determined in conjunction with the *ab initio* calculations. The frequencies given in brackets have been scaled by the factor necessary to bring the corresponding monomer (HCO⁺, H₂) calculated and observed frequencies into line. The last two columns provide frequencies and intensities for isoelectronic H₂-HN₂⁺ complex calculated at similar level of theory. Intensities (heavily rounded) are given in atomic units ($1 \text{ km}\times\text{mol}^{-1} = 1.379\times 10^{-4} \text{ cm}^{-2} \text{ atm}^{-1}$).

mode		description	<i>ab initio</i> frequency H ₂ -HCO ⁺	exp. frequency	int. km/mol	<i>ab initio</i> frequency H ₂ -HN ₂ ⁺	int. km/mol
1	a ₁	H-H stretch	4324 (4073)	4060	80	4243 (4011)	70
2	a ₁	C-H stretch	2990 (2850)	2840	700	2689 (2538)	1900
3	a ₁	C-O stretch	2168 (2139)		700	2122 (2114)	800
4	a ₁	H ₂ ···HCO stretch	353 {320 ^a }	305 ^b 300 ^c	60	569 {438 ^a }	190
5	b ₁	HCO ⁺ out-of-plane bend	956 (1034)		10	1014 (995)	80
6	b ₁	intermolecular out-of- plane bend	197		20	231	0
7	b ₂	HCO ⁺ in-plane bend	973 (1053)		0	1123 (1101)	20
8	b ₂	H ₂ rock	608		10	824	70
9	b ₂	intermolecular in- plane bend	195		20	228	0

^a derived from the effective intermolecular stretching potential; ^b assuming that the 3145 cm⁻¹ band is $\nu_2+\nu_4$; ^c derived from measured centrifugal distortion constants

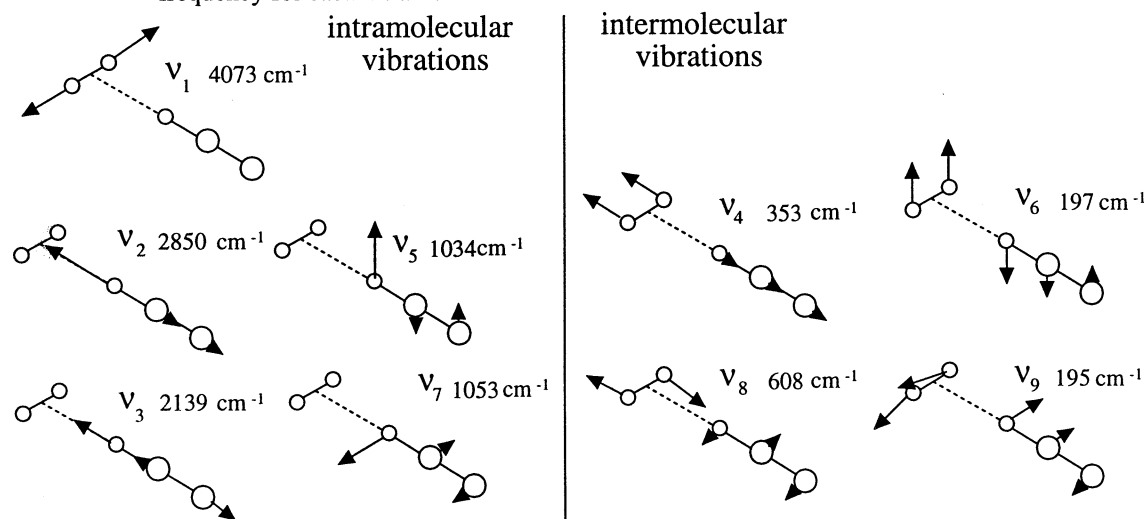
Beside vibrations involving deformations of the complexes' constituents, there are four intermolecular vibrations - the stretching vibration of the H₂·····HCO⁺ bond (ν_4), an H₂ rocking vibration (ν_8) and two bending vibrations which principally entail in-plane and out-of-plane motion of the H₂ unit (ν_9 and ν_6). Regarding these *intermolecular* vibrations as a collection of normal modes may not be a good approximation. Flat intermolecular potential energy surfaces and small reduced masses imply substantial vibrational displacements and thus exploration of the PES well away from the minimum. In order to investigate anharmonic effects for the intermolecular stretching and bending motions, a series of potential energy points away from the minimum energy configuration were calculated. For the intermolecular stretch, an effective *ab initio* stretching potential was determined by calculating the energy at a number of different intermolecular bond separations, all other degrees of freedom being allowed to relax. Equipped with the resulting potential the radial Schrödinger equation was solved numerically to yield vibrational energy levels. This calculation strategy presumes effective decoupling between intermolecular stretch and the other molecular motions. As expected the first vibrational spacing for the intermolecular

stretch potential (320 cm⁻¹) is somewhat lower than the corresponding harmonic frequency (353 cm⁻¹).

Analysis of the large amplitude intermolecular bending motions is more complicated. In the limit of negligible steric hindrance the three bending vibrations will correlate to internal rotations - the H₂ rock with internal rotation of the H₂, and the two low frequency bends with an internal rotation of the HCO⁺ ion. The two internal rotational motions will be coupled to some extent by cross terms in the potential energy expansion, so that if one really wishes to understand the full problem it is necessary to treat the two motions simultaneously. Unfortunately the experimental spectra are not sufficiently detailed to warrant a complete analysis of the coupled bending problem and further discussion is confined to a qualitative examination of the nature of the H₂ internal rotation considered in isolation from the other low frequency motions.

Figure 6.1: Normal modes of H₂-HCO⁺ from *ab initio* calculations

The modes factor into five intramolecular vibrations and four lower frequency intermolecular vibrations. The frequency for each intramolecular motion has been scaled as described in the text.



Some insight into the character of the H₂ rock/internal rotation can be derived by considering a simple atom-diatom hindered rotor hamiltonian

$$\hat{H} = b\hat{j}^2 + B\hat{I}^2 + V(\theta) \quad (6.4)$$

useful discussions of which can be found in ref. [197]. Here \hat{j} and \hat{I} are angular momentum operators pertaining respectively to the rotation of the diatomic (H₂) and of the entire complex. Usually the potential function $V(\theta)$ is expanded in a sum of Legendre polynomials in $\cos\theta$,

$$V(\theta) = \sum_{\lambda} V_{\lambda} P_{\lambda}(\cos\theta) \quad (6.5)$$

where θ is the angle between the diatomic bond and the line joining the diatomic centre of mass and the atom. The eigenfunctions of the hamiltonian are expanded in terms of basis functions that are simultaneous eigenfunctions of \hat{j}^2 , \hat{I}^2 , \hat{J}^2 and \hat{J}_z (where \hat{J} is the total angular momentum operator; $\hat{J} = \hat{j} + \hat{I}$). Such a basis can be constructed as the sum of spherical harmonic products

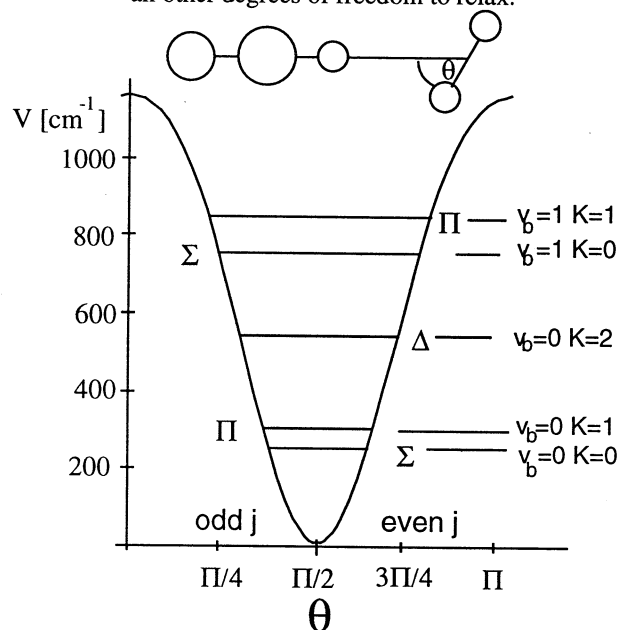
$$\psi_{jl}^{JM} = \sum_{m_j m_l} \langle jlm_j m_l | JM \rangle Y_{jm_j} Y_{lm_l} \quad (6.6)$$

where the $\langle jlm, m_l | JM \rangle$ are Clebsch-Gordan coefficients. For a homonuclear diatomic only even potential terms need be considered and the problem separates into ones involving even and odd j terms.

An approximate effective potential for the H₂ rocking motion was determined by calculating the complexes' energy with the H-H bond tilted at angles of 0, 10, 30, 60, 80 and 90 degrees with respect to the HCO⁺ axis (the H₂ centre of mass being constrained to lie on the HCO⁺ axis), all other molecular degrees of freedom being allowed to relax at each angular point. The resulting energies were used to find least squares values for the first two even coefficients in the Legendre expansion for the model potential yielding $V_2=818\text{ cm}^{-1}$ and $V_4=-118\text{ cm}^{-1}$. Equipped with the angular potential, the hindered rotor hamiltonian was diagonalized to yield eigenvalues and eigenvectors.

Figure 6.2: *Ab initio* H₂ rocking potential for H₂-HCO⁺

The potential was determined by varying the angle between the intermolecular and H₂ axes while allowing all other degrees of freedom to relax.



The lowest rotational levels of the first few K manifolds are shown together with the fitted potential in figure 6.2. As mentioned above, wavefunctions of even and odd j parentage are not mixed by the potential, and thus there are independent ortho (j odd) and para (j even) modifications of H₂-HCO⁺ which should exist in 3:1 population ratio. Symmetries of the states deriving from even and odd j combinations are shown respectively on the right and left of the potential. It is possible to correlate the two lower levels with those of a T-shaped prolate top with quantum numbers $v_b=0$ for the bending vibration and K for the projection of the angular momentum onto the intermolecular axis. This is done on the right side of figure 6.2. For any particular K manifold the rotational level spacings are approximately as they are for a diatomic molecule

$$E(K, J) = E_K + B_{\text{eff}} J(J+1) \quad (6.7)$$

For $K > 0$ there are $p' = (-1)^{j+1} = +1$ and -1 parity levels for each J , the energetic disposition of which for low J can be represented by equation (6.7) with slightly different effective rotational constants. The splitting is largest for $K=1$ states, and depends sensitively upon the size of the anisotropic terms in the potential, manifesting itself in the P and R branch of a parallel infrared band with pairs of transitions which are displaced slightly from one another, in much the same way as asymmetry doublets of a near prolate symmetric top. By fitting the bottom few J levels of the $p' = +1$ and -1 manifolds of the lowest $K=1$ level the

effective rotational constants of 0.5018 cm⁻¹ and 0.4983 cm⁻¹ respectively we derived, implying a J dependent splitting in the P and R branch transitions which increases approximately as J×0.007 cm⁻¹.

6.2.3. Observed spectra and assignment

Assignment and analysis of the vibrational band structure is based largely on the expectation that complexation of H₂ and HCO⁺ will not greatly perturb the intramolecular vibrational frequencies and also upon the *ab initio* and normal coordinate calculations described in the preceding section. The vibrational predissociation spectrum of H₂-HCO⁺ in the 2600-4200 cm⁻¹ range is shown in figure 6.3.

Although the spectrum appears at first sight to consist only of two major bands centred near 2840 cm⁻¹ and 4060 cm⁻¹, closer examination reveals that the 2840 cm⁻¹ system is in fact composed of three close lying transitions (figure 6.4) and that the 4060 cm⁻¹ system (figure 6.5) is comprised of two overlapping bands. In addition a very weak band appears at around 3145 cm⁻¹. Positions, structures and assignments of the different vibrational bands are given in table 6.2.

Figure 6.3: Vibrational predissociation spectrum of H₂-HCO⁺

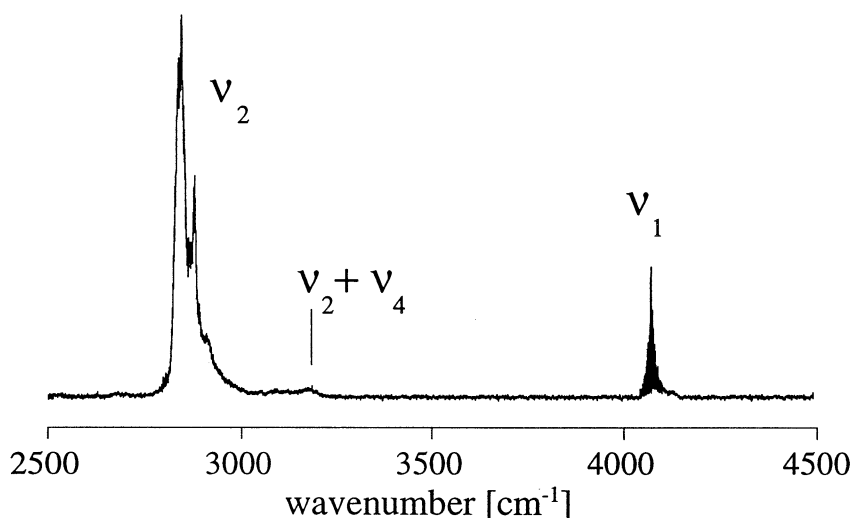


Table 6.2: Observed H₂-HCO⁺ transitions

Observed vibrational band positions and assignments for H₂-HCO⁺.

band wavenumber (cm ⁻¹)	description	proposed assignment
2840	parallel (v. strong)	v ₂
2876.36	perpendicular (strong)	v ₂ +v ₉
2879.08	perpendicular (strong)	v ₂ +v ₆
3145	parallel (v. weak)	v ₂ +v ₄
4060.315	parallel (strong)	v ₁ (Π-Π band)
4063.822	parallel (weak)	v ₁ (Σ-Σ band)

Between 2800 and 2900 cm⁻¹ three band systems can be distinguished, none exhibiting resolved rotational lines. The most intense of the three is the one to lower energy at 2840 cm⁻¹ (figure 6.4). Its strength and position immediately encourage one to assign it as arising from the excitation of the CH stretching fundamental of the HCO⁺ subunit,

consistent with the calculations, which predict the occurrence of a strong band at 2850 cm⁻¹. The two higher lying bands are somewhat sharper, and are separated by only around 3 cm⁻¹. Their close spacing and rather sharp structure, indicative of the Q branches of perpendicular transitions, leads one to suspect that they may represent two close lying combination bands involving the two lowest frequency bending levels (ν_6 and ν_9) and the C-H stretch (ν_2). The normal harmonic frequencies of the two bends are only 2.5 cm⁻¹ apart at 194.7 cm⁻¹ and 197.2 cm⁻¹, although if the bands in question involve the $\nu_2+\nu_6$ and $\nu_2+\nu_9$ combinations, the calculated harmonic frequencies must considerably overestimate the true ν_6 and ν_9 values. This is quite possible given that these two bending vibrations will have large amplitudes and should sample regions of the potential well away from the minimum.

Figure 6.4: The ν_2 band of H₂-HCO⁺

Expanded view of the 2840 cm⁻¹ system, composed of the ν_2 and $\nu_2+\nu_6$ and $\nu_2+\nu_9$ bands. The last two assignments correspond to the pair of closely spaced sharp features and they are not certain.

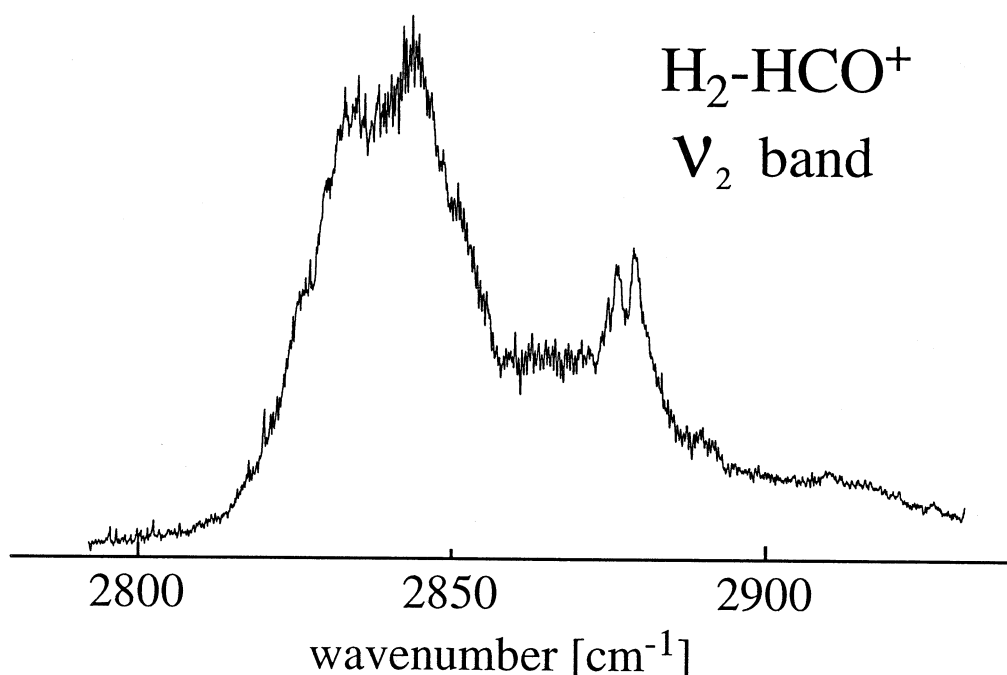


Table 6.3: H₂-HCO⁺ ν_1 band constants

Constants (in cm⁻¹) for $\Sigma\leftarrow\Sigma$ and $\Pi\leftarrow\Pi$ sub-bands of the H₂-HCO⁺ ν_1 transition. Values given in brackets are the 2σ uncertainties in the last two digits of the measured constants.

	$\Pi\leftarrow\Pi$ subband	$\Sigma\leftarrow\Sigma$ subband
origin	4060.315(08)	4063.822(11)
B''	0.4872(04)	0.4863(06)
D''	3.54e-6(63)	2.6e-6(2.3)
B'	0.4884(04)	0.4877(06)
D'	3.18e-6(67)	1.5e-6(1.8)

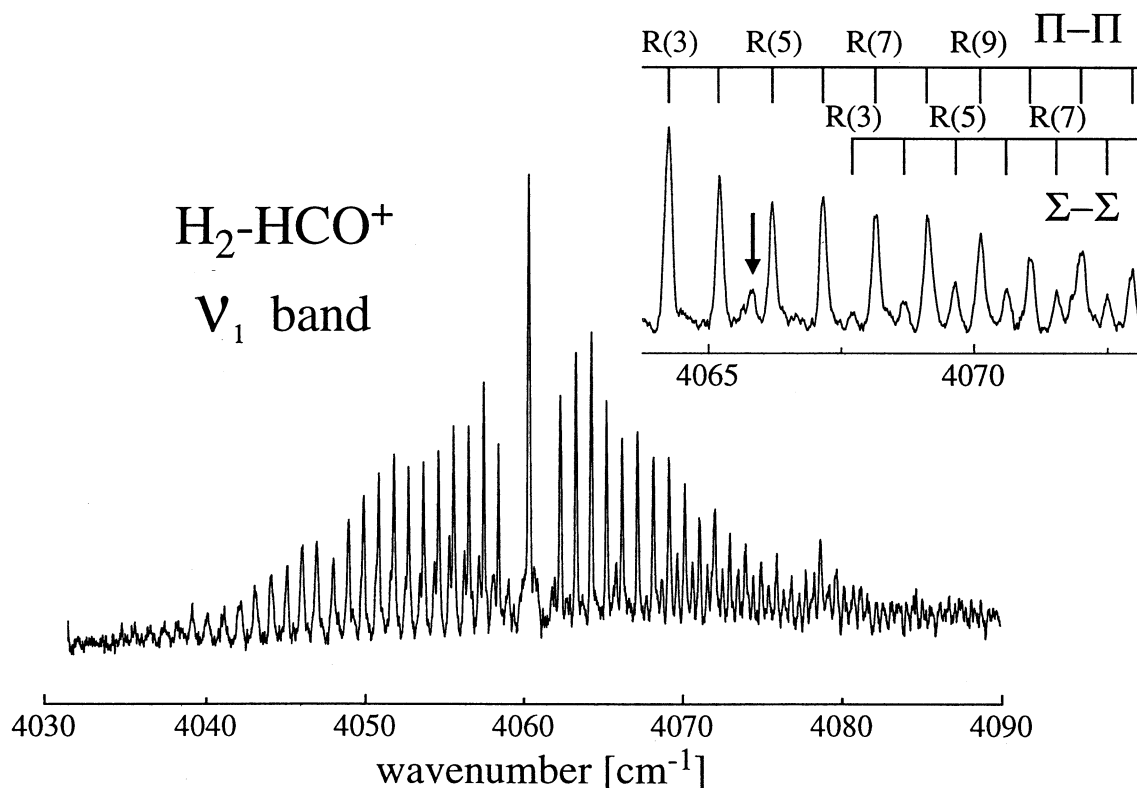
Somewhat higher in energy, at around 3145 cm⁻¹ is an extremely weak band having the appropriate wavenumber and structure (parallel band) for assignment to the $\nu_2+\nu_4$ combination, that is the C-H stretch vibration in conjunction with the low frequency H₂...HCO⁺ stretch. The displacement from the ν_2 fundamental is 305 cm⁻¹ in good

agreement with the value calculated for ν_4 using the effective intermolecular stretching potential (320 cm⁻¹).

Finally, occurring near 4060 cm⁻¹ are two rotationally resolved subbands having the $\Sigma \leftarrow \Sigma$ and $\Pi \leftarrow \Pi$ structures anticipated for parallel $\Delta K=0$ subbands from $K=0$ and $K=1$ manifolds of a near prolate symmetric top (figure 6.5). The two subbands occur some 100 cm⁻¹ to lower energy from the free H₂ stretch vibration (4161 cm⁻¹), and are almost indisputably associated with the ν_1 vibration of the complex. We note that the $\Sigma \leftarrow \Sigma$ subband is somewhat weaker than the $\Pi \leftarrow \Pi$ one, consistent with the nuclear spin weights for para and ortho H₂, and thus suggesting that the H₂-HCO⁺ complex contains two equivalent hydrogen atoms. Such a finding is compatible with both a T-shaped semi-rigid prolate symmetric top structure and also with a situation where the hydrogen molecule undergoes hindered internal rotation.

Figure 6.5: The ν_1 band of H₂-HCO⁺

Expanded view of the 4060 cm⁻¹ ν_1 band system of H₂-HCO⁺. The arrow marks the position of the unidentified Q branch.



Splittings in the P and R branches of the $\Pi \leftarrow \Pi$ band expected for both a rigid slightly asymmetric prolate top and a hindered atom diatom system were not resolved in the present study. For this reason rotational line wavenumbers for the two subbands were fitted separately to the pseudodiatomic expression (4.3) with $K''=K'=0$ and 1 for respectively to $\Sigma \leftarrow \Sigma$ and $\Pi \leftarrow \Pi$ transitions. Constants derived from the fit are given in table 6.3. Observed line positions R(1)-R(20) and P(2)-P(22) in the $\Pi \leftarrow \Pi$ band, and R(3)-R(15) and P(3)-P(14) in the $\Sigma \leftarrow \Sigma$ band can be reproduced from these constants within the experimental precision. Due to better signal to noise ratio, parameters are more precisely determined for the $\Pi \leftarrow \Pi$ subband than for the $\Sigma \leftarrow \Sigma$ one. As well, the rather prominent Q branch makes rotational numbering for the $\Pi \leftarrow \Pi$ subband straightforward. Matters are

more difficult for the $\Sigma \leftarrow \Sigma$ subband where due to the absence of a Q branch and difficulty in locating the first few P and R branch lines the numbering remains somewhat tentative. The numbering eventually adopted places the subband origin midway between the estimated intensity maxima of the P and R branches, between the R(2) and R(3) lines of the $\Pi \leftarrow \Pi$ transition. But the assignment is not certain and may change in the future if spectra with a better resolution and S/N ratio become available. Introduction of the rotational and centrifugal distortion constants into Millen's relationship (4.10) allows an estimate for the intermolecular stretch frequency of around 300 cm⁻¹ in good agreement with previous assignment of the 3145 cm⁻¹ band to the $\nu_2 + \nu_4$ combination. Another point that should be emphasized is that the derived rotational constants (table 6.3) agree very well with the *ab initio* predictions made for H₂-HCO⁺ in this and other theoretical works [216, 226] but not with that for either H₂-HOC⁺ [217] or H₂COH⁺ (experiment) [220], which proves that it is indeed the H₂-HCO⁺ isomer that is detected.

Table 6.4: Rotational constants of different isomeric forms of H₃CO⁺

Predicted and measured rotational constants (in cm⁻¹) for various isomers of H₃CO⁺. Calculated constants are equilibrium values while the experimental ones are vibrationally averaged.

	H ₂ COH ⁺ ^a	H ₂ -HOC ⁺ ^b	H ₂ -HCO ⁺ ^c	H ₂ -HCO ⁺ ^d	H ₂ -HCO ⁺ ^e	H ₂ -HCO ⁺ ^f
A	6.5903	55.1403	59.4693	60.9168	59.8183	
B	1.1459	0.6471	0.4763	0.4992	0.5042	
C	0.9730	0.6396	0.4725	0.4951	0.4999	
(B+C)/2	1.0595	0.6434	0.4744	0.4972	0.5020	0.4872

^a exp. Reference [220]; ^b calc. Reference [217]; ^c calc. Reference [216]; ^d calc. Reference [226]; ^e calc. present work; ^f exp. B₀ value obtained from the analysis of the ν_1 Π - Π subband

6.2.4. Discussion

While it may be useful to think of H₂-HCO⁺ as merely an H₂ molecule electrostatically bound to an HCO⁺ cation, subtle effects involving transfer of electron density from one of the moieties to the other should express themselves through small changes in the constituents' vibrational frequencies and geometries as they approach one another. The experimental spectra of H₂-HCO⁺ provide information on two 'intramolecular' vibrations - the H-H stretch localized on the H₂ ($\nu_1=4060$ cm⁻¹) and the C-H stretch localized on the HCO⁺ ($\nu_2=2840$ cm⁻¹). In both cases, comparison with the corresponding vibrations of the isolated molecules (H₂ $\nu_0=4161$ cm⁻¹ [227]; HCO⁺ $\nu_1=3089$ cm⁻¹ [172]) shows that the frequency decreases upon complexation. For the H₂ stretch, a simple explanation may be that the positive charge localized on the HCO⁺ withdraws electron density from the H-H bond, thereby weakening it. In the case of the HCO⁺ part of the complex the reduction in CH stretching frequency can be explained by flattening of the effective potential for the proton motion, which occurs when the HCO⁺ unit interacts with H₂.

Where comparison between calculated and measured molecular properties is possible the agreement is good. Particularly satisfying is the close correspondence between computed and measured rotational constants (table 6.4). It should be remembered that the effective B_v values determined spectroscopically are related to the vibrationally averaged value of the inverse moment of inertia, and as the bond between the H₂ and HCO⁺ ion is relatively weak, B_v values will be somewhat less than the B_e ones. The calculations overestimate both the ν_1 and ν_2 intramolecular vibrational frequencies, as they also do for the corresponding motions in the monomer subunits. It is reassuring to note that almost identical proportional corrections are necessary to bring the measured and calculated H-H and C-H frequencies into line for the subunits and for the complex. For the intermolecular motions it is necessary to go beyond the harmonic approximation presuming infinitesimal displacements, and to explicitly consider the large amplitude nature of the vibrations. When this is done for the intermolecular stretch, with calculation of an effective *ab initio* stretch

potential and solution of the radial Schrödinger equation, there is excellent agreement between the experimental value based upon centrifugal distortion constants and spacing of combination bands ($\approx 300 \text{ cm}^{-1}$) and the theoretical value (320 cm^{-1}). The experimental results suggest that the calculated harmonic frequencies for the two lowest bending motions which principally entail the in and out of plane displacement of the H₂ ligand (ν_6 and ν_9) may be overestimations.

Worthy of note is the increase in rotational constant for both Π - Π and Σ - Σ bands when the ν_1 stretch is excited. From an electrostatic point of view a shortening of the intermolecular bond is not unexpected as the quadrupole moment of H₂ is around 10% larger in the $v=1$ than the $v=0$ state ($2.17 \times 10^{-40} \text{ Cm}^2$ for $v=0$, $2.40 \times 10^{-40} \text{ Cm}^2$ for $v=1$) [228]. Thus exciting the ν_1 vibration might be expected to have the combined effects of shortening the intermolecular bond and deepening the intermolecular potential.

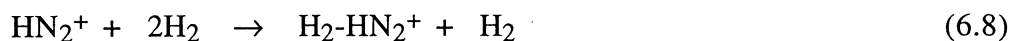
Although poor signal to noise ratio for the higher J lines makes it difficult to resolve expected doublets in PR branches, it is possible to estimate the combined width of the parity doublets in the P and R branch lines of the $\Pi \leftarrow \Pi$ subband. Both P and R branch linewidths show a roughly linear J dependence. The linewidths increase rather more quickly than anticipated if the broadening was merely due to asymmetry doubling in a near prolate symmetric top where, using the geometrical parameters given by the *ab initio* calculations, one predicts a doubling that increases as $\Delta \approx 0.004 (J+1)$ for the R branch and $\Delta \approx 0.004 J$ for the P branch. Best linear fits to the experimental data have slopes of $0.008 \pm 0.002 \text{ cm}^{-1}$ (R branch) and $0.011 \pm 0.002 \text{ cm}^{-1}$ (P branch), around twice the value expected for a prolate symmetric top, but more or less consistent with the value (0.007 cm^{-1}) expected from the hindered rotor analysis using the *ab initio* V_2 and V_4 terms.

The H₂-HCO⁺ predissociation is decidedly non-statistical, as the ν_1 state with over 1000 cm^{-1} more energy than the ν_2 state, has at least a few orders of magnitude slower vibrational predissociation rate. The variation is almost certainly due to differences in the coupling between the coordinate in which the energy is originally deposited and the other modes of the complex. The normal coordinate analysis reveals that the ν_1 vibration is almost a pure H₂ stretch motion entailing little motion of the H₂ ligand with respect to the HCO⁺. On the other hand, the ν_2 vibration involves appreciable relative movement of the subunits, presumably enhancing the opportunity for coupling with the dissociative coordinate (H₂...HCO⁺ stretch). Observations of slower IVR/vibrational predissociation rates for the H₂ stretch vibration compared to the other intramolecular motions agrees with findings for the H₃O⁺-H₂ complex [61], in which the only vibrational transition to exhibit rotationally resolved structure is the ν_1 band, again involving excitation of the H-H stretching vibration.

6.3. The H₂-HN₂⁺ complex

6.3.1. General

The H₂-HN₂⁺ complex is in many ways similar to its isoelectronic brother H₂-HCO⁺ discussed in the previous chapter. However, due to not very large difference in the proton affinities of N₂ and H₂ ($\Delta PA=75$ kJ/mol) the central proton in H₂-HN₂⁺ is expected to be delocalized somewhat more strongly. This may lead to an increase in the intermolecular binding energy and concomitant decrease in the NH and H₂ stretching frequencies. Indeed thermochemical high pressure mass spectrometry data demonstrate that the complex is reasonably strongly bound, having a heat of formation from HN₂⁺+H₂ of 30 kJ/mol [229](≈ 2500 cm⁻¹). A value of the similar magnitude ($D_e=28$ kJ/mol) is predicted from *ab initio* study of Kraemer et al [154] which compares the properties of the H₂-HXY⁺ series (XY = NN, OC, CO). Thus the dissociation threshold for the complex is close to the energy range of the spectroscopic investigations (2500-4200 cm⁻¹). Apart from the weakly bound complex H₂-HN₂⁺, that is typically formed in three body association reactions



there exist another well documented isomer of the N₂H₃⁺, an ion with structure HNNH₂⁺ (hydrazil cation) [230]. The latter can be formed by an electron impact on, or discharge through, or hydrogen abstraction from the N₂H₄. In present work the experimental conditions for production of H₂-HN₂⁺ complexes were identical to those used for H₂-HCO⁺ except that CO was replaced by N₂. Though it is possible that some amount of hydrazil cation may be formed under these conditions it is not going to interfere with the photodissociation experiment on the isomeric complex



since it is a normal molecular ion with a high binding energy [230]. The situation is entirely similar to the relationships between the H₂-HCO⁺ complex and the protonated formaldehyde.

6.3.2. *Ab initio* calculations

Since in the earlier study on the analogous H₂-HCO⁺ complex *ab initio* molecular orbital calculations were able to provide structural and spectroscopic information to satisfactory accuracy it was decided to perform computations with a similar theoretical approach for the H₂-HN₂⁺ complex. For details of the calculations see ref. [231]. The H₂-HN₂⁺ complex prefers a C_{2v} structure (figure 6.6) consisting of largely undistorted H₂ and HN₂⁺ subunits. The calculated intermolecular bondlength of 1.435Å is significantly shorter than previous theoretical predictions of 1.657Å [232] and 1.53Å [154], with the difference, perhaps, due to basis set incompleteness in the earlier studies. The D₀ for the intermolecular bond energy is calculated to be 24 kJ/mol including zero point, harmonic vibrational energy corrections. Although an experimental value for D₀ has not been reported, thermochemical experiments provide an enthalpy for the H₂ + HN₂⁺ → H₂-HN₂⁺ association reaction of $\Delta H^0=-30\pm 0.8$ kJ/mol [229]. Once the necessary thermodynamical corrections are made to the calculated bond energy a theoretical value of $\Delta H^0=-27$ kJ/mol is extracted in satisfactory agreement with the experimental value. As for H₂-HCO⁺, the normal vibrational modes of H₂-HN₂⁺ are factored into inter- and intramolecular modes. Vibrations in the latter category are similar in nature to those of the isolated monomer subunits. For example, the ν_1 vibration of H₂-HN₂⁺ can be compared to the H₂ stretch, ν_2

and ν_3 respectively to the N-H and N-N stretches of HN₂⁺, and ν_5 and ν_7 to the degenerate bend of HN₂⁺. It should be reasonable to assume that the anharmonicity of the intramolecular vibrations are not greatly altered when the constituents are brought together to form the complex, so that a fair guide to the complexes' intramolecular frequencies should be attained by scaling each frequency by the factor necessary to bring the corresponding calculated monomer frequencies into line with the experimental ones.

Figure 6.6: Minimum calculated energy structure for H₂-HN₂⁺ and HN₂⁺

The complex consists of essentially undistorted H₂ and HN₂⁺ subunits bound together in a T-shaped fashion. The numbers shown in parentheses are Mulliken atomic charges.

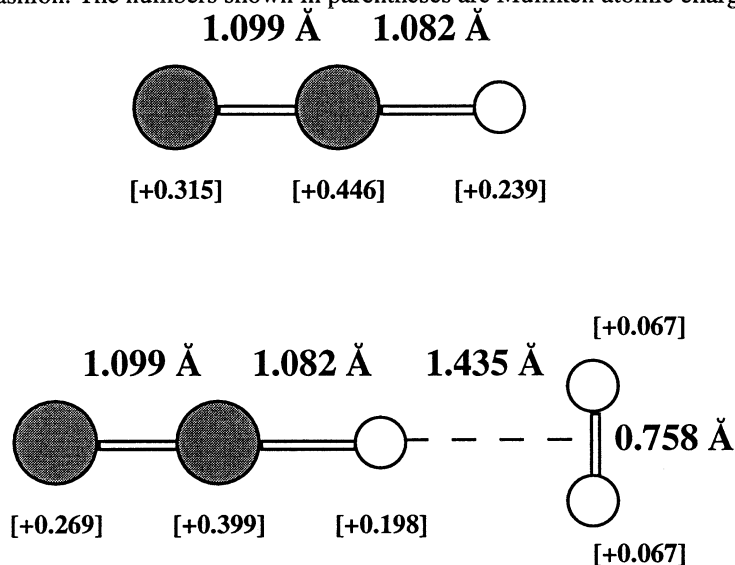
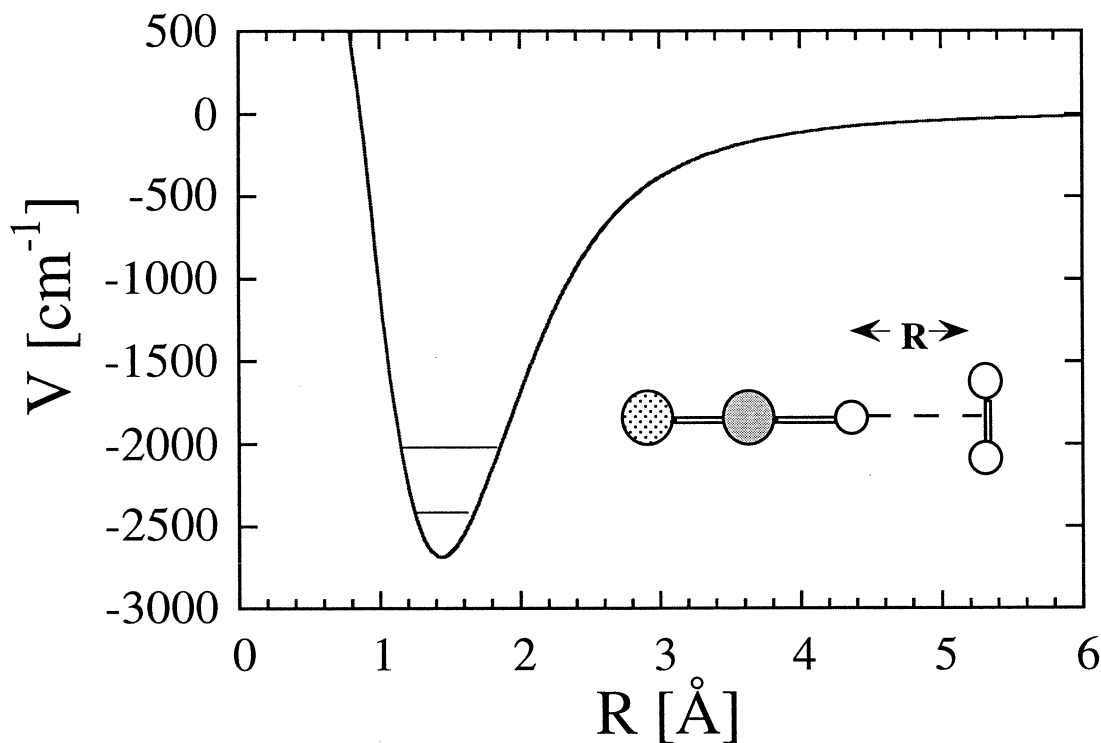


Figure 6.7: Intermolecular stretching potential for H₂-HN₂⁺

The potential was determined by varying the H₂··HN₂⁺ intermolecular separation whilst allowing all other degrees of freedom to relax. Vibrational level spacings were determined by numerically solving the radial Schrödinger equation.



Calculated and scaled frequencies are provided in table 6.1 together with respective values for the H₂-HCO⁺ complex. The effects of anharmonicity are likely to be greater for intermolecular modes than they are for the intramolecular ones, perhaps rendering the calculated vibrational frequencies somewhat unreliable. For the intermolecular stretching frequency an effective potential was developed in the way similar to that used for H₂-HCO⁺. The first vibrational energy spacing calculated from the effective potential (438 cm⁻¹, figure 6.7) is indeed much lower than the corresponding harmonic frequency (569 cm⁻¹). Both higher intermolecular stretching frequency and a significantly shorter, stiffer intermolecular bond for H₂-HN₂⁺ compared to H₂-HCO⁺ reflect considerably higher binding energy in the former system.

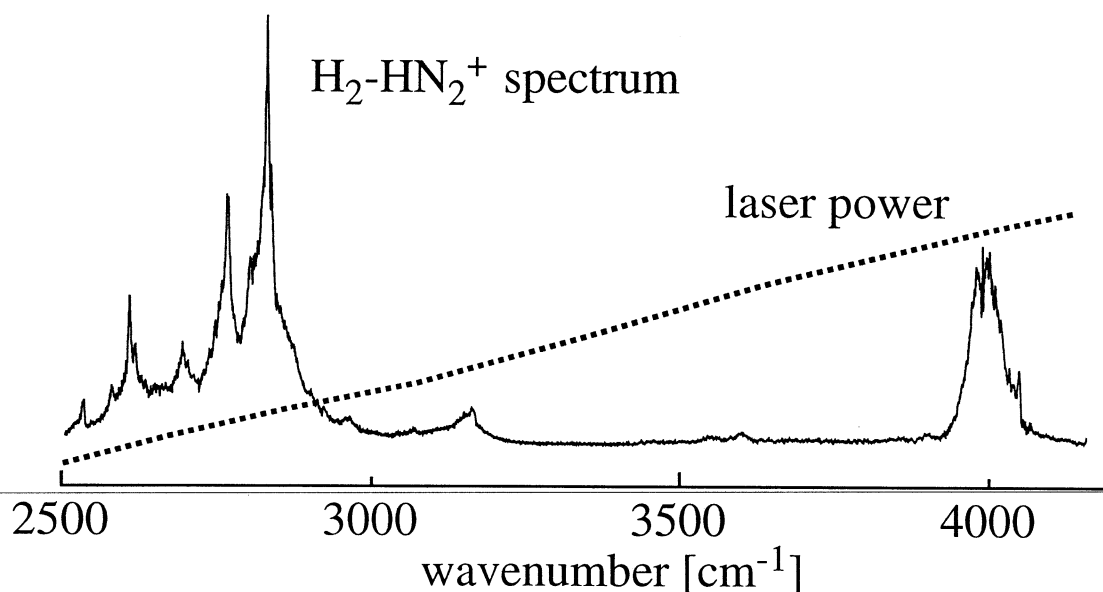
A qualitative impression of the nature of the HN₂⁺···H₂ intermolecular bond can be developed by inspecting the Mulliken populations on each atomic centre. The Mulliken analysis (figure 6.6) indicates a migration of 0.134 e of electron density away from the H₂ moiety. It is interesting to note that according to the Mulliken analysis, the electron density gained by the HN₂⁺ subunit upon association with H₂, is roughly equally shared by all HN₂⁺ atomic constituents.

6.3.3. Results and assignments

The vibrational predissociation spectrum of H₂-HN₂⁺ has been recorded in a series of shorter scans, each approximately 100-200 cm⁻¹ long, which have been pieced together to produce the spectrum displayed in Figure 6.8. Band positions are given in Table 6.5.

Figure 6.8: Vibrational predissociation spectrum of H₂-HN₂⁺

The relative intensities of different bands may be somewhat distorted, as the spectrum is a composite built up from several shorter scans, and is not corrected for laser power (shown as the dotted curve).



Although relative intensities of adjacent vibrational bands should be more or less correct, this will be less true for bands separated by large energy gaps. While none of the prominent vibrational bands occurring in the 2500-4200 cm⁻¹ range displays well resolved rotational lines, there do appear to be two distinct types of rotational band contours, corresponding to infrared transitions in a near prolate symmetric top with the transition moment either parallel or perpendicular to the A axis. The 3962 cm⁻¹ band shown in more detail in figure 6.9 is an example of a parallel transition, and exhibits a pronounced Q branch with relatively broad, intense, unresolved P and R branches (band fwhm 50 cm⁻¹). In contrast, all of the stronger, lower energy bands display structures more consistent with

perpendicular transitions; that is they possess a prominent central band but lack broad P and R branch wings.

Apart from the band at 3962 cm⁻¹, which is almost unambiguously due to excitation of the H-H stretch vibration, no other vibrational band has received a secure assignment. Significantly, none of the bands possesses the parallel structure expected for the N-H stretch transition of the complex, implying that there has been drastic decrease by more than 700 cm⁻¹ in the N-H stretch frequency from its free HN₂⁺ value (3234 cm⁻¹). Obviously, the 2500-3000 cm⁻¹ bands must be due to overtones or combinations involving either the intramolecular HN₂⁺ bending vibrations (ν₅ and ν₇), the intermolecular H₂ rock (ν₈) or quasidegenerate intermolecular bends (ν₆ and ν₉). Possible combinations are numerous, but the upper state probably involves the bending motions excited in combination with either the N-H or N-N stretch vibrations. Perpendicular bands predicted to fall in the same range include ν₂+ν₆ and ν₂+ν₉, ν₃+ν₅, ν₃+ν₇ and ν₃+ν₆. In order to learn more about the structure of H₂-HN₂⁺ and establish the frequencies of the vibrational fundamentals it would be most useful to observe vibrational bands below 2500 cm⁻¹.

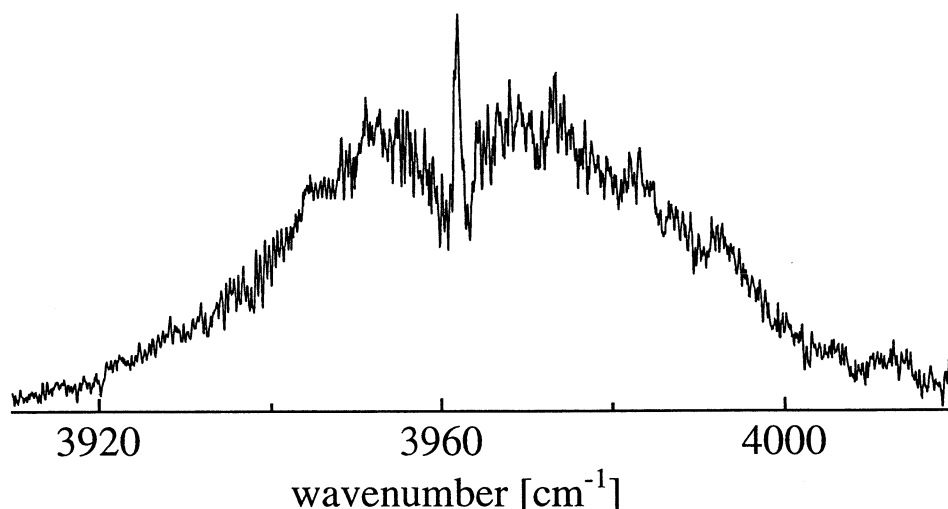
Table 6.5: Observed H₂-HN₂⁺ transitions

Experimental vibrational band positions and estimated intensities for the H₂-HN₂⁺ complex in the 2500-4200 cm⁻¹ range.

Position (cm ⁻¹)	Estimated Intensity	Assignment
2534	weak	
2580	weak	
2609	medium	
2618	weak	
2693	medium	
2766	strong	
2803	medium	
2830	v. strong	
2836	medium	
2963	v. weak	
3165	weak	
3962	medium	ν ₁ (H ₂ stretch)

Figure 6.9: The ν₁ band of H₂-HN₂⁺

Expanded view of the ν₁ band (H-H stretch) of H₂-HN₂⁺. While the Q branch (at 3962 cm⁻¹) is clearly apparent other rotational features are obscured because of lifetime broadening.



The most noticeable experimental results for the H₂-HN₂⁺ system are the rather large complexation induced red shifts for the N-H stretching vibration (>700 cm⁻¹) and H₂ stretch (199 cm⁻¹). These two effects are probably linked together in the following way. As the H₂ molecule approaches to the proton end of the HN₂⁺ molecule in a T-shaped configuration, transfer of electron density from the H₂ bond to the protonated ion occurs. Thereby the H₂ bond is weakened and at the same time, the effective potential for the bridging proton becomes broader and flatter due to the presence of a second centre of attraction. A very flat effective potential for the central proton may result in an extreme anharmonicity and might not be properly taken into account by the scaling procedure. For this reason the scaled *ab initio* result of 2538 cm⁻¹ for NH stretch may be too high.

The almost complete absence of discernible rotational features in the H₂-HN₂⁺ spectrum in the 2500-4200 cm⁻¹ range, implies extremely rapid vibrational energy redistribution. Contour simulations for the ν_1 band (H-H stretch) band, where at least a central Q branch is apparent (figure 6.9), suggest that rotational linewidths are of the order of 1-2 cm⁻¹, implying that redistribution occurs on picosecond timescale. A lack of resolved rotational features in the 2500-3000 cm⁻¹ range is an evidence for similar rates for these lower vibrational levels.

6.4. The $\text{H}_2\text{-NH}_4^+$, $\text{H}_2\text{-H}_3\text{O}^+$, XeH_3^+ , and ArH_3^+ complexes

In the row ammonia, water, xenon, and argon the proton affinity of the neutrals drops in comparison with that for molecular hydrogen. As a consequence binding energies, vibrational predissociation rates, and the red shifts in the ν_1 vibrational frequencies for the four ionic complexes significantly differ. Proton affinity of Ar is even lower than that of H_2 making it improper to consider the ArH_3^+ complex as $\text{H}_2\text{-HAr}^+$. (It is better viewed as H_3^+ ion with the Ar atom weakly attached to it). The only reason these four complexes are placed together in one chapter is that the amount of data about each one in particular is at present rather limited. Transitions correlating with the excitation of H_2 subunit stretching vibration have been recorded for all of them. In XeH_3^+ and ArH_3^+ complexes rapid vibrational predissociation renders the absorption bands completely unresolved in spite of the expected large spacings between their rotational lines. For $\text{H}_2\text{-H}_3\text{O}^+$ and $\text{H}_2\text{-NH}_4^+$ complexes the ν_1 bands are rotationally resolved but the spectra are complicated somewhat by tunneling of H_2 and $\text{H}_3\text{O}^+/\text{NH}_4^+$ subunits and they still await complete understanding. However approximate H_2 stretching frequencies can easily be derived for all of them (table 6.6) and these frequencies will be used in section 10.1 for the discussion of the correlation between proton affinities, red shifts, and binding energies in the $\text{H}_2\text{-HM}^+$ complexes. Figure 6.10 displays the ν_1 spectra of the $\text{H}_2\text{-H}_3\text{O}^+$ and $\text{H}_2\text{-NH}_4^+$ complexes. Signal to noise ratio in the spectrum of the latter complex is appreciably smaller than that in the spectrum of the former indicating some reduction in binding energy and simultaneous decrease in transition dipole moment for $\text{H}_2\text{-NH}_4^+$.

Figure 6.10: The ν_1 transitions of $\text{H}_2\text{-H}_3\text{O}^+$ and $\text{H}_2\text{-NH}_4^+$

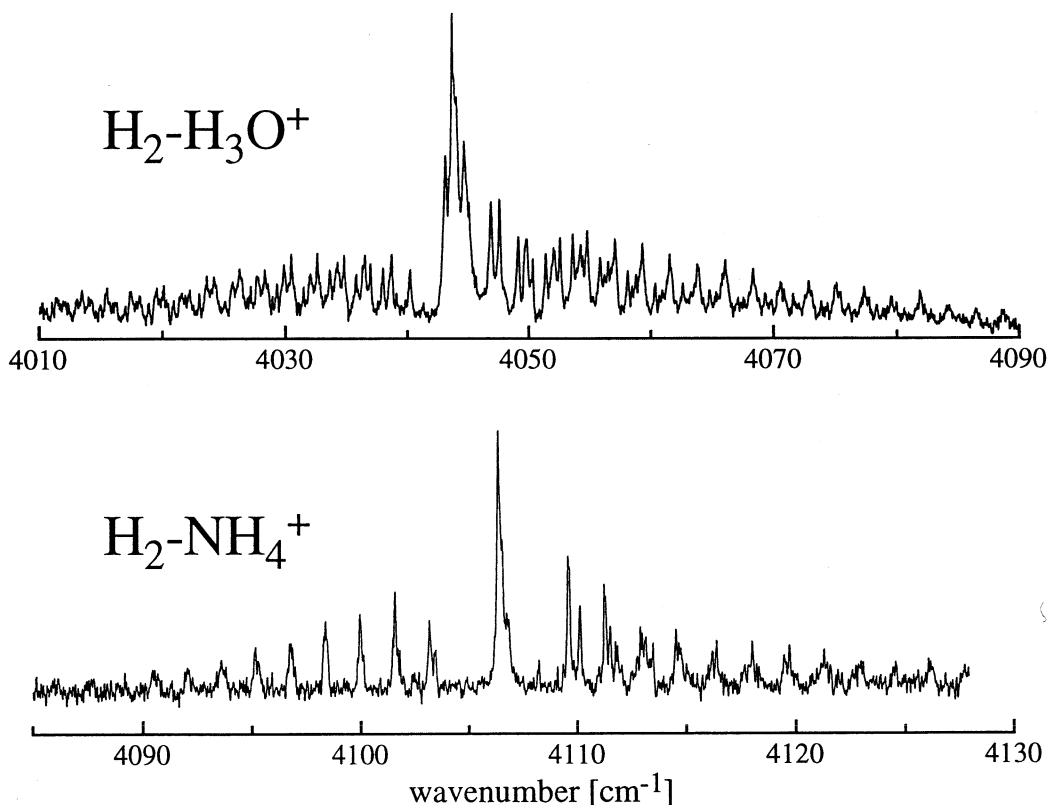


Table 6.6: Band centers of the ν_1 transitions of other $\text{H}_2\text{-HM}^+$ complexes

complex	$\text{H}_2\text{-NH}_4^+$	$\text{H}_2\text{-H}_3\text{O}^+$	XeH_3^+	ArH_3^+
ν_1 frequency	4106.4 ± 0.1	4043.7 ± 0.8	3890 ± 20	3460 ± 20

7. HM vibrations in Rg-HM⁺ complexes

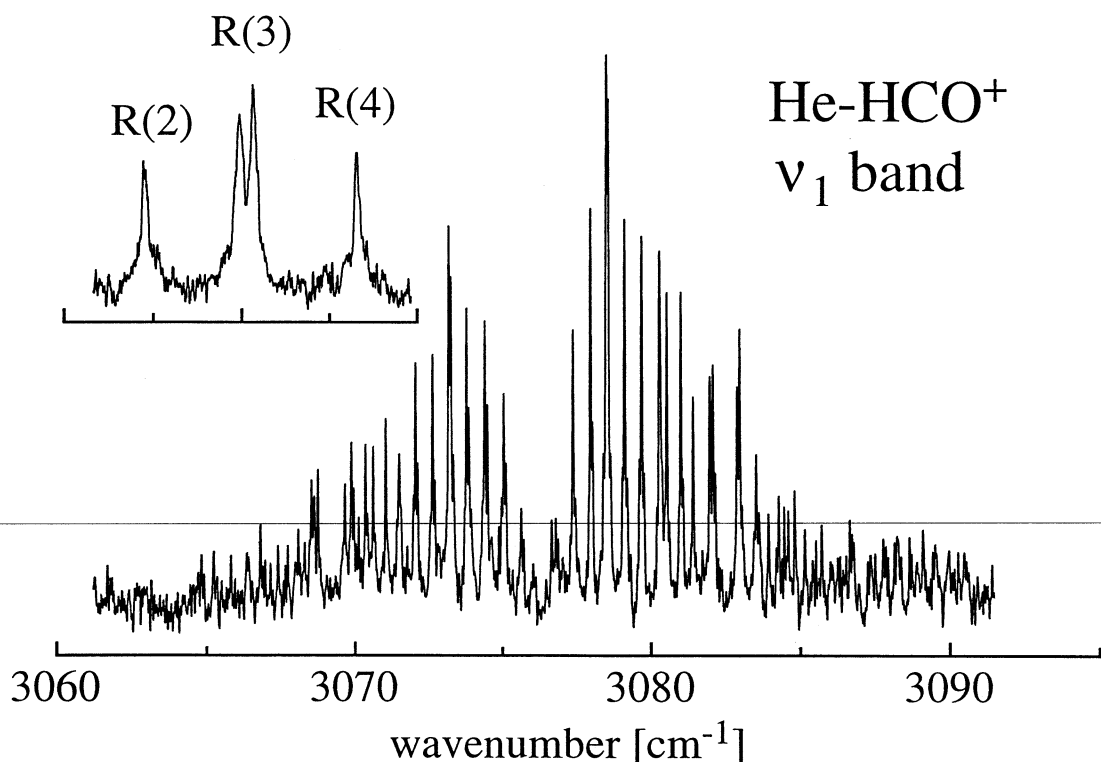
7.1. The He-HCO⁺ complex

7.1.1. Spectrum

To manufacture the He-HCO⁺ complex, a mixture of He, CO and H₂ at 6 bar stagnation pressure and 100:1:1 ratio was used. CID signal was relatively weak particularly when compared to complexes of HCO⁺ with Ne and Ar formed under similar experimental conditions reflecting smaller intermolecular binding energy between He and HCO⁺. After a thorough search in the 2950-3290 cm⁻¹ region a single band red shifted from the free HCO⁺ ν_1 origin by 12.4 cm⁻¹ was found. The band is displayed in figure 7.1. It is presumed that it arises from excitation of the He-HCO⁺ ν_1 C-H stretch vibration. Because of the unfavorable signal to noise ratio in the spectrum it was not possible to observe weaker combinations of ν_1 with intermolecular stretching vibration typical for other Rg-HCO⁺/HN₂⁺ complexes.

Figure 7.1: The ν_1 band of He-HCO⁺

Vibrational predissociation spectrum of the C-H stretch band (ν_1 vibration) of He-HCO⁺. Although the spectrum has roughly the structure expected for a linear molecule Σ - Σ transition, there are irregularities caused by upper state perturbations. The inset shows splitting in the R(3) line due to perturbation of J'=4.



The spectrum shown in figure 7.1 appears to possess the structure anticipated for a *linear* molecule Σ - Σ transition with regularly spaced P and R branch lines and no Q branch lines, in agreement with a recent *ab-initio* study [233]. However a closer inspection reveals deviations from regular line spacings in both P and R branches, often with the concurrent presence of additional lines. Certain bands in the photodissociation spectra of other

Rg-HCO⁺/HN₂⁺ also display similar anomalies attributed to the perturbations in the upper vibrational state rotational manifolds. There, ground state combination differences derived from unperturbed bands guide the analysis of the bands beset by perturbations. Here, with only one band at hand and in the absence of prior ground state information, the presence of the perturbations make spectral assignment somewhat troublesome, especially for the higher J levels. Assignments were accomplished progressively by forming the combination differences between lines with a presumed common upper state in the P and R branches, calculating the lower state rotational constants with this chosen set, extrapolating combination differences to higher J values and searching new pairs of lines that would match them. Final assignments along with the measured line positions are given in table 7.1. Ground state B'' and D'' values are respectively 0.2900±0.0002 cm⁻¹ and (1.00±0.06)×10⁻⁵ cm⁻¹. Confidence in the extracted constants and assignments is engendered by the fact that in all cases the difference between the measured and calculated combination differences are less than 0.01 cm⁻¹. Virtually all of the observed lines are accounted for in this assignment scheme. Alternative numberings resulted in ground state constants that were appreciably less well determined and more unassigned lines. Rough estimation of the upper state rotational constants and ν₁ vibrational origin was obtained by fitting the positions of the low J lines that do not suffer obvious large shifts to the standard linear molecule expression (4.3). Taking lines terminating in J'≤9, excluding J'=4 and 8, constraining B'' and D'' to the values determined from the combination difference analysis, and fixing D' to be equal to D'' resulted in the following upper state constants: ν₀ = 3076.318±0.010 cm⁻¹ and B' = 0.2898±0.0010 cm⁻¹. Differences between the measured line positions and those predicted using these molecular constants are given in the final column of table A1. It can be seen that while, with the exception of J' =4 and 8, the positions of lower J' peaks are predicted reasonably well using the fitted constants, for J'>10 substantial deviations from the predicted positions are more or less the rule. Note that differences between the experimental and fitted positions of lines terminating in the same J' levels are within experimental uncertainty the same for P and R branch transitions as it should be for case of an upper state perturbation. Small adjustments to the upper state constants do not help in diminishing deviations between measured and calculated positions.

Table 7.1: The He-HCO⁺ ν₁ band constants

Constant [cm ⁻¹]	Ground state	ν ₁
ν		3076.313 (10)
B	0.2900 (02)	0.2898 (10)
D (×10 ⁻⁵)	1.00 (06)	1.00*

Widths of rotational lines in the spectrum are laser bandwidth limited. This allows a lower limit of approximately 250 ps to be put on the upper state vibrational predissociation lifetime. Also there does not appear to be any J dependence for the linewidths.

If one neglects zero point excursions and assumes an undistorted HCO⁺ monomer, a centre of mass separation of 3.65 Å is found from formula (4.9) using the ground state rotational constants. This correspond to H...He distance of 1.98 Å. It is worth pointing out that the alternative He...OCH⁺ structure requires a considerably longer intermolecular He...O distance of 3.13 Å to be consistent with the measured rotational constant. Although this is slightly less than the sum of the He and O van der Waals radii (≈3.4 Å), the proton bound form is more consistent with the C-H stretch red shift (≈12.4 cm⁻¹), as it is with the notion that the intermolecular bonding should be dominated by induction interactions between the He and the electropositive side of HCO⁺.

Unfortunately obtained experimental information is not sufficient to define the angular and radial parts of the intermolecular potential. An estimation of the intermolecular stretching frequency and bond strength can be derived by inserting the ground state rotational and centrifugal distortion constants into Millen's expressions (4.10) and (4.11).

With $B_{\text{HCO}^+} = 1.487 \text{ cm}^{-1}$ this yields $v_s = 89 \pm 3 \text{ cm}^{-1}$, and an harmonic force constant of $1.6 \pm 0.1 \text{ N/m}$. However, as briefly mentioned in the introduction, relating the spectroscopically determined B and D values to a purely radial potential can be problematic for ball-and-stick systems if large zero-point angular excursions resulting in changing of the optimum radial centre of mass separation are present. Since increased rotation tends to bring the intermolecular bond back into alignment with the stick axis, and reduce the magnitude of angular zero-point motion (thus changing the effective centre of mass separation) there appears a rotational dependence of the effective rotational constant, manifesting itself as an anomalously large centrifugal distortion constant. As He-HCO⁺ features a 50% larger ground state centrifugal distortion compared to isoelectronic He-HN₂⁺ complex and may have an intermolecular potential energy surface permitting facile access to a T shaped configuration, it is reasonable to wonder whether it also undergoes large amplitude zero point bending displacements. Though combination bands involving intermolecular bending vibrations are not observed experimentally, there are several pieces of evidence that suggest a reasonably stiff potential. First the appearance of a single Σ - Σ type band with line spacings corresponding to twice the rotational constant of the entire complex, is itself an indication that the complex is more or less effectively 'locked into' a semi rigid linear geometry. Transitions that would correlate to excitation of internal rotation of the HCO⁺ with respect to He are not seen. Also the spectrum does not seem to fit the structure expected for slightly to intermediate hindering potentials in which case it should consist of a Σ - Σ type band corresponding to the nominally forbidden $(v_1=1, j'=0) \leftarrow (v_1=1, j''=0)$ free rotor transition along with Σ - Σ and Π - Σ type combination bands both corresponding to the allowed $(v_1=1, j'=1) \leftarrow (v_1=1, j''=0)$ free rotor transition. Additional piece of evidence for a relatively stiff He-HCO⁺ structure comes from the apparent absence of bending sequence bands in the He-HCO⁺ spectrum. A pack of sequence bands is readily visible in the spectra of Ne-HCO⁺ and Ar-HCO⁺ complexes blue shifted from the respective v_1 transitions. From S/N ratio one can estimate that bending hot band transitions (e.g., $v_1+v_b-v_b$) would be observable if the v_b state had more than 20% of the ground state population. Assuming a Boltzmann distribution and a vibrational temperature matching the rotational one ($\approx 30 \text{ K}$) one can estimate that $v_b \geq 35 \text{ cm}^{-1}$. The fact that in a molecular beam vibrational temperature(s) may significantly exceed rotational one(s) will have an effect of shifting the lower limit for the bending frequency even higher.

7.1.2. Perturbations

Now the perturbations afflicting some v_1 rotational levels are considered. The fact that there are perturbations in the v_1 band is somewhat surprising since respective transitions of other Rg-HCO⁺/HN₂⁺ complexes presented here appear to be unperturbed. Even more surprising is the way the perturbations are distributed across the upper state rotational manifold. For the lower J' values they are localized, principally at J'=4 and J'=8, while for J' ≥ 11 almost all levels appear to be affected. As the total angular momentum of any two interacting levels must be identical, it is difficult to believe that all perturbing levels are associated with a single vibrational state. Using the fact that J'=4 levels is perturbed while J'=3 and 5 levels appear unaffected (to within 0.01-0.02 cm^{-1}) from a simple two level J' independent perturbation calculation one can deduce that the perturbing state's rotational constant must differ from the one of the v_1 level by at least 0.003 cm^{-1} . For the J'=8 level a similar line of reasoning based on the fact that the J'=7 level is apparently unperturbed to within 0.03 cm^{-1} leads to the conclusion that the rotational constant associated with the perturbing state differs in this case by approximately 0.1 cm^{-1} . This large change in rotational constant is consistent with a perturbing state(s) involving intermolecular motion. Candidates for the perturbing states are the vibrations of the type $v_2+v_3+v_s(+nv_b)$ or possibly $v_2+v_3+nv_b$. For the free HCO⁺ molecule the v_1 vibration (CH stretch, 3089 cm^{-1})

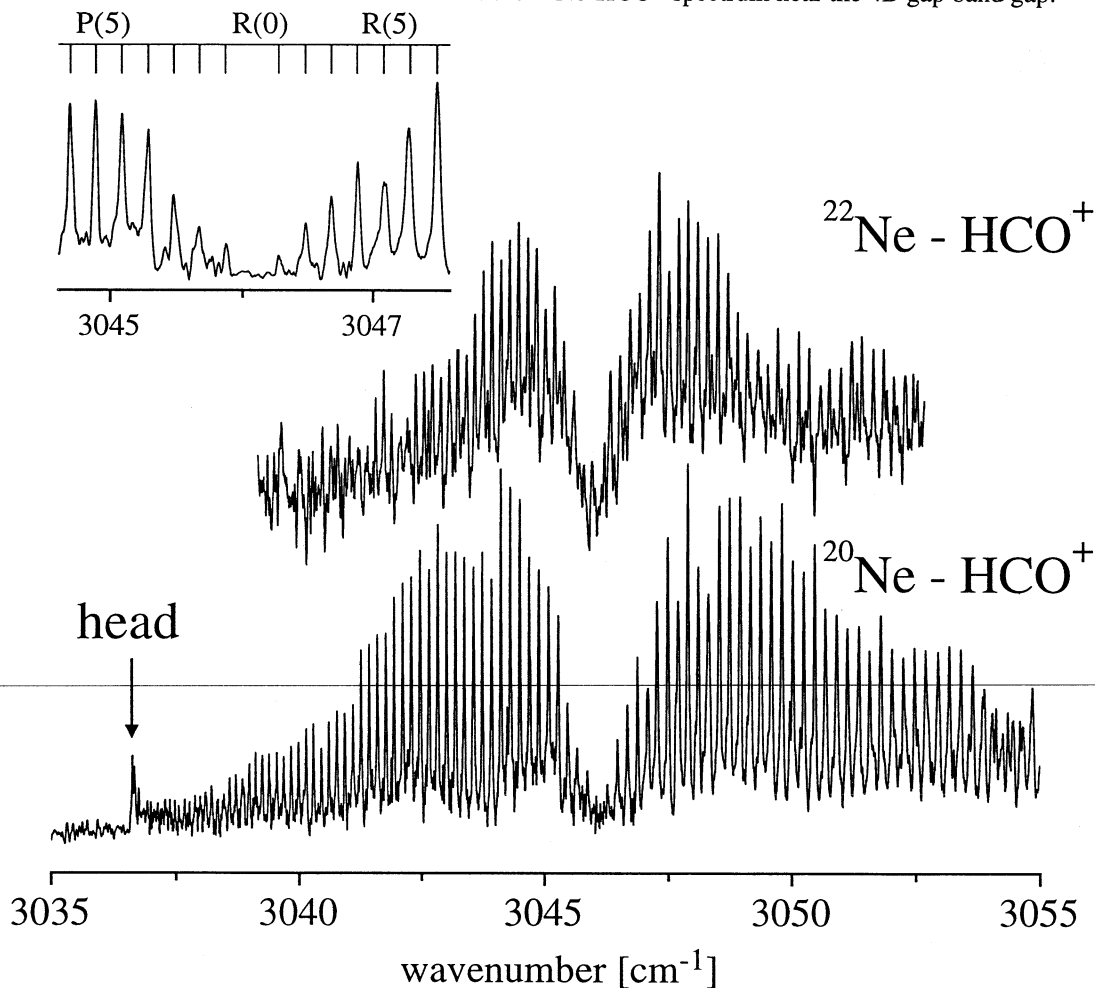
lies around 80 cm⁻¹ above the $\nu_2+\nu_3$ combination (HCO bend + CO stretch, 3012 cm⁻¹) which roughly corresponds to the intermolecular ν_s stretching frequency, estimated from the inertial and centrifugal rotational constants (≈ 90 cm⁻¹). Due to its larger average intermolecular separation compared to the ground state, excitation of ν_s should have the effect of significantly decreasing the effective potential anisotropy, perhaps to the point where the bending motion is closer to being a free internal rotor. In this case bending vibrational levels correlating with the $j=0$ and $j=1$ free internal rotor states should lie within a few wavenumbers of one another making it quite possible for several reasonably strongly coupled vibrational levels to lie close by ν_1 . The corresponding ν_1 band of isoelectronic He-HN₂⁺ is apparently unperturbed presumably reflecting the fact that for HN₂⁺ the $\nu_2+\nu_3$ combination lies almost 300 cm⁻¹ below ν_1 so that any near-resonant perturbing state built on $\nu_2+\nu_3$ would need to have considerable energy in the intermolecular motions and would necessarily interact with the ν_1 state through the agency of higher order (and therefore presumably weaker) coupling terms.

7.2. The Ne-HCO⁺ complex

The Ne-HCO⁺ and Ne₂-HCO⁺ complexes were synthesized from a mixture of Ne, H₂, and CO (ratio 400:20:1) at 4 bar stagnation pressure. Optimization of the Ne_n-HCO⁺ ion signal was accomplished in a usual way by introducing a buffer gas (e.g. He) into the octopole region with the second quadrupole tuned to the Ne_{n-1}-HCO⁺ collision induced dissociation product. Subsequently, the laser induced fragmentation signal was maximized by tuning the laser to a cluster resonance. Spectra of ²²Ne-HCO⁺ were recorded as well using natural Ne with ²²Ne/²⁰Ne ratio of the order of 0.1. The CID signal from Ne₃-HCO⁺ and higher clusters was too weak for the practical purposes. This is to be contrasted with the isoelectronic series Ne_n-HN₂⁺ for which photodissociation spectra were recorded for n up to 5 under similar experimental conditions. Under typical conditions the ion current issuing from the ion source is dominated by the HCO⁺ molecular ion, with the Ne_n-HCO⁺ current being several orders of magnitude smaller. Preliminary IR spectral searches were concentrated in the region of the strong HCO⁺ ν₁ band near 3.2 μm. Later the scanning range was extended to include the region of OH vibration of HOC⁺ to check whether any amount of isoformyl ion is formed in the expansion.

Figure 7.2: The ν₁ band of Ne-HCO⁺

Vibrational predissociation spectra of ²⁰Ne-HCO⁺ and ²²Ne-HCO⁺ (high-power scan) taken in the vicinity of the C-H stretch band. The inset shows the ²⁰Ne-HCO⁺ spectrum near the 4B gap band gap.



Scans in the 2960-3390 cm⁻¹ range revealed a prominent Σ-Σ transition centered near 3046 cm⁻¹ for both ²⁰Ne-HCO⁺ and ²²Ne-HCO⁺ which is assigned to the ν₁ vibration

(C-H stretch) of the respective complexes (see figure 7.2). The ²⁰Ne-HCO⁺ spectrum recorded with a reduced laser power (50 μJ/pulse) to prevent saturation displayed a flat background and laser limited linewidths, implying a lower value for the upper state lifetime of 250 ps. For the less abundant isomer, the higher laser power (0.5-1.0 mJ/pulse) was necessary to obtain spectra with a reasonable signal-to-noise ratio. This leads to the rotational line broadening and to the appearance of a background underlying the P and R branches.

Whereas for ²⁰Ne-HCO⁺ the P(1) and R(0) lines are clearly apparent and rotational numbering is straightforward, for ²²Ne-HCO⁺ poorer S/N ratio makes numbering less obvious. However, an examination of the band-gap region in several independent spectra prompted a numbering whereby the origin of the ²²Ne-HCO⁺ transition lies 0.106 cm⁻¹ below the one of ²⁰Ne-HCO⁺. This shift of the vibrational origin arises from different zero point energies for the intermolecular vibrations in the ground and ν_1 states. Since reduced mass for the intermolecular bending vibration is very insensitive to the isotopic substitution of the Ne atom it is probably a fair approximation to consider only the change in the zero point energy associated with intermolecular stretching vibration. In the harmonic approximation the separation of the isotopomer ν_1 origins is given by

$$\Delta = \frac{1}{2}(\nu'_s - \nu''_s) \left(\sqrt{\frac{\mu_{20}}{\mu_{22}}} - 1 \right) \quad (7.1)$$

where ν' and ν'' are the harmonic frequencies for the intermolecular stretch vibration of ²⁰Ne-HCO⁺ in the ground and ν_1 states, and μ_{20} and μ_{22} are the stretching vibration reduced masses for ²⁰Ne-HCO⁺ and ²²Ne-HCO⁺. Inserting the harmonic frequencies estimated from rotational constants B and D (see below), one finds that $\Delta = -0.06 \pm 0.05$ cm⁻¹, consistent with the observed shift.

Table 7.2 : The Ne-HCO⁺ ν_1 band constants

Constants (in cm⁻¹) for the ground and ν_1 levels of the ²⁰Ne-HCO⁺ and ²²Ne-HCO⁺ isotopomers obtained from the fit of experimental line positions. Center-of-mass distances (in Å) of the intermolecular bond are evaluated from the rotational constants assuming an undistorted HCO⁺ monomer.

	²⁰ Ne-HCO ⁺	²⁰ Ne-HCO ⁺	²² Ne-HCO ⁺	²² Ne-HCO ⁺
	$\nu_1=0$	$\nu_1=1$	$\nu_1=0$	$\nu_1=1$
ν_0		3046.120 (6)		3046.014 (6)
B	0.09954 (5)	0.10003 (5)	0.09450 (15)	0.09499 (15)
D (x10 ⁻⁷)	5.30 (30)	4.89 (30)	3.4 (1.8)	3.1 (1.5)
H (x10 ⁻¹¹)	1.1(9)	1.6 (9)		
r_{cm} [Å]	3.654 (1)	3.643 (1)	3.655 (3)	3.644 (3)

Following transitions have been observed and assigned: P(1)-P(61) and R(0)-R(51) for ²⁰Ne-HCO⁺, and P(1)-P(25) and R(0)-R(30) in the case of ²²Ne-HCO⁺. Line positions are listed in table A2. There is a head in the P branch of ²⁰Ne-HCO⁺ transition occurring at $J \approx 70$. A least squares fit of the transition energies to the pseudo-diatomic expression yields the parameters presented in table 7.2. The quality of the fit is evident from the relatively low standard deviation (0.003 and 0.006 for ^{20/22}Ne-HCO⁺, respectively). Ground and excited state B, D, and H values obtained by forming the appropriate combination differences did not differ within the error margins from the ones given in table 7.2. While for ²²Ne-HCO⁺ the rotational line positions were fit within experimental error using only B and D values, for ²⁰Ne-HCO⁺ the quality of the fit was slightly improved by including H values, although their uncertainties are of the same order as the values themselves. However the position of

the head in the P branch (at $J'' \approx 70$) cannot be fitted to experimental uncertainty without inclusion of the H constants.

The uncomplicated nature of the Ne-HCO⁺ ν_1 spectrum, consisting of a single strong band with regular P and R branches, a 4B band gap, and the absence of a Q branch, suggests that the complex has a linear equilibrium structure. Assuming that the ν_1 transition moment remains directed along the HCO⁺ axis, a rigid non-linear structure would result in the appearance of a Q branch and more complicated patterns in the P and R branches. On the other hand, a free internal rotor structure, where there is little impedance to the internal rotation of the HCO⁺, would lead to the occurrence of more widely spaced bands associated with ± 1 changes in the internal rotation quantum number j , again contrary to observation.

Assuming that the HCO⁺ monomer is not distorted by the presence of the Ne atom and neglecting zero-point-energy effects, an approximate separation between the center-of-mass of the monomer and the ²⁰Ne atom can be estimated as 3.654(2) Å for the ground state and 3.643(2) Å for the ν_1 vibrational state, respectively, i.e. the intermolecular bond length decreases by 0.011 Å upon ν_1 excitation (table 7.2). In principle, the Ne atom can approach the HCO⁺ core from either the oxygen or the hydrogen end to form a linear complex. With the ground state HCO⁺ substitution structure taken from Woods Ne-O and Ne-H distances can be estimated as 3.12 Å for the Ne-OCH⁺ and 1.99 Å for the Ne-HCO⁺ structures, respectively. One can almost certainly rule out the oxygen-bonded structure on the basis of the substantial ν_1 (C-H stretch) vibrational band shift (-42.5 cm^{-1}), which is more consistent with a geometry where the proton is adjacent to the Ne atom. This is in line with observations for neutral hydrogen-bonded complexes. For example, in the linear van der Waals dimer HCN-HF, the free C-H stretching frequency is practically unaffected by complex formation, whereas the bonded hydrogen stretch (F-H stretch) frequency is reduced by around 245 cm^{-1} [196]. A proton-bound Ne-HCO⁺ structure is also consistent with *ab initio* calculations done on similar proton-bound species [233, 234].

The strength of the Ne-HCO⁺ intermolecular bond can be estimated from the perturbation expressions for the intermolecular stretching frequency and the harmonic force constant (4.10-4.11). For the ground state of ²⁰Ne-HCO⁺ this yields $\nu_s = 83 \pm 3 \text{ cm}^{-1}$ and $k_s = 4.8 \pm 0.3 \text{ N/m}$ (table 7.2). In the ν_1 excited state the intermolecular bond is stronger, with a larger force constant ($k_s = 5.3 \pm 0.4 \text{ N/m}$) and intermolecular stretching frequency ($\nu_s = 87.4 \pm 3.0 \text{ cm}^{-1}$). Stronger intermolecular interaction in the ν_1 state is consistent with 0.011 Å shortening of the intermolecular bond upon excitation.

About 200 additional weak lines belonging to at least three different vibrational transitions were observed in the ²⁰Ne-HCO⁺ spectrum between 3054 and 3075 cm^{-1} . In addition some amount of unresolved background extending up to 3100 cm^{-1} is present.

Intensity of this weaker structure compared to the ν_1 band is relatively insensitive to the laser power indicating that the involved transition moments should be quite similar. This implies that sequence transitions build on ν_1 may be responsible for the appearance of the additional bands. Provided that vibrational state distribution of the complexes is characterized by higher effective temperature than rotational one, states with 1 or 2 quanta deposited in intermolecular vibrations should be appreciably populated. The fact that all sequence bands are placed on the blue side of the ν_1 band is consistent with stiffening of the intermolecular bond in the ν_1 state compared to the vibrationless state. Unfortunately the lines are distributed so densely that the analysis at this stage is unfeasible. Though it is possible to pick up few progressions of lines that belong together the values for the band origins are left undefined. More compact rotational distribution and somewhat higher resolution are desirable to make a proper assignments for this bunch of lines.

Curiously, in the Ne-HCO⁺ ν_1 spectrum there is no evidence for the type of isolated upper state perturbations, which were found in the ν_1 rotational manifold of He-HCO⁺. For the He containing complex the perturbations were tentatively ascribed to an accidental resonance between ν_1 and the combination of the intramolecular $\nu_2+\nu_3$ vibration with quanta of intermolecular modes. In Ne-HCO⁺ the ν_1 vibration is depressed by roughly 30 cm⁻¹ compared to He-HCO⁺, and it is possible that the interacting states have moved away from resonance.

From the rotational constants the combined RKR/DMA potential was constructed with a D_0 value of 438 cm⁻¹ for $\nu_1=0$ and 454 cm⁻¹ for $\nu_1=1$ state [235]. Estimated intermolecular stretching frequency of 87 cm⁻¹ is in a fair agreement with the value of 83±3 cm⁻¹ predicted using harmonic approximation. A peculiar thing about the spectrum of Ne-HCO⁺ complex is that there is no evidence for the combination band of ν_1 with the intermolecular stretch. The transition was readily observable in the spectra of related complexes He-HN₂⁺ and Ne-HN₂⁺ which displayed similar S/N ratio for the ν_1 band. One possible explanation for the weakness of the $\nu_1+\nu_s$ transition could be an extremely short upper state lifetime due to an accidental resonance with some other vibrational state(s) facilitating dissociation. Another option would be a shift of the upper $\nu_1+\nu_s$ vibrational state due to perturbations. Notably, there is some rather weak activity in both Ne-HCO⁺ and the Ne₂-HCO⁺ spectra around 67 cm⁻¹ above the ν_1 origin, although this could also be either $\nu_1+\nu_b$ or higher order sequence bands.

In summary, spectroscopic data and the rotational RKR/DMA potentials demonstrate that Ne-HCO⁺ is a relatively strongly bound complex, possessing a linear proton-bound structure, a center-of-mass intermolecular separation of roughly 3.65 Å, and an estimated intermolecular stretching frequency of 87 cm⁻¹. The intermolecular interaction between the Ne atom and the HCO⁺ core becomes slightly more attractive upon ν_1 excitation as evidenced by the shorter intermolecular bond and the larger intermolecular stretch frequency. The complexation induced red shift of the HCO⁺ ν_1 frequency (42.5 cm⁻¹) is also a symptom of a stronger Ne...HCO⁺ bond in the ($\nu_1=1$) state.

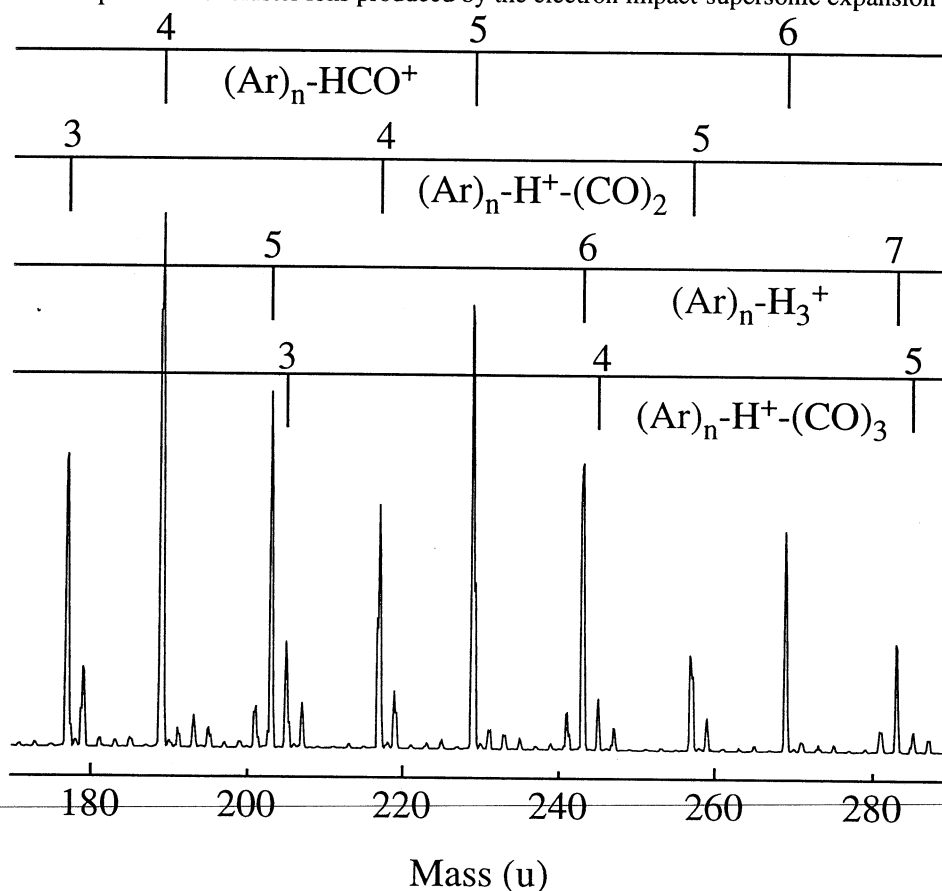
7.3. The Ar-HCO⁺ complex

7.3.1. Experimental Details

The cooled Ar_n-HCO⁺ cluster ions are produced in a pulsed supersonic expansion of H₂, CO, He and Ar at a ratio of 2:1:50:100 at 4-7 bar stagnation pressure. As can be seen from the selected portion of the mass spectrum in figure 7.3 a variety of heterogeneous cluster ions issue from the ion source, the dominant series being Ar_n-H₃⁺ and Ar_n-H⁺-(CO)_m. Introduction of He into the octopole region of the apparatus facilitates the identification and optimization of the desired Ar_n-HCO⁺ parent species through the monitoring of collision induced Ar_{n-1}-HCO⁺ fragments. As expected, an increase in either the stagnation pressure or the proportion of Ar in the gas mixture shifts the Ar_n-HCO⁺ ion distribution towards a higher degree of solvation. In all cases, the resolution of the initial and final quadrupole stages was adjusted so that parent and daughter masses were clearly resolved. Unfortunately, an upper limit on the mass transmitted by the first quadrupole (≈ 560 u) precludes characterization of Ar_n-HCO⁺ clusters larger than n=13.

Figure 7.3: Mass spectrum from an Ar/He/H₂/CO expansion

Portion of mass spectrum for cluster ions produced by the electron impact-supersonic expansion ion source.



Two distinct spectral ranges were covered in search for Ar-HCO⁺ infrared absorptions. The first one between 2650 and 4100 cm⁻¹ includes for the most part the ν_1 transition of the complex (CH stretch) and various combination and sequence bands built on it. The second range between 5300 and 5650 cm⁻¹ contains the first overtone of ν_1 and its combination with intermolecular stretching vibration. Complexes Ar_n-HCO⁺ with n>1 were studied in a more limited range of frequencies between 2800 and 3100 cm⁻¹. Their spectra are discussed later together with the other Rg_n-HXY⁺ (n \geq 2) systems.

Certain bands were studied for the naturally occurring ¹³C (1.1%) and ³⁶Ar (0.34%) isotopes. Though the deuterium containing complex, Ar-DCO⁺, has the same mass as the ¹³C species there is no interference since D is not as abundant with respect to H as is ¹³C with respect to ¹²C, and in addition DCO⁺ and HCO⁺ absorb in completely different spectral ranges. All assignments and numbers in the text, tables and figures correspond to the isotopically most abundant species ⁴⁰Ar-1H¹²C¹⁶O⁺ (\equiv Ar-HCO⁺) unless it is explicitly stated otherwise.

7.3.2. Overview

At least 10 strong transitions are observed between 2650 and 4100 cm⁻¹. Out of them one has a structure appropriate for a perpendicular (Π - Σ) band of a linear molecule and all the others are of parallel (Σ - Σ) type. All of the bands are rotationally resolved and possess laser limited linewidths, permitting a lower limit of roughly 250 ps to be put on the upper state lifetimes. Most of the bands appear to suffer from reasonably strong perturbations in the upper rovibrational states. The strongest band in this range is a parallel transition with origin at 2815.066 cm⁻¹ (2815.35 cm⁻¹ for ³⁶Ar-HCO⁺ and 2785.740 cm⁻¹ for Ar-H¹³CO⁺). The position, strength, and structure of the band immediately invite its assignment to the ν_1 (C-H stretch) transition of the complex. In addition there is a dozen of other very weak transitions, presumably sequence hot bands, located here and there between 2650 and 3200 cm⁻¹ with an especially high concentration of them on the blue wing of the ν_1 transition. Not all weaker transitions have been scanned with slow speed and they are not considered here.

The area between 5300 and 5650 cm⁻¹ was searched since it was expected that the first overtone of ν_1 falls somewhere in this range. Three bands can be seen there, the strongest one (of parallel type) lying at 5480.6 \pm 0.20 cm⁻¹. The position, relative strength, and shading of this band is indeed consistent with the overtone assignment. The three bands are poorly rotationally resolved and their origins are estimated from the band profiles.

Now all intense bands are considered in detail separately or in groups linking bands of similar origin or/and appearance. Vibrational assignments are given to the bands where it is possible, and if not, the bands are referred by their vibrational origins in the normal isotopomer (⁴⁰Ar-1H¹²C¹⁶O⁺) spectrum.

7.3.3. The ν_1 band

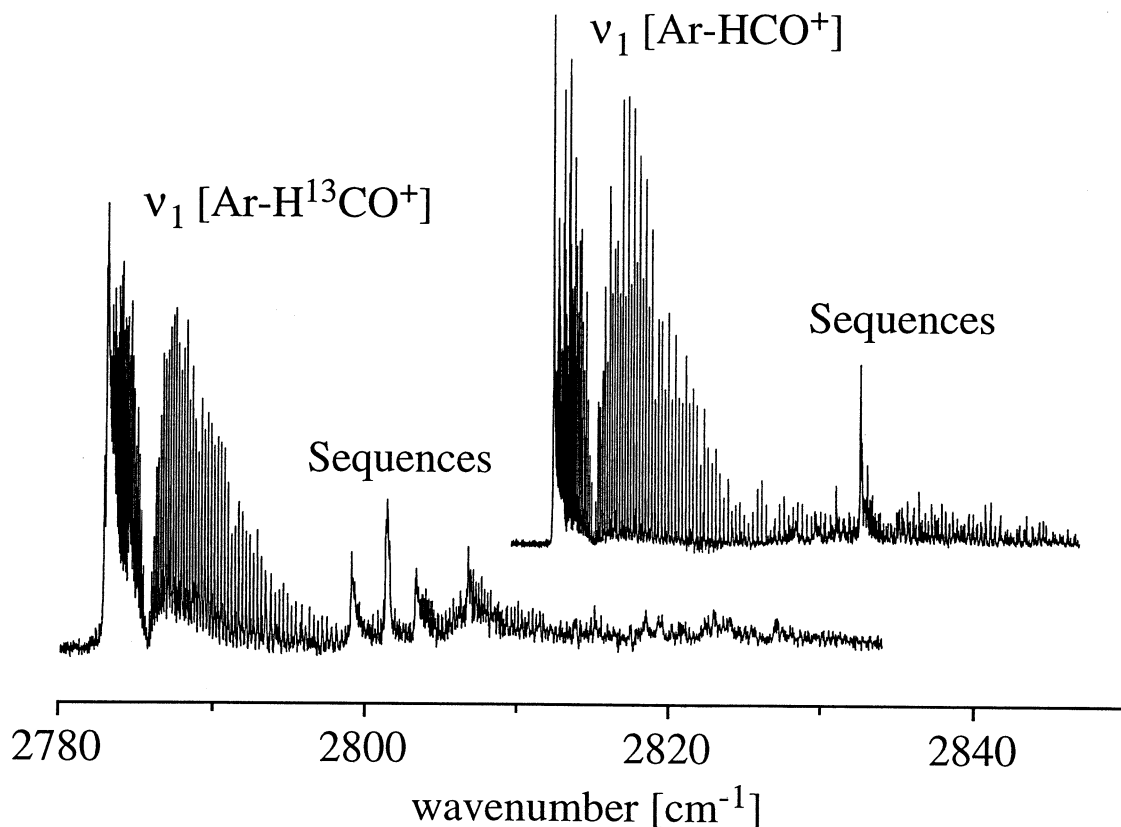
The ν_1 band of the Ar-HCO⁺ complex is shown in figure 7.4. The transition is strong and easily saturable. Nominally the laser power had to be reduced by 2 orders of magnitude from its unattenuated value (down to roughly 10 μ J/pulse) to obtain a good background and broadening free spectrum. Under the lower excitation power conditions photoinduced dissociation signal is still much higher than ions' metastable decay providing signal to noise ratio in excess of 200.

The band has an appearance characteristic for a linear molecule Σ - Σ transition with an easily discernible band gap. Rotational constant of the complex increases upon excitation leading to the formation of a sharp head in the P branch at 2812.39 cm⁻¹. Because of the head formation lines in the P branch could only be resolved for J" up to 36. In the R branch, the lines run up to J"= 65 above where they get lost among the sequence band lines and heads. For Ar-H¹³CO⁺ and ³⁶Ar-HCO⁺ similar spectra were obtained except that S/N ratio was lower, particularly for the latter isotopomer. For them lines ranging respectively from P(29) to R(45) and P(17) to R(23) were observed. Because of the increased mass of the ¹³C isotopomer its ν_1 vibration has a substantially smaller frequency (by roughly 29 cm⁻¹).

Unfortunately, in recent work of Martin et al [236] concerned with an accurate quartic force field for HCO⁺, no anharmonicity constants for minor isotopic modifications are provided. For the replacement of the central ¹⁴N atom by ¹⁵N in isoelectronic HNN⁺ ion the theory predicts a shift in ν_1 frequency of similar order of magnitude (17 cm⁻¹) [132]. On the other hand isotopic substitution of ⁴⁰Ar on ³⁶Ar vibration has virtually no influence on the intramolecular ν_1 frequency. Line positions for Ar-HCO⁺ and Ar-H¹³CO⁺ are listed in table A3. Due to unfavorable S/N ratio the ³⁶Ar-HCO⁺ ν_1 band line positions are not as accurate as the ones for the other isotopomers and so they are not given in the table A3. However their positions can be reproduced with sufficient accuracy (± 0.02 cm⁻¹) using fitted parameters from tables 7.3 and 7.4.

Figure 7.4: Spectra of the Ar-HCO⁺ and Ar-H¹³CO⁺ ν_1 bands

The spectrum of the latter isotopomer was recorded under slightly increased laser power conditions and displays somewhat more prominent and less resolved sequence hot bands.



Analysis of the Ar-HCO⁺ ν_1 band proceeded in the following way. Initially, the ground state combination differences were calculated from the experimental P and R branch line positions. They were compared with the lower state combination differences derived from other rotationally resolved bands. The combination differences from all bands that unambiguously shared the same lower (vibrationless) state were weighted according to the relative intensities of the bands, S/N ratio, and calibration accuracy and averaged. This provided reasonably accurate ground state combination differences for $J = 1\div 35$ for Ar-HCO⁺ and for $J = 1\div 29$ for Ar-H¹³CO⁺. From these the ground state rotational constants were established (see table 7.3). Subsequently, these constants were used to obtain origin, B' and D' values for the ν_1 band and for the other bands originating from the vibrationless state of the complex. In the case of the ³⁶Ar-HCO⁺, ν_1 band is the only one for which rotational structure was obtained with sufficient S/N ratio and it does not contain enough lines in the P branch to get a reliable D'' value from the lower state combination

differences. For this isotopomer the ν , B', and B'' constants were varied simultaneously and constants D', D'' were taken to be the same as in Ar-HCO⁺.

For Ar-HCO⁺ and Ar-H¹³CO⁺ fitting the positions of the P and R branch lines of the ν_1 band with B'' and D'' constrained to the values obtained from combination differences produced a relatively poor fit. Figure 7.5(a) and 7.5(c) plots the difference between the experimental and fitted line positions. Irregular behaviour in the R branch line positions of both normal and ¹³C isotopomers above J≈40 cannot be fitted within experimental accuracy even if the lower state constants are released and/or hexic centrifugal distortion constants are added to the expansion. Deviations from the expected course of line positions is most probably arising from perturbations in the upper vibrational state. Though respective lines in the P branch are not observed, and it is not possible to prove unambiguously which state is affected, a perturbation in the lower state is not very likely since the selection rule for the coupling ($\Delta J=0$) requires the perturbing state to have a very low frequency ($\ll 10^2$ cm⁻¹) and a significantly different rotational constant. According to the results *ab initio* calculations [233] and experimental data (see below) neither of the two intermolecular vibrations of the complex suit this description. For ³⁶Ar-HCO⁺ no obvious anomalies were evident for J'≤24 (maximum J' observed in the spectrum).

Table 7.3: The Ar-HCO⁺ lower state constants

Lower state molecular constants of different Ar-HCO⁺ isotopomers determined from the fits of averaged combination differences. Last row gives the χ^2 of the fit. Due to poor S/N ratio for ³⁶Ar-HCO⁺ its constants are not very well defined.

Constant [cm ⁻¹]	Ar-HCO ⁺	Ar-H ¹³ CO ⁺	³⁶ Ar-HCO ⁺
B'' (×10 ⁻²)	6.6455(19)	6.5757(26)	6.937(12)
D'' (×10 ⁻⁸)	6.6(1.1)	8.2(1.4)	6.6 [‡]
χ^2 (×10 ⁻⁴)	0.66	1.6	7.7

[‡] Taken to be the same as for Ar-HCO⁺

Table 7.4: The Ar-HCO⁺ ν_1 state constants

Molecular constants (in cm⁻¹) determined for the ν_1 band Ar-HCO⁺ isotopomers. Below the rotational constants the χ^2 of the fits are given. Last rows collect distances from Ar atom to H atom and to the HCO⁺ centre of mass for the ground and ν_1 states.

Constant [cm ⁻¹], [Å]	Ar-HCO ⁺ All J levels [‡]	Ar-HCO ⁺ J'≤30	Ar-H ¹³ CO ⁺ All J levels [‡]	Ar-H ¹³ CO ⁺ J'≤30	³⁶ Ar-HCO ⁺ All J levels
ν_1	2815.084(7)	2815.066(2)	2785.749(3)	2785.740(3)	2815.357(5)
B' (×10 ⁻²)	6.819(1)	6.829(1)	6.745(1)	6.745(1)	7.131(16)
D' (×10 ⁻⁸)	10.7(3)	17.7 (1.0)	3.5(1.5)	12.2(1.7)	17.7 [‡]
χ^2 (×10 ⁻⁴)	220	2.5	195	6.0	33
R _{cm''}		3.797(1)		3.779(1)	3.799(3)
R _{cm'}		3.743(2)		3.728(2)	3.743(4)
ΔR_{cm}		-0.054(2)		-0.051(2)	-0.056(5)
R _{Ar-H''}		2.132(1)		2.133(1)	2.132(3)
R _{Ar-H'}		2.078(2)		2.082(2)	2.079(4)

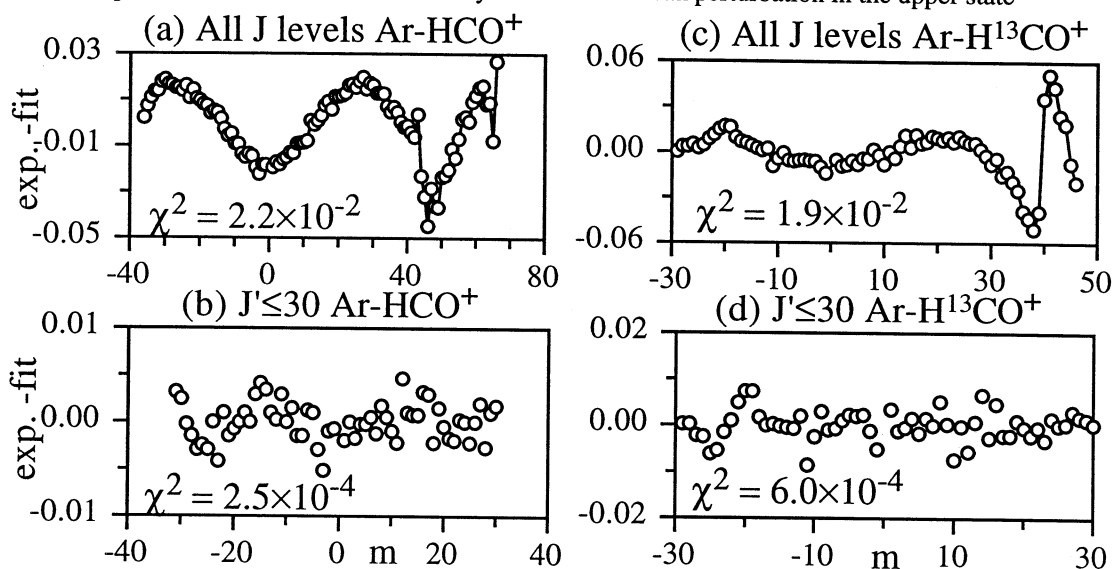
[‡] Poor fit because of the upper state perturbation; [‡] Obtained from combination differences (table 7.3). Kept fixed during the fit; [‡] Taken to be the same as for Ar-HCO⁺. Kept fixed in the fit.

From inspection of figure 7.5(a) and (c) one can see that low J transitions appear to be free of the perturber's influence. Indeed fitting of the P and R branch lines terminating in J'≤30, with B'' and D'' being constrained, yielded much smaller deviation between the fit and experiment (Figure 7.5(b) and (d)). Within the experimental uncertainties the upper state constants derived from this fit are very close to those obtained from the upper state combination differences fitted for J≤30. Though the quality of the fit with restricted J range is substantially higher (χ^2 drops by two orders of magnitude) the upper state centrifugal

distortion constant still looks corrupted. Positive ΔB value for the ν_1 band, large red shift of the ν_1 vibrational frequency on going from the free monomer to the complex, and a set of blue shifted sequence bands (see below) are all symptoms of a stiffer intermolecular bond in the upper vibrational state, which according to the formula (4.11) would require lowering of D constant upon excitation, contrary to what is actually observed. The ν_1 constants are gathered in table 7.4 for all studied isotopomers.

Figure 7.5: Results of fitting the ν_1 band of Ar-HCO⁺

Deviation between the experimental and fitted ν_1 line positions. Only restricted fit can reproduce line positions with a sufficient accuracy because of a weak perturbation in the upper state



In a crude diatomic model, the B and D values can be linked to the radial attributes of the Ar \cdots HCO⁺ intermolecular bond. Neglecting zero point vibration and assuming an undistorted HCO⁺ subunit, one deduces a proton-argon separation of 2.13 Å in the ground state and 2.08 Å in the excited ν_1 state (table 7.4). Separation between the Ar atom and HCO⁺ centre of mass is respectively 3.80 Å and 3.74 Å for the normal isotopomer. Actually, upon complexation one might expect marginal proton transfer in the system, with a lengthening of the C-H bond, but because of the small proton mass the center of mass separation is not going to be affected too much. The intermolecular stretching frequency ν_s , can be estimated by inserting the experimental B'' and D'' values from table 7.4 into Millen's relationships (4.10-4.11). One obtains the values $\nu_s'' = 131 \pm 11$ cm⁻¹ and $k_s'' = 16.9 \pm 2.9$ N/m. Large uncertainties in the harmonic parameters carry over from the uncertainties in D'' value.

7.3.4. The $\nu_1 + \nu_2$ band

Another transition in the predissociation spectrum of Ar-HCO⁺ that from its strength and isolated position appears to involve just intramolecular vibrations is situated at ≈ 3697 cm⁻¹, roughly 882 cm⁻¹ above the ν_1 band. The transition is displayed in figure 7.6. The strong Q branch and missing P(1) line indicates a $\Pi \leftarrow \Sigma$ type band. Combination differences built from the P and R branch line positions show that this transition originates from the ground state of the complex. The position and perpendicular structure of the band are consistent with its assignment to the $\nu_1 + \nu_2$ transition, i.e. the combination of the CH stretching and HCO bending vibrations. The frequency of ν_2 vibration in free HCO⁺ ion is somewhat lower, $\nu_2^0 \approx 828$ cm⁻¹. Unfortunately the $\nu_1 + \nu_2$ transition has not been

observed for the free ion and out of the anharmonic corrections only χ_{33} and χ_{13} were measured experimentally. Using the calculated harmonic frequencies and anharmonicities from a recent force field [236] one can predict that in the free monomer ν_2 gets lower by $\approx 22 \text{ cm}^{-1}$ when excited in combination with ν_1 . However in the complex an *increase* in ν_2 frequency is anticipated since the Ar atom tries to make the proton stay on the C---Ar axis with the net effect of stiffening of the HCO bending coordinate.

Figure 7.6: The $\nu_1 + \nu_2$ band of Ar-HCO⁺

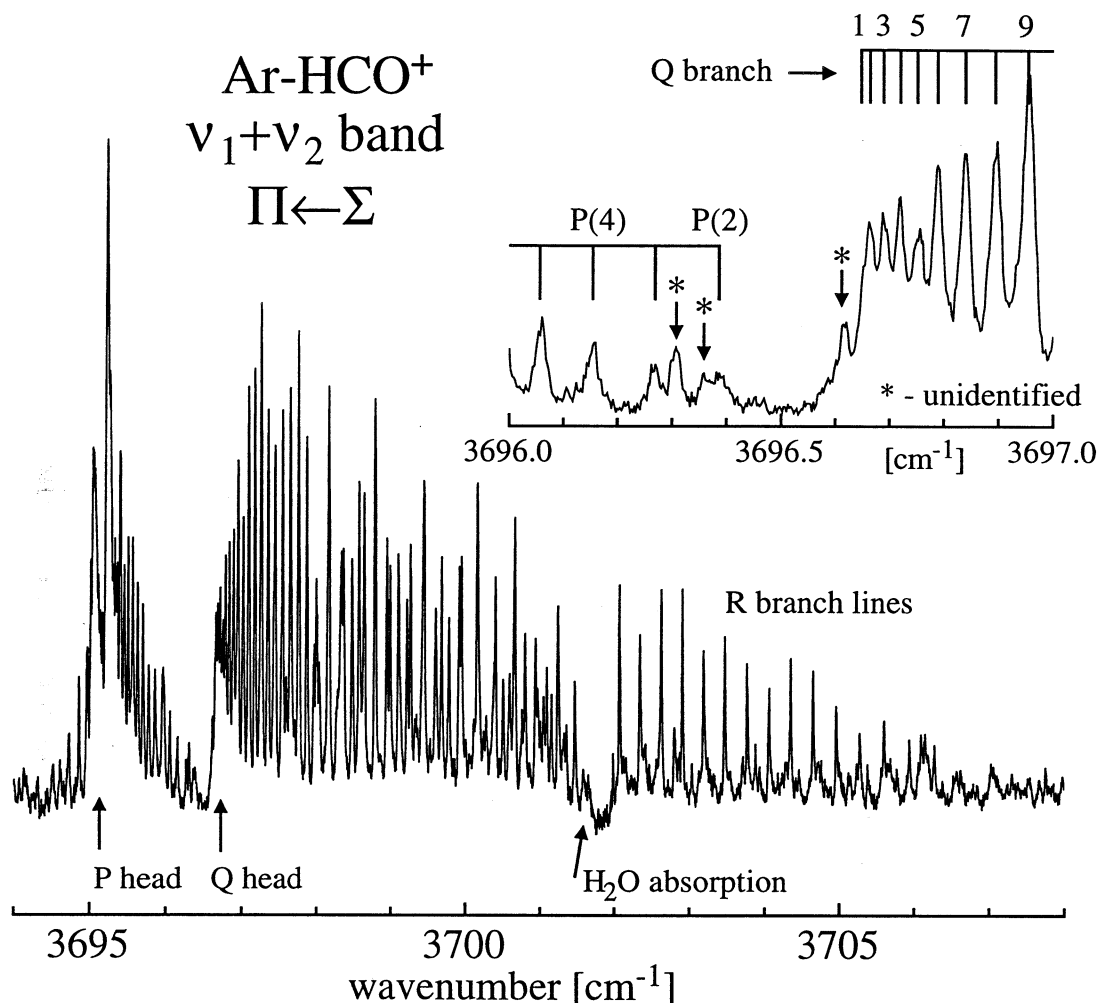


Table 7.5: Ar-HCO⁺ $\nu_1 + \nu_2$ band constants

Molecular constants (in cm^{-1}) determined for the $\nu_1 + \nu_2$ band of Ar-HCO⁺. The two fits for the $J \leq 16$ lines differ from each other by constraining D' to D'' in the second fit.

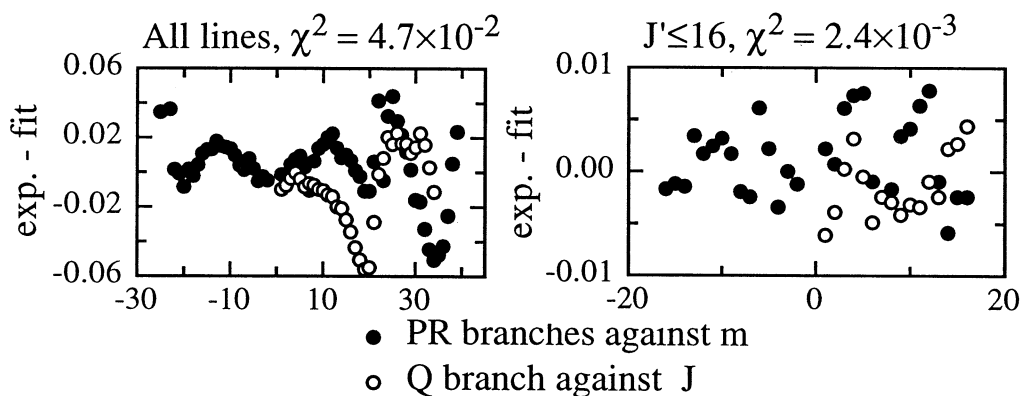
Constant [cm^{-1}]	All J levels [¶]	$J \leq 16$	$J \leq 16$
ν_1	3696.720(10)	3696.716(3)	3696.723(4)
B' ($\times 10^{-2}$)	6.993(5)	7.005(8)	6.981(5)
D' ($\times 10^{-8}$)	44.2(4.0)	104(29)	6.6 [¥]
q' ($\times 10^{-5}$)	-8.8(2.3)	8.9(2.8)	9.7(4.6)
χ^2 ($\times 10^{-3}$)	47	0.9	2.4

[¶] Poor fit because of the upper state perturbation; [¥] Taken to be the same as in the lower state. Kept fixed in the fit.

Because of a relatively large ΔB value for this band, its Q branch becomes fully resolved already at $J \geq 2$ and rotational assignment is rather straightforward. In the P branch, where a head is formed at $J \approx 20$, lines remain resolved up to $J'' = 17$. In the Q and R branches lines are observed up to $J = 34$ and $J'' = 39$ respectively. Line positions are provided in table A4. Few low J lines in the R branch are blended with stronger Q branch lines since

maximum in the rotational population distribution falls on the intermediate J range (figure 7.6). The line positions were fitted to the expression (4.3), with B'' and D'' being constrained to the previously determined values and ν , B', D', and q' varied. Similarly to the ν_1 case, the regularity in the rovibrational transitions of the $\nu_1 + \nu_2$ band is slightly affected by a perturbation. This unpleasant phenomenon is obvious from an inspection of figure 7.7(a) where the difference between experimental and fitted line positions is plotted. One can see that above $J \approx 20$ there is a clear singular behaviour in the Q branch line positions and possibly in the P and R branches too. Inclusion of hexic centrifugal distortion constants does not improve the situation a lot. Fitting the restricted set of transitions terminating in $J' \leq 16$ resulted in an improved χ^2 for the fit but also a substantial correlation between D' and q' values. Results of the restricted fit, in which additional constraint $D' = D''$ was introduced, are depicted in figure 7.7(b). Constants are listed in table 7.5.

Figure 7.7: Ar-HCO⁺ $\nu_1 + \nu_2$ fit results



There is a weak parallel band lying ca. 102 cm⁻¹ above $\nu_1 + \nu_2$ transition coming from the ground state of the complex and beset by a weak perturbation in the upper state. Identity of the band is at present unclear but possibly it represents the $\nu_1 + \nu_2 + \nu_b$ combination. Line positions are available from table A5 and constants are gathered in table 7.6.

Table 7.6: Ar-HCO⁺ 3799 cm⁻¹ band constants

Molecular constants (in cm⁻¹) determined for the $\nu_1 + \nu_2$ band of Ar-HCO⁺. The two fits for the $J' \leq 16$ lines differ from each other by constraining D' to D'' in the second fit.

Constant [cm ⁻¹]	All J levels [¶]	J' ≤ 15
ν_1	3798.60(5)	3798.55(2)
B' ($\times 10^{-2}$)	6.884(30)	6.961(5)
D' ($\times 10^{-8}$)	-117(30)	6.6 [¥]
χ^2	0.12	0.002

[¶] Poor fit because of the upper state perturbation; [¥] Taken to be the same as in the lower state. Kept fixed in the fit

7.3.5. The $2\nu_1$ band

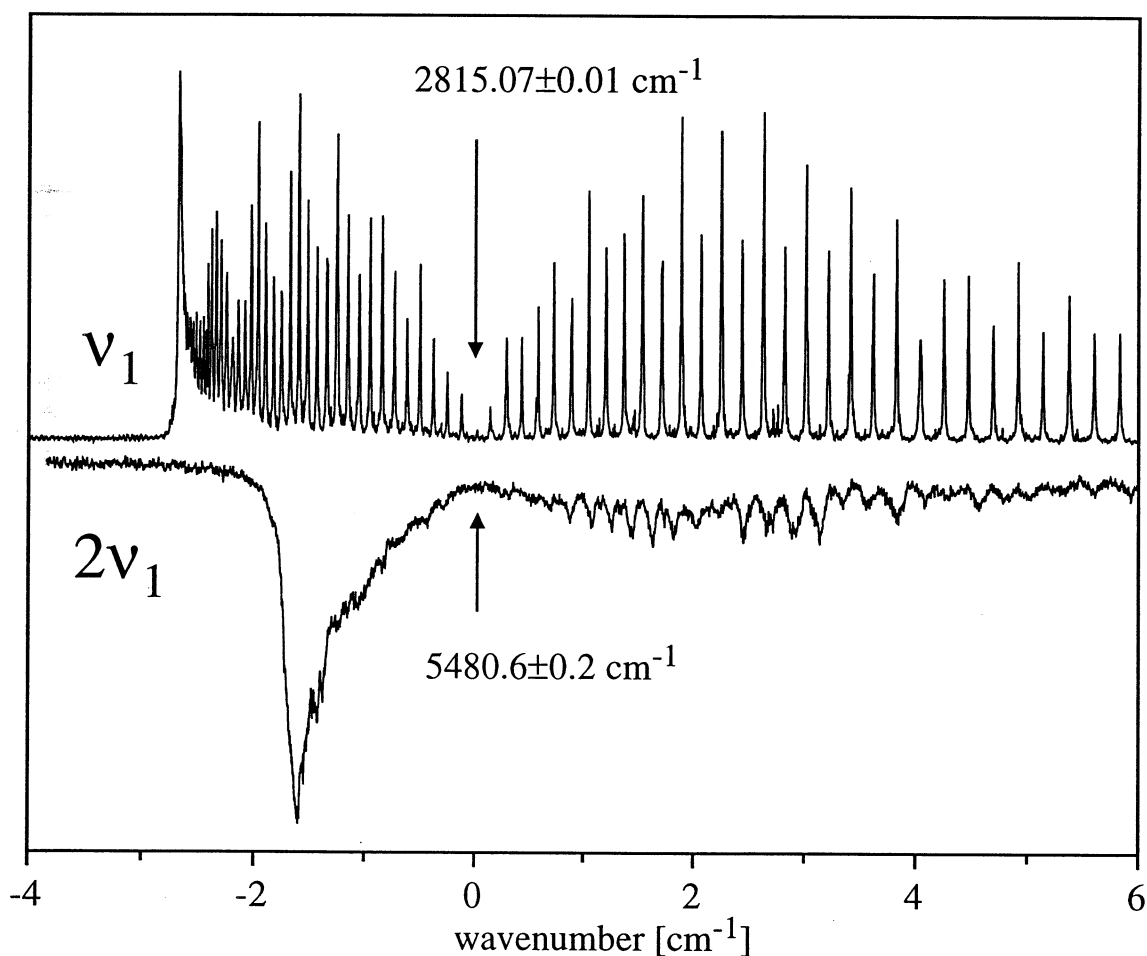
The transition centered at 5480.6 ± 0.2 cm⁻¹ is assigned as the first overtone of the ν_1 vibration. The assignment is based on the fact that the observed band is a reasonably strong, isolated, and situated around where one could expect the $2\nu_1$ transition to occur (with the corrections for anticipated anharmonicity taken into account). It is very unlikely that this transition represents some other combination of intramolecular vibrations. Out of three intramolecular vibrations of the complex, the CH stretch (ν_1) is expected to be more anharmonic than either CO stretch or HCO bend since the outer part of the ν_1 vibrational potential is heavily distorted by the presence of Ar ligand. Only anharmonic vibrations are

expected to have reasonably strong overtones. Besides assigning the transition to some other combination like $2\nu_3+2\nu_2$ would rise the question why $\nu_3+2\nu_2$, etc. are not observed.

Rotational lines in the band appears to be broadened (figure 7.8). Only few stronger lines in the R branch look half resolved. Unfortunately single mode locking mechanism in the utilized OPO laser does not work reasonably well at this spectral range and this could be partly responsible for the observed broadening. Line widths of the narrowest observed lines in the best spectra where SLM scanning was acceptable are of the order of 0.04 cm^{-1} . This value is too close to the laser resolution to make any quantitative conclusion about the upper state lifetime. Because of the poor resolution of the individual rotational lines the origin of the transition had to be determined approximately from the analysis of the band profile. In addition the accuracy is reduced somewhat by the fact there were not enough optoacoustic lines to calibrate the spectrum to a precision better than $\approx 0.2 \text{ cm}^{-1}$.

Figure 7.8: The first overtone of the Ar-HCO⁺ ν_1 vibration

Comparison of the CH stretch fundamental and first overtone. Earlier P branch head in the overtone band indicates further contraction of the intermolecular bond in the complex



The spectra of the ν_1 fundamental and its overtone are compared in figure 7.8. From the inspection of the figure one can see that the head in the P branch of $2\nu_1$ band is formed much earlier (at lower J) than it happens in the case of the ν_1 band. Simple simulation aimed to reproduce the shape of the P branch showed that rotational constant should increase by roughly $0.0026-0.0028$ upon excitation of the $2\nu_1$ overtone transition. This correspond to intermolecular centre of mass separation of $\approx 3.72 \text{ \AA}$, i.e. to further contraction of intermolecular bond by $0.04-0.05 \text{ \AA}$ compared to the ν_1 state. Curiously, the excitation of ν_1 transition affects intermolecular separation by similar amount.(ca. -0.05 \AA , table 7.4).

7.3.6. The $\nu_1 + \nu_3 - \nu_3$ band

Lying ca. 27 cm⁻¹ below the ν_1 band and a by factor of 20÷50 less intense is another transition of a Σ - Σ type (figure 7.9). For Ar-H¹³CO⁺ isotopomer a very similar transition is found shifted by ca. 22 cm⁻¹ from the ν_1 band. Because the band is well separated from all the others and there is no underlying background very high J levels could be observed. In addition, the difference in the upper and lower state rotational constants happens to be very small so that the transition's P branch remains well resolved even for J≥40. For Ar-HCO⁺ lines ranging from P(48) to R(91) are observed (table A6). Except for two weak perturbation located at J'=12 and J'=69 the band is very clean. The Ar-H¹³CO⁺ spectrum is perturbed respectively at J'=35 above which P branch becomes unresolved. Eliminating the perturbed areas and fitting the line positions to a linear molecule expression (4.3) returned parameters given in table 7.7.

Table 7.7: Ar-HCO⁺ $\nu_1 + \nu_3 - \nu_3$ band constants

There are weak perturbations centered at J'=12 and J'=69 in Ar-HCO⁺ and at J'=35 in Ar-H¹³CO⁺ spectra.
Perturbed areas were excluded from the fit.

Constant [cm ⁻¹]	Ar-HCO ⁺ J'≤50, J'=7-17 removed	Ar-H ¹³ CO ⁺ J'≤25
ν	2787.963(2)	2764.090(2)
B'' (×10 ⁻²)	6.643(5)	6.570(3)
D'' (×10 ⁻⁸)	6.3(1.6)	8.2*
B' (×10 ⁻²)	6.749(5)	6.661(3)
D' (×10 ⁻⁸)	5.6(1.5)	8.2*
χ^2 (×10 ⁻⁴)	11	3.4

* Kept fixed

The fact that the band shifts down from the respective ν_1 vibrations by roughly the same amount for both normal and ¹³C isotopomers suggests an assignment of this transition to a sequence build on ν_1 . This supposition is supported by the fact that for the second strongest transition, $\nu_1 + \nu_3$, there is a similar weak satellite displaced by roughly the same amount and in the same direction. Lower state combination differences for the 2788 cm⁻¹ band are virtually identical to those of the ground vibrationless state of the complex. In fact they are almost indistinguishable within our experimental precision implying that the vibration excited in the lower state does not affect the rotational constants of the complex very much. Thus intermolecular vibrations, which are expected to alter the rotational constant considerably, fall out of consideration, plus their sequence bands should be blue shifted contrary to what is observed for the 2788 cm⁻¹ band. The ν_1 vibration does not fit either since it has a marked influence on the rotational constant. Moreover the first overtone of ν_1 is observed at ≈ 5480 cm⁻¹ which allows to predict the band $2\nu_1 - \nu_1$ to lie at much lower frequency of ≈ 2665 cm⁻¹ and be poorly rotationally resolved. The ν_2 vibration can be ruled on the basis of comparison of upper state combination differences for the 2788 cm⁻¹ band and for the experimentally observed $\nu_1 + \nu_2$ band. Besides, the sequence band involving ν_2 should contain Q branch lines. The only vibration that is left out is the CO stretch. This vibration is indeed believed to have the lowest impact on the complex's rotational constant. Though both CO and CH bonds should expand slightly upon excitation of the ν_3 vibration this expansion might be compensated by a parallel shrinking of the intermolecular bond, which should occur as in the case with the ν_1 vibration but to a lesser

degree (normal coordinate for the ν_3 mode involves a certain amount of motion of the hydrogen atom). The blue shift and Σ - Σ structure of the band are consistent with this assignment as well. The $\nu_1+\nu_3-\nu_3$ vibration was not observed for free HCO⁺ ion but for the isoelectronic HN₂⁺ ion this vibration has been detected ca. 22 cm⁻¹ to the blue with respect to ν_1 in good agreement with the situation observed here. In addition, from Martin and Taylor's theoretical quartic field for the HCO⁺ ion [236] a shift of the order of - 22 cm⁻¹ is predicted.

There is, however, one problem with this assignment. The ν_3 state of the complex should lie at roughly 2180 cm⁻¹ above the ground state while dissociation energy of the complex is predicted to be in the range of 1100-1700 cm⁻¹ [205, 233]. This means that the ν_3 state has a lifetime of at least ≈ 100 μ s (the time needed to get from the source chamber into the octopole) which correspond to surviving ca. 10^{10} vibrations before dissociation. Long IR predissociation lifetimes are not uncommon among simple Van der Waals complexes. A lower limit of 0.4 ms for the lifetimes of Ar-HCl($\nu=1$) and Ar-DF($\nu=1$) complexes was measured recently with optothermal detection technique [125]. A long lifetime usually reflects an empirical fact that the probability of the energy flow from internal to translational degrees of freedom decreases sharply with the amount of released translation energy. This tendency is known under the names "energy gap low" and "momentum gap low" [237, 238]. In the case of the Ar-HCO⁺ ν_3 vibration those ≈ 600 -1000 cm⁻¹, that need to be disposed of, have a good chance of being redistributed among ν_2 vibration and rotation of the HCO⁺ fragment, with little energy stored in translation. Thus, one would expect that ν_3 state should dissociate reasonably quickly, but strangely enough this does not seem to happen.

One more evidence that the observed transition indeed represent a hot band was obtained from a simple experiment in which relative intensities of this band and ν_1 fundamental were measured under various source conditions. Different ratios of the integrated intensities of the two bands were obtained for different expansion conditions indicating that the respective lower vibrational states for the two bands are not identical. From the other hand varying the flight time of the complexes from the source to the octopole region from 110 to 230 μ s did not seem to have a noticeable effect on the intensity ratio suggesting that the lower state lifetime is $\gg 200$ μ s.

Possibly there are mechanisms that could slow the predissociation of the ν_3 state of the Ar-HCO⁺ complex down by that much. However a much more prosaic explanation hiding in underestimation of the complex's binding energy might exist. It is possible that the binding energy of the complex in the ν_3 intramolecular state is higher than ν_3 frequency in which case the complex simply cannot predissociate. Intermolecular binding energy for *the ground state complex* from the available calculations [205, 233] range from 1100 to 1700 cm⁻¹ depending on the method. Though this range overlaps with the interaction strength expectations based on comparison with related species, in view of the persistent inconsistency between the short lifetimes of other observed stretching and stretch-bending states lying above 2500 cm⁻¹ and the long lifetime for the ν_3 state it may be necessary to reevaluate the value of the binding energy of the complex.

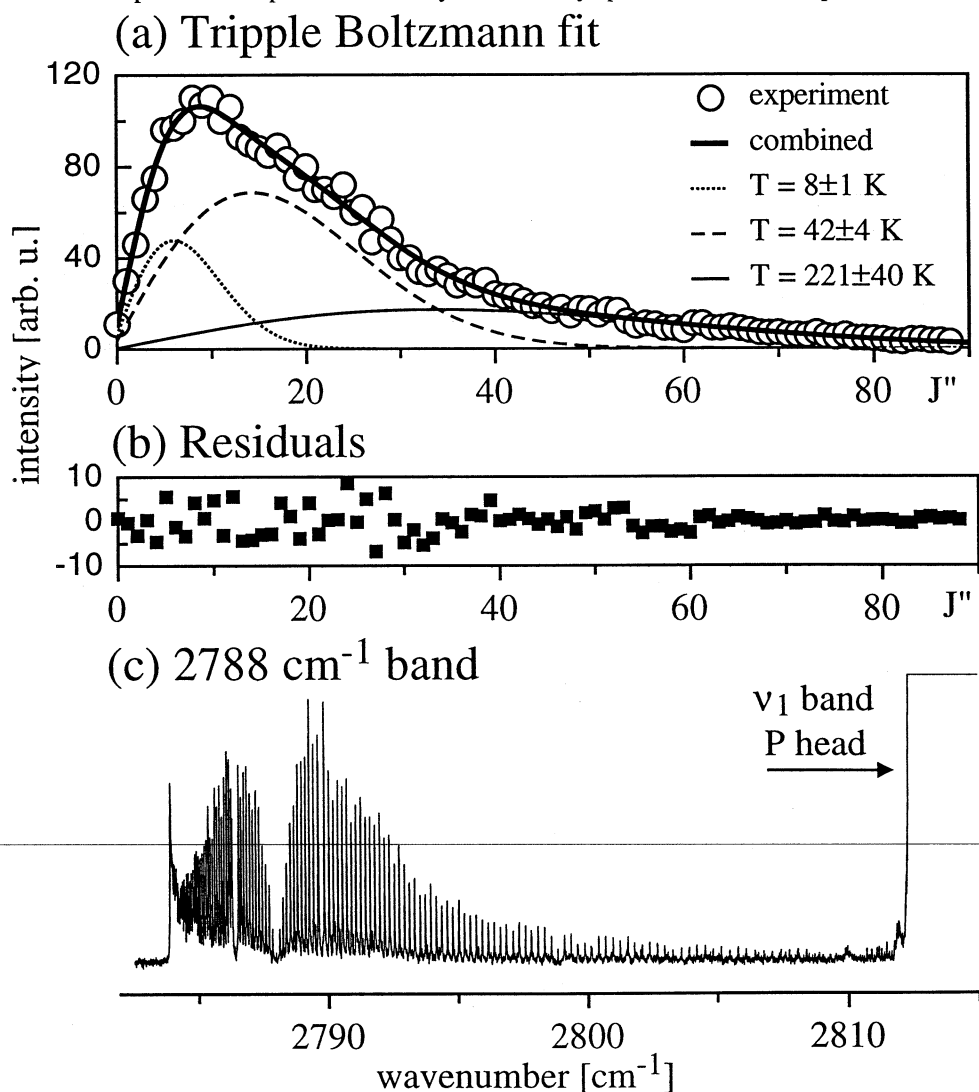
7.3.7. Rotational energy distribution in the $\nu_1+\nu_3-\nu_3$ band

Because of the very low background dissociation the R branch of $\nu_1+\nu_2-\nu_2$ band was used to measure rotational energy distribution of Ar-HCO⁺ ions generated in the electron impact ionization source. Of some concern may be the fact that the transition

originates from a vibrationally excited state and the correctness of the assumption that the rotational and vibrational energy distributions are independent. As far as one could ascertain this is a very good approximation since the other transitions from the ground state (such as ν_1) with more limited range of observed J levels (due to overlap of neighboring bands) had a very similar pattern of the rotational energy distribution. Experimental intensities of the rotational lines in the R branch of the 2788 cm⁻¹ band are plotted in figure 7.9(a) as a function of J. It is not immediately obvious from the figure that presented distribution is not of Boltzmann type. However if logarithm of intensity normalized by $(2J+1)$ is plotted against rotational energy a highly non-linear dependence is produced. It was found that a sum of at least three Boltzmann functions is needed to reproduce the measured distribution. The fit shown in figure 7.9(a) is composed of three components with temperatures 8K, 42K, and 221K with pre-exponential factors 6.0, 3.8 and 0.42 respectively.

Figure 7.9: Rotational distribution in Ar-HCO⁺ from its $\nu_1+\nu_3-\nu_3$ band

The R branch of the $\nu_1+\nu_3-\nu_3$ band of Ar-HCO⁺ (c) was used to examine the rotational energy distribution. Measured intensity distribution (a) could be reproduced with a sum of three Boltzmann functions. Middle trace (b) provides the residuals of the fit. The presence of a substantial amount of warm molecules in the expansion complicates the analysis of closely spaced bands in the spectra.



If other bands of Ar-HCO⁺ or other linear or non-linear complexes are taken to examine the rotational energy distribution qualitatively similar results are observed. A proper thermal equilibrium has never been obtained. Instead that the measured distributions seem to be composed out of two or more sub-populations with markedly different temperatures. While a large proportion of the molecules prefers to cool down to roughly 20-40 K there is

always a long tail characterized by temperatures in excess of 150 K. Notably this "cool & warm" behaviour seems to be quite common for molecules produced in a pulsed supersonic expansion coupled to a discharge. For example non Boltzmann rotational energy distribution was observed in a slit-jet expansion electron impact ion source [239]. Existence of such effect is usually related to the decrease in the efficiency of rotational energy transfer with increase in the rotational energy level spacings (i.e. with J).

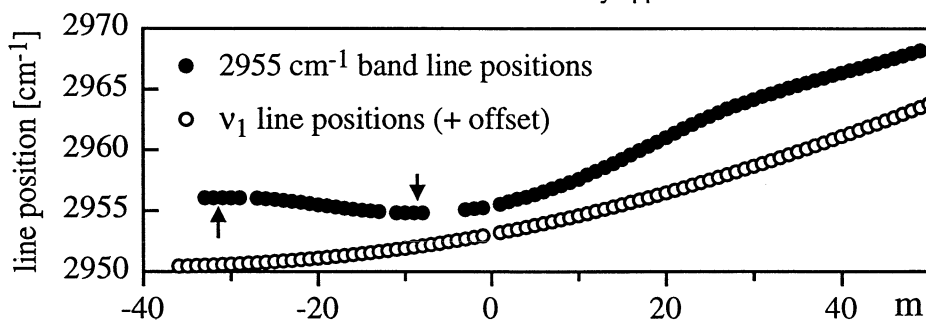
Having a long high temperature tail in the rotational energy distribution is advantageous sometimes since it allows to observe more rotational lines for an isolated band like in this case. From the other hand hotter molecules may in certain case be responsible for severe spectral congestion since they allow even to moderately spaced bands penetrate into each other. The spectrum of Ar-HCO⁺ complex features regions where a number of densely spaced rotational lines are observed. For example the space 10-60 cm⁻¹ above the ν_1 band is occupied by sequence bands involving intermolecular modes of which only one could be partly assigned. Similarly high activity of sequence bands around the respective ν_1 transition was found for the other Rg-HX⁺ complexes. Since effective vibrational temperatures are expected to exceed the rotational ones it is not very surprising that intermolecular vibrations with typical frequencies of 50-150 cm⁻¹ are considerably populated in the expansion.

7.3.8. The 2955 cm⁻¹ band

Approximately 140 cm⁻¹ above the ν_1 transition a strong band with a very exotic contour is found (figure 7.11). A series of widely spaced lines comes out of a dense structure with sharp head-like boundaries on either side. Because of the peculiar band structure assigning rotational quantum numbers to the individual lines would be quite difficult without any assumptions concerning the nature of the involved vibrational states. Given the relative strength of the band it is not unreasonable to presume that the transition originates from the ground state of the complex. Indeed with the Ar-HCO⁺ ground state combination differences, it was possible to assign the outgoing lines as the R branch and the dense bundle of lines as the P branch of a Σ - Σ transition with the band origin at 2955.40 cm⁻¹. Practically all of the observed lines are accounted for in this assignment scheme. The P branch lines first start progressing in the usual direction but change it very quickly forming an early head at J \approx 7-10. Then they go to the blue forcing the observed fairly large separation between the successive R branch lines. Formation of a stronger head at J \approx 27-33 reverts the direction of the P branch propagation one more time and provides the observed band with this unusual shape.

Figure 7.10: Line positions of the 2955 cm⁻¹ band

Line positions of the 2955 cm⁻¹ band are compared to those of ν_1 band as a function of m. Formation of two heads in the P branch is clearly apparent.



Apart from the shape there are other peculiarities in the behaviour of the 2955 cm⁻¹ band. Firstly, it is observed only for the normal isotopomer and for ³⁶Ar-HCO⁺. No sign of it was found in the spectrum of Ar-H¹³CO⁺ isotopomer. At the same time the closest neighbor of this transition, $\nu_1 + \nu_s$ band, was observed for all isotopic modifications.

Secondly, its intensity distribution seems to be much different from that of other bands. For example, the ν_1 band has a maximum in transition intensity falling at $J \approx 10$. For the 2955 cm^{-1} band the strongest lines are observed at $J \approx 20-30$.

Line positions of the 2955 cm^{-1} band are displayed in figure 7.10 as a function of m (see also table A7). Offset positions of ν_1 band lines are also drawn for comparison. There is a clear difference between the two data sets. One can see that while the ν_1 line positions follow a simple low-order polynomial curve, the 2955 cm^{-1} band line positions undertake a more complex behaviour. Least square fit of the line positions of the 2955 cm^{-1} band using ν , B' , and D' as parameters gave extremely poor results. Clearly either higher order centrifugal terms become important or the upper state reached by the 2955 cm^{-1} transition is perturbed similar to many other states observed in the Ar-HCO⁺ spectrum. Fitting the line positions with inclusion of H' , L' , and M' in the rotational energy expressions improved the situation somewhat but still produced systematic deviations of the order of 0.08 cm^{-1} . Better fit is obtained if a limited set of lines is taken. The constants obtained from the fit of transitions terminating in $J' \leq 30$ are given in table 7.8 compared to the result of similar fit with full set of available line positions. Apart from the origin value and rotational constant, which substantially increases upon excitation, the other constants do not convey any physically meaningful information. One can see that H' even changes sign when the fit is constrained to the lower J values.

Table 7.8: Ar-HCO⁺ 2955 cm^{-1} band constants

Constant [cm^{-1}]	All J levels	$J' \leq 30$
ν_1	2955.40(3)	2955.41(2)
B' ($\times 10^{-2}$)	7.54(3)	7.49(2)
D' ($\times 10^{-6}$)	5.0(2)	3.2(4)
H' ($\times 10^{-10}$)	9.6(5)	-5(3)
χ^2 ($\times 10^{-3}$)	140	9

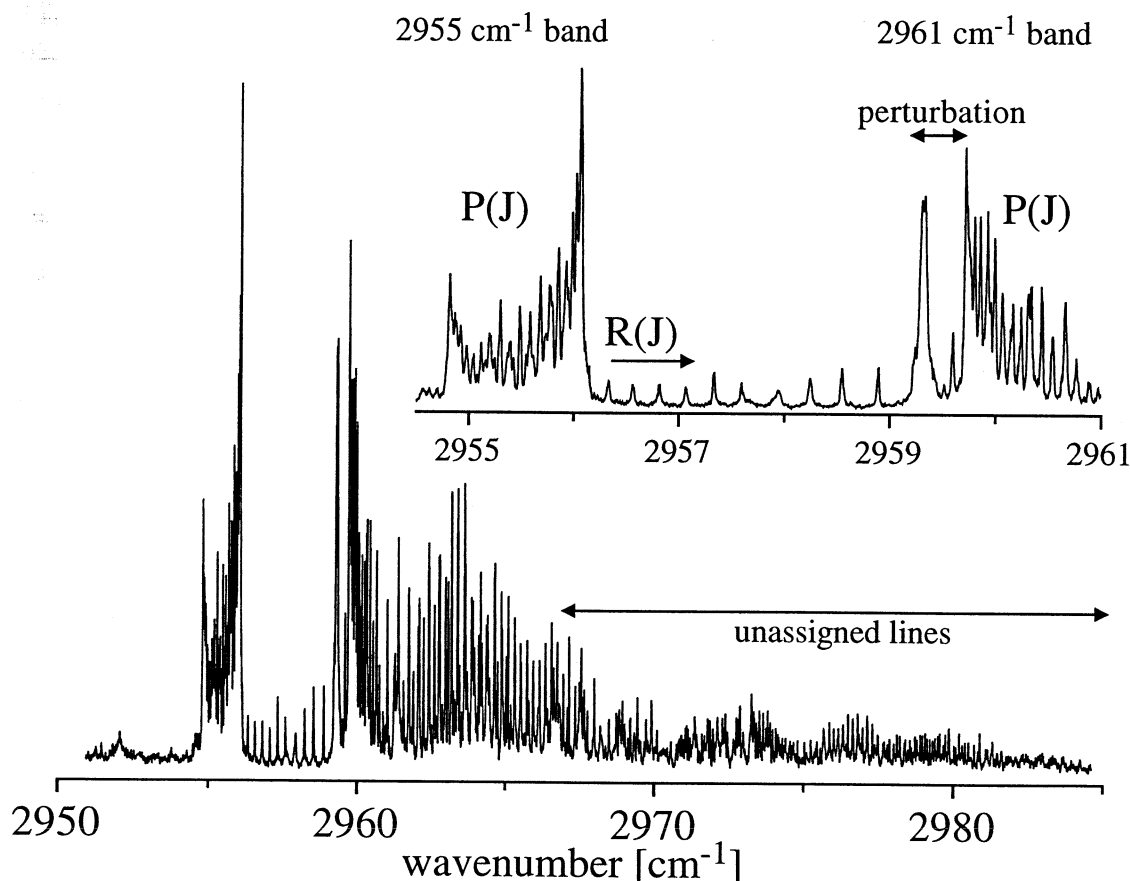
An increase of $\approx 0.009 \text{ cm}^{-1}$ in rotational constant corresponds to a contraction of the intermolecular bond by $\approx 0.24 \text{ \AA}$ upon excitation. Such a dramatic change implies that one or several quanta of intermolecular bending vibration might be excited in the upper vibrational state. The Σ - Σ appearance of the band prevents it from being assigned to the $\nu_1 + \nu_b$ combination expected somewhere in this range [205, 233]. A transition into a bending state can give rise to a band of parallel type if the bending vibration is doubly excited or it occurs in combination with another bending vibration. The fact that the band is intense only in the spectra of the normal isotopomer and $^{36}\text{Ar-HCO}^+$ but not in the spectrum of Ar-H¹³CO⁺ indicates that the band is not the $\nu_1 + 2\nu_b$ combination. Besides such an assignment would reduce the bending frequency too much compared to the theoretical value ($\approx 130-170 \text{ cm}^{-1}$ [205, 233]). Most probably the band represents a combination build on ν_3 and the upper state accessed in this transition is in Fermi resonance with another strong state, presumably with $\nu_1 + \nu_s$, which lies only 6 cm^{-1} higher in energy. The fact that the isotopic substitution $^{12}\text{C} \rightarrow ^{13}\text{C}$ affects the ν_1 and ν_3 frequencies in different ways, thus moving the two interacting states out of resonance, may explain the disappearance of the band in the Ar-H¹³CO⁺ spectrum. Fermi resonance requires the vibrational symmetry of the interacting states to be the same which is consistent with the assumption of even number of bending modes. The simplest combination bands that might fall in this spectral range and include ν_3 and an even number of bending vibrations are $\nu_2 + \nu_3 + \nu_b$, $\nu_3 + 2\nu_b + n\nu_s$ ($n \approx 3-4$), or $\nu_3 + 4\nu_b + n\nu_s$ ($n \approx 1-2$). Unfortunately apart from ruling out the $\nu_2 + \nu_3 + \nu_b$ combination ($\nu_2 + \nu_3$ in the free monomer is as high as 3012 cm^{-1} [180]) nothing more can be done at present for the assignment of this band.

7.3.9. The 2961 ($\nu_1+\nu_s$), 3068, and 3125 cm⁻¹ bands

There are three bands of Σ - Σ type originating from the ground state of the complex with very similar structures lying 146, 253, and 320 cm⁻¹ above the ν_1 transition. The identity of the lower state is supported (but not proven, see the $\nu_1+\nu_3-\nu_3$ example) with the ground state combination differences. Relative intensities of the bands drop with increase in transition frequencies. The line positions are given in table A8. The strengths of the P branch heads also decreases in that direction. From inspection of figures 7.11-7.13 one can easily recognize that there is something common in the bands' profiles. In all three cases a relatively large gap is formed within the P branch concurrent with a break in the regularity of the R branch lines at about the same J level. This behaviour is interpreted as a result of a strong perturbation in the upper vibrational state whereby rotational manifold of a dark perturbing state crosses rotational levels of the state to be perturbed at a certain J^* value. The perturbation tends to repel the levels of the perturbed state and of the perturber having the same J away from each other. If rotational constants of the two interacting states are not equal the rotational energies of one of them will start to condense around J^* while those of the other state will be pushed away from it. Such reorganization of rotational energy levels may lead to anomalies in the spectra as observed here.

Figure 7.11: The $\nu_1+\nu_s$ and 2955 cm⁻¹ bands of Ar-HCO⁺

Hundreds of weaker unassigned lines on the blue wing of the $\nu_1+\nu_s$ band are due to sequence hot transitions. It is suspected that the unobserved $\nu_1+\nu_b$ combination is also concealed in this area

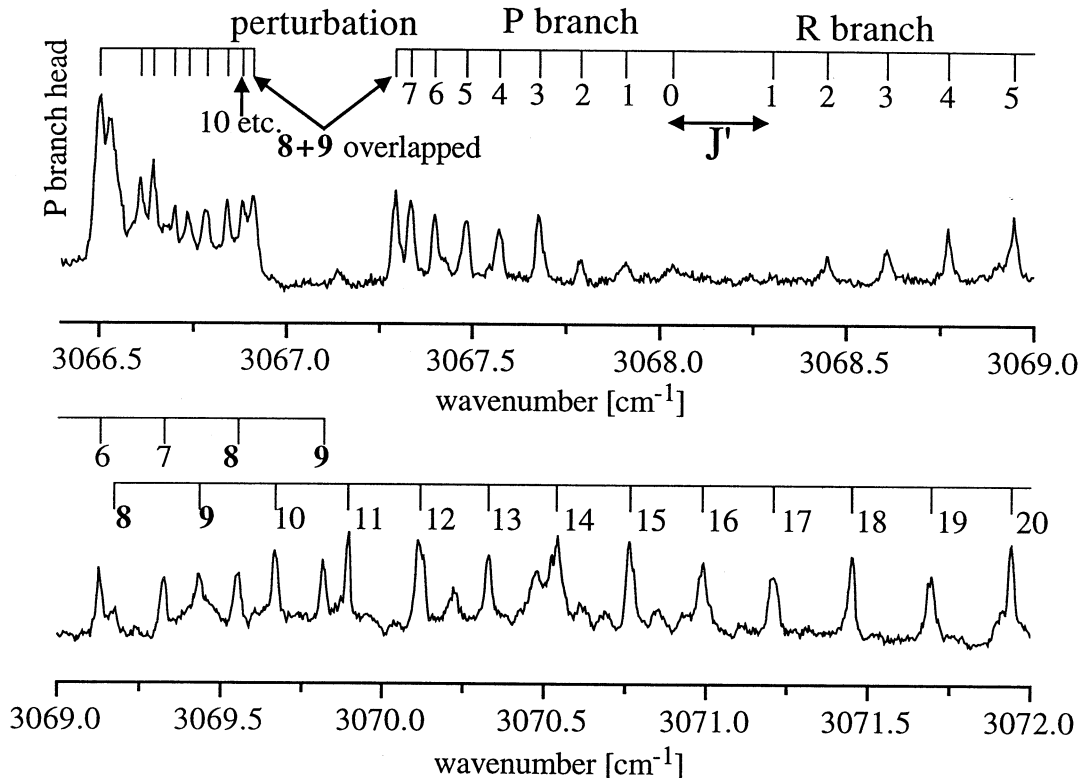


A very good example is provided in figure 7.12 displaying the 3068 cm⁻¹ band. One can see that initially P and R branch transitions look quite normally. Then the line progressions terminate abruptly in both branches at the same J' value ($J'=9$). As this happens a new series of lines appears shifted from the original one by ≈ 0.5 cm⁻¹ again in both P and R branches. After this the lines proceed without further "adventures". Head in

the P branch at $\approx 3066.5 \text{ cm}^{-1}$ results from a positive ΔB difference for this transition. Thus there are three places in the P branch with increased concentration of rotational lines which can effectively be labeled as heads.

Figure 7.12: The 3068 cm⁻¹ band of Ar-HCO⁺

Detailed look at the perturbation pattern in the 3068 cm⁻¹ band. Similar perturbations are found in all three bands considered in this section.



For 2961 cm⁻¹ band (figure 7.11) a very curious effect happens. The second head which results from the perturbation is almost coincident with the third "normal" head. As a result, the P branch lines terminating in $J' \approx 16-22$ are all collected within a single relatively narrow feature at 2959.31 cm⁻¹ separated from the rest of the P branch by ca. 0.4 cm⁻¹. For 3125 cm⁻¹ band ΔB is not large enough to make the third head strong (figure 7.13). However, the effects of the perturbation are easily apparent, in fact for this band they are largest. The 2961, 3068, and 3125 cm⁻¹ bands are perturbed at around $J'^* \approx 16, 8,$ and 23 respectively. Situation in which both P and R branch transitions are shifted to higher energies for J' lower than J'^* and to lower energies for J' higher than J'^* implies that the rotational constant of the invisible perturbing state is larger than that of the observed perturbed state.

Figure 7.13:

3125 cm⁻¹ band of Ar-HCO⁺

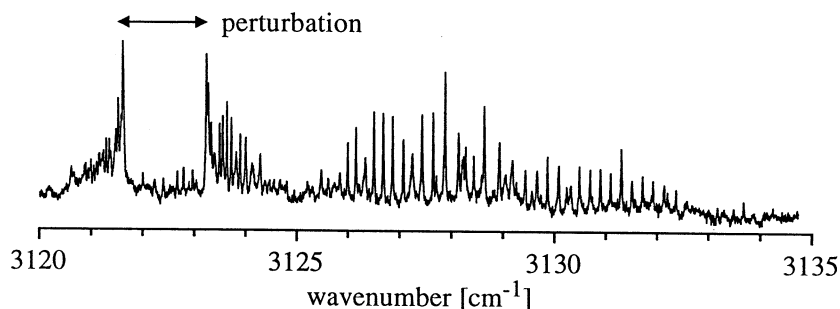
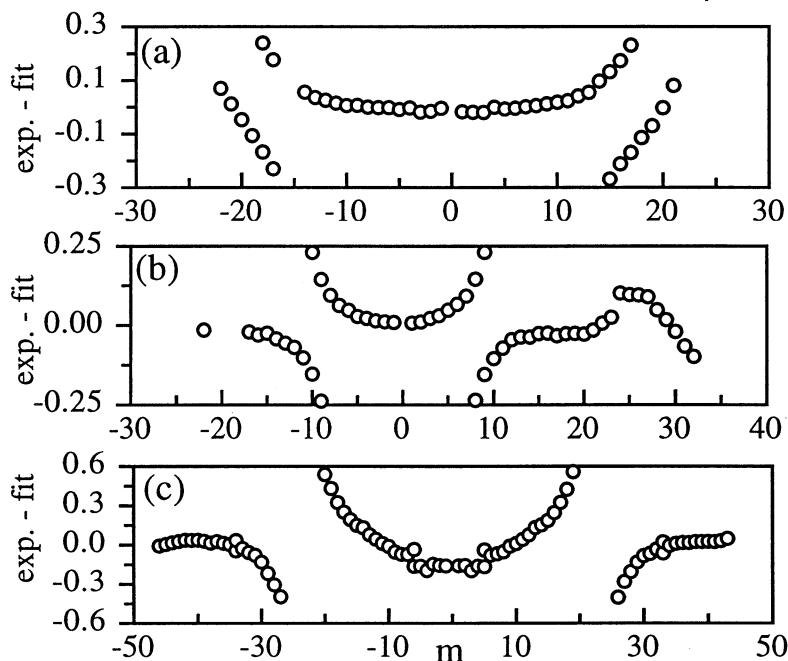


Figure 7.14 shows the result of fitting the line positions of these bands to a linear molecule expression in form of the deviations between the fit and experiment. Lower state rotational constants were fixed in the fits. One can see that the three bands are indeed perturbed in a very similar way. In addition to the strong perturbation there are other less significant perturbations such as doubling of upper state rotational levels at $J'=5$ and $J'=33$ for the 3125 cm^{-1} band. Results of the least square fits are given in table 7.9. Many rotational constants are corrupted by the perturbation as can be seen from their large uncertainties. More or less the only useful information coming out of the fits are the origins and signs and rough magnitudes of the changes in rotational constant B upon excitation. Excitation in any of the involved upper states leads to a contraction of the intermolecular bond. The degree of contraction decreases somewhat towards higher transition energies.

Figure 7.14: Fitting the $\nu_1+\nu_s$, 3068 cm^{-1} , and 3125 cm^{-1} bands

Deviations between experimental and fitted line positions for the $\nu_1+\nu_s$ (a), 3068 cm^{-1} (b), and 3125 cm^{-1} (c) bands considered in this section. As can be seen all three feature a similar perturbation pattern.



An analog of the 2961 cm^{-1} band was observed for Ar-H¹³CO⁺ isotopomer at $\approx 2929\text{ cm}^{-1}$, ca. 143 cm^{-1} above the respective ν_1 transition. However, the ¹³C band was not degraded so much to the blue as the normal isotopomer's one. Besides, the perturbation was not as strong and had a completely different pattern. Breaks of similar magnitude in regularity of P and R branches were located at $J'=5$ and $J'=19$. Line positions are provided in table A9. For the ³⁶Ar-HCO⁺ isotopomer the band was not rotationally resolved sufficiently well because of a poor signal to noise ratio. The band centre was estimated from a band contour as 2965 cm^{-1} , which places the transition ca. 150 cm^{-1} above ³⁶Ar-HCO⁺ ν_1 band. Perturbation pattern was very similar to that in the respective band of the normal isotopomer. An analog of the 3068 cm^{-1} band was detected for Ar-H¹³CO⁺ too, though due to a lowered signal to noise ratio only few lines with $J=2-14$ were resolved. Line positions are reproduced with reasonable accuracy with parameters given in table 7.9. The band is located at 3033 cm^{-1} , ca. 247 cm^{-1} above ν_1 . For the observed J range no apparent perturbations were noticed. The third, 3125 cm^{-1} band, was too weak to be observed for isotopically substituted compounds.

The assignment of the bands is by far not trivial. A separation of the same order of magnitude between 2961 (and 3068) and ν_1 band origins for both normal and ¹³C isotopomers suggests an assignment to the combinations of ν_1 vibration with intermolecular

modes. For the third band considered here no information about the isotopomers' spectra is available and its identity cannot be guessed. Given the Σ - Σ structures of the three bands, and also the fact that their intensities, degree of intermolecular bond contraction, and separation between the adjacent bands drop in one and the same direction it is tempting to assign the bands to the progression in intermolecular stretching vibration ($\nu_1+n\nu_s$). Let us consider first whether the assignment of 2961 cm⁻¹ band to $\nu_1+\nu_s$ vibration complies with what one expect for an intermolecular stretching vibration. One can note that an intermolecular frequency of 146 cm⁻¹ is in a good agreement with theoretical predictions. A harmonic value of ≈ 140 cm⁻¹ is calculated for Ar-HCO⁺ at MP2 level of theory [233]. Respective anharmonic value (not provided) should of course be lower but since ν_s fundamental is also lower then intermolecular vibrational frequency in ν_1 state arisen disagreement will be partly compensated. A value of 143 cm⁻¹ is predicted from a theoretical PES for Ar-HCO⁺ [205]. A value of similar order of magnitude is also predicted from Millen's formula ($\nu_s'' \approx 130$ cm⁻¹). Isotopic shifts are in a very good agreement with this assignment as well. In an harmonic approximation, considering Ar-HCO⁺ complex as a quasidiatomic molecule, one can predict that exchange of ⁴⁰Ar for ³⁶Ar will increase the intermolecular stretching frequency by ≈ 3.4 cm⁻¹ and ¹²C \rightarrow ¹³C replacement will lower it by 2.8 cm⁻¹. Experimental values are respectively 3.5 and -3.2 cm⁻¹. Finally, the strength of the 2961 cm⁻¹ band in the spectrum of Ar-HCO⁺ is consistent with the fact that $\nu_1+\nu_s$ transition could be easily detected in some other complexes of this kind. Thus the $\nu_1+\nu_s$ identity of the 2961 cm⁻¹ band can be regarded as proven.

Table 7.9 : Constants for remaining Ar-HCO⁺ bands

band	Isotopomer and J range	ν	B' ($\times 10^{-2}$)	D' ($\times 10^{-8}$)	χ^2 ($\times 10^{-2}$)
2961 cm ⁻¹ ($\nu_1+\nu_s$)	Ar-HCO ⁺ ¶	2961.17(8)	6.91(9)	99*	48
	Ar-HCO ⁺ (J \leq 10)	2961.15(1)	6.923(8)	6.6 [¥]	0.05
	Ar-H ¹³ CO ⁺ ¶	2928.8(1)	6.78(1)	65(9)	30
	Ar-H ¹³ CO ⁺ (J \leq 4) ³⁶ Ar-HCO ⁺ †	2928.62(1) 2965.0(5)†	6.87(3)	8.2 [¥]	0.003
3068 cm ⁻¹	Ar-HCO ⁺ ¶	3068.16(6)	6.90(4)	-38*	44
	Ar-HCO ⁺ (J \leq 4)	3068.17(0)	7.01(4)	6.6 [¥]	0.003
	Ar-H ¹³ CO ⁺	3032.79(0)	6.936(7)	8.2 [¥]	0.16
3125 cm ⁻¹	Ar-HCO ⁺ ¶	3125.1(2)	6.71(3)	-3*	250
	Ar-HCO ⁺ (J \leq 2)	3124.93(1)	6.86(18)	6.6 [¥]	-
3799 cm ⁻¹	Ar-HCO ⁺ (J \leq 15)	3798.541(5)	6.992(9)	145(50)	0.08

¶ Poor fit because of the upper state perturbation; * Undefined (uncertainty larger then the value itself); ¥ Taken to be the same as for the lower state. Kept fixed during the fit; † From the band contour

Assignment of the 3068 and 3125 cm⁻¹ bands is more problematic. If one assumes that they are respectively the second and the third member of the intermolecular stretching progression ($\nu_1+2\nu_s$ and $\nu_1+3\nu_s$), it would make the series converge far too rapidly. According to the theoretical predictions [205, 233], Ar-HCO⁺ is a moderately bound complex and its intermolecular vibrations probably should not be that anharmonic. From the other hand there are not so many alternatives for combination bands in this spectral range. For example assigning one of the bands to $\nu_1+2\nu_b$ combination would rise the question why the $\nu_1+\nu_b$ perpendicular band was not observed (a demanding question in any case). There

is a remote possibility that the 3068 cm⁻¹ band is in fact $\nu_1+2\nu_s$ combination, which is supported by the spectrum of Ar-H¹³CO⁺. However because of the poor signal to noise ratio in the latter spectrum this assignment should be considered as tentative. The identity of 3125 cm⁻¹ band is completely unclear at present.

7.3.10. The $\nu_1+\nu_s-\nu_s$ band

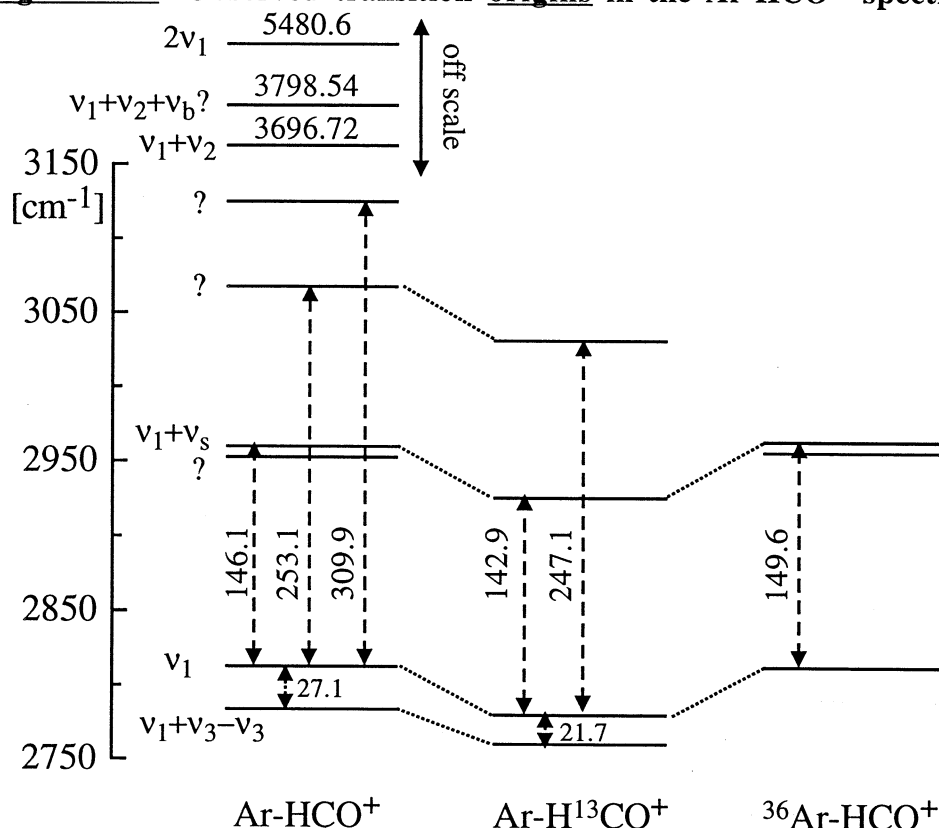
A number of weak transitions is observed at ca. 20-40 cm⁻¹ above the ν_1 band. The transitions appear to be relatively strong and easily saturable, and under the normal laser operating conditions rotational lines from the individual bands merge in a continuous background. Only when the laser power is reduced by a factor of 50-100 down to the level of the full resolution of the ν_1 transition, one can distinguish individual rotational lines in this range. At the same time the relative intensity of some of the weak features and ν_1 band is not affected very much by the laser power variations. Such behaviour is indicative of sequence transitions which typically have similar transition moments with the respective fundamentals. The sequence band range has been shown in figure 7.4 for the normal and ¹³C isotopomers in conjunction with CH stretching transition. As one can visualize from the figure, somewhat higher laser power used to record the ¹³C scan resulted in a poor rotational resolution within this range. In the spectrum of the normal isotopomer, under very low excitation power conditions, one band lying some 19 cm⁻¹ above the ν_1 transition stands more or less clearly among the others and should probably represent a sequence transition from a reasonably populated vibrational state. When the power is increased more features become apparent. In a preliminary report on Ar-HCO⁺ vibrational predissociation spectroscopy [37] the head in the P branch of this transition was given a false assignment of the Q branch of $\nu_1+\nu_b$ combination. Obviously both the degree of the Ar-HCO⁺ angular rigidity and the inefficiency of vibrational cooling in the ion source were underestimated at that time. In present work this transition is reassigned as $\nu_1+\nu_s-\nu_s$ difference band based on the following arguments.

- (1) Intermolecular modes (ν_s and ν_b) are the ones that are expected to be most populated in the expansion after the ground state of the complex. Since the transition does not have any Q-branch like feature it is not of the $\Pi\leftarrow\Pi$ type and therefore it is not $\nu_1+\nu_b-\nu_b$ transition.
- (2) If the $\nu_1+\nu_s-\nu_s$ assignment is correct ν_s fundamental is predicted at 127 cm⁻¹ in excellent agreement with either theoretical predictions [205, 233] and with estimations from the ground state rotational constants.
- (3) Finally, the upper state combination differences derived for this band and $\nu_1+\nu_s$ transitions match reasonably well. Unfortunately it is not a very strong argument since the range for comparison is quite small ($J=3-12$) and line positions in the band in question are not particularly accurate because of the interference from the other sequence transitions. Nevertheless the origin value (2834.38 cm⁻¹) supported by the combination difference analysis is believed to be reasonably accurate.

The inefficiency of vibrational cooling in the source can be appreciated from the relative intensities of the ν_1 and $\nu_1+\nu_s-\nu_s$ transitions. Under certain expansion conditions the latter can be as intense as 1/3 of the former. Under these conditions, assuming similar transition moments for the two bands and Boltzmann distribution of vibrational state levels, one can estimate a vibrational temperature of ≈ 170 K. Clearly with such temperature even doubly excited intermolecular vibrations will be significantly populated and will produce an amount of spectral congestion sufficient to complicate the analysis. Besides there is no reason to believe that the distribution is of Boltzmann type and the situation may in fact be worse.

7.3.11. Discussion

Figure 7.15: Observed transition origins in the Ar-HCO⁺ spectrum



Observed vibrational transition origins in the photodissociation spectra of different isotopomers of Ar-HCO⁺ complex are shown in figure 7.15. Though the spectrum of Ar-HCO⁺ provides a useful impression of the intermolecular interactions within the complex many questions are left unanswered, particularly the ones that concerned with the degree of *angular* anisotropy. For some inexplicable and frustrating reason the transition into the combination of CH intramolecular stretch with intermolecular bend has not been observed in the spectrum. The transition into the pure intermolecular bending state is predicted to be as strong as the intermolecular stretching fundamental and they are expected to have comparable frequencies (132 and 138 at the highest level of theory) [233]. Though explicit calculation of vibrational energy levels on a high-quality theoretical intermolecular potential indicates that the *ab initio* result for v_b [233] may be underestimated somewhat [205] the combination state correlating to v₁+v_b is still predicted to occur within 180 cm⁻¹ from the v₁ transition, i.e. in the area of an extensive scanning. One possible explanation for the apparent absence of the v₁+v_b transition in the spectrum may be that it is comparatively weak and is blended by the stronger v₁+v_s transition or numerous sequence bands lying on the blue wing of the latter (figure 7.11). Since a large change in the average intermolecular separation is expected upon excitation of the v₁+v_b transition, its Q branch is not going to be a very prominent feature (compare v₁+v₂ band displayed in figure 7.6). It is estimated that the v₁+v_b transition has to be weaker than v₁+v_s by a factor of at least 7-10 to be "successfully" lost between 2960 and 2980 cm⁻¹. Weakness of the band is not that unreasonable if Ar-HCO⁺ is compared to the related complexes. The v₁+v_b combination was observed in He-HN₂⁺ and Ne-HN₂⁺ complexes (see Rg-HN₂⁺ section). While in He-HN₂⁺ the v₁+v_s and v₁+v_b bands had comparable intensities in Ne-HN₂⁺ the former was about 3-5 times smaller. Unfortunately neither was observed in the spectra of He-HCO⁺ and Ne-HCO⁺ complexes. Though the factors governing the relative intensities

of the two transitions are not clear it is conceivable that the stronger is the angular rigidity of the complex the weaker is the $\nu_1+\nu_b$ band intensity compared to that of $\nu_1+\nu_s$. To test whether the $\nu_1+\nu_b$ band is situated in the 2960-2980 cm^{-1} range a spectrum of considerably cooler complexes (≤ 10 K) has to be observed.

The degree of influence of the Ar ligand on the intramolecular vibrational motions of the HCO⁺ unit is best illustrated by considering ν_1 and $2\nu_1$ bands. The magnitude of the ν_1 vibrational band shift for Ar-HCO⁺ (274 cm^{-1} to the red) is quite impressive. In comparable neutral systems involving diatomic or triatomic molecules complexed with rare-gas atoms, vibrational shifts of just a few wavenumbers are typical. For example, the isoelectronic Ar-HCN van der Waals molecule features a ν_1 red shift of only 2.69 cm^{-1} [203]. In the Ar_n-HF series, the first Ar atom lowers the HF vibrational frequency by only 9.6 cm^{-1} (a relative shift of 0.24 % of the HF vibrational frequency), and completely encasing the HF molecule in an Ar matrix still only produces a relative red shift of 1.1% [240]. In fact, the magnitude of the Ar-HCO⁺ red shift is more akin to the ones for strongly hydrogen bonded complexes (e.g., ≈ 245 cm^{-1} for ν_1 of HF-HCN [196]), emphasizing the substantial interaction between the HCO⁺ cation and the linearly disposed Ar atom. Presumably the fact that the proton is attracted by both the CO *and* the Ar results in a flattened effective proton potential and a reduced characteristic frequency for its motion. Apart from the frequency reduction the anharmonicity of the CH stretching vibration is boosted up in the complex. From the ν_1 and $2\nu_1$ band positions taking a common quartic expansion the anharmonicity term χ_{11} can be calculated as -75 cm^{-1} which exceeds the respective value of -54 cm^{-1} for the free monomer [236]. Though harmonic description with first order anharmonicity corrections may not be quite appropriate in this case, the increase in the value for χ_{11} indicates that flattening of the effective proton potential does happen.

One more interesting feature of Ar-HCO⁺ is a number of perturbations afflicting the bands in the infrared spectrum. Even the fundamentals and low-order combination bands appear to be affected. Evidently a large number of dark states capable of interacting with the bright states exist already at moderate excitation energies. Since Ar atom is a heavy and an easily polarizable ligand the Ar-HCO⁺ ionic complex happens to represent a curious breed that combines a relatively high binding energy with relatively low frequency intramolecular modes. As a result a high density of intermolecular states can be obtained in the energy range $1000 \text{ cm}^{-1} \leq E \leq$ dissociation threshold ($\approx 1700 \text{ cm}^{-1}$ [205]). When combined with intramolecular states ν_3 , ν_2 , $2\nu_2$, etc. this swarm of intermolecular states is shifted up by the respective amount of energy and can easily be brought in the overlap with the comparatively simple states probed in this work. The fact that interactions between such highly excited vibrational states and say ν_1 or $\nu_1+\nu_2$ are so efficient is an indication of the severe violation of the normal coordinate picture in this complex.

7.4. The He-HN₂⁺ complex

7.4.1. Spectrum

The He-HN₂⁺ complexes are created using a mixture of N₂, H₂ and He at 1:1:100 ratio at 6 bar stagnation pressure. Initial spectroscopic searches were first conducted in the N-H stretch spectral region (3000-3200 cm⁻¹) and later the range was extended to higher frequencies to include the expected summation bands. The He-HN₂⁺ mid-infrared spectrum from 3100 cm⁻¹ to 3400 cm⁻¹ is shown in figure 7.16. Three rotationally resolved bands are apparent. The lower lying one with origin at ≈3158 cm⁻¹ is positively the most intense. It is red shifted by around 75 cm⁻¹ from the free N₂H⁺ ν₁ transition, has the form of a linear molecule Σ←Σ band, and features a head in the P branch. This band is assigned as the ν₁ (N-H stretch) fundamental of the complex. The band immediately to higher energy at ≈3255 cm⁻¹ has a noticeable Q branch and possesses the characteristic structure of a linear molecule perpendicular Π←Σ transition. The highest energy band at 3321 cm⁻¹ again possesses a Σ←Σ structure though in contrast to the other Σ←Σ band, features a head in the R branch. Rotational line wavenumbers for all three bands are provided in tables A10-A11.

Table 7.10: He-HN₂⁺ rotational constants

Fitted constants for the ground, ν₁, ν₁+ν_b and ν₁+ν_s levels of He-HN₂⁺. Values for the ν₁+ν_b and ν₁+ν_s states were obtained by fitting with the ground state constants fixed at the values derived from the ν₁ band analysis. Last column provides intermolecular separation calculated from rotational constants B.

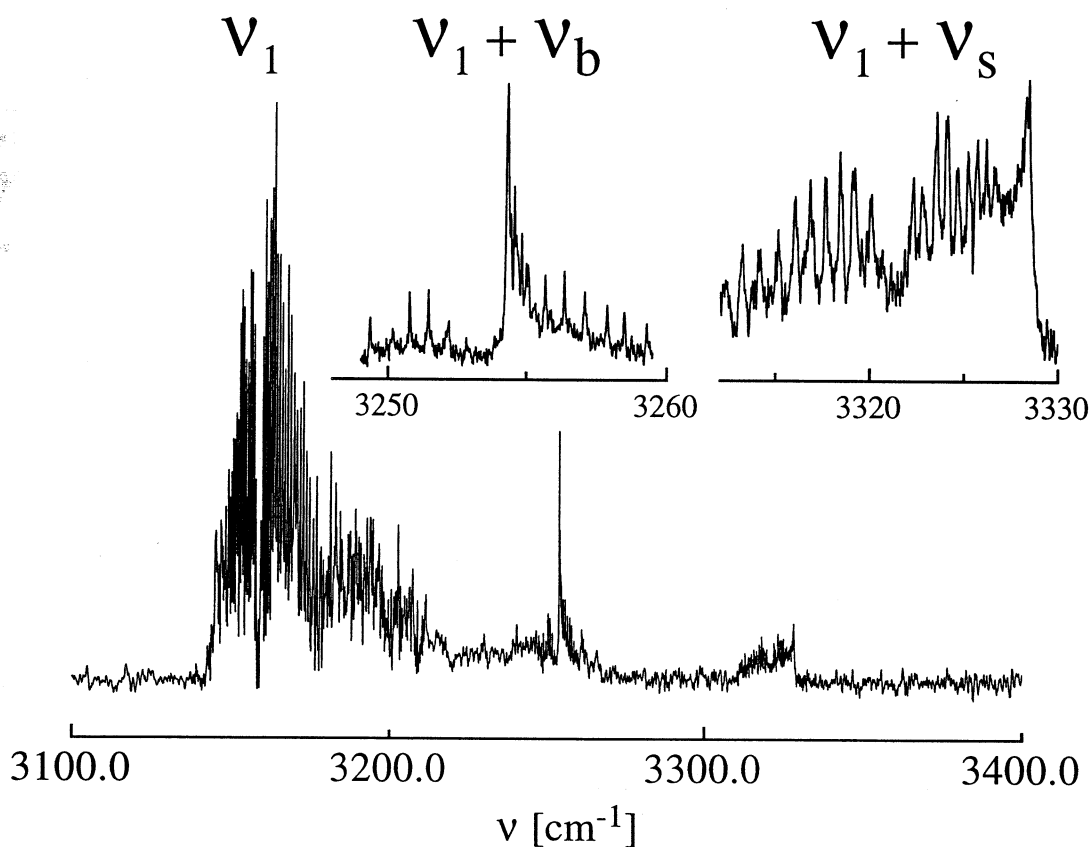
Vibrational level	v ₀ [cm ⁻¹]	B [cm ⁻¹]	D (×10 ⁶)[cm ⁻¹]	R _{cm} [Å]
0		0.3517 (05)	5.8 (0.5)	3.247(3)
ν ₁	3158.419 (09)	0.3579 (05)	3.9 (0.6)	3.210(3)
ν ₁ +ν _b	3254.671 (50)	0.3559 (21)	28 (20)	3.22(1)
ν ₁ +ν _s	3321.466 (50)	0.3393 (15)	18 (09)	3.32(1)

Constants from a linear molecule fit of the ν₁ band are listed in table 7.10. Inclusion of higher order terms in the expansion did not greatly improve fitting of line positions, with errors associated with the higher order constants exceeding the constants themselves. The differences between the measured line positions and those calculated using the fitted values are small, suggesting that the rotational levels of the upper state are relatively unperturbed. Neglecting zero point vibrations, and assuming as usual that HN₂⁺ does not distort when complexed with He, one can estimate a H-He separation of 1.724 Å for the linear NNH⁺-He structure. Due to a rather soft intermolecular bond and low reduced mass for the stretching motion the equilibrium intermolecular separation must be a bit smaller. While the rotational constants are also consistent with a physically reasonable bond distance for the alternative He-NNH⁺ structure (r_{N-He}=2.64 Å) inductive stabilization will be maximized when the He is situated near the proton. A rather large red shift in the N-H stretch frequency from the free molecule value also suggests that the He is adjacent to the proton.

Using the upper state rotational constant one can predict that intermolecular bondlength contracts upon N-H stretch excitation by approximately 0.037 Å. This, along with the 75 cm⁻¹ red shift in the ν₁ vibration and smaller upper state D value, suggest a somewhat stronger intermolecular interaction in the upper vibrational level. The reason for vibrational enhancement of the intermolecular bonding may be related to the anharmonicity in the N-H stretch motion. Namely excitation of the N-H vibration leads to the proton spending less time near the N₂ molecule, allowing it to interact more effectively with the He atom. With use of Millen's relationship (4.10) one arrives at a harmonic intermolecular stretch vibrational frequency of 150±10 cm⁻¹ for ν₁=0 and 190±15 cm⁻¹ for ν₁=1 states. Increase in the ν_s frequency reflects concomitant decrease in centrifugal distortion constant.

The P and R branch lines of the $\Pi \leftarrow \Sigma$ band are easily discerned, making the rotational numbering relatively straightforward. As expected P(1) line is missing for this transition. On the other hand, due to congestion in the head region, assignment of the Q branch rotational lines was not possible. The ground state combination differences formed from the R and P branch lines are in good agreement with those of the ν_1 band encouraging one to presume that both bands share a common lower vibrational state. Rotational analysis proceeded by fitting the lines to expression (4.3) (taking $K''=0$ and $K'=1$), with the lower state constants fixed at the values determined from the ν_1 band analysis. Constants determined in this manner are provided in table 7.10. Inspection of the deviations between the calculated and measured transition energies shows that they are in some cases quite large, with P and R branch lines terminating in a common upper state being displaced by similar amounts. This immediately suggests that upper state levels are perturbed. The presence of isolated perturbations makes it impossible to provide accurate values for the $\nu_1 + \nu_b$ rovibrational constants. As can be seen from table 7.10 they are almost an order of magnitude less defined than the constants for the ground and ν_1 states.

Figure 7.16: Vibrational predissociation spectrum of He-HN₂⁺



The Q branch band shape is poorly reproduced using the constants derived from the P and R branches. Simulated contours are degraded to lower rather than to higher energy as experimentally observed. This fact becomes not so surprising if one recalls that different manifolds of rotational levels are accessed in PR and Q branch transitions. The latter terminate in f parity levels while in the former e parity levels are accessed. The levels with the same J but distinct parities have slightly different energies. This splitting is known as l -type doubling when referred to vibrationally excited bending states of a linear molecule. While a determination of the f manifold constants is precluded by the overlapping of lines in the head region, one obtains a much better match between the measured and calculated contours if the upper state B value is increased somewhat (to around 0.36 cm^{-1}), and the D value is decreased (to roughly $8 \times 10^{-6} \text{ cm}^{-1}$).

Analysis of the weak $\Sigma \leftarrow \Sigma$ band proceeded in much the same fashion as for the $\Sigma \leftarrow \Pi$ band, although due to the band's weakness and the relatively broad rotational lines, uncertainties in line positions are larger than for the other two transitions. The line positions were fitted to expression 4.3 (with $K' = K'' = 0$), again with the lower state parameters fixed to those determined from the main band analysis. Constants determined in the fit are listed in table 7.10. The fact that the complex expands in the upper state immediately follows from a negative ΔB value and head in the R branch.

Now the identities of the weak $\Pi \leftarrow \Sigma$ and $\Sigma \leftarrow \Sigma$ transitions are considered. The possibility that either band is an overtone or combination band involving intramolecular vibrations appears to be remote. The appropriate higher order transitions like $\nu_2 + \nu_3$ 01[±]1 (2947 cm⁻¹) or $4\nu_2$ 04⁰ (2726 cm⁻¹) are expected to be extremely weak and indeed they have not been observed for the monomer. Furthermore, in order for these levels to be responsible for the two weak bands, they would need to be shifted by several hundred wavenumbers, which is improbable for a He containing complex. Another conceivable possibility is that the bands represent some combinations built on ν_1 , of type $\nu_1 + \nu_x - \nu_x$. However, because of large displacement from ν_1 and the tolerable agreement between the ground state combination differences for all three bands, it seems unlikely that either of the transitions is a sequence hot band. A bunch of rotational lines at around 3200 cm⁻¹ is a much better candidate for the sequence transitions. One is thus encouraged to conclude that unless addition of a He atom leads to extraordinarily large shifts in the HN₂⁺ vibrational frequencies, the two bands are due to combinations of intermolecular vibrations with ν_1 . Given their energies and structures it is almost certain that they are indeed the $\nu_1 + \nu_b$ and $\nu_1 + \nu_s$ combination bands. Notably, large increase in intermolecular separation for the $\Sigma - \Sigma$ band assigned as $\nu_1 + \nu_s$ combination is consistent with excitation of the anharmonic intermolecular stretching motion. In addition there is a fair agreement between experimental ν_s frequency of 163 cm⁻¹ and value of 190 ± 15 cm⁻¹ calculated in harmonic approximation from B and D constants.

The occurrence of the $\nu_1 + \nu_b$ band 96 cm⁻¹ higher than ν_1 implies a comparatively stiff He...HN₂⁺ bending coordinate. Normally, neutral He containing van der Waals molecules are distinguished by the flexibility of the intermolecular bond, with the angular motion often possessing considerable free internal rotor character. If the band assignments proposed here are correct, the intermolecular bending coordinate in He-HN₂⁺ is far more rigid than in any previously characterized He containing complex.

Knowledge of the bending frequency and molecular geometry enables one to estimate the extent of the angular motion in the ground state. For an undistorted, linear HN₂⁺ interacting harmonically with a He atom

$$\langle \phi^2 \rangle = h / (4\pi^2 \mu_b \bar{\nu} c) \quad (7.2)$$

where ϕ is the angle (in radians) between the HN₂⁺ axis and the bond between the constituents' centres of mass, $\bar{\nu}$ is the wavenumber of the bending vibration and μ_b is its reduced mass. The bending reduced mass (μ_b) for the rod+ball system is given by [241]

$$\mu_b = \frac{1}{(1/I + 1/(Mr^2) + 1/(mr^2))} \quad (7.3)$$

I being the rod's moment of inertia about its centre of mass, M the rod's mass, and m the atom's mass. Substituting the appropriate values for the He-HN₂⁺ complex (I=10.83 amu Å², M=29 amu, m=4 amu, r=3.2 Å), one finds that $\mu_b = 8.32$ amu Å² and $\langle \phi^2 \rangle^{1/2} = 11.8^\circ$.

While the zero point excursion is certainly substantial, it is nonetheless significantly less than the corresponding ones for rare gas atoms bound to the isoelectronic HCN molecule (26.8° for Kr-HCN, 31.0° for Ar-HCN 31.0°, 46.8° for Ne-HCN and essentially a free rotor for He-HCN [198]).

Excitation of the bending vibration in conjunction with ν_1 leads to the exploration of angular configurations even further from equilibrium. Assuming the small angle harmonic approximation, the average bending angle for $\nu_1+\nu_b$ can be estimated as $\langle \phi^2 \rangle^{1/2} = 23.6^\circ$. Significantly, the B values for the ν_1 manifold and the $\nu_1+\nu_b$ *e* parity manifold are quite close to one another, suggesting that there is little alteration in the average radial equilibrium separation as the He atom begins to traverse about the HN₂⁺ core. This is in marked contrast to the situation in the Ar-HCN van der Waals molecule, where due to the combination of a sharp decrease in the radial centre-of-mass minimum distance as the system moves away from linearity and an extraordinarily low bending frequency, the lowest van der Waals bending states have B values that are 25 % larger than the ground state ones [202].

7.4.2. One-dimensional RKR potential

The He-HN₂⁺ complex served as a model system for the spectroscopic data inversion procedure which is used to develop one dimensional (1-D) radial potentials appropriate for the interaction of He with HN₂⁺ in its (000) and (100) vibrational states [205]. The algorithm involves partitioning the potential into short and long range portions, the former part, valid in potential regions accessed in the spectroscopic transitions, being determined empirically by direct inversion of spectroscopic data using the rotational RKR procedure while the long range part is assumed to have a form consistent with the long range polarization interaction. The combined RKR/polarization potential for He-HN₂⁺(100), constructed using the ν_1 and $\nu_1+\nu_s$ data, is shown in figure 7.17. It is interesting to note that the long range polarization potential practically coincides with the RKR curve between the $\nu_s=0$ and $\nu_s=1$ outer turning points, demonstrating that in this region the intermolecular potential is effectively dominated by the long range polarization interaction.

Table 7.11: He-HN₂⁺ RKR potential properties

Properties of the He-HN₂⁺ complex determined from the collinear RKR/polarization potentials. Included are energies for the lowest five vibrational levels, dissociation energies (D_0), and radial equilibrium distances (r_e). For He+HN₂⁺(100) two potentials were generated, the first employing both the ν_1 and $\nu_1+\nu_s$ data, the second with only the ν_1 data. Note that the experimental E(1,0) spacing for He+HN₂⁺(100) is 163 cm⁻¹.

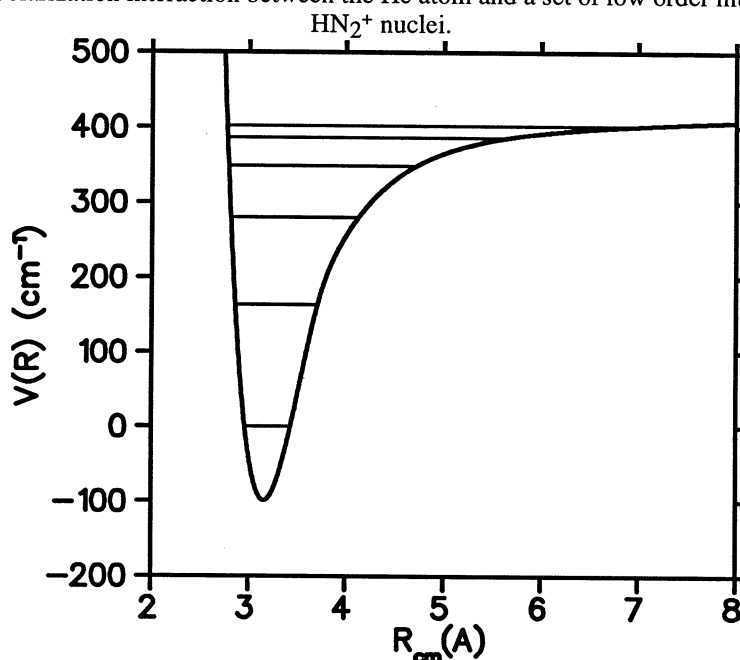
HN ₂ ⁺ vibrational state	levels used	D_e (cm ⁻¹)	D_0 (cm ⁻¹)	r_e (Å)	E(1,0) (cm ⁻¹)	E(2,0) (cm ⁻¹)
(100)	ν_1 and $\nu_1+\nu_s$	528.8	430.8	3.159	163.6	280.6
	ν_1	527.6	430.3	3.180	174.0	291.2
(000)	ν_1	456.8	378.4	3.210	144.9	250.8

Potential obtained using the $\nu_s=0$ data alone is very similar, for example D_e values for the two potentials are within 1 cm⁻¹ of one another (see table 7.11). The agreement is encouraging as there are proton-bound complexes for which $\nu_1+\nu_s$ stretching combination band has not yet been observed. Furthermore, the conformity of the He+HN₂⁺(100) potentials determined with and without the $\nu_1+\nu_s$ data can be seen as strong evidence that the weak Σ - Σ band has indeed been correctly assigned as $\nu_1+\nu_s$. The model potentials enable one to compare the interaction of HN₂⁺ in its (000) and (100) states with between He. This

is probably most appropriately done by comparing potentials obtained without the $\nu_1+\nu_s$ data (second and third rows of table 7.11). The He interaction with the vibrationally excited molecule is somewhat stronger, with a 0.03 Å shorter equilibrium intermolecular distance and 52 ± 16 cm⁻¹ larger D_0 compared to the ground state molecule. This compares fairly well with the vibrational red shift ($\Delta\nu\approx 75.5$ cm⁻¹) for the level of approximations used here.

Figure 7.17: One dimensional radial intermolecular potential for He+HN₂⁺

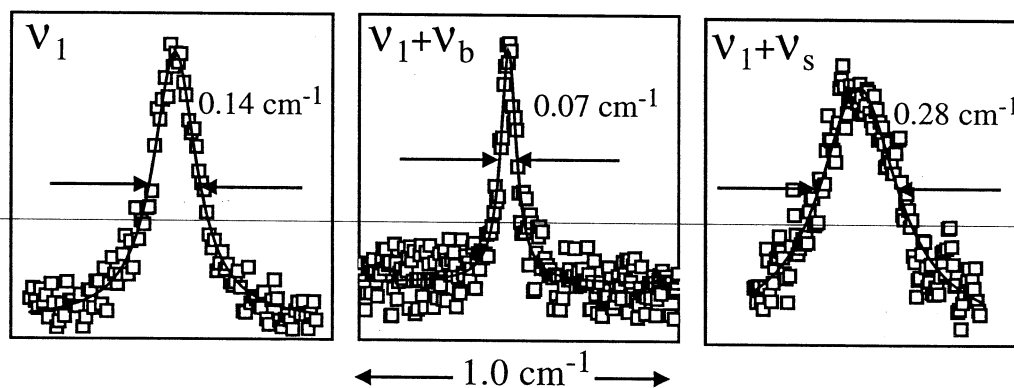
This (100) state potential is given along with the six lowest vibrational levels. The potential up to the $\nu_s=1$ level was determined using the rotational RKR procedure using the ν_1 and $\nu_1+\nu_s$ data, while the long range part is due to the polarization interaction between the He atom and a set of low order multipoles sited on the HN₂⁺ nuclei.



7.4.3. Vibrational predissociation

Figure 7.18: Linewidths in the He-HN₂⁺ spectrum

Slow scans over individual rotational lines for the ν_1 , $\nu_1+\nu_b$ and $\nu_1+\nu_s$ bands. The fitted Lorentzian curves have widths of 0.14 ± 0.02 cm⁻¹ (ν_1), 0.07 ± 0.02 cm⁻¹ ($\nu_1+\nu_b$) and 0.28 ± 0.08 cm⁻¹ respectively.



From complexes presented in this work He-HN₂⁺ appears to be the only one displaying rotational linewidths greater than the laser resolution. Rotational linewidths can be used to infer lower limits for the lifetime of the initially prepared state. To accurately measure the widths, slow scans at reduced power were taken over individual rotational lines for all three bands (see figure 7.18). These were subsequently fitted to Lorentzian profiles to yield widths of 0.14 ± 0.02 cm⁻¹ (ν_1), 0.07 ± 0.02 cm⁻¹ ($\nu_1+\nu_b$) and 0.28 ± 0.08 cm⁻¹ ($\nu_1+\nu_s$). No noticeable variation in the widths with rotational level was apparent in any of

the three bands. If the broadening is homogeneous, the widths correspond approximately to upper state lifetimes of 38 ps, 76 ps and 19 ps respectively. A firm upper limit for the time scale of the fragmentation process is provided by the ion's flight time through the octopole region of the apparatus (roughly 50 μ s).

It is interesting to note the contrasting effects on the vibrational predissociation / relaxation rate caused by exciting the intermolecular stretching and bending motions in combination with ν_1 . Although the precise reason for the lifetime variations is at present unclear, it is possible that the longer lifetime for the $\nu_1+\nu_b$ combination level is due to a decreased averaged projection of the N-H stretch displacement onto the intermolecular bond, while the increase in the rate for the $\nu_1+\nu_s$ combination may reflect a more favorable overlap between the bound and continuum wavefunctions.

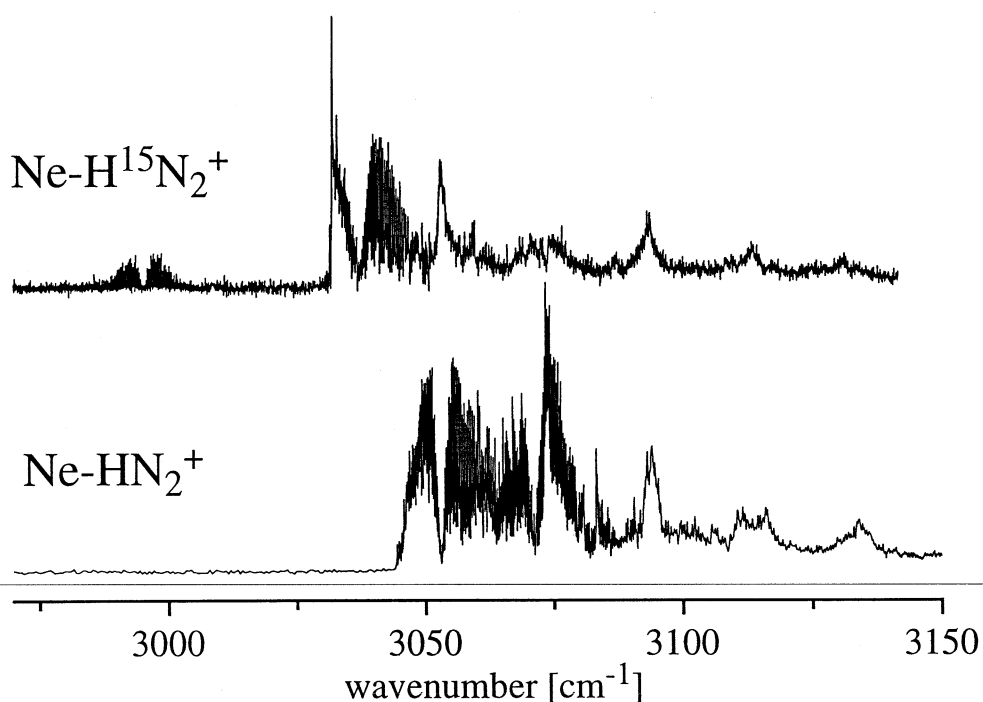
7.5. The Ne-HN₂⁺ complex

7.5.1. Spectrum

Three isotopic modifications of this complex have been studied. In addition to the most abundant isotopomer ²⁰Ne-1H¹⁴N₂⁺ called "normal" hereafter certain bands of ²²Ne-1H¹⁴N₂⁺ and ²⁰Ne-1H¹⁵N₂⁺ have also been recorded. The ²⁰Ne-HN₂⁺ and ²²Ne-HN₂⁺ complexes were created using a mixture of N₂, H₂, He, and Ne at 1:8:50:600 or similar ratio at 6-8 bar stagnation pressure. Natural abundance of ²²Ne is high enough (≈10 %) to allow observation of the substituted complex. To produce the Ne-H¹⁵N₂⁺ isotopomer a mixture containing ¹⁵N₂, H₂, and Ne was prepared with an initial ratio of 1:5:20. The mixture was refilled with H₂ and Ne as it was used so the proportion of ¹⁵N₂ in the bottle dropped from scan to scan until the signal became too weak for practical purposes. Due to the cost of ¹⁵N₂ only a limited number of scans have been taken. Consequently, the precision of rotational line wavenumbers in the Ne-H¹⁵N₂⁺ spectra is reduced somewhat compared to that for the other two isotopomers. Covered spectral ranges for the normal, ²²Ne, and ¹⁵N isotopomers are respectively 2700-3500 cm⁻¹, 3000-3250 cm⁻¹, and 2960-3140 cm⁻¹.

Figure 7.19: Vibrational predissociation spectrum of Ne-HN₂⁺

Vibrational predissociation spectra of Ne-H¹⁵N₂⁺ and normal isotopomer. Due to an increased mass of the former its spectrum is shifted to lower frequencies

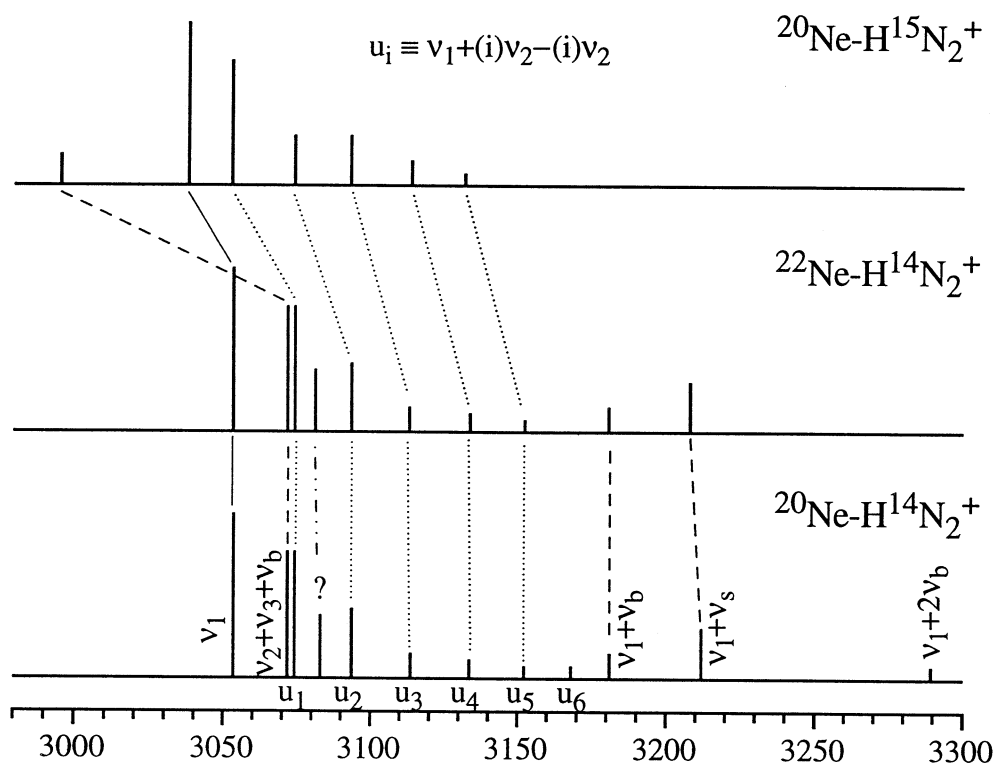


From the experience with He-HCO⁺, Ne-HCO⁺, and He-HN₂⁺ complexes, spectra of which were recorded before, it was expected that the spectrum of Ne-HN₂⁺ would be dominated by a strong transition corresponding to the ν_1 (NH stretch) vibration of the complex. Besides weaker combination bands involving intermolecular vibrations were anticipated. Surprisingly a more complicated spectrum with a variety of bands was obtained. Figure 7.19 displays the spectra of normal and Ne-H¹⁵N₂⁺ isotopomers between 2950 and 3150 cm⁻¹. The ²²Ne-HN₂⁺ spectrum is not shown, since, apart from a small shift, it is very similar to the spectrum of Ne-HN₂⁺. For the normal isotopomer only a portion of the

observed spectrum is presented, there are at least four more rotationally resolved bands appearing at higher frequencies. For Ne-H¹⁵N₂⁺ only this limited portion was recorded because of the lack of ¹⁵N₂.

The spectrum of Ne-HN₂⁺ as well as of ²²Ne-HN₂⁺ is dominated by two strong transitions of similar intensity with origins at around 3053 and 3072 cm⁻¹. The 3053 cm⁻¹ transition is of Σ-Σ type with a characteristic 4B band gap. It has a prominent head in the P branch reflecting a contraction of the complex upon excitation. The transition seems to be free of strong perturbations. The 3072 cm⁻¹ transition does not have an apparent Q branch either but it is really difficult to decide whether it has a 4B or 6B band gap because of the presence of few weak unidentified lines in this range. The transition is virtually unshaded but at J'=39 a weak head in the R branch is formed somewhat unexpectedly. Similar cases of quick head formation have been documented in the spectra of Ar-HCO⁺ where they come from perturbations of the upper state rotational levels by another state, with two rotational manifolds crossing at a certain J level. If the Ne-HN₂⁺ 3072 cm⁻¹ band is actually perturbed it might happen that a weak head-like structure at 3083 cm⁻¹ (3081 cm⁻¹ for ²²Ne-HN₂⁺) also belongs to this transition. Below these two bands no photodissociation activity is detected down to 2700 cm⁻¹.

Figure 7.20: Observed vibrational transitions in the Ne-HN₂⁺ spectra



Immediately to higher energy a series of relatively narrow unresolved bands separated by roughly 20 cm⁻¹ is observed, with the first and the most intense member of the series lying right under the R branch of the 3072 cm⁻¹ transition. Notably the separation between the first unresolved band and the 3053 cm⁻¹ transition origin is of the same order of magnitude (20 cm⁻¹) suggesting a certain interdependence. Six and respectively five of these unresolved structures are discerned in the spectra of Ne-HN₂⁺ and ²²Ne-HN₂⁺. Their intensity decreases quickly as they become more and more separated from the 3053 cm⁻¹ transition and their positions do not appear to be sensitive to the isotopic substitution. The contours of these unresolved bands suggest that they either contain ΔJ=0 transitions (Q branches) or represent heads of highly degraded bands. Finally there are four more bands at higher excitation energies, a weak perpendicular transition with Q branch onset at 3181

cm⁻¹, a band of Σ - Σ type of a reasonable intensity at around 3212 cm⁻¹, a strongly perturbed parallel band at 3289 cm⁻¹, and an extremely weak band of uncertain type at 3465 cm⁻¹ (all wavenumbers refer to the normal isotopomer). Due to their weakness the last two bands could be recorded only for the normal isotopomer. For the ²²Ne analog of the perpendicular band, only the position of the Q branch was measured.

The spectrum of Ne-H¹⁵N₂⁺ isotopomer is looking in some respects similar to the spectra of ^{20/22}Ne-HN₂⁺. As expected the overall spectrum shifts to the red since the replacement of nitrogen by its heavier isotope increases the reduced mass for the intramolecular NH vibration. The spectrum contains two rotationally resolved parallel transitions and a group of near equidistant relatively narrow unresolved features. However the relative intensities and separation between the parallel bands changes drastically in comparison with the other isotopomers. The stronger band, definitely of Σ - Σ type, with origin at 3038 cm⁻¹ has a prominent head in the P branch similar to the 3053 cm⁻¹ transition of the normal isotopomer. The other transition appears ca. 42 cm⁻¹ below it and is at least four times weaker. The unresolved bands are separated from each other by roughly 18-21 cm⁻¹ but only by 15 cm⁻¹ from the 3038 cm⁻¹ band (contrary to the case of normal and ²²Ne isotopomers where the separation is of the same order). Unfortunately there was not enough ¹⁵N₂ to probe the behavior of the other bands.

A summary of all transitions observed for the Ne-HN₂⁺ complex is presented in figure 7.20 in form of the stick spectra.

7.5.2. Ground state rotational constants

Rotational line wavenumbers for the rotationally resolved bands for all isotopes are available from tables A12-A15. The bands of the normal isotopomer are considered first since its rotational line positions are known with a higher precision and more of them are available for the analysis. In the spirit of investigation of other spectra of the complexes, containing multiple transitions with initially unclear vibrational assignments, the lower state combination differences for all available bands are calculated and compared as a first step. If most of the bands happen to have the same lower state one can assign it to the ground (vibrationless) state of the complex with a high degree of confidence, since supersonic expansion in the ion source usually takes care of some vibrational relaxation of a large proportion of complexes. Surely the source produces a certain amount of ions in vibrationally excited states, which have low propensity for collisional relaxation, but the density of cooled molecules is expected to be largest. It is assumed that at least one of the two strong parallel bands originates from the ground state and corresponds to the complex's NH stretching vibration.

Table 7.12: Ne-HN₂⁺ lower state constants

Lower state molecular constants for different Ne-HN₂⁺ isotopomers determined from the fits of averaged combination differences. Certain properties of the complex derivable from the constants are also given in the last four rows.

property	²⁰ Ne-H ¹⁴ N ₂ ⁺	²² Ne-H ¹⁴ N ₂ ⁺	²⁰ Ne-H ¹⁵ N ₂ ⁺
B'' [cm ⁻¹]	0.12194 (2)	0.11590 (3)	0.11814 (10)
D'' [cm ⁻¹] ($\times 10^{-7}$)	3.65 (10)	3.26 (10)	taken as 3.5
Rg - HN ₂ ⁺ ν_s frequency [cm ⁻¹]	135 (2)	133 (2)	
Rg - HN ₂ ⁺ force constant [N/m]	12.8 (4)	13.0 (4)	
Rg - HN ₂ ⁺ cm separation [Å]	3.281 (1)	3.281 (1)	3.371 (2)
Rg-H separation [Å]	1.756 (1)	1.756 (1)	1.758 (2)

A comparison of the lower state combination differences reveals that they coincide with an excellent precision for all of the observed bands. It is not improbable that few specific vibrational states of the complex, like a singly excited NN stretching vibration (ν_3), might happen to have a set of combination differences similar to that of the ground state (experimental precision is only 0.02 cm⁻¹). However none of the observed bands seems to have the position and intensity expected for the $\nu_1+\nu_3-\nu_3$ sequence transition which should be stronger than other conceivable sequences involving ν_3 . Hence, it is believed that all the rotationally resolved transitions start from the ground state of the complex. Determination of the rotational constants proceeded by fitting a weighted average of the lower state combination differences to equation (4.7). The data is weighted according to the band intensities, number of observed lines, and the accuracy of calibration. Constants derived from the fit can be found in table 7.12. The averaged data could be fitted with sufficient accuracy by using B and D rotational constants, inclusion of higher order centrifugal terms did not improve the fit quality.

For ²²Ne-HN₂⁺ and Ne-¹⁵N₂⁺ isotopomers the ground state constants were determined in the same way. For them too all lower state combination differences derived from the observed rotationally resolved transitions coincided. The constants obtained from respective fits are placed in table 7.12. This table also contains structural parameters of the complex derived under assumption of the unchanged geometry of the HN₂⁺ core, and the estimates of intermolecular stretching frequency and force constant from Millen's expressions (4.10-4.11). Separations between Ne and H atoms derived from the three isotopomers' rotational constants converge quite well at a value of 1.756 Å. Agreement between harmonic parameters is also quite good. The increase in the separation between Ne atom and centre of mass of HN₂⁺ when nitrogen atoms are replaced by ¹⁵N isotope arises from the obvious shift of center of mass of the core away from Ne atom.

7.5.3. Vibrational assignment

Assignment of the rotationally resolved transitions is simplified by the fact that they all originate from the ground vibrational state of the complex. Thus the transition origins from table 7.13 provide a direct access to the vibrational energies of the upper state levels with respect to the ground state of the complex. As mentioned above the ν_1 transition of the complex is supposed to be the strongest in the investigated spectral range. The fact that there are two equally strong bands at 3053 and 3072 cm⁻¹ of parallel type in the spectra of Ne-HN₂⁺ and ²²Ne-HN₂⁺ is unprecedented. Indeed for most of the ionic complexes studied in this laboratory, the intramolecular HX fundamentals are strong and undoubled. Splittings in the degenerate vibrations of non-linear chromophores upon complexation, that arise from the reduction of the symmetry of the system, may be considered as a natural exception. The ν_1 vibration of HN₂⁺ as well as that of Ne-HN₂⁺ are fully symmetric and no splitting is possible.

The satellite band near ν_1 transition can be explained by postulating an existence of a Fermi resonance between the NH vibration and some other state which may acquire intensity from it. The simplest intramolecular state in this range, $\nu_2+\nu_3$, represents combination of the NN stretching with HNN bending vibration. In the free monomer the vibrational energy of this state is of the order of 2945 cm⁻¹. In the complex the NN stretching frequency is expected to become somewhat lower than in the monomer, though the magnitude of the frequency shift should be not as large as for the ν_1 vibration. On contrary the intramolecular bending frequency should increase upon complexation due to angular stiffening of the NH bond. For example according to a recent *ab initio* study [233] the values of ν_1 , ν_2 , and ν_3 in the related Ar-HCO⁺ complex shift from the monomer frequencies by ≈ -270 , -30 , and $+90$ cm⁻¹ respectively. For Ne-HN₂⁺ the experimental ν_1 red shift is of the order of 160-180 cm⁻¹ depending on the assignment of the two strong

bands. Accordingly the shifts in ν_2 and ν_3 are expected to be smaller than they are in Ar-HCO⁺. One can speculate that in the complex the vibrational energy of the $\nu_2+\nu_3$ combination will be increased by some 0-30 cm⁻¹ compared to that in the free monomer. Estimated spacing between $\nu_2+\nu_3$ and two unidentified parallel bands is thus of the order of 100 cm⁻¹. This compares well to value expected for the intermolecular bending frequency of the complex and one can presume that it is the $\nu_2+\nu_3+\nu_b$ state that resonates with ν_1 . Note that one of the two components of the $\nu_2+\nu_3+\nu_b$ state (the one with zero vibrational angular momentum) has a fully symmetric vibrational species and therefore the Fermi interaction with ν_1 is allowed. Though the intermolecular stretching frequency is of the same order of magnitude as the bending one the $\nu_2+\nu_3+\nu_s$ and ν_1 states cannot be in Fermi resonance with each other since their vibrational species do not match.

Table 7.13: Ne-HN₂⁺ vibrational origins and heads

Uncertainties in the band positions are indicated only if they exceed 0.02 cm⁻¹ limit set by the laser resolution.

band	²⁰ Ne-H ¹⁴ N ₂ ⁺	²² Ne-H ¹⁴ N ₂ ⁺	²⁰ Ne-H ¹⁵ N ₂ ⁺
ν_1	3053.54	3053.26	3037.85
$\nu_2 + \nu_3 + \nu_b$	3071.85	3071.70	2995.37
unidentified blue-shaded head	3083.05±0.03	3081.10	
$\nu_1 + \nu_b$ Q branch onset	3181.04±0.05	3180.65±0.05	
$\nu_1 + \nu_b$ origin (from PR fit, l'=1)	3181.17		
$\nu_1 + \nu_s$	3211.97	3208.04	
$\nu_1 + 2\nu_b$	3289.39±0.10		
unidentified red-shaded head	3465.0±2.0		
$\nu_1 + \nu_2 - \nu_2$	3074.3±0.3	3074.2±0.3	3052.6±0.3
$\nu_1 + 2\nu_2 - 2\nu_2$	3093.7±0.4	3093.4±0.3	3073.9±1.0
$\nu_1 + 3\nu_2 - 3\nu_2$	3113.7±3.0	3113.1±3.0	3093.0±0.6
$\nu_1 + 4\nu_2 - 4\nu_2$	3133.7±0.6	3133.8±0.6	3113.7±0.6
$\nu_1 + 5\nu_2 - 5\nu_2$	3152.3±1.2	3152.4±1.2	3131.9±1.2
$\nu_1 + 6\nu_2 - 6\nu_2$	3168.1±1.2		

To decide which of the two strong bands in the Ne-HN₂⁺ spectrum is ν_1 and which is the trespasser, data on isotopically substituted complexes can be used (in fact this is the actual reason for recording the spectra of ²²Ne-HN₂⁺ and Ne-H¹⁵N₂⁺). Substitution of ²⁰Ne by its heavier and less abundant brother ²²Ne is expected to have virtually zero effect on intramolecular frequencies. Out of intermolecular frequencies only the stretch will be appreciably affected (decreased by a couple of wavenumbers) since in the rod-and-ball picture the effective bending reduced mass is less sensitive to the isotopic substitution of the ball compared to the reduced mass for the stretching mode. In the experimental spectra the 3053 and 3072 cm⁻¹ bands shift by less than 0.3 cm⁻¹ on going from the normal to ²²Ne substituted isotopomer. This observation does not contradict to the assignment of either of the bands to the $\nu_2+\nu_3+\nu_b$ combination and gives further support to the conclusion that interacting state may not be of the $\nu_2+\nu_3+\nu_s$ form. However it still does not help to assign the bands.

Substitution of both nitrogen atoms in the complex by ¹⁵N isotopes should produce a more dramatic effect on the intramolecular frequencies. According to the force field calculation of Botschwina [132] on CEPA-1 level, the ¹⁴N/¹⁵N substitution of both nitrogen atoms in the free monomer suppresses the ν_1 frequency by 19 cm⁻¹ and ν_3 by 66 cm⁻¹. The bending coordinate has not been considered in ref. [132], however it is clear that ν_2 may not increase on going to the heavier isotopomer. Therefore one can expect that in the spectrum of Ne-H¹⁵N₂⁺ the ν_1 band will be shifted by some ≈ 20 cm⁻¹ to the red compared to the spectrum of the normal isotopomer and the $\nu_2+\nu_3+\nu_b$ band will be displaced by at least 70 cm⁻¹ in the same direction. With such large shifts it is possible that the separation between interacting bands will become sufficiently large to take them out of the resonance and to change the qualitative appearance of the spectrum. Indeed, an examination of the experimental spectrum of the Ne-H¹⁵N₂⁺ complex reveals two bands of parallel type at 3038 and 2995 cm⁻¹, the latter being at least four times weaker than the former. Now if this band with decreased intensity is assigned as the $\nu_2+\nu_3+\nu_b$ combination then the stronger band at 3038 cm⁻¹ has to receive the ν_1 label. From this using the predicted substitution shifts one condemns the 3053 and 3072 cm⁻¹ bands of the normal isotopomer to be respectively the ν_1 and $\nu_2+\nu_3+\nu_b$ transitions. If this assignment is correct one obtains substitution shifts for ν_1 and $\nu_2+\nu_3+\nu_b$ of respectively 16 and 76 cm⁻¹ which are in very good agreement with the predictions of Botschwina [132]. Besides, the relative intensity of the two bands in the spectra of the normal and ¹⁵N isotopomers can be explained easily. Intensity of the inherently weak $\nu_2+\nu_3+\nu_b$ band should drop as it moves away from ν_1 which supplies the transition strength for both of them. In the spectrum of Ne-H¹⁵N₂⁺ the bands are separated by 42 cm⁻¹ and $\nu_2+\nu_3+\nu_b$ transition is less intense than ν_1 , while for the normal isotopomer separation decreases down to 18 cm⁻¹, the respective upper states get a chance to interact stronger, and the intensities become comparable. Notably, the rotational structure of the bands is too consistent with this assignment. For all studied isotopes the ν_1 transition is characterized by a modest positive change in rotational constant upon excitation leading to the formation of a strong head in the P branch. On contrary the $\nu_2+\nu_3+\nu_b$ transition looks relatively unshaded. Therefore it is believed that the assignment of the 3053 cm⁻¹ band to the ν_1 transition is correct and vibrational labeling of the other observed bands relies on this hypothesis.

Next band to higher energy (out of the rotationally resolved ones) is a weak perpendicular transition with Q branch onset at 3181 cm⁻¹. The transition lies roughly 127.5 cm⁻¹ above the ν_1 band. The corresponding separation for the ²²Ne isotopomer amounts to 127.4 cm⁻¹. Position, structure, small isotopic shift (ca. 0.3 cm⁻¹ shift is expected for ²²Ne/²⁰Ne substitution from the reduced mass (7.3) change), and relatively low intensity of this band make it a suitable candidate for the $\nu_1+\nu_b$ combination. Unfortunately the position of this and other higher lying transitions are not available for the ¹⁵N isotopomer.

Next comes a band of Σ - Σ type of a reasonable intensity at around 3212 cm⁻¹. In the spectrum of the ²²Ne isotopomer this band is shifted by ca. 4 cm⁻¹ towards lower frequencies. Contrary to all the other bands ΔB for this transition is negative which is a sign of a lengthening of the intermolecular bond upon excitation. These two experimental observations encourage one to assign the band as the $\nu_1+\nu_s$ combination. Notably the $\nu_1+\nu_s$ transition was observed for some other ionic complexes of this type, with stretching frequencies being of the same order of magnitude. If the observed separation of 158 cm⁻¹ between the ν_1 and $\nu_1+\nu_s$ bands is inserted into harmonic pseudodiatom expression (7.1)

to estimate the frequency shift arising from the isotopic substitution of ²⁰Ne by ²²Ne a value of 4.3 cm⁻¹ is obtained in good agreement with the experimental observation.

Two more transitions are found at around 3289 and 3465 cm⁻¹. Due to their weakness they could be recorded only for the normal isotopomer. As mentioned above the 3289 cm⁻¹ transition is of parallel type and is rotationally resolved. The position and structure of this band suggest that it might be combination transition into Σ subcomponent of the $\nu_1+2\nu_b$ state. The band is separated from the $\nu_1+\nu_b$ transition by roughly 108 cm⁻¹ while the $\nu_1+\nu_b$ to ν_1 separation amounts to 128 cm⁻¹, a reasonable difference for a presumably anharmonic mode. The 3465 cm⁻¹ transition has not been assigned yet.

Apart from the rotationally resolved bands a series of unresolved features is present in the spectra of all three isotopomers. Their near-constant separation and intensity decreasing as the series progresses towards higher frequencies away from the ν_1 transition are suggestive of sequence bands of the type $\nu_1+n\nu_x-n\nu_x$. Here x should represent a vibration of Ne-HN₂⁺ complex different from either ν_1 or ν_3 since the sequence transitions for these two are supposed to be shifted to lower frequencies. From the other hand it is difficult to believe that the sequence series is based on the intermolecular vibrations, considering the uniform spacings between its members. As can be seen from table 7.13 the spacing between the first five members of the sequence is around 20 cm⁻¹ for either of the isotopomers. The HN₂⁺ intramolecular bending vibration ν_2 is probably the only one that satisfies the necessary requirements for ν_x as far as the small anharmonicity of the vibration and direction of the sequential shift are concerned. Indeed, since the HN₂⁺ monomer in ν_1 state interacts more efficiently with Ne atom than does the ground state ion, the central proton becomes more constrained in the angular sense and the intramolecular bending frequency should increase. However, the assignment of the unresolved features to the $\nu_1+n\nu_2-n\nu_2$ sequence bands raises a couple of questions that have no simple answers. Firstly, with expected intermolecular binding energy of the order of 500-1000 cm⁻¹ [205], all substates of the multiply excited bending vibration $n\nu_2$ with $n \geq 2$ land above the dissociation threshold of the complex. The fact that the sequence bands originating from them are observed in the photodissociation spectrum implies the lower state lifetimes in excess of 10² μ s for all of them, which is the time necessary to surmount the distance between the ion source and the octopole. Moreover if photodissociation is initiated after the Ne-HN₂⁺ complexes were trapped in the octopole for few milliseconds the spectrum barely changes. From the other hand the sequence transitions are heavily broadened indicating predissociation of intramolecular bending states excited in combination with the NH stretch on a picosecond time scale. These vastly different lifetimes reflect highly mode-specific predissociation dynamics, somewhat unusual for this medium-sized system. Secondly, even if a very long lifetime for the $n\nu_2$ states is assumed, estimated relative abundance of the complexes in $n\nu_2$ states is still quite high, indicating extremely poor cooling of intramolecular bending vibrations in the ion source. One can see from the spectrum of the normal isotopomer that the first unresolved feature at 3074.3 cm⁻¹ is nearly as intense as the ν_1 band and the integrated intensity of all sequence transitions surely exceeds the one of the NH fundamental. Though for other ionic complexes some amount of hot ions is always formed in the source, as evident from the patches of poorly resolved background in their photodissociation spectra, the effect seems to be just tremendous for Ne-HN₂⁺ complex. Curiously the spectrum of Ne-HCO⁺ also seemed to contain an increased number of hot transitions in comparison with the He-HCO⁺ spectrum. It is possible that for the employed ion source inefficient cooling is a general feature of the expansions dominated by neon. Though the high intensity of the hot sequence bands in the spectrum of Ne-HN₂⁺ and long predissociation lifetime of the intramolecular bending states seem very strange there does not

appear to exist at this stage any alternative explanation for the unresolved bands. The features themselves probably represent heads in the P branches of certain components of the $\nu_1 + \nu_2 - \nu_2$ transitions. This view is supported by equal separation between the P branch head of the ν_1 transition and the first sequence band on one hand and average distance between the sequence series members ($\approx 20 \text{ cm}^{-1}$) on the other in the spectrum of Ne-H¹⁵N₂⁺. The spectrum of the normal isotopomer is more affected by Fermi resonance which shifts the ν_1 band to lower frequency and makes the separation between its P-head and the first sequence feature at 3074.3 cm^{-1} somewhat larger. One can actually speculate on the basis of this observation that ν_1 transition was shifted by Fermi interaction with $\nu_2 + \nu_3 + \nu_b$ by $-4 \div 6 \text{ cm}^{-1}$, the latter band being displaced from the unperturbed position by same amount in the opposite direction.

Vibrational assignments proposed in this chapter are summarized in table 7.13. Some of the labels should not be taken as final however and can change in the future when more spectroscopic information is accumulated about this intriguing complex.

7.5.4. Rotational fits

Using the ground state rotational constants the upper state parameters are obtained for all bands in a usual way. Namely, line positions of a given transition are fitted to the equation (4.3) with the lower state constants fixed to obtain ν , B', and D'. If the transition suffers from a perturbation in the upper vibrational state the fit quality may be substantially reduced, i.e. large deviations between experimental and fitted line positions may appear. To check whether the observed deviation is due to an actual perturbation, the lower state constants can be released or higher order centrifugal terms can be added to the expansion. While small aberrations arising from a slight inaccuracy in lower state rotational constants can be corrected in this way, the deviations arising from the perturbations stay or lead to constants with an unphysical magnitude or sign. To get at least some idea about rotational constants of the states affected by perturbations the corrupted J ranges are eliminated from the fit. As in the case of Ar-HCO⁺ complex it appears that rotational line positions of virtually every band in the photodissociation spectrum of Ne-HN₂⁺ cannot be fitted to the rigid linear molecule expression (4.3). The peculiarities of individual bands are summarized below.

Fits of a reasonable quality are obtained for the ν_1 band of all isotopomers. However even for this transition anomalous behavior of rotational line positions is observed for higher J values ($J > 30$) in the P branch. In the R branch, only transitions up to $J \approx 35$ have been tabulated since in this range the R branch overlaps with relatively strong P branch of the $\nu_2 + \nu_3 + \nu_b$ transition. To get more accurate values for the rotational constants, only levels terminating in $J' \leq 30$ were taken for the fit. For the Ne-H¹⁵N₂⁺ isotopomer the upper limit is placed on $J' = 25$ since the ground state combination differences are not available for the higher J values and besides they are not that accurate. The vibrational origins for the normal, ²²Ne, and ¹⁵N isotopomers derived from the fits are respectively 3053.537 , 3053.264 , and 3037.847 cm^{-1} . Though the position of the band has probably been shifted by the Fermi resonance with $\nu_2 + \nu_3 + \nu_b$ the isotopic shifts are of the expected order of magnitude and direction.

Available line positions for the $\nu_2 + \nu_3 + \nu_b$ transition of the normal and ²²Ne isotopomers cannot be fitted to experimental precision as well. Again the levels terminating in higher J seem to present a problem. The fit quality may be improved somewhat if H' as added to the list of the upper state parameters however the values of obtained constants are rather spurious. Again only a limited set of data below $J' \leq 20$ ($J' \leq 25$ for ¹⁵N isotopomer) is fitted to obtain the estimates of the rotational constants and band origin values. A small head formed in the R branch of the normal and ²²Ne isotopomers at around $J \approx 40$ bears

resemblance to the features frequently found in the bands of Ar-HCO⁺ photodissociation spectrum that arise from point perturbations of the upper state rotational manifold. If one extrapolates the line positions from the respective values for the lower J no head is predicted at this place. Unfortunately there is no way to test this supposition since further lines are observed neither in R nor in P branches. Occurrence of perturbations at J'[>]30-40 for both ν_1 and $\nu_2+\nu_3+\nu_b$ transitions must be the result of their mutual interaction. Though the upper state rotational manifolds do not cross at the observed J ranges, it might have crossed "before" the Fermi resonance pushed the two states apart. In addition the $\nu_2+\nu_3+\nu_s$ state which should have a higher energy but a smaller rotational constant has a good chance of perturbing the ν_1 and $\nu_2+\nu_3+\nu_b$ states. Since these three vibrational states fall so close to each other one can expect that the states obtained from these by adding an intermolecular vibration might interact too. So it is not surprising that perturbations are similarly found in the $\nu_1+\nu_s$ and other combination bands. Since not enough information is available about the perturbing states, no deperturbation is attempted at this stage. The upper state accessed in the $\nu_1+\nu_s$ transition is perturbed at around J'=40 as evident from a gap in the R branch. Only lines up to J'=25 were used for the fit. The $\nu_1+\nu_b$ transition has apparently unperturbed P and R branches and its Q branch is not resolved sufficiently well. On contrary in the $\nu_1+2\nu_b$ transition a very strong perturbation located on J'=14 is found. Transitions terminating in J'=5-21 were excluded from the fit. The upper state rotational constants for all rotationally resolved bands are gathered in table 7.14.

Table 7.14: Upper state constants for the Ne-HN₂⁺ transitions

Constants of the appropriate lower states were fixed on the values obtained from combination differences (table 7.12). If isotopomer is different from the normal one it is indicated in the second column. The third column shows J range used for fitting of the bands. Last columns provides the constants and the average deviations of the fits.

band	isotopomer	J range for fit	ν	B'	D' ($\times 10^{-7}$)	χ^2 ($\times 10^{-3}$)
[ν_1]	normal	J' \leq 30	3053.537(3)	0.12428(2)	4.37(17)	0.9
	²² Ne	J' \leq 30	3053.264(2)	0.11816(2)	4.1(2)	0.5
	¹⁵ N	J' \leq 25	3037.847(4)	0.12084(3)	4.9(5)	1
[$\nu_2+\nu_3+\nu_b$]	normal	J' \leq 20	3071.850(2)	0.12223(2)	6.0(6)	0.2
	²² Ne	J' \leq 20	3071.696(4)	0.11604(5)	7.1(9)	1
	¹⁵ N	J' \leq 25*	2995.369(6)	0.11816(6)	4.5(9)	3
[$\nu_1+\nu_b$] (I'=1)	normal	\approx all	3181.171(5)	0.12421(4)	4.5(4)	2
[$\nu_1+\nu_s$]	normal	J' \leq 25	3211.971(3)	0.12074(3)	4.1(3)	0.4
	²² Ne	J' \leq 25	3208.036(2)	0.11476(3)	2.9(3)	0.4
[$\nu_1+2\nu_b$]	normal	J' \leq 4 and J' \geq 22	3289.34(2)	0.12338(9)	16(1)	5

7.5.5. Discussion

As similar to the case of the He-HN₂⁺ complex, for Ne-HN₂⁺ both intermolecular vibrations are observed in combination with NH stretch, allowing to draw some conclusions about the degree of flexibility of the intermolecular bond. If the assignments for $\nu_1+\nu_b$ and $\nu_1+\nu_b$ proposed above are correct, one can estimate the frequencies of the intermolecular bending and stretching vibrations in the $\nu_1=1$ state as 128 and 158 cm⁻¹ respectively. Because of the Fermi resonance between the ν_1 and $\nu_2+\nu_3+\nu_b$ states, which presumably shifts the ν_1 vibrational origin somewhat, these intermolecular frequency values might not be very accurate, but there are indications that they are overestimated by not more than 4-6 cm⁻¹. Substituting necessary parameters in the expression for the bending reduced mass and

average bending angle given in the He-HN₂⁺ section (7.2) one obtains a value of 9.3° for $\langle \phi^2 \rangle^{1/2}$. For the He-HN₂⁺ complex the corresponding value amounted to 11.8°. Together with an increased intermolecular force constants (12.8 vs. 4.8 N/m) the lower average bending angle signifies that Ne-HN₂⁺ loses in both axial and radial floppiness as compared to the He containing complex. As expected the effect of replacing He by Ne on the bending motion is relatively small. Indeed the strength of the charge-induced dipole interaction, which is believed to contribute most to the binding energy, should not depend greatly on the relative orientation of the charged particle (HN₂⁺) and of an isotropically polarizable ligand (Rg). Slight decrease in the average bending angle may result from two conceivable reasons. First, the increased polarizability of Ne necessitates a more substantial induced dipole moment on the Ne ligand, and consequently a stronger (anisotropic) interaction between the induced dipole and the permanent moment of HN₂⁺. Secondly, the larger size of the Ne atom may cause more repulsion between its electrons and π orbitals of HNN⁺. For Ar-HN₂⁺ complex both effects should be more prominent and even smaller bending excursions are expected. Increase in the intermolecular stretching force constants by a factor of 2-3 agrees nicely with twofold enlargement of the polarizability of Ne compared to that of He, once more emphasizing the fact that interactions in the complex are dominated by the electrostatic forces.

7.6. The Ar-HN₂⁺ complex

7.6.1. Expectations

Ar-HN₂⁺ completes the list of the complexes of HCO⁺ and HN₂⁺ molecular ions with He, Ne, and Ar rare gas atoms. Based on the experience with five previous members, spectra of which were discussed above, one can make certain presumptions about the properties and the infrared spectrum of Ar-HN₂⁺. Firstly, it is natural to assume that the complex has a linear proton-bound equilibrium structure as do the other complexes of this kind. Secondly, a large change in the NH intramolecular stretching frequency is expected. In previous studies of the Rg-HCO⁺ series (Rg=He, Ne, Ar) a linear dependence between the difference in proton affinities of CO and Rg, $\Delta PA (=PA_{CO}-PA_{Rg})$, and the complexation induced red shift of the CH stretching vibration of the HCO⁺ ion has been found. Assuming a similar relationship exists for the isoelectronic Rg-HN₂⁺ series, a red shift of around 950 cm⁻¹ is calculated for the ν_1 vibration (NH stretch) of Ar-HN₂⁺ from known experimental values for He-HN₂⁺ and Ne-HN₂⁺. Such a large shift, if estimated correctly, should take the ν_1 frequency outside the range covered by the OPO laser. Thirdly, comparatively low ΔPA value for Ar-HN₂⁺ implies a relatively high dissociation energy for this complex which means that many of its IR transitions do not lead to predissociation. Besides, because of the increased intermolecular binding energy one can anticipate a large degree of anharmonicity in the NH stretching mode which will push the related combination and overtone bands higher in intensity. These predictions agree with the results of a recent *ab initio* calculation [234]. The calculation finds that the complex is linear and that ν_1 frequency drops from the value of 3233.95 cm⁻¹ in the free monomer down to 2330±100 cm⁻¹ in the complex. Binding energy is calculated to be as high as ~3000 cm⁻¹ with respect to dissociation into HN₂⁺ and Ar fragments. This value is greater than any intramolecular fundamental so one can hope to observe just combination or difference bands in the vibrational photodissociation spectrum of the complex.

7.6.2. Spectrum

The complexes are synthesized in a pulsed supersonic expansion of Ar, H₂, and N₂ at a ratio of 100:20:1 and at 3-5 bar stagnation pressure. Photodissociation spectrum has been recorded in the range of 2470 - 6000 cm⁻¹. In total, more than 25 bands with widely different intensities have been observed in the scanned frequency range, with 14 of them being at least partly rotationally resolved. The proportion of completely unresolved bands increases with excitation energy. Above 3800 cm⁻¹ only such unresolved transitions are encountered. Every resolved band appears to have a structure appropriate for a $\Sigma \leftarrow \Sigma$ transition of a linear molecule, except one band of a $\Pi \leftarrow \Sigma$ type. An overview spectrum of the complex in the range 2470-4000 cm⁻¹ is displayed in figure 7.21. All the bands shown in the figure originate from the second output of the laser (see experimental section for more details). In the frequency range of 4000-5400 cm⁻¹, which corresponds to the master oscillator wavelengths from 745 to 710 nm, the second output bands are mixed with the ones due to the first output. Though it is trivial to establish whether the first or the second output is absorbed at a given master oscillator wavelength, presenting this frequency range on the overview figure is not that simple. Fortunately at no master oscillator wavelength the first and second outputs are absorbed simultaneously. Between 5400 and 6000 cm⁻¹ no transitions have been detected.

A closer look at rotationally resolved bands reveals that most of them display deviations from regularity in rotational line spacings, some of the anomalies being of the type never encountered in the spectra of other known Rg-HX⁺ systems. Three selected bands out of the Ar-HN₂⁺ spectrum are presented in figure 7.22(a-c). The specialty of the

first band displayed in figure 7.22 (a) is a perturbation in the upper state rotational manifold at around $J'=7-10$. The state with a high IR transition probability interacts with an IR inactive state leading to sharing intensity between the two states. For this limited J range, the transitions into levels of both perturbed and perturbing states are observed. Most of the observed bands are affected by similar perturbations. Sometimes there are two or even more perturbations in a single band localized at different J' levels. For example, one can see that for the band shown in figure 7.22(a) high J transitions are distributed in a fairly irregular fashion.

Figure 7.21: An overview spectrum of Ar-HN₂⁺

. Bands above 4000 cm⁻¹ are not shown. Relative intensities of the widely separated bands may be inaccurate by more than a factor of 2. The bands at lower frequency edge of the spectrum are by far the most intense.

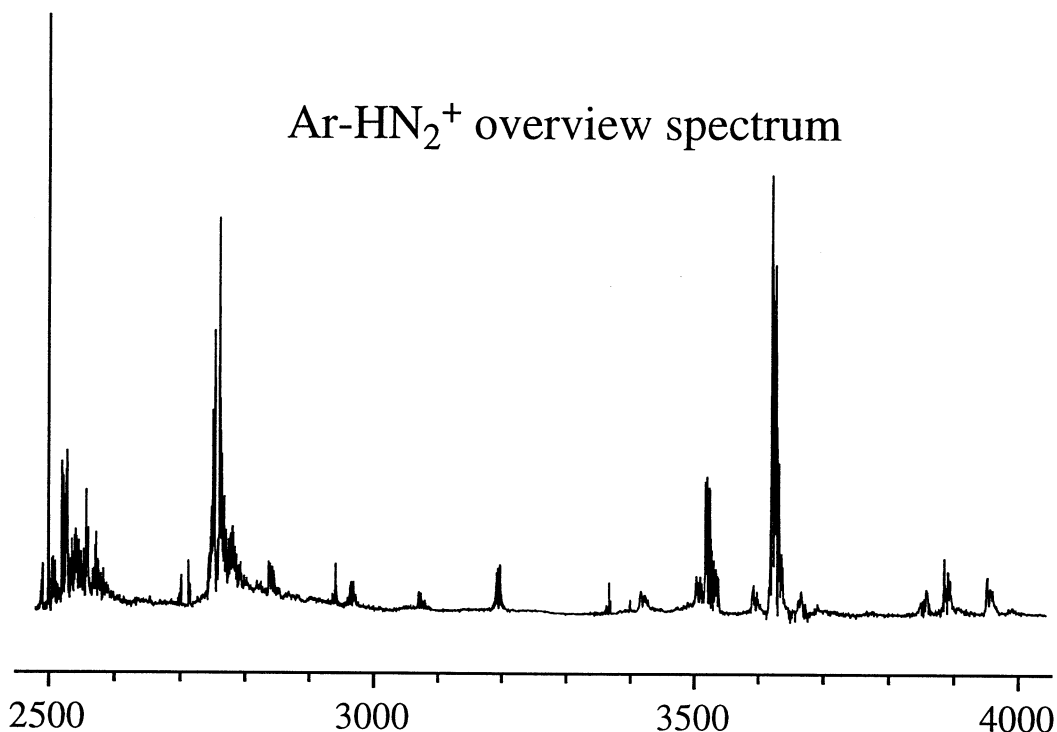
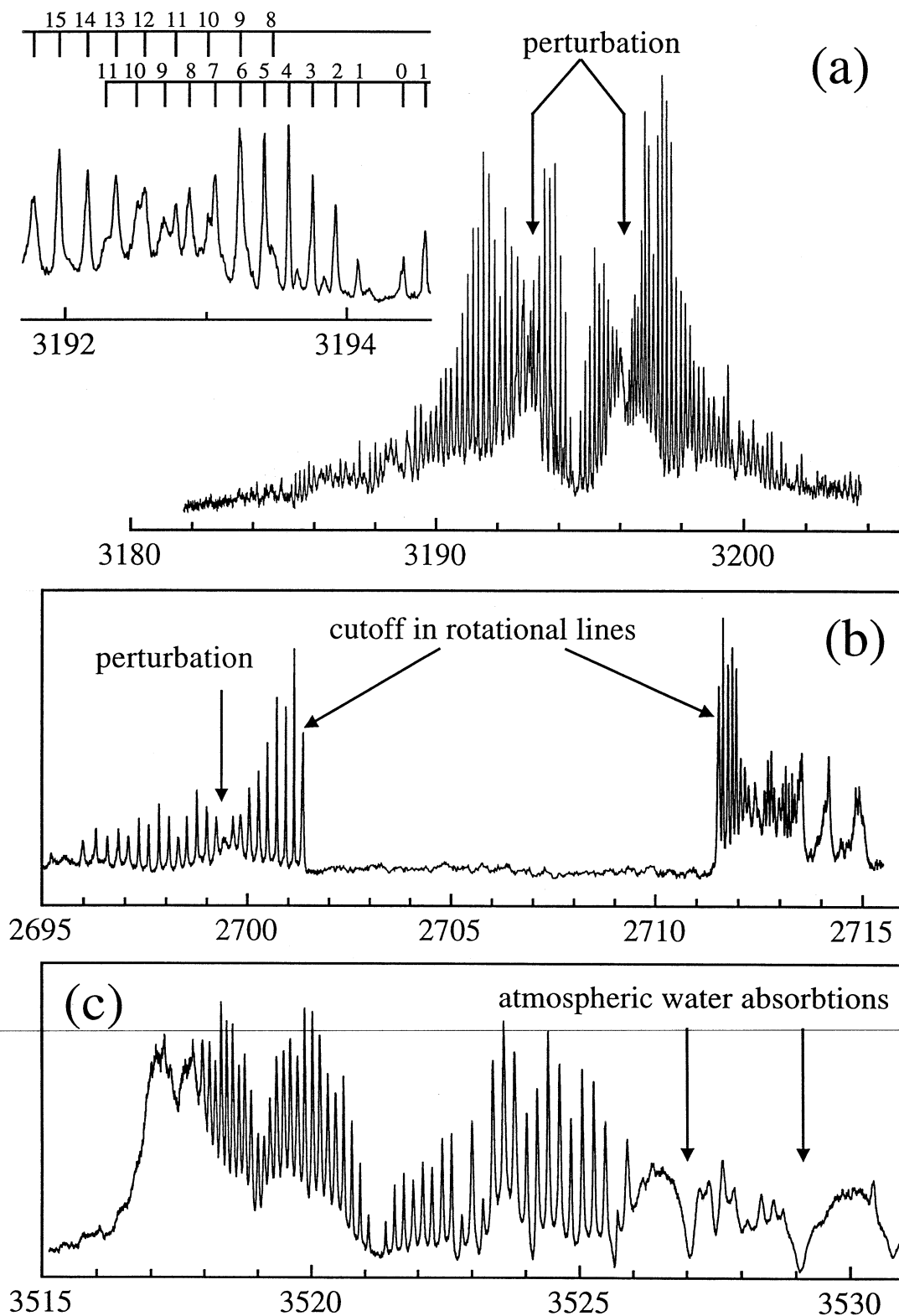


Figure 7.22(b) shows another example of anomalous behavior of rotational lines in certain bands. Four bands are of this type and all of them are located at low frequency edge of the spectrum. The peculiarity here is that the transitions into levels below certain J' , which is different for each band, are completely absent. For example for the band shown in figure 7.22(b) the first lines that are observed are P(32) and R(30) (rotational assignment is discussed later). These bands too are not free from the isolated perturbations as indicated in the figure. The third type of strange behavior is presented in figure 7.22(c) and involves sudden disappearance of high J rotational transitions. This can possibly be accounted for by perturbations but it may as well be due to J dependent line broadening. The later phenomenon has been observed in the spectra of certain neutral Van der Waals complexes excited above dissociation threshold [242-246]. Also many bands in the spectrum are broadened much more extensively up to the level of washing out the rotational structure completely so it is not surprising that some rotational transitions do not have laser limited linewidths. Apart from this, there are additional complications in the spectrum of the Ar-HN₂⁺ complex. Here and there relatively sharp features are found that can possibly be interpreted as Q branches of some weak perpendicular transitions (there are two of them in figure 7.22(b)). The high frequency sides of strongest transitions are infested with a number of weak unassigned lines most probably originating from sequence bands of some sort. And the last but not least complication is the fact there is no obvious pattern in the distribution of vibrational bands in the spectrum, as one can see from figure 7.21, the intensities of the bands are rather jumbled too. Taking into account these factors full understanding of the spectrum seems to be a fairly remote goal at this stage. Nevertheless a number of useful

conclusions about this interesting complex can be drawn from the available experimental data already now and this is done below.

Figure 7.22: Selected bands out of the Ar-HN₂⁺ spectrum

Three selected bands out of the vibrational predissociation spectrum of Ar-HN₂⁺. Anomalous behavior of rotational lines observed in these three bands is encountered in other rotationally resolved transitions of the complex too. See text for details.

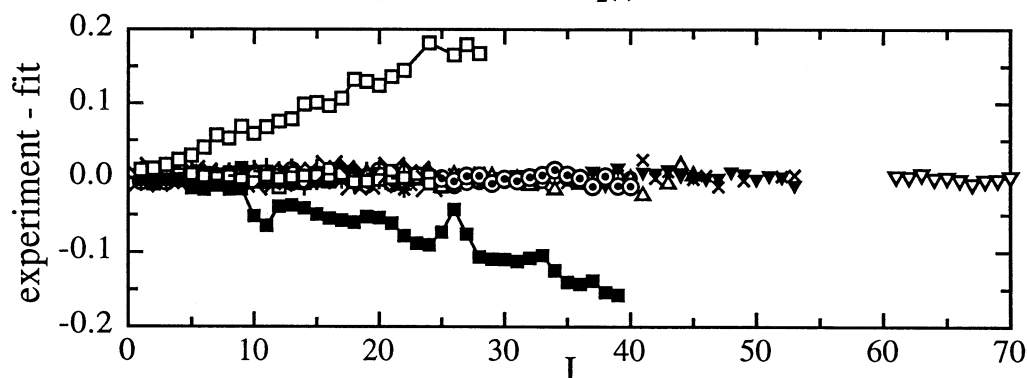


7.6.3. Ground state rotational constants

The treatment of the rotationally resolved bands started from the analysis of their lower state combination differences. Firstly they were calculated and compared for the bands with no missing J transitions, i.e. the four bands of the type shown in figure 7.22(b) were not included. For 10 bands analyzed in this way the lower state combination differences were identical within the precision of the experiment indicating that the transitions most probably shared a common lower vibrational state. We presume that this state is the vibrationless ground state of the complex, because hot bands have rarely dominated the spectra of other proton bound complexes generated in the cluster ion source (the case of Ne-HN₂⁺ complex represents a peculiar exception). Using the average of the lower state combination differences and assuming that the bands with missing J levels originate from the ground state of the complex as well, a rotational assignment of these bands was attempted. For three out of four such bands the assignment could be readily done, however the fourth one had an incompatible set of lower state combination differences. Thus out of 14 rotationally resolved bands considered here 13 appeared to share a common lower vibrational state. Lower state combination differences from these 13 bands were weighted according to the respective band intensities and quality of the calibration and averaged. This procedure provided data for J ranging from 1 to 70 and fitting them to a standard linear molecule expression gave the rotational constants $B''=0.080862(15)$ cm⁻¹ and $D''=5.25(20)\times 10^{-8}$ cm⁻¹. The error in brackets represent 2 σ limits in the last two digits.

Figure 7.23: Ar-HN₂⁺ combination differences

Deviation between the experimental ground state combination differences $\Delta F''_2(J)$ obtained from the various rotationally resolved bands and those calculated from the B'' and D'' constants given above. Similar deviations are also given for a couple of vibrationally excited states to show that their $\Delta F_2(J)$ is markedly different from $\Delta F''_2(J)$.



To appreciate how different the lower state rotational constants are from the ones for upper states one can take a look at figure 7.23 which shows the deviation between the experimentally observed lower state combination differences and the ones calculated from the above constants and similar deviations calculated for a couple of selected upper vibrational states. In fact not only these two but all the upper state combination differences are markedly different from the lower state ones. Thus one can be pretty confident that even with the relatively low resolution of the laser different vibrational states can be recognized on the basis of comparison of their combination differences. So far only in the case of Ar-HCO⁺ a hot band was found to have the lower combination differences virtually identical to those of the ground state of the complex but the assignment there is still questionable and it can be considered as a rare exception.

7.6.4. Rotational fits and vibrational origins

Upper state rotational constants and vibrational origins are obtained by fitting the experimental line positions for a given transition to a pseudodiatomic expression (4.3) with the lower state rotational and centrifugal distortion constants held fixed on the values obtained from the ground state combination differences. For bands containing perturbed

lines this procedure results as a rule in a poor fit quality. Since the present amount of data is clearly insufficient for a proper deperturbation treatment the perturbed bands are analyzed in a brutal way by eliminating the perturbed area from the fit. Unfortunately for certain bands it is not easy to decide which levels are perturbed more and which less and for these all lines are fitted despite the resulting high standard deviations of the fits. For bands with missing J levels there is still another problem of relatively large uncertainties in the origin values that result from the fact that they are most sensitive to the transitions involving low J levels. To minimize the influence of the correlation between different fit parameters the value of the upper state centrifugal distortion constant D' was often constrained to that of the ground state of the complex. For strongly perturbed bands releasing this parameter in the fit usually resulted in either unphysically large or even negative value of D'.

Table 7.15: Ar-HN₂⁺ rovibrational constants

Molecular constants (in cm⁻¹) determined for the band of Ar-HN₂⁺ observed in the photodissociation spectrum. Except for the first two rows of the table the constants refer to the upper vibrational states. Ground state constants were obtained from the combination difference analysis described in the text and they were held fixed in the fits of the transitions originating from the ground state.

band	perurbations	fitted J range	origin	B	D ×10 ⁻⁸	χ ² ×10 ⁻³
ground state	no	1-53; 61-70	-	0.080862(15)	5.25(20)	0.6
v ₁ +v _s +v _b -v _b	?	all	2496.62(8)	B'=0.08141 B''=0.08103	D'=D''= 5.25*	33
v ₁ +v _s (A band)	at J' > 76	J'=61-75	2505.4(2)	0.08177(5)	5.25*	0.2
(B band)	J' ≈ 40	J'=31-37	2707.34(3)	0.08004(5)	5.25*	0.4
v ₁ +2v _s (C band)	many J'	J'=18-49	2755.61(5)	0.08065(5)	5.25*	100
2840 cm ⁻¹ band	J'=24	J'≤20	2839.80(1)	0.08257(4)	5.25*	1.4
v ₁ +v ₂ (l'=1) [§]	J'=11 in PR	J _{PR} '≤6; Q all	2940.45(2)	0.0821(2)	11(1)	1.4
v ₁ +3v _s	many J'	all	2966.04(2)	0.08016(5)	12(2)	12
3071 cm ⁻¹ band	J'≥20	J'≤15	3070.89(1)	0.0816(1)	5.25*	0.4
3078 cm ⁻¹ band	no?	all	3077.96(1)	0.0807(2)	58(5)	1
3195 cm ⁻¹ band	J'=7+12	all	3194.6(2) [¥]	0.0808(2)	5.25*	2200
3365 cm ⁻¹ band	J'≥ 24	J'=2-20	3364.90(1)	0.07913(5)	5.25*	0.9
⊥. band	-	unresolved	3398.40(3)	-	-	-
⊥. band	-	unresolved	3399.06(3)	-	-	-
paral.band	-	unresolved	3419.0(1)	-	-	-
3508 cm ⁻¹ band	J'=15+18	J'≥29; J'≤5	3507.53(2)	0.0809(1)	9(2)	2
3521 cm ⁻¹ band	no?	J'≤15	3521.23(1)	0.0823(1)	5.25*	0.8
3623 cm ⁻¹ band	J'≥ 23	J'≤15	3623.47(2)	0.0819(2)	5.25*	1.9
paral.band	-	unresolved	3853.3(1.5)	-	-	-
2v ₁	-	unresolved	3888.9(4)	-	-	-
paral.band	-	unresolved	3955.0(4)	-	-	-
paral.band	-	unresolved	3987.2(5)	-	-	-
paral.band	-	unresolved	4379(11)	-	-	-
paral.band	-	unresolved	4598.2(6)	-	-	-
3v ₁	-	unresolved	5098.9(4)	-	-	-
paral.band	-	unresolved	5289.0(4)	-	-	-

* kept fixed on the ground state value; [§]q' changes from -1×10⁻³ to +2×10⁻⁴ depending on Q branch J assignment. For the assignment given in table A18 and v, B',D' parameters from this table q'=-2×10⁻⁴; [¥]average of P(1) and R(0) is at 3194.55 cm⁻¹

There is only one perpendicular band in the spectrum and it has a partially resolved Q branch. Unfortunately a strong perturbation in the e rotational manifold (accessed in P and R branch transitions, (l'=1)←(l''=0) transition is assumed) at around J'=11 as well as possible influence of l-type doubling in the upper state precludes unambiguous numbering of the Q branch lines. Assignments contained in table A18 are preferred since they give the best fit to the Q branch profile calculated at reasonable temperatures and the least deviation in the combined fit for Q branch lines and P/R branch transitions terminating in low J levels (J_{PR}'≤6). The Q branch numbering can easily be shifted by as much as ±2 without affecting the quality of the combined fit too much since parameters D' and q' (describes l-doubling)

are correlated. Additional information about the expected magnitudes of q' and D' is required to label the Q branch lines more precisely. Somewhat better resolution would certainly help too. At this stage the obtained estimates of the vibrational origin and upper state rotational constant provide sufficient basis for the discussion of the vibrational assignment of this band.

Another band deserving a special attention is one of the four transitions with missing low J levels with origin at around ≈ 2497 cm⁻¹. According to the combination difference analysis the transition does not originate from the ground state of the complex. To obtain rotational numbering for this band the following approach was adopted. First it was assumed that for this band (as for the other three of this type) the first observed rotational transitions in P and R branches terminate in one and the same J_0' level in the upper state. This fixes the relative numbering in the two branches. Then different values for J_0' were assumed and for each one, both lower and upper state combination differences were calculated and compared with those for the other observed vibrational levels. As can be seen from inspection of figure 7.23, combination differences for different vibrational states of Ar-HN₂⁺ deviate from each other only for higher J values while for low J they are roughly of the same order of magnitude. Only for one choice of $J_0'=41$ the lower and upper combination differences of the 2497 cm⁻¹ band seemed to converge to the right point and this value of J_0' was selected to fix the absolute J numbering of rotational lines. The assignment should be essentially correct unless there is a massive perturbation of J' or J'' levels below J=41. Another observation that contrasts this band to the others is small splitting of rotational lines in both P and R branches. The size of the splitting is not correlated with either J' or J'' which signifies that it does not result from a perturbation in either lower or upper vibrational state. Taking into account additional fact that there is no sign of lines in this frequency range, that could belong to the possible Q branch of this transition, one can assume that this band is of the type $l'=l''\neq 0$. Though parallel bands of this type do contain Q branch lines, these are not expected to be strong for higher J transitions. The best assignment for this band would probably be either $\nu_0+\nu_b-\nu_b$ or $\nu_0+\nu_2-\nu_2$ sequence, where ν_b and ν_2 are the inter- and intra-molecular bends, and ν_0 is the vibration corresponding to the strong nearby transition with origin at 2505.4 cm⁻¹.

Results of the fits of all transitions are gathered in table 7.15. For every band the table indicates which upper state J levels are perturbed, and which transitions were selected for the fit. Vibrational assignments given in the first column of the table are discussed later. Vibrational origins of unresolved bands estimated from the analysis of the bands' profiles are listed in the table as well. A number of very weak transitions are not included here.

7.6.5. Intermolecular binding energy of the complex

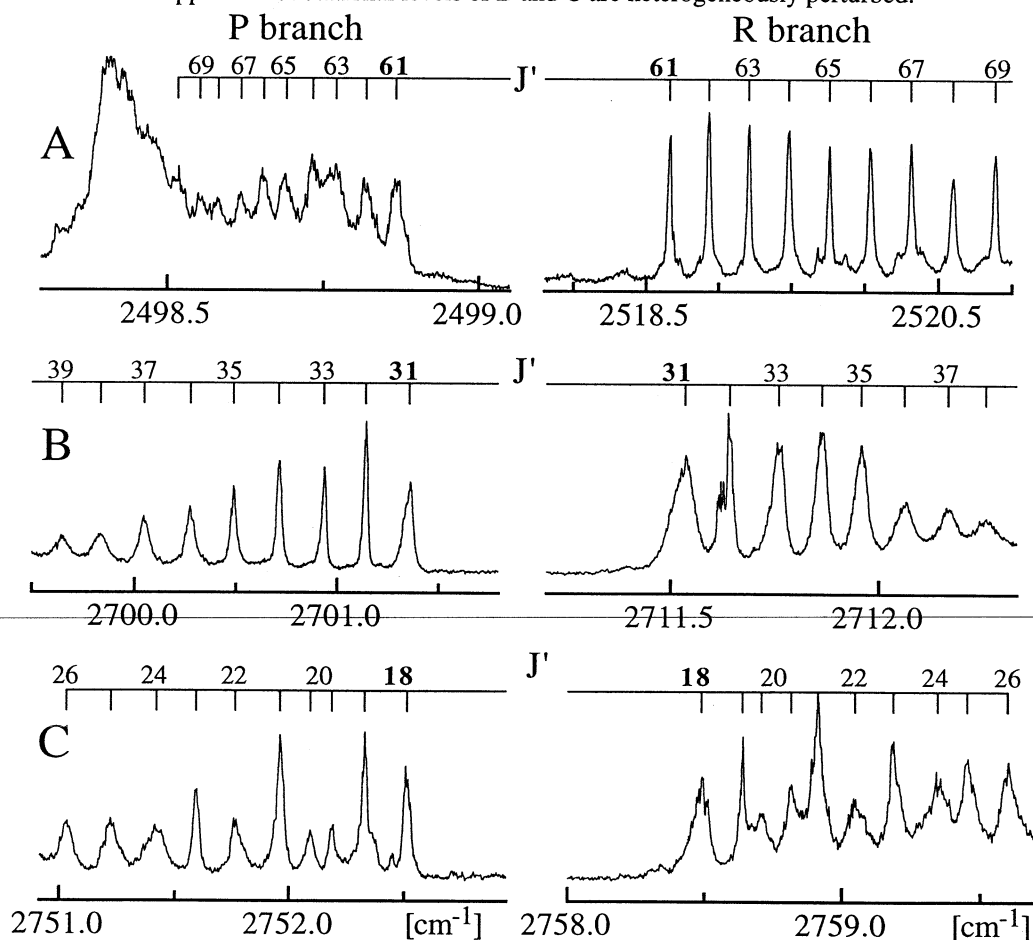
As mentioned above, four bands observed at lower energy have an unusual structure, with transitions into levels below certain J' being completely absent. The bands lack Q branch transitions for the observed J ranges and are probably of parallel type. Three of the bands, denoted A-C, apparently originate from the ground state of the complex, and are shown in figure 7.24. Their origins are determined respectively as $\nu_0=2505.40\pm 0.10$ (band A), 2707.34 ± 0.05 (B), and 2755.62 ± 0.05 cm⁻¹ (C). Bands A and C are the strongest ones observed in the examined spectral range. Comparison with the *ab initio* predictions for ν_1 and ν_s of respectively 2330 ± 100 and ~ 210 cm⁻¹ [234] suggests an assignment of A and C to the combination bands $\nu_1+\nu_s$ and $\nu_1+2\nu_s$, where ν_s is the intermolecular stretch mode. This provides rough estimates of $\nu_1\leq 2255$ cm⁻¹ and $\nu_s\geq 250$ cm⁻¹ for the fundamental frequencies. The combination differences and an additional evidence given below are consistent with the assumption that the less intense band B ($\leq 10\%$ of band C) originates from the vibrational ground state as well. Though its upper state assignment is not definitive at the present stage, it does not influence the outcome of the analysis presented in this section. The fourth band with missing low J' levels (not shown in the figure, $\nu_0\sim 2496.5$

cm⁻¹) has a different set of lower state combination differences and, as mentioned above, must be a sequence band associated with band A. The relative positions of the upper state rotational energy levels of the bands A-C are shown in figure 7.25. Although their vibrational origins are quite different, the first *J'* levels subject to photodissociation are roughly at the same total energy, being almost coincident for bands B and C. This observation is attributed to vibrational predissociation of the upper rovibrational levels of the complex leading to cold HN₂⁺ fragments.

Upper rovibrational levels with *J'* ≤ 60, 30, and 17 for bands A, B, and C respectively do not appear in the corresponding photodissociation spectra. This indicates predissociation lifetimes for these levels of at least 50 μs, a typical flight-time through the octopole ion guide. Slowing the ions down in order to increase the residence time in the octopole region above 1 ms did not affect the photodissociation spectra. The most probable conclusion is that these *J'* levels are either *intrinsically stable* with respect to dissociation or have to overcome an impenetrably thick centrifugal barrier. This presumption provides an upper limit for the binding energy of the Ar-HN₂⁺ complex based on the energy of the lowest observed rovibrational level capable of predissociation, $D_0 < 2783.23 \pm 0.03$ cm⁻¹ (figure 7.25). If the resulting HN₂⁺ fragments were rotationally and vibrationally cold and the relative kinetic energies of the recoiling particles were small then the quoted value would be quite close to the real dissociation energy.

Figure 7.24: J-selective predissociation in the Ar-HN₂⁺ spectrum

Three selected bands in the IR vibrational predissociation spectrum of Ar-HN₂⁺ showing the onset of dissociation at *J'*=61, 31, and 18 for the bands A ($\nu_1+\nu_2$), B (unassigned), and C ($\nu_1+2\nu_3$), respectively. Upper states rotational levels of B and C are heterogeneously perturbed.



The fact that the energy intervals bracketed by the first dissociating *J'* level and last non-dissociating *J'* level for the bands A-C do not overlap (figure 7.25) is indicative of

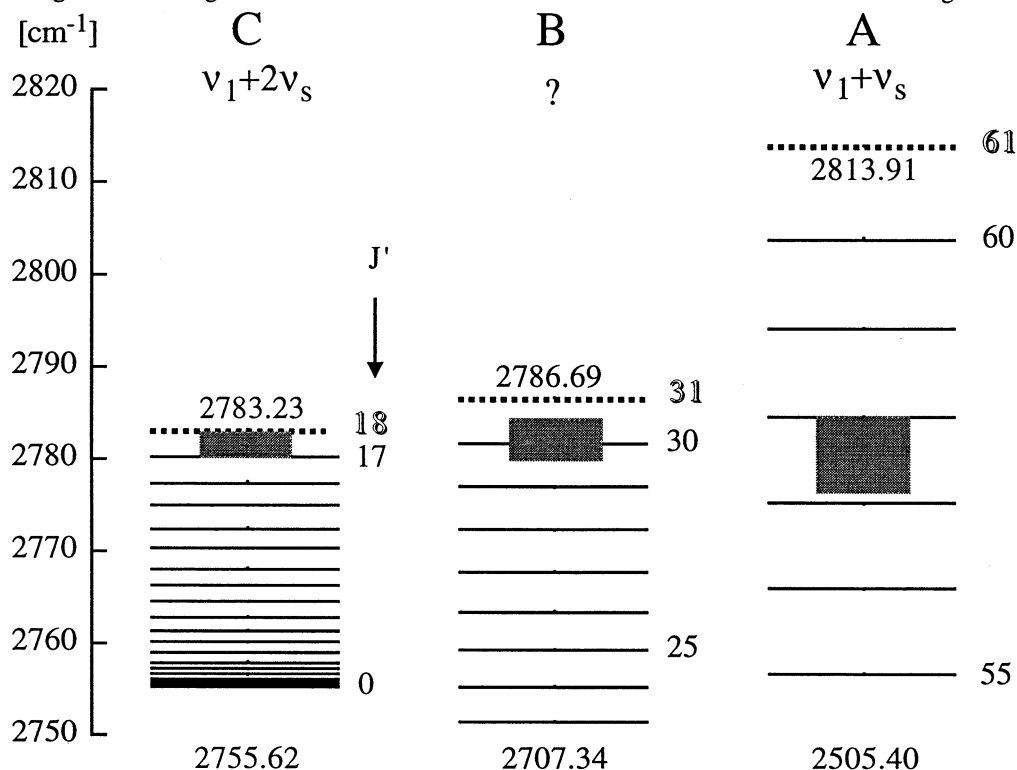
different degrees of internal and kinetic energy in the photofragments. This difference is explicable from a mechanistic viewpoint where the fragment kinetic energy release is related to the initial angular momentum of the rotating complex by classical conservation laws. Predissociation of Ar-HN₂⁺ arises from coupling of the initially prepared quasibound levels with continuum states. Neglecting tunneling, the first available continuum channel occurs at the top of the J dependent centrifugal barrier of the vibrational ground state. Assuming for the moment that the HN₂⁺ fragments possess no vibrational and rotational energy, one can estimate the energy necessary to surmount the rotational barrier by considering the long range part of the intermolecular potential (V_{LR}). To a first approximation this contribution is given by the sum of the rotational and charge induced dipole potential terms

$$V_{LR} = \frac{\hbar^2 J(J+1)}{8\pi^2 \mu R^2} - \frac{\alpha q^2}{2(4\pi\epsilon_0)^2 R^4} \quad (7.4)$$

where μ is the reduced mass of the Ar-HN₂⁺ pseudodiatomic, R the intermolecular centre of mass displacement and α the polarizability of the Ar atom ($1.83 \times 10^{-40} \text{ C}^2 \text{m}^2 \text{J}^{-1}$). Here we have assumed that the centre of charge coincides with the HN₂⁺ centre of mass.

Figure 7.25: Determination of the Ar-HN₂⁺ binding energy

Rovibrational energies of the upper vibrational states accessed in the transitions A, B, and C. Energy levels shown by solid lines do not predissociate: these include levels up to $J'=17, 30,$ and 60 for C, B, and A respectively. Predissociation starts from levels represented by dotted lines (i.e. $J'=18, 31, 61$). The dissociation threshold is believed to be located somewhere within the shaded areas which represent differences in energy levels of $J'=17$ and $18, 30$ and $31, 60$ and 61 for bands C, B, and A corrected by the respective centrifugal barrier heights. The numbers below each manifold are the bands' vibrational origins in cm^{-1} .



According to this approximation, the rotational barriers occur at $R \sim 23.6, 13.8,$ and 7.1 \AA for $J=18, 31,$ and 61 , with respective heights of $0.3, 2.6,$ and 37.8 cm^{-1} . Adjustment of the dissociation thresholds for the pseudodiatomic kinetic energy releases in all three cases leads to excellent agreement for the intervals calculated from the bands B and C. On the other hand, the agreement is not so good for band A. However here, because of the high angular momentum involved, the rotational barrier is much closer in and the long range approximation to the potential is less likely to be valid. It is worth noting however, that if the centre of charge is placed anywhere between the midpoint of the NH bond and the central N atom (this position is expected from the Mulliken analysis), better agreement

between all three energetic limits is obtained. Figure 7.25 demonstrates perfect overlap of the energy intervals between $J'=17-18$, $30-31$, and $60-61$ for bands C, B, and A, corrected by the centrifugal barrier heights calculated with the charge located on the central nitrogen. Practically the same result is obtained when the charge distribution is taken from the distributed multipole analysis over the atomic centres (0.244 e on the terminal N, 0.389 e on the central N, and 0.366 e on H [247]) Overlap of the three energy intervals is consistent with the previous assumption that these bands share the same lower state and dissociate in the same vibrational state of the HN₂⁺ fragment.

Finally, the possibility is considered that the HN₂⁺ fragment is formed in a vibrationally excited state. It appears very unlikely that the fragment can be in the ν_3 state (2258 cm⁻¹ [147]), because this would lead to a binding energy of less than 530 cm⁻¹, a value far away from the *ab initio* estimate of 3000 cm⁻¹ [234], and also inconsistent with the binding energies for related proton bound species He-HN₂⁺ (~380 cm⁻¹ [247]) and Ar-HCO⁺ (1100-1500 cm⁻¹ [233]) which are expected to be less strongly bound. Excitation of ν_2 (685 cm⁻¹ [148]) in the fragment also appears to be somewhat unlikely given the observations of a sharp cut-off at particular J' values and the spectra's unchanging appearance when the complexes are trapped for up to 1 ms. Closing of the HN₂⁺ (010) channel below a particular J' value would still allow the complex to dissociate to HN₂⁺ (000). The absence of lower J' lines (even for 1 ms trapping times) would imply that this process must be very much slower than dissociation into HN₂⁺ (010). Excitation of ν_2 in the fragment HN₂⁺ for all three bands (A-C) would shift the binding energy interval by roughly 685 cm⁻¹ down to 2100 cm⁻¹ which is again less consistent with the theoretical prediction [234].

In conclusion of this section, under the presumptions outlined above the range for D_0 can be confined to the interval between $J'=0$ level (2783.2 cm⁻¹), which has no angular momentum restriction for the dissociation into rovibrationally and translationally cold fragments, and $J'=18$ (2755.6 cm⁻¹) of the C band (figure 7.25). If centrifugal barrier corrections are taken into account even narrower interval for the dissociation energy of the Ar-HN₂⁺ complex is obtained, $D_0=2781.5\pm 1.5$ cm⁻¹, again taken from the C band. This value is comparable to binding energies obtained for other proton-bound heterodimers of similar composition, for example Ar-H₃⁺ where D_0 is of the order of 2700 cm⁻¹ [36]). The presented experimental values for rotational constants and dissociation energy suggest Ar-HN₂⁺ to be a suitable system for testing quantum chemical methods applied to charged complexes.

7.6.6. Vibrational assignment

Vibrational assignment of transitions in Ar-HN₂⁺ spectrum relies on comparison with related systems, particularly with Ar-HCO⁺, as well as on the results of the recent *ab-initio* calculation of Kolbuszewski [234]. It is expected that the spectrum should be dominated by the overtones and combination bands involving for the most part only highly IR active vibrations. According to the *ab-initio* calculation out of the five normal vibrations of the complex ν_1 and ν_5 fundamentals have the largest dipole transition strengths. In addition large anharmonicity of the NH stretching coordinate should make its overtones relatively strong as well. The vibrations ν_3 and ν_2 should have intermediate intensities and may possibly be observed in combination with ν_1 . The intermolecular bending vibration is predicted to have a considerably smaller transition strength and may escape observation. These conclusions are in fair agreement with the experimental observations for the other complexes. Their spectra are indeed dominated by a strong ν_1 band, with $\nu_1+\nu_5$ being the next in the strength. For Ar-HCO⁺, the $\nu_1+\nu_2$ and $2\nu_1$ transitions were quite strong too. One should note, however, that specific spectroscopic behavior cannot be always smoothly

transferred within this row of complexes and conclusions based solely on comparison should be accepted with caution. For example $\nu_1+\nu_b$ combination band is relatively strong in the spectrum He-HN₂⁺ complex while no sign of this band is observed in the spectra of Ne-HCO⁺ and Ar-HCO⁺ complexes. Besides the spectra of Ar-HCO⁺ and Ne-HN₂⁺ are strongly affected by the interaction of different vibrational states (perturbations) and they are not the best examples for studying intensity distributions in the IR spectra.

The ν_1 fundamental of the Ar-HN₂⁺ complex is not observed in this experiment but it may be estimated from several sources. The first and probably a fairly accurate guess is the *ab-initio* result [234] of $2330\pm 100\text{cm}^{-1}$. As mentioned above this value is consistent with the result of linear extrapolation of the dependence of ν_1 red shift in He-HN₂⁺ and Ne-HN₂⁺ against the differences in respective proton affinities of Rg and N₂, though the latter derivation should not be taken too seriously. Other estimates may be obtained from consideration of potential combination bands of ν_1 with itself and with the other vibrations of the complex. The most obvious choice here is the $\nu_1+\nu_2$ combination, since it was observed with a reasonable intensity in Ar-HCO⁺ and since it should have a distinguished perpendicular appearance. The strongest perpendicular band in the spectrum appears to be the one with origin at 2940.45cm^{-1} . If it is assigned to the $\nu_1+\nu_2$ combination one can obtain an upper limit of 2255cm^{-1} for ν_1 from known ν_2 frequency of ca. 685cm^{-1} in free HN₂⁺. The notion of the upper limit comes from the fact that in the complex, the ν_2 frequency should be somewhat higher than in the free monomer. In free HCO⁺ ion the cross-anharmonicities between ν_1 and ν_2 tend to push the $\nu_1+\nu_2$ combination in the direction of lower frequencies. However in Ar-HCO⁺ complex $\nu_1+\nu_2$ band has about 54cm^{-1} higher frequency than the sum of free monomer ν_1 and ν_2 fundamentals. Assuming the effect of a similar order of magnitude in Ar-HN₂⁺ allows to place an estimation of the ν_1 frequency in the complex at $\approx 2200\text{cm}^{-1}$. If this value is correct the *ab-initio* prediction must overestimate the frequency somewhat.

Next band that may be considered to estimate the ν_1 position is $\nu_1+\nu_s$ combination which is expected to be very strong in the spectrum. The strongest transition observed in the spectrum of Ar-HN₂⁺ above 2470cm^{-1} is the A band (the label used in previous section) with origin at 2505.4cm^{-1} . The strength of the band is exemplified by the fact that its head formed in the P branch above $J>70$ (!) is the strongest feature in the unnormalized spectrum. The R branch visible for $J''\geq 60$ is quite strong too. If the spectrum is corrected for laser power the band gains even higher relative intensity. The next band in relative strength, labeled as C in the previous section, lies at 2755.6cm^{-1} . Considering the separation of $\approx 250\text{cm}^{-1}$ between A and C bands and also the intensity dropping towards higher excitation frequencies one is encouraged to assign them as two successive members of the progression in intermolecular stretching mode. *Ab initio* calculation predicts the corresponding harmonic frequency in the *ground state* to be around 210cm^{-1} [234]. If one inserts the ground state B and D constants into Millen's expression (4.10) a value of the same order of magnitude (195cm^{-1}) is obtained. Since a substantial increase in ν_s frequency is expected on going from $\nu_1=0$ to $\nu_1=1$ state (red shift in the ν_1 vibration may be correlated with strengthening of the intermolecular bond) the value of the order of 250cm^{-1} does not seem to be too unreasonable for the $\nu_1=1$ state intermolecular stretching frequency. The bands A and C are assigned respectively as $\nu_1+\nu_s$ and $\nu_1+2\nu_s$ combinations. Assignment of A band to $\nu_1+2\nu_s$ would shift the ν_1 frequency down too much in comparison with *ab initio* and other predictions. On contrary with the present assignment one estimates the upper limit for ν_1 to be at 2255cm^{-1} in very good agreement with the result obtained from the $(\nu_1+\nu_2)-\nu_2$

difference. Corrections for the expected anharmonicity in the intermolecular stretching vibration (few tens of wavenumbers) will shift this upper limit down towards the previous estimation of 2200 cm⁻¹. With anharmonic corrections of the same order of magnitude the band at ≈2966 cm⁻¹ (also reasonably strong but weaker than either $\nu_1+\nu_s$ and $\nu_1+2\nu_s$) can be provisionally assigned as the $\nu_1+3\nu_s$ combination. To summarize the discussion in this paragraph the value of 2220±40 cm⁻¹ is our best estimation for the complex's ν_1 frequency.

With estimated ν_1 frequency one can try to filter its overtones out of the spectrum. Certainly the strong anharmonicity of the NH stretching coordinate should be taken into serious consideration. In his paper, Kolbuszewski [234] generated effective potentials for the central hydrogen motion under the conditions when the heavy atoms (Ar and both nitrogen atoms) are clamped at physically reasonable separations and solved the vibrational problem numerically to generate the vibrational energy levels. His result for the separation between Ar and N closest to the experimentally determined value (Exp.=2.93 Å, his=2.92 Å) is 2232 and 1655 cm⁻¹ for the spacing between the levels with $\nu_1=0$ and 1, and respectively between $\nu_1=1$ and 2. Separation between $\nu_1=2$ and 3 is expected to drop down even further. Thus position of the first overtone in ν_1 can be estimated to be around 3900 cm⁻¹ and $3\nu_1$ may possibly be situated somewhere at around 5000 cm⁻¹. There two unresolved bands of comparable intensities and one weak band at around 3900 cm⁻¹ but fortunately there is only one reasonably strong and isolated band at 5099 cm⁻¹ (also unresolved) which seems to be the best candidate for $3\nu_1$. Out of the bands lying around 3900 cm⁻¹ the stronger one is situated at 3889 cm⁻¹. It has a more prominent head in the P branch than its somewhat weaker neighbor at 3955 cm⁻¹ and for this reason it is assigned as the $2\nu_1$ transition, though in the absence of more reliable predictions this assignment is not quite certain. If the assignment is accepted and the energies of the states $\nu_1=0,2$, and 3 (0, 3899, and 5099 cm⁻¹) are interpolated with a quadratic polynomial (i.e. only first order anharmonicities included) the energy of $\nu_1=1$ state is predicted to be at ≈ 2200 cm⁻¹ in agreement with the estimation made in the previous paragraph. Anharmonic correction in this case is as high as $\chi^2 \approx -250$ cm⁻¹, about 4 times large than in the free monomer (-65.6 cm⁻¹ [151])! Note that respective anharmonicity constant was only 50% larger for Ar-HCO⁺ complex in comparison with free HCO⁺. The effects of anharmonicity of the NH stretching potential seem to be extreme in the Ar-HN₂⁺ complex.

The hot band with the origin ≈2496 cm⁻¹ can also be assigned. As argued above on the basis of the band position and splittings in P and R branch lines the band represents a sequence involving a bending state build on the strong $\nu_1+\nu_s$ transition, i.e. $\nu_1+\nu_s+\nu_x-\nu_x$ where x stays for either inter- or intramolecular bend. Since the low J transitions (terminating in $J' \leq 40$) do not show up in this band one can apply a strategy similar to that used in section 7.6.5 to obtain the estimate for the ν_x fundamental from the band's origin, rotational constants, and complex's dissociation energy. After centrifugal barrier corrections the estimated value for ν_x amounts to 150-160 cm⁻¹, thus ν_x is unambiguously identified as the intermolecular bend. Curiously, the $\nu_1+\nu_s+\nu_b-\nu_b$ combination is blue shifted by ≈9 cm⁻¹ with respect to the $\nu_1+\nu_s$ transition indicating the anticipated softening in the bending coordinate when it is excited simultaneously with ν_s .

Assignment of the remaining bands is quite challenging at the present stage of the analysis. Particularly disturbing is the fact that two relatively strong bands at 3521 and 3623 cm⁻¹ are left unassigned. And in fact, the number of the infrared active transitions for the overtone and combination bands range in Ar-HN₂⁺ is really astounding. Nothing like that

has been observed for complexes with somewhat lower binding energies like H₂-HCO⁺ and Ar-HCO⁺. For complexes of similar strength like H₂-HN₂⁺ and ArH₃⁺ a number of unassigned bands is observed as well, but still, Ar-HN₂⁺ seems to be the champion (ArH₃⁺ is not presented in this work. It absorbs with different efficiency at quite a few wavenumber ranges within the accessibility range of the OPO laser). It is possible that highly excited combination bands become allowed by means of the large anharmonic couplings between different vibrations. Since possible combinations of intra- and intermolecular vibrations that can fall in this range are quite numerous and since the assignment of some other bands (e.g. 2ν₁) is already quite speculative and relies very much on the ab initio studies the assignment of the remaining bands (see list in table 7.15) is not attempted at present. The efforts of spectroscopists should now be concentrated on obtaining the information about the complex's fundamental vibrations and simpler combination bands below 2500 cm⁻¹ by direct absorption spectroscopy.

7.6.7. Conclusions

As the result of this preliminary study of Ar-HN₂⁺ complex the following conclusions have been arrived at.

- (1) Intermolecular binding energy of the complex is found to be 2781.5±1.5 cm⁻¹.
- (2) Rotational constants of the complex were determined with sufficient precision to start search for its microwave transitions (B''=0.080862(15) cm⁻¹ and D''=5.25(20)×10⁻⁸ cm⁻¹). The rotational constants correspond to the center of mass separation between Ar and HN₂⁺ of 3.43 Å and intermolecular force constant of ≈38 N/m.
- (3) Intramolecular NH stretching fundamental is predicted to occur at 2220±50 cm⁻¹.
- (4) Intermolecular stretching frequency in the ν₁=1 state is at least 250 cm⁻¹.
- (5) Intermolecular bending frequency is estimated to be in the range of 150-160 cm⁻¹. This relatively large frequency corresponds to the average intermolecular bending angle $\langle \phi^2 \rangle^{1/2}$ of only 8° (7.2-7.3).
- (6) Compared to the other Rg-HCO⁺/HN₂⁺ complexes (Rg=He, Ne, Ar) Ar-HN₂⁺ appear to possess the strongest and least flexible intermolecular bond.

8. The Rg-NH₄⁺ complexes

8.1. Overview

Two ionic complexes, He-NH₄⁺ and Ar-NH₄⁺, stay as outsiders in this thesis in the sense that for them, the spectroscopic manifestations of anisotropic intermolecular interactions are much more prominent than for any of the dimers described above. In the former the barrier for the internal rotation of NH₄⁺ unit is sufficiently small and the spectrum of the complex closely resembles that of the monomer. In the latter the barrier is higher, but the signatures of the tunneling motion of the core are readily apparent from splitting of the Q branches of the ν₃ transition. Neutral van der Waals complexes, containing tetrahedral molecules, feature this sort of behavior as well. Among them, those involving a rare gas atom as a ligand have been studied most extensively, particularly in the region of the triply degenerate ν₃ vibration of the free monomers (Ar/Kr-CH₄ [248], Ar/Ne-SiH₄ [249, 250], and Ar/Kr-SiF₄ [251]). According to the available theoretical models [252-254], a reasonable representation of the interaction between the rare gas atom and the tetrahedral molecule is attained by employing a potential involving a few parameters related to the anisotropy of the interaction. The basic assumptions of these models can be summarized as follows. (I) The tetrahedral geometry of the monomer is not distorted upon complexation with the rare gas atom. (II) The intramolecular vibrational degrees of freedom as well as the end-over-end rotation of the complex can be separated in an adiabatic sense from the internal rotational levels of the tetrahedron.

The hamiltonian of the system in a body-fixed representation is written as

$$\hat{H} = \frac{\hbar^2}{2\mu} \left(\frac{(J-j)^2}{R^2} - \frac{\partial^2}{\partial R^2} \right) + H_{\text{mon}} + V \quad (8.1)$$

Here R is a pseudodiatom bondlength, μ is the complex's reduced mass, **J** is total angular momentum of the complex, and **j** refer to that of the tetrahedral subunit. Projection of both **J** and **j** onto the body-fixed axis is called K. The first term of the hamiltonian describes the end-over-end rotation of the complex, with energy levels described by a simple power expansion in J and K

$$E_{\text{rot}} = B[J(J+1) - K^2] - D[J(J+1) - K^2]^2 \quad (8.2)$$

The second term accounts for the stretching motion of the pseudodiatom complex. H_{mon} is a standard spherical top hamiltonian for the NH₄⁺ unit. The intermolecular potential V is expanded in a power series

$$V(R\alpha\beta\gamma) = V_0(R) + \sum_i V_i(R) T_i(\alpha\beta\gamma) \quad (8.3)$$

where T_i are symmetric combinations of spherical harmonics of ith. order and α, β, and γ specify the orientation of the spherical top with respect to the body-fixed axes. With the assumptions outlined above, the number of parameters describing the anisotropy of the potential may be considerably reduced. Most significant are: (I) a *vibrational* anisotropy parameter V₂ which is responsible for lifting the three-fold degeneracy of the ν₃ vibration of the free tetrahedral monomer; (II) *rotational* anisotropy parameters (V₃, V₄) that characterize the anisotropy of the intermolecular potential for internal rotation along paths between possible minimum structures (vertex-bound, face-bound, and side-bound geometries) of the complex. Effect of V₃ on the energy levels is such that only its magnitude but not sign can be determined from the spectra [253]. The ionic Ar-NH₄⁺ complex with V₂~90 cm⁻¹ and V₃~220 cm⁻¹ [255] appears to be more rigid than neutral Ar-SiH₄ (V₂~1 cm⁻¹, V₃~60 cm⁻¹

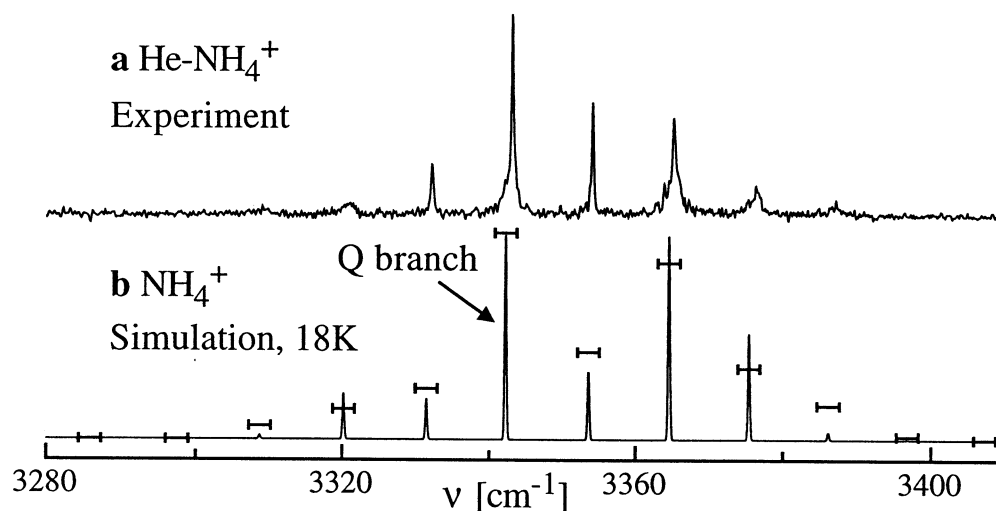
[249]). For the He-NH₄⁺ complex it was not possible to determine such parameters from the experiment. However, the floppiness of the complex could be assessed with help of *ab initio* calculations.

8.2. The He-NH₄⁺ complex

He-NH₄⁺ complexes were produced in an expansion of He, NH₃, and H₂ at a 1000:1:1 ratio and 4-6 bar stagnation pressure. Figure 8.1(a) shows a portion of the experimental IR photodissociation spectrum of the He-NH₄⁺ complex in the region of the triply degenerate ν_3 vibration (t_2) of the free ammonium ion. Observed transition energies are summarized in table 8.1. The illustrated band is the only one observed between 3100 and 3500 cm⁻¹ and consists of a series of regularly spaced peaks separated by 11.12±0.07 cm⁻¹, with decreasing intensities on either side of the central feature at 3343.19 cm⁻¹. The spacings are very close to the value of $B_0+B_1-2B_1\xi_3=11.10$ cm⁻¹ of free NH₄⁺ [189]. The small blue shift of the most intense peak (3343.2 cm⁻¹) with respect to the free ammonium ion ν_3 transition origin (3342.35 cm⁻¹ [189]) and the similarity in the rotational spacings suggest that neither the rotational nor the vibrational motion of the NH₄⁺ ion is strongly affected by the complexation with He.

Figure 8.1: The ν_3 band of He-NH₄⁺

(a) Vibrational predissociation spectrum of He-NH₄⁺ in the region of the ν_3 vibration of free NH₄⁺. (b) Simulated IR spectrum of the ν_3 vibration of free NH₄⁺. For comparison, integrated intensities of the He-NH₄⁺ transitions are indicated by bars.



Evidence for only slightly hindered internal rotation in He-NH₄⁺ arises from examination of the band's rotational structure. For both rigid and semi-rigid atom - spherical top complexes an e-type band (C_{3v}) should be dominated by a series of prominent Q branches ($\Delta J=0$) corresponding to $\Delta K=\pm 1$ transitions, quite similar in appearance to the structure shown in figure 8.1(a). However, the P and R branch transitions due to the changes in the overall angular momentum ($\Delta J=\pm 1$) should also be seen with appreciable intensity surrounding each of the Q-branch peaks. As the angular anisotropy of the intermolecular potential is decreasing quantum numbers j and l (characterizing the angular momentum of the spherical top and the end-over-end rotation of the entire complex, respectively) gain in quality, with l becoming as rigorous as j in the limit of completely free internal rotation. Transitions with $\Delta l=\pm 1$ (leading to the P and R branches) are forbidden in the free rotor limit and should be weak when the potential energy barriers for internal

angular motion are small. The He-NH₄⁺ spectrum *lacks* any discernible structure where the P and R branches might be expected.

Table 8.1: Observed He-NH₄⁺ transitions

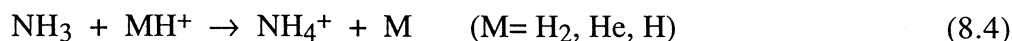
Assignment and line positions (in cm⁻¹) of the experimental spectrum of He-NH₄⁺ (Fig. 8.1(a)). Line positions of NH₄⁺ are intensity-weighted averages over Coriolis splittings (Fig. 8.1(b)).

Transition	NH ₄ ⁺	He-NH ₄ ⁺
P(3)	3308.75	3309.15 ± 0.25
P(2)	20.19	20.95 ± 0.10
P(1)	31.44	32.26 ± 0.03
Q-branch	42.35	43.19 ± 0.03
R(0)	53.63	54.26 ± 0.03
R(1)	64.57	65.26 ± 0.03
R(2)	75.41	76.46 ± 0.10
R(3)	86.13	87.22 ± 0.16

A further effect of the V₃ rotational anisotropy is the splitting of the 4-fold degeneracy of each K level which, in addition to the usual 2-fold degeneracy for levels with K≠0, arises from the fact that the rare gas can be connected to the tetrahedron, either to the faces or to the vertices, in four equivalent ways. For finite anisotropy, tunneling between these equivalent positions results in splittings of the rovibrational transitions. The splitting is negligibly small for a rigid complex, does not exist in a free internal rotor system, and may follow a rather complicated pattern in intermediate cases [253]. This splitting is of the order of 1 cm⁻¹ for Ar-NH₄⁺ (see below), whereas for He-NH₄⁺ no splitting is evident (figure 8.1(a)). The absence of P and R branches and any resolvable Q-branch splittings indicates that the rotational anisotropy is relatively small for the He-NH₄⁺ complex. However from the widths of some of the Q branch features (around 0.5 cm⁻¹), which substantially exceed the laser resolution (0.02 cm⁻¹), it is evident that some amount of hindrance to internal rotation may exist.

Secondly, the vibrational structure of the transition is considered. For a rigid proton bound complex, the triply degenerate ν₃ vibration (t₂/T_d) of the free monomer would be split into perpendicular and parallel components (a₁+e/C_{3v}), both being IR allowed. The magnitude of the e/a₁ splitting and the relative intensities of these two bands can be correlated with the degree of vibrational anisotropy of the intermolecular potential characterized by the parameter V₂ [253]. In case of Ar-NH₄⁺, for which a V₂ value of ~92 cm⁻¹ was estimated, the splitting is approximately 40 cm⁻¹, with transitions to both vibrational levels showing comparable intensities (see below). A further consequence of vibrational anisotropy is that the ν₁ (a₁/T_d) symmetric stretch vibration, which is dipole-forbidden for free NH₄⁺, becomes allowed (a₁/C_{3v}) upon attachment of the rare gas. For Ar-NH₄⁺ this transition appears with appreciable intensity (~10% of the allowed a₁/e components of the ν₃ vibration) reflecting the significant vibrational anisotropy. Thus, for He-NH₄⁺ at least three vibrational bands (a₁+a₁+e/C_{3v}) might be expected in the investigated spectral range. However, only a single perpendicular band is observed indicating a small vibrational anisotropy for the interaction.

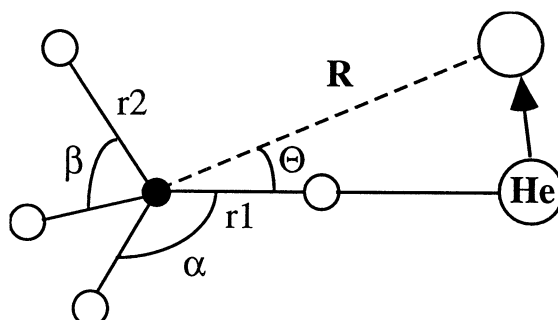
Since the He-NH₄⁺ complex seems to have a reasonably isotropic intermolecular potential it is expected that its spectrum should closely resemble that of the free ammonium ion. It was attempted to predict how the spectrum of free NH₄⁺ generated in our ion source would look like using a simple model. The relative weights for the nuclear sub populations corresponding to A, E, and F symmetries of the rotational levels were assumed to be 5, 2, and 9, respectively. This assumption is fair considering that the ammonium ion is formed directly in the expansion from the ammonia molecule in a proton exchange process



Prior to the expansion the ammonia molecules are fully equilibrated behind the nozzle at a room temperature. For NH₃, with its moderate rotational constants, this correspond to a high temperature limit wherein all possible combinations, eight in total, of projections of the nuclear spins on the reaction coordinate are equally probable. Adding another nucleus will presumably proceed in a statistical fashion creating 16 equivalent nuclear spin projection combinations for the NH₄⁺ ions, i.e. high temperature limited population as well. We note that for this ion the ratio of nuclear state partition functions becomes equal to 5:2:9 with very good precision already when the effective temperature exceeds 80K. As the next approximation, a Boltzmann rotational energy distribution was assumed. Lowest possible rotational level within each nuclear sub population was taken as zero of energy, i.e. $j=0,1,2$ levels for the state with A,F,E rotational symmetries respectively. Rotational temperature was then varied to reproduce the integrated intensities of the He-NH₄⁺ transitions. The best fit (figure 8.1(b), convolution width 0.3 cm⁻¹) shows qualitative agreement with the experimental He-NH₄⁺ spectrum (figure 8.1(a)) and yields a temperature of 18K, typical for ions formed in this ion source.

To test the experimental conclusions about the anisotropy of He-NH₄⁺ potential an *ab initio* calculation of the complex at the MP2 level using the Gaussian 94 package was undertaken. For details of the calculations see ref. [256]. The results of the calculation are summarized below in terms of a coordinate system presented in figure 8.2.

Figure 8.2: Coordinate system for He-NH₄⁺



The vertex-bound structure ($\theta=0^\circ$) was found to be the global minimum, with a radial well depth of $D_e=147$ cm⁻¹ and an equilibrium intermolecular separation of $R=3.17$ Å. As expected, the complexation has little effect on the monomer geometry. A value of 1.020 Å is calculated for the NH bondlength in free NH₄⁺. For the vertex-bound minimum, r_1 increases somewhat (0.0001 Å), while r_2 decreases by similar amount, reflecting a slight tendency for proton transfer from NH₃ to He. The angle α increases a little, while β decreases correspondingly. Analysis of the harmonic molecular vibrational frequencies for the global minimum structure of He-NH₄⁺ indicate that the complexation induced frequency shifts and splittings are small (of the order of 1 cm⁻¹) for all normal modes. The face-bound structure was found to be a local minimum ($\theta=180^\circ$, $D_e=130$ cm⁻¹). The barrier between two vertex-bound minima (via the side-bound structure ($\theta=54^\circ$, $D_e=124$ cm⁻¹)) is less than 25 cm⁻¹ supporting the view of the expected small angular anisotropy of the potential. The local minimum with the face-bound structure possesses the shortest bond length ($R_e=2.96$ Å) whereas for the global minimum, the vertex-bound geometry, it is somewhat longer ($R_e=3.17$ Å). In spite of the larger charge-induced dipole interactions in the former configuration, anisotropy in the higher order terms of the electrostatic expansion makes the vertex-bound structure more favorable [257].

8.3. The Ar-NH₄⁺ complex

8.3.1. Spectrum

Figure 8.3: A portion of the Ar-NH₄⁺ photodissociation spectrum

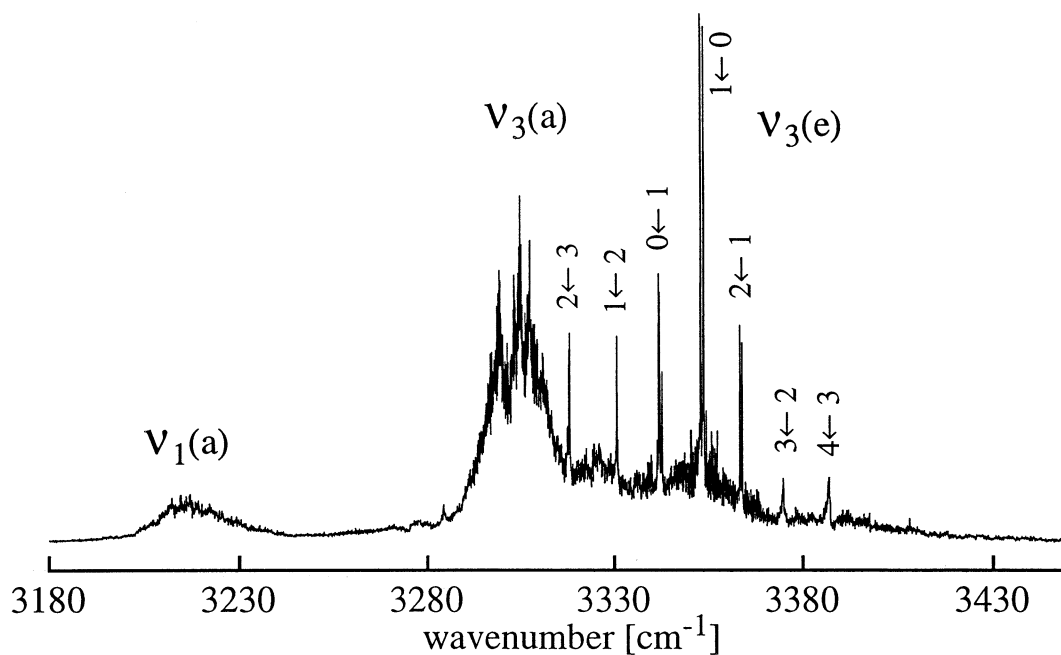
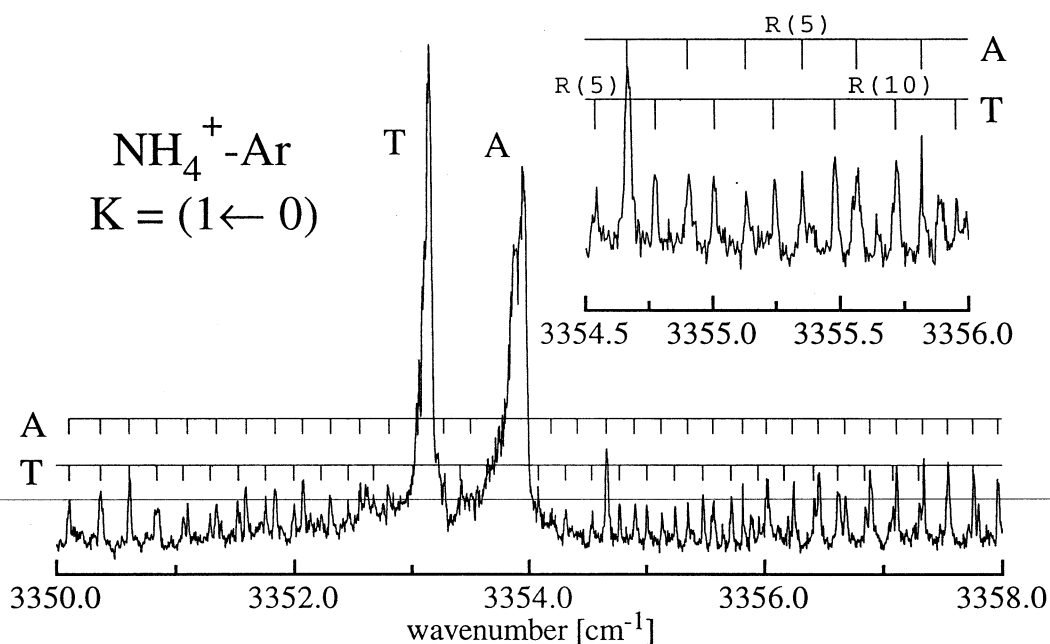


Figure 8.4: Expanded view of the v₃(e) (1←0) subband

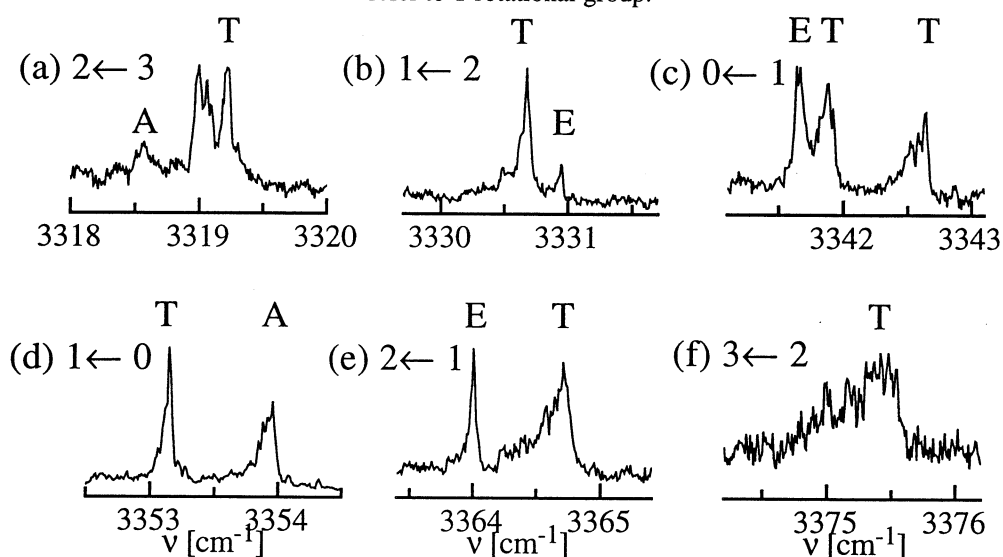


The complexes between Ar and NH₄⁺ were produced from a mixture of Ar, H₂, and NH₃ at a 60:4:1 ratio expanded at 5 bar stagnation pressure. Figure 8.3 shows a portion of the spectrum of the Ar-NH₄⁺ complex between 3180 and 3450 cm⁻¹. One can see that, as different from the He-NH₄⁺ case, the spectrum of Ar-NH₄⁺ consist of three major bands. Two of them at ≈3215 and ≈3305 cm⁻¹ are apparently of parallel type, while the third one at ≈3348 cm⁻¹ is looking as a perpendicular transition of a C_{3v} molecule. The parallel bands are both unresolved, and the one to lower energy has a relatively small intensity. On the

other hand, the perpendicular band system consists of a number of Q branch-like features separated by $\approx 11.3 \text{ cm}^{-1}$, with some of them being surrounded by a dense structure due to the P and R branch transitions. These are partly resolved as can be seen from figure 8.4. Overall the transition would nicely fit a pattern expected for a perpendicular band of a rigid prolate symmetric top molecule, with the most intense feature at $\approx 3353 \text{ cm}^{-1}$ assigned as $K'=1 \leftarrow K''=0$ subband. However, there are important differences. As revealed by a close examination of the individual Q branches many of them are split in several subcomponents. The splitting is displayed in figure 8.5 for the most intense $\Delta K=1$ and -1 subbands.

Figure 8.5: Q branch splitting in the $\nu_3(e)$ transition of Ar-NH₄⁺

The fine structure of selected $K' \leftarrow K''$ subband Q branches of the $\nu_3(e)$ transition. The rotational symmetries refer to T rotational group.



8.3.2. Assignment

Vibrational assignment of the observed bands is relatively straightforward. All three transitions can be interpreted as intramolecular vibrations of the NH₄⁺ core. There are two NH₄⁺ vibrations in this frequency range, the fully symmetric ν_1 stretching mode at 3236.6 cm^{-1} , and the triply degenerate ν_3 vibration at 3345.1 cm^{-1} . If a sufficiently rigid C_{3v} complex is formed between Ar and NH₄⁺, the former vibration will retain its symmetry in the new molecular symmetry group, while the latter will split into a_1 and e species. All three are expected to be IR allowed in the dipole approximation. The parallel bands at 3215 and 3305 cm^{-1} and the perpendicular band at 3348 cm^{-1} are assigned respectively as $\nu_1(a_1)$, $\nu_3(a_1)$, and $\nu_3(e)$ vibrations of the complex, where the symmetry refer to C_{3v} group. An extended discussion of the vibrational assignment is given in the Ar_n-NH₄⁺ section (9.5).

Table 8.2: Ar-NH₄⁺ rotational constants

Molecular constants derived from the fits of the rotational line wavenumbers to equation (4.3). P and R branch structure was resolved for a very limited number of Q branches.

$K' \leftarrow K''$, symmetry	range of J levels	origin [cm^{-1}]	B'' [cm^{-1}]	D'' ($\times 10^{-6}$) [cm^{-1}]	B' [cm^{-1}]	D' ($\times 10^{-6}$) [cm^{-1}]
$1 \leftarrow 0$, T	P(24)-R(26)	3353.31(2)	0.1165(5)	1.5(7)	0.1165(5)	1.5(7)
$1 \leftarrow 0$, A	P(32)-R(31)	3354.12(2)	0.1166(5)	0.75(30)	0.1160(5)	0.62(30)
$2 \leftarrow 1$, E	P(19)-R(24)	3365.10(2)	0.1162(5)	1.7(7)	0.1161(5)	1.7(7)

Assignment of the individual rotational P and R branch lines did not cause any difficulties either. Unfortunately, the overall rotation structure was resolved only for a

limited number of ΔK subbands. Observed line positions can be reproduced with a sufficient accuracy from the constants given in table 8.2. From rotational constant an argon nitrogen separation of 3.41 Å can be estimated. This correspond to Ar-H bondlength of 2.12 Å in a vertex-bound structure, which is of the same order of magnitude as Ar-proton separation in the Ar-HCO⁺ complex. As opposed to the complexes of rare gas atoms with HCO⁺ and HN₂⁺, the vibrational ν_3 excitation of NH₄⁺ produces a negligibly small effect on the intermolecular separation. Also the rotational constants seem to be relatively insensitive to the K quantum number, at least for the small K values sampled in table 8.2.

The internal structure of the Q branches is assumed to result from the tunneling of the NH₄⁺ unit between its four equivalent vertex-bound configurations. The splitting was analyzed using the model by Howard and co-workers [253]. This was accomplished by predicting the splitting pattern of the $\nu_3(e)$ Q branches for a wide range of V_2 , V_3 , and V_4 parameters. It was found that V_2 depended more or less on the magnitude of the $\nu_3(e)$ - $\nu_3(a_1)$ splitting and was not correlated with either of the rotational anisotropy terms. Relatively high value of $|V_2|$ was necessary to reproduce the observed appearance of the $\nu_3(e)$ with widely separated Q branches and small (0.5-1 cm⁻¹) internal splitting. The best results were obtained when the absolute value of V_4 was kept small. The values $V_2 \approx 90$ cm⁻¹ and $V_3 \approx 220$ cm⁻¹ reproduced the splitting pattern and the relative positions of the Q branches best. Symmetry labels of the experimentally observed Q branches (table 8.3) were obtained by comparison with the spectrum simulated with these V_2/V_3 values. For further details see ref. [255].

Table 8.3: Q branch positions of the Ar-NH₄⁺ $\nu_3(e)$ band

Assignment of the sub-structure of the K subband Q branches and results of a fit to a hindered rotor model

Subband K' ← K''	Symmetry in T group	V _{obs} [cm ⁻¹]	V _{calc} [cm ⁻¹]
2 ← 3	A	3318.59	3318.25
	?	3319.02	not included
	T	3319.25	3319.17
1 ← 2	T	3330.66	3330.45
	E	3330.95	3331.10
0 ← 1	E	3341.69	3341.50
	T	3341.90	3341.89
	T	3342.65	3342.61
1 ← 0	T	3353.18	3353.19
	A	3353.98	3354.06
2 ← 1	E	3364.07	3364.13
	T	3364.75	3364.95
3 ← 2	T	3375.39	3375.76
4 ← 3		3386.19	not included
5 ← 4		3396.90	not included
6 ← 5		3407.74	not included
0 ← 0 ^a	T	3305	3304.96

^a $\nu_3(a)$ parallel band

8.4. Conclusion

Unfortunately, the vertex-bound structure of the He-NH₄⁺ and Ar-NH₄⁺ complexes cannot be proven by present experiments, and this conclusion relies solely on the *ab initio* results. The calculations (see section 9.5) predict that the vertex bound structure is somewhat more stable for the He-NH₄⁺ complex and significantly more stable for Ar-NH₄⁺. On contrary the related neutral Ar-SiH₄ complex seems to possess a face-bound global minimum [249]. The size of the V_3 anisotropy parameter can be correlated with the barrier for tunneling between the equivalent NH₄⁺ configuration in the complex.

Specifically, *ab initio* calculations performed on Ar-NH₄⁺, at a level similar to that used for He-NH₄⁺, show that the former is more strongly bound ($D_e=470\text{ cm}^{-1}$) and the barrier for internal motion (via side) in it is substantially higher, about 200 cm^{-1} , with the effect of localizing the complex in a C_{3v} structure. Thus, from the experimental and *ab initio* results it is obvious that the degree of anisotropy is much smaller in He-NH₄⁺ than in the homologous Ar-NH₄⁺ complex. Such result can possibly be rationalized with help of simple arguments. The weaker intermolecular interaction and smaller reduced mass for the He-NH₄⁺ complex will tend to produce a larger intermolecular separation between the rare gas atom and the NH₄⁺ core as compared to the complex with Ar. However, even if the separations are similar in both systems, the Ar atom with its substantially larger volume will experience far more severe steric hindrance in rolling over the tetrahedron surface and consequently the effect of the anisotropic short-range Pauli repulsion on it will be greater. Similar arguments can be applied to explain the increase in rotational anisotropy between the charged Ar-NH₄⁺ and neutral Ar-SiH₄ complexes.

9. Larger complexes

9.1. Complexes Rg_n-HCO⁺/HN₂⁺. General remarks

Sufficient currents of the Rg_n-HCO⁺/HN₂⁺ cluster ions are often available for probing their photodissociation behavior. The experiments with such moderately sized systems are conducted in the same fashion as for their simpler predecessors Rg-HCO⁺/HN₂⁺, the only difference being a possibility of photodissociation in more than one fragment channel. In this work photodissociation spectra of complexes with n≥2 are studied in the vicinity of their CH (or respectively NH) intramolecular vibration. Initially it was hoped that for the trimers (n=2) some rotationally resolved features providing clues to the structure may persist in the spectra in spite of their increased mass. For reasonable trimer structures, given the 0.02 cm⁻¹ laser bandwidth, the spectra should be at least partially resolved. As experience showed, however, either the spectra obtained for the trimers are definitively unresolved due to some broadening mechanism (e.g. Ar₂-HCO⁺) or rotational resolution is difficult to ascertain because of a poor S/N ratio (e.g. He₂-HN₂⁺). Though rotational information is not accessible from the experiment, the spectra of the polymers can still be used to draw conclusions on their structures from following the development with cluster size of particular cluster properties such as ν₁ vibrational band shifts, ν₁ band profiles, and intermolecular frequencies. For neutral van der Waals molecules vibrational and electronic band shifts have been related to cluster structures within the framework of the band shift rule. The rule assumes that occupation of a particular solvent site leads to a well specified displacement of the transition frequency. The band shift arising from the presence of a solvent atom depends upon its relative position with respect to the chromophore, and to first order is more or less independent of the presence of other solvent entities. Thus similar incremental shifts for addition of any two solvent atoms might be taken as evidence that they occupy equivalent positions with respect to the core. Sometimes additional information about relative binding energies of the complexes can be derived from discontinuities in their distribution in the mass spectra as well as from occurrences of specific photofragment ions in the IR photodissociation spectra.

Maximal size of the complexes that can be formed under similar experimental conditions can in general be correlated with binding energy of the dimer complex (n=1), which is in turn related to the experimentally observable red shift in the XH intramolecular vibration. Unfortunately, the ν₁ vibration of the complex Ar-HN₂⁺, which has the highest binding energy out of six possible He/Ne/Ar-HCO⁺/HN₂⁺ combinations, is outside the range covered by the utilized "Mirage" OPO laser system. Complex Ar-HCO⁺ is the next one in terms of binding energy, and for the series Ar_n-HCO⁺ the spectra were observed for n up to 13 with an excellent S/N ratio, upper limit for n being set by the maximal mass transmitted by the first quadrupole (≈560 u). The complex He₂-HCO⁺ could not be generated in sufficient quantities reflecting its insignificant binding energy. For Ne_n-HCO⁺ and He_n-HN₂⁺ only spectra of the trimers were observed. The largest cluster size studied in the Ne_n-HN₂⁺ series corresponds to n=6. Since the amount of available experimental information is largest for the Ar_n-HCO⁺ complexes most of the discussion in this section is devoted to them. Conclusions for the Ar_n-HCO⁺ series are easily transferred on the results obtained for the other complexes.

9.2. Ar_n-HCO⁺ complexes

9.2.1. Some experimental details

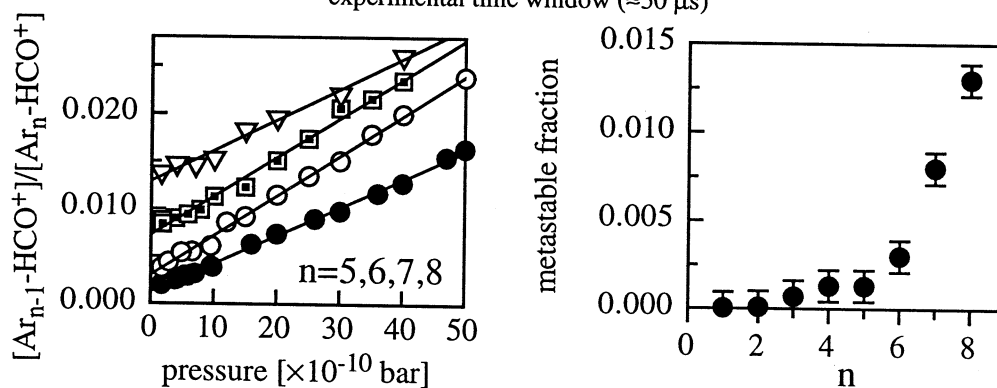
The gas composition used to produce Ar_n-HCO⁺ complexes was identical to that for the Ar-HCO⁺ dimer (see before) except that slightly higher backing pressure was utilized.

For Ar₂-HCO⁺ trimer and Ar₃-HCO⁺ tetramer scanning was accomplished in the range of 2700-3200 cm⁻¹. Two strongest transitions observed for them in this range are assigned to the intramolecular CH stretch (ν_1) vibration and a combination band correlating to $\nu_1+\nu_8$ in the dimer spectrum. For the larger complexes the range was narrowed to include only these two transitions. Generally, exposure of a particular sized Ar_n-HCO⁺ cluster to IR photons leads to the production of several different sized daughter ions. Photodissociation spectra were recorded for all significant fragment channels. The branching ratio between the channels depends sensitively upon the photon frequency, for example it may be different when measured at ν_1 and at the combination band, and besides it is possible that absorption profiles for one and the same band recorded on different channels are not coincident.

While under normal experimental conditions the power dependence of the photoinduced signal was found to be linear, implying that multiphoton processes were not of great significance, in larger clusters the effects of two photon absorption are discernible. For example, when the Ar₁₂-HCO⁺ cluster is irradiated at the peak of its ν_1 absorption, the daughter product distribution is bimodal. Whereas Ar₇-HCO⁺ and Ar₈-HCO⁺ constitute the major photoproducts, Ar₄-HCO⁺ is also formed ($\approx 0.5\%$ of the Ar₈-HCO⁺ signal under typical conditions). The secondary n=4 channel can be convincingly explained as arising from a two photon absorption by Ar₁₂-HCO⁺, as both Ar₇-HCO⁺ and Ar₈-HCO⁺ photodissociate predominantly into Ar₄-HCO⁺.

Figure 9.1: Metastable decay in the Ar_n-HCO⁺ series

Dependence of the (n)→(n-1) fragmentation signal on the pressure of background He in the octopole. Extrapolation to zero pressure provides fraction of internally hot ions capable of metastable decay in the experimental time window ($\approx 50 \mu\text{s}$)



In an effort to ascertain whether disintegration following ν_1 excitation occurs on timescale longer than the typical flight time through the octopole region, measurements of daughter photofragment branching ratios were taken with different parent translational energies. For example, in one experiment Ar₁₀-HCO⁺ was introduced into the octopole with either an energy of 4.0 eV or 0.5 eV (corresponding to octopole flight times of roughly 250 μs and 750 μs respectively) and irradiated at the ν_1 maximum. It was found that the branching ratio for production of Ar₅-HCO⁺ and Ar₆-HCO⁺ was the same within experimental error ($\pm 5\%$) at both energies suggesting that the dissipation/evaporation process transpires on a timescale of less than 100-200 μs .

Depending on their size, parent clusters enter the octopole some 80-200 μs after formation in the ion source with about 4 eV of translational energy in the laboratory frame. Metastable decay and collision induced fragmentation of the clusters are assessed by allowing them to collide with He in the octopole region. Monitoring the $(\text{Ar}_{n-1}\text{-HCO}^+)/(\text{Ar}_n\text{-HCO}^+)$ ratio as a function of the background pressure provides an estimate of the metastable fraction from the intercept of the Stern-Volmer plot. The results can be summarized as follows: (1) in the 80-200 μs time window, the metastable fragmentation

fraction increases with cluster size (figure 9.1); (2) decomposition into the n-1 channel predominates; (3) even for the largest clusters investigated (Ar₈-HCO⁺), less than 2% of the clusters decompose. The non-zero decomposition fraction reflects deficiencies in vibrational cooling in the supersonic ion source. Steep increase in metastable fraction for larger clusters may be connected with quickly increasing number of low frequency intermolecular modes that can accommodate more internal energy than smaller sized complexes and also with respectively smaller binding energies. Specifically, the proportion of hot clusters seem to increase drastically after n=6, in agreement with the conclusion that the Ar ligands occupy different structural sites for n<6 and n≥6 (see below).

9.2.2. Results and analysis. The ν_1 band shifts

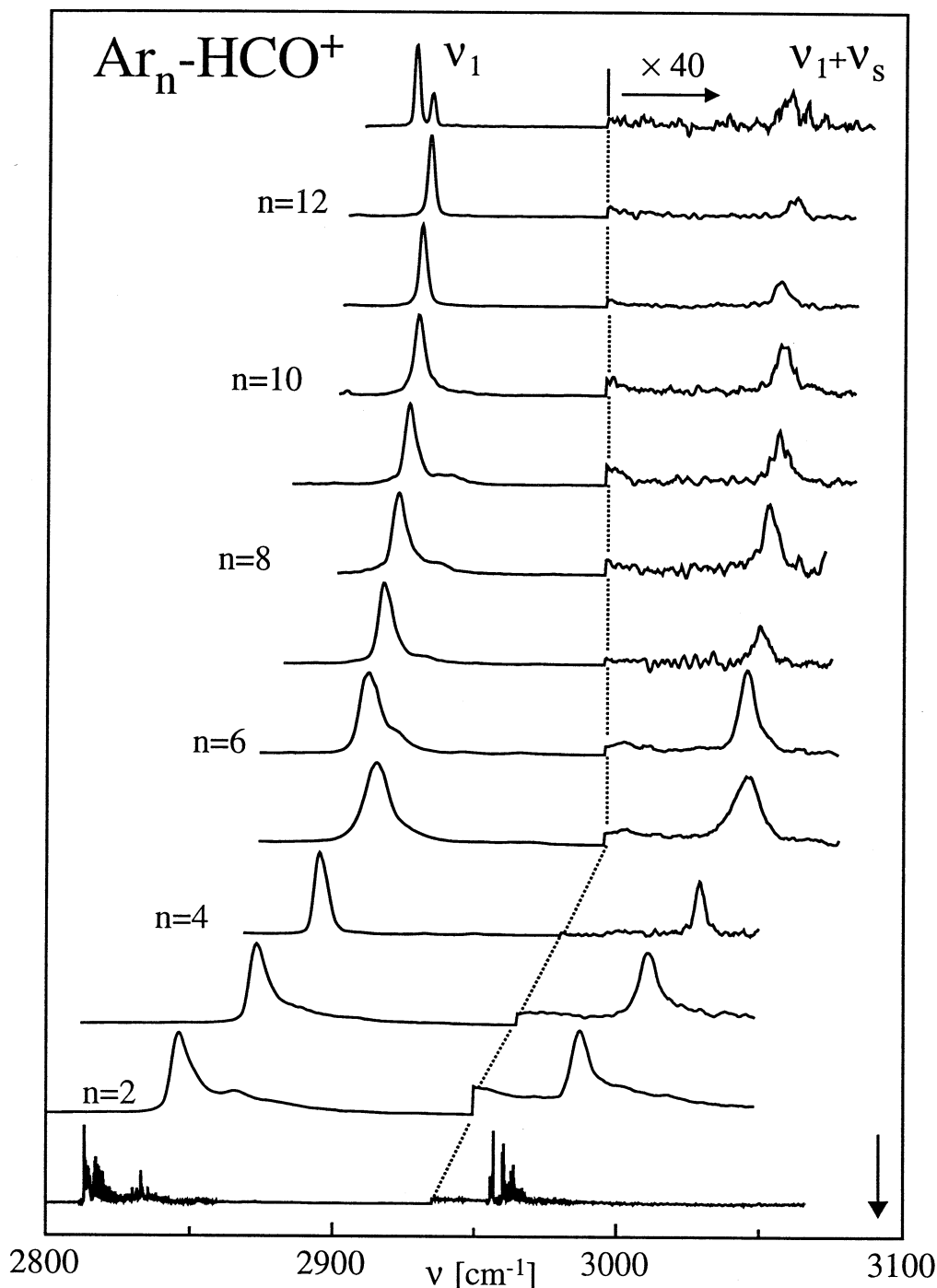
For almost all cluster sizes, absorption of an infrared photon results in the formation of only one or two different sized daughter fragments, with the branching ratio depending on the IR frequency. Figure 9.2 depicts infrared vibrational predissociation spectra of mass selected Ar_n-HCO⁺ (n=1-13) clusters recorded on the dominant photofragment channel. Figure 9.3 displays the range around the strongest feature in the spectra for the clusters, where photofragmentation proceeds into two channels. The ν_1 vibrational band shifts, the relative positions of the combination bands, and the photofragment branching ratios along with other information are summarized in Table 9.1.

As can be seen by inspecting Figure 9.2, the spectra for n≤12 are dominated by a prominent, relatively sharp band (fwhm<10 cm⁻¹), certainly associated with the chromophore HCO⁺ ν_1 vibration. Significantly, for Ar₁₃-HCO⁺ two peaks separated by ≈5.8 cm⁻¹ are apparent. The shifts in the ν_1 band, plotted as a function of cluster size in Figure 9.4(a), vary in a fairly systematic fashion as the number of Ar atoms in the cluster increases. While addition of the first Ar atom results in a massive 274 cm⁻¹ displacement to lower energy of ν_1 from the free molecule value, adding more Ar atoms brings the transition almost monotonically back to higher energy, so that for example at n=12 the total red shift is only 156 cm⁻¹. For the larger clusters the incremental shifts (i.e. the displacement of the Ar_n-HCO⁺ ν_1 transition from the one of Ar_{n-1}-HCO⁺, $\Delta v_{inc}(n)=v_1(n)-v_1(n-1)$) are modest and are generally back to the blue (higher energy), although between n=5 and n=6 there is a small incremental red shift. For n=2-5 the incremental blue shift is roughly 25 cm⁻¹ per Ar atom, while for n=6-12 it is only around 4 cm⁻¹ per Ar atom.

Within the framework of the band shift rule, the large red shift accompanying addition of the first Ar and the smaller constant ones for the ranges n=2-5 and n=6-12 are consistent with Ar_n-HCO⁺ structures in which a single Ar atom adopts a privileged, linear configuration (associated with the 274 cm⁻¹ red shift), with subsequent Ar atoms completing first a primary solvation ring (where the blue shift averages 25 cm⁻¹ per Ar atom) and then a secondary solvation ring (blue shift of 4 cm⁻¹ per Ar atom), each containing four to five Ar atoms.

While the large red shift accompanying the addition of the first Ar atom presumably reflects a flatter effective proton potential (arising from the proton's tendency to move across onto the Ar atom), it may be asked why addition of Ar atoms to primary and secondary solvation rings about an Ar-HCO⁺ core should lead to small incremental blue shifts. One explanation may be that in the larger complexes, the band shift is again determined principally by the terminal Ar atom, but that introduction of Ar atoms into the first solvation ring cause it to be pushed away from the proton. This should have the effect of diminishing its interaction with the proton, so leading to a reduced total red shift i.e., an incremental blue shift. The same effect should accompany addition of Ar atoms to the second solvation ring, with members of the second ring nudging the first ring against the terminal Ar. The significantly smaller average incremental blue shift for n=6 to n=12 is consistent with such a second order effect.

Figure 9.2: Predissociation spectra of Ar_n-HCO⁺ (n=1-13) clusters
 The spectra were taken by monitoring the dominant photofragmentation product. Note that the right hand part of the spectrum has been expanded by a factor of 40 to allow a clear view of the ν₁+ν_s band. The position of the free HCO⁺ ν₁ transition is marked with an arrow.



Interestingly, for Ar₁₃-HCO⁺ there are two ν₁ bands, the smaller one of which is virtually undisplaced from the Ar₁₂-HCO⁺ peak (0.5 cm⁻¹ blue shift), while the other more intense one is red shifted by 5.3 cm⁻¹. It is tempting to associate the latter of these with an Ar₁₃-HCO⁺ isomer in which the thirteenth Ar atom is the first member of the second solvation shell and is positioned at the proton end of the cluster where due to favorable induction interactions it should be most firmly bound. In such a position it is liable to *compress* the bond between the linearly positioned Ar atom and the proton, so producing the observed incremental red shift. On the other hand, the undisplaced peak may be

associated with one or more of the other three possible isomers where the thirteenth Ar atom is between the two solvation rings or at the oxygen end. In these other sites, the additional Ar atom should have little direct interaction with the proton-bound Ar atom and so should effect a smaller change in the ν_1 frequency.

Figure 9.3: Different fragmentation channels in the $\text{Ar}_n\text{-HCO}^+$ spectra

The ν_1 bands of $\text{Ar}_n\text{-HCO}^+$ ($n=2,3,4,5,10,$ and 12) taken on two different mass channels. In all cases the spectrum recorded on the smaller daughter mass is broader.

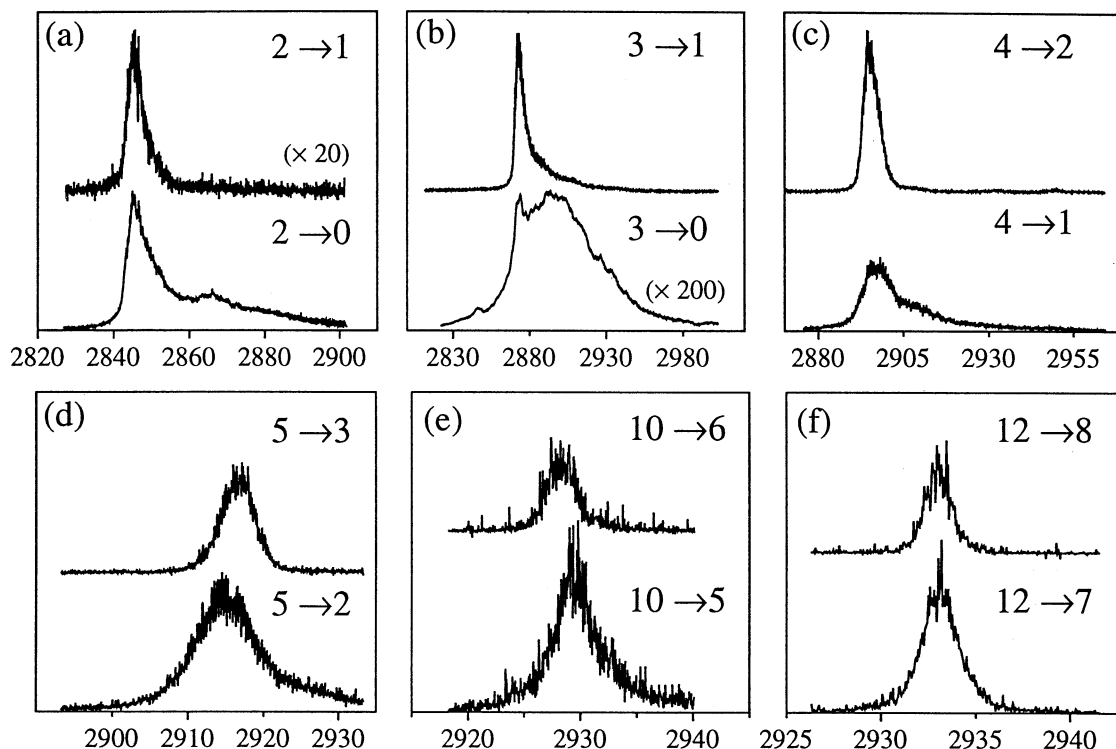
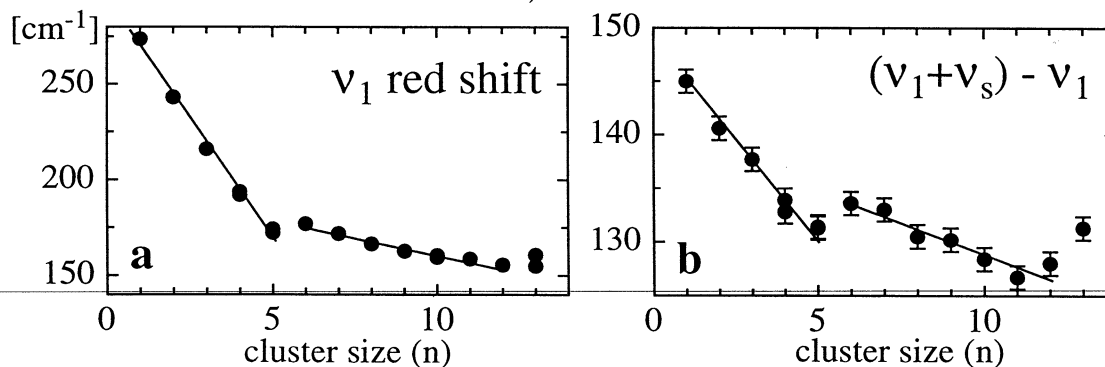


Figure 9.4: Development of $\text{Ar}_n\text{-HCO}^+$ properties with cluster size

(a) Incremental ν_1 band shifts resulting from the addition of an Ar atom to the $\text{Ar}_{n-1}\text{-HCO}^+$ cluster. (b) The $(\nu_1+\nu_s)-\nu_1$ separation



The observed ν_1 band shifts are more difficult to reconcile with alternative $\text{Ar}_n\text{-HCO}^+$ structures. For example, consider a T-shaped C_{2v} structure for the $\text{Ar}_2\text{-HCO}^+$ trimer in which the proton is shared by the CO molecule with *two* equivalent Ar atoms. Under such circumstances, the further delocalization of the proton would be expected to result in a lower characteristic frequency compared to the Ar-HCO^+ dimer. One would therefore anticipate an incremental *red* shift accompanying addition of the second Ar atom, contrary to the observed incremental *blue* shift. Similarly for a C_{3v} $\text{Ar}_3\text{-HCO}^+$, with the proton directed at the centre of an equilateral triangular Ar_3 unit in which the proton is shared by the CO with three equivalent Ar atoms, one would expect an even lower

characteristic ν_1 frequency and again, contrary to observation, an incremental red shift. Furthermore, the almost equal incremental blue shifts for Ar₂-HCO⁺ to Ar₅-HCO⁺ strongly suggest that the second to the fifth Ar atoms are being added to roughly equivalent positions, which is not consistent with C_{2v} and C_{3v} trimer and tetramer structures.

Table 9.1: Ar_n-HCO⁺ absorptions

Data for mid-infrared transitions of Ar_n-HCO⁺ clusters. Listed for each parent size (n=1+13) are the photofragment sizes (n_f), the ν_1 frequency, the incremental ν_1 band shift $\Delta\nu_{inc}(n)=\nu_1(n)-\nu_1(n-1)$, combination band ($\nu_1+\nu_s$) wavenumbers, and measured photofragment branching ratios. For n=13 two peaks are apparent in the spectrum, the lower energy one of which is 2.5 times the intensity of the other. The branching ratio data for n=13 were recorded at the more intense peak.

n	n _f	ν_1 [cm ⁻¹]	$\Delta\nu_{inc}$ [cm ⁻¹]	$\nu_1+\nu_s$ [cm ⁻¹]	fwhm [cm ⁻¹]	% ν_1	% $\nu_1+\nu_s$
0		3088.7					
1	0	2815.1	-273.6	2961.0		100	100
2	0	2845.7	30.6	2986.3	7.7	95	100
2	1	2845.6		not observed	4.9	5	0
3	0	broad		not observed	60	1	3
3	1	2872.7	27.0	3010.4	7.5	99	97
4	1	2896.8		3029.6	11.0	32	59
4	2	2895.1	22.4	3028.9	5.5	68	41
5	2	2914.6	19.5	3045.9	10.2	55	83
5	3	2916.5		3047.8	5.4	45	17
6	3	2911.9	-2.7	3045.5	7.7	99	
6	4	nor recorded		nor recorded		1	
7	3	nor recorded		nor recorded		6	
7	4	2917.0	5.1	3050.0	5.9	94	
8	4	2922.4	5.4	3052.9	6.1	90	
8	5	nor recorded		nor recorded		10	
9	5	2926.1	3.7	3056.3	4.7	100	
10	5	2929.3	3.2	3057.7	4.1	68	
10	6	2928.4		nor recorded	3.4	32	
11	6	2930.2	0.9	3056.9	2.8	92	
11	7	nor recorded		nor recorded		8	
12	7	2933.4	3.2	3061.4	2.3	70	
12	8	2933.2		nor recorded	1.8	30	
13	8	2928.1	-5.3	3059.4	2.2	90	
13	9	nor recorded		nor recorded		10	
13	8	2933.9	0.5	not observed	2.2		

It is of some interest to compare the vibrational bandshifts of the Ar_n-HCO⁺ clusters and ones of the Ar_n-HF (n=1-4) van der Waals molecules for which the minimum energy structures are known from both microwave [258, 259] and infrared [260, 261] studies to be C_{2v} for the trimer, C_{3v} for the tetramer and C_{3v} for the pentamer (proton pointed to the base of an Ar₄ tetrahedron). In contrast to Ar_n-HCO⁺, the Ar_n-HF (n=1-4) series exhibits incremental shifts which are always to the red, a situation which persists up to n=12 if recent rovibrational calculations which reproduce the smaller cluster red shifts are correct [262-265] Significantly, the predicted band shift for Ar₁₂-HF (corresponding to the complete encasement of the HF in a solvation sphere) is already close to the one for HF trapped in an Ar matrix. Unfortunately at present there appear to be no corresponding Ar matrix data for HCO⁺.

9.2.3. ν_1 band profiles

Inspection of the Ar_n-HCO⁺ spectra demonstrates that the ν_1 band profiles depend sensitively upon both the size of the parent cluster and also upon which photo daughter mass is monitored. Invariably the ν_1 peak recorded on the smaller daughter channel is broader than on the larger mass channel, and often exhibits a shoulder extending 10-20 cm⁻¹ to higher energy from the main peak. This behaviour is illustrated in figure 9.3 where

spectra of Ar_n-HCO⁺ (n=2-5, 10 and 12), recorded on the higher and lower mass fragmentation channels are shown. In some cases, there are extreme differences between the spectra, particularly when the probability for dissociation into the lower mass channel is small. For example, the Ar₃-HCO⁺ spectrum recorded on the dominant 3→1 channel is relatively sharp (fwhm≈7.5 cm⁻¹) compared to the very much broader 3→0 one (fwhm≈60 cm⁻¹), although the latter retains a sharp peak at the same position as the former.

A number of different effects probably contribute to the ν_1 profiles. For the smaller clusters, the rotational constants should be large enough to produce reasonably broad rotational contours. In fact, rigid rotor simulations of the Ar₂-HCO⁺ spectrum using rotational constants corresponding to the calculated geometry, suggest that resolved rotational structure should be just apparent with the 0.02 cm⁻¹ bandwidth light source. Its absence may be due either to homogeneous line broadening caused by rapid vibrational relaxation/predissociation or to congestion arising from hot bands or isomers. Although the Ar-HCO⁺ lines are unbroadened at the 0.02 cm⁻¹ experimental resolution, it is possible that the presence of an additional Ar atom hastens the flow of energy from ν_1 into the intermolecular modes.

One obvious cause for heterogeneous ν_1 broadening may be the presence of closely spaced sequence bands arising from clusters endowed with some measure of energy in the low frequency intermolecular motions. Sequence transitions involving these intermolecular vibrations will be displaced slightly from the ν_1 transition due to cross anharmonicity. Cluster temperatures (about 30-40 K if they are the same as the rotational temperature of Ar-HCO⁺) are almost certainly high enough for the intermolecular vibrational modes to be populated. Following infrared absorption, clusters which were initially hot will possess more energy than initially cold ones, and so on average will shed more Ar atoms, thus explaining the occurrence of broader ν_1 bands on the deeper mass channel. A very good example is provided by the spectra of Ar₂-HCO⁺ (figure 9.3(a)). While the spectrum of the trimer recorded into the monomer channel retains a feature, interpreted as $\nu_1+\nu_s-\nu_s$ transition in Ar-HCO⁺ spectrum, there is no sign of it in the 2→1 channel. Another example is the Ar₃-HCO⁺ spectrum recorded on HCO⁺ fragment channel which seem to consist exclusively of sequence transitions. Blue shifted sequence bands would imply that excitation of the C-H stretch vibration raises the frequency of the intermolecular vibrations (i.e. there is positive cross anharmonicity). This is consistent with observations for the Ar-HCO⁺ dimer, where exciting the C-H stretch vibration (ν_1) leads to a contraction of the intermolecular bond and to an increase in the intermolecular frequencies.

Following a similar line of reasoning the observation that the ν_1 bandwidths diminish with cluster size can also be explained. The intermolecular modes most strongly coupled to ν_1 will primarily be the ones associated with the Ar atoms closest to the proton, particularly the Ar atom lying on the HCO⁺ axis. Addition of Ar atoms to the primary and secondary solvation rings should serve to support the terminal Ar atom so raising its characteristic frequencies. Thus at a given temperature, modes strongly coupled with ν_1 are less likely to be populated in the larger clusters.

9.2.4. Combination bands

Lying some way to higher energy from the ν_1 band are weaker transitions that can be tentatively assigned as combinations involving ν_1 and intermolecular vibrational motion(s). One of these peaks, which can be seen in all of the n=1-13 spectra, is separated from ν_1 by roughly 130-140 cm⁻¹, and is presumably due to a combination of ν_1 and the *intermolecular*

stretching vibration (ν_s). The alternative possibility, that the band arises from an intramolecular HCO⁺ combination band seems improbable given the weak bands' more or less constant displacement from ν_1 for the entire Ar_n-HCO⁺ series.

Table 9.2: Ar_n-HCO⁺ unassigned absorptions

Displacement of minor combination bands from ν_1 in Ar_n-HCO⁺ clusters (in cm⁻¹). The uncertainty in the displacements is ± 1 cm⁻¹. The two vibrations' identities are at present uncertain.

n	$(\nu_1+\nu_a)-\nu_1$	$(\nu_1+\nu_b)-\nu_1$
4	55	37
5	57	39
6	54	33
7	55	33
8		30

In addition to the above mentioned bands, between $n=4$ and $n=7$ there are two weaker bands apparent in the spectrum, one displaced from ν_1 by between 30 and 40 cm⁻¹, the other by between 50 and 60 cm⁻¹. While the identities of these two bands is at present uncertain, they may possibly be associated with the intermolecular bending and stretching motions of equatorially disposed Ar atoms. It is not clear why these bands are only visible in the $n=4-7$ size range. The positions of the combination bands with respect to ν_1 are listed in table 9.2.

The development of the $(\nu_1+\nu_s)-\nu_1$ spacing with increasing cluster size, which is depicted in figure 9.4(b), can be seen to mirror the development of the vibrational band shifts (figure 9.4(a)). Thus the stretch frequency diminishes almost linearly from $n=1$ to $n=5$ (3.4 cm⁻¹ per Ar), increases slightly from $n=5$ to $n=6$, and again decreases roughly linearly from $n=6$ to $n=12$ (1.1 cm⁻¹ per Ar). From $n=12$ to $n=13$ there is an increase in the ν_s frequency. Presumably the general decrease in the $(\nu_1+\nu_s)-\nu_1$ spacing reflects a weakening of the intermolecular bond between the proton and the terminal Ar atom as further Ar atoms are added. The constant incremental decreases in the intermolecular stretching frequency for $n=2$ to $n=5$ and for $n=6$ to $n=11$ support a picture of the larger Ar_n-HCO⁺ clusters being built up through the formation of primary and secondary solvation rings each containing 4 to 5 Ar equivalent atoms, with a progressive weakening of the bond between the terminal Ar and the HCO⁺ core.

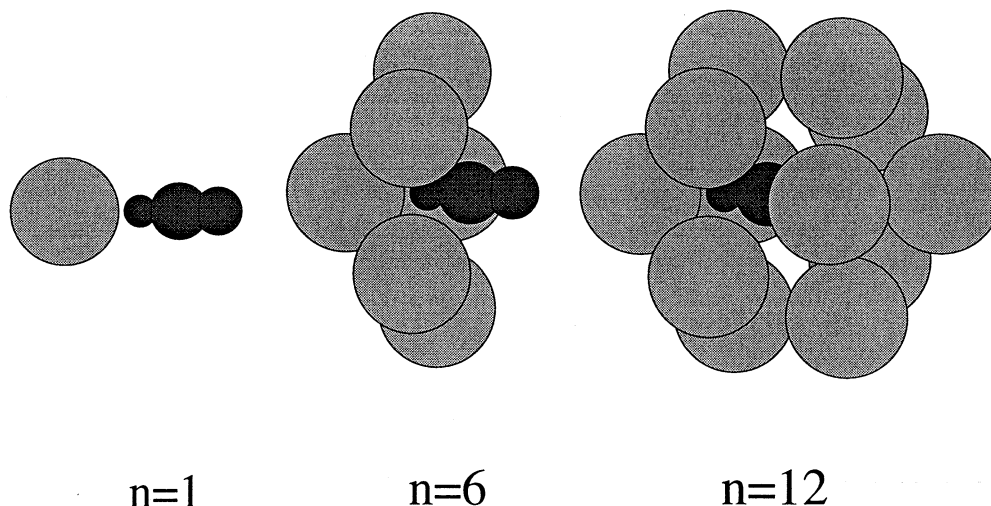
9.2.5. Structure modeling

To help clarify issues surrounding the structure of Ar_n-HCO⁺ complexes, minimum energy configurations using a simple semi-empirical form for the potential energy function have been calculated. Details of the calculation can be found in reference [37] and here only brief description and the results are reproduced. For the Ar_n-HCO⁺ clusters the total cluster potential energy is represented as a sum of atom-atom Lennard-Jones (12-6) type terms, supplemented by charge induced dipole (*cid*) contributions and second order charge induced dipole-charge induced dipole (*cid-cid*) interactions between the Ar atoms. It was assumed that the Ar_n-HCO⁺ clusters are built up by addition of Ar atoms to a frozen linear Ar-HCO⁺ core whose geometry is derived from the dimer spectrum. Using this potential energy representation, the energy minimization for the Ar_n-HCO⁺ ($n=2-13$) series was accomplished using the downhill simplex method. As expected, the minimum energy cluster geometries (see figure 9.5 for $n=1$, 6 and 12) were those that optimized the charge induced dipole interaction between the positive charge and the Ar atoms. The first five Ar atoms added to the Ar-HCO⁺ core form a primary solvation ring, equatorially disposed about the C-H bond midpoint (the position of the positive charge). Addition of a further Ar atom begins a second solvation ring, which is staggered with respect to the first and is completed

at Ar₁₁-HCO⁺. A twelfth Ar atom sits over the oxygen end of the cluster so completing the primary solvation shell.

Figure 9.5: Semi-empirical structures for selected Ar_n-HCO⁺ clusters

Calculated minimum energy structures for Ar₁-HCO⁺, Ar₆-HCO⁺ and Ar₁₂-HCO⁺. The dimer structure is determined from rotational analysis of its ν₁ transition. Structures for the two larger clusters have been calculated assuming a frozen Ar₁-HCO⁺ core and using a semi-empirical potential.



For clusters up to Ar₁₂-HCO⁺ the powerful charge induced dipole forces ensure that no matter the starting configuration for the geometry optimization, the clusters find their way to the same minimum. However, for Ar₁₃-HCO⁺ there are several distinct isomers with similar minimum energies (within 60 cm⁻¹) which are separated by appreciable isomerization barriers. The thirteenth Ar atom can be either located between one of the solvation rings and a terminal Ar atom at either the proton or oxygen end, or alternatively positioned between the primary and secondary solvation rings, with the additional Ar atom coordinated with two Ar atoms in the first ring and one in the second or *vice versa*.

The calculated incremental binding energies are summarized in table 9.3. From the perspective of the model potential calculations, the lower binding energies for Ar atoms in the second solvation ring compared to those in the first reflect their greater displacement from the centre of charge, and the consequently smaller *cid* interaction. Within the first ring, the incremental binding energies are roughly constant for all five Ar atoms. This comes about because the attractive Lennard-Jones interactions are balanced by roughly equal *cid-cid* repulsive ones. In the second ring, which is further away from the charge centre, the repulsive *cid-cid* interaction is smaller and is overridden by the dispersion forces. This results in a small increase in the incremental binding energies between n=6 and n=11.

Table 9.3: Ar_n-HCO⁺ binding energies

Ar binding energies for the Ar_n-HCO⁺ series calculated using the simple pairwise potential augmented by polarization and induced dipole-induced dipole interactions.

n	D(n) [cm ⁻¹]	n	D(n) [cm ⁻¹]
2	955	8	680
3	980	9	690
4	965	10	690
5	950	11	780
6	945	12	735
7	595	13	488

9.2.6. Discussion

Generally one may expect that the most stable Ar_n-HCO⁺ cluster structures will be ones which maximize coordination between the Ar atoms and the most positively charged part of the HCO⁺ core and to a lesser extent with one another. The mid-infrared spectra strongly suggest that this is indeed the case with Ar atoms preferentially adopting positions close to the hydrogen and carbon atoms, which according to the Mulliken population analysis should carry most positive charge. The first Ar atom occupies a linear proton-bound position with further argons placed in primary (n=2-5) and secondary (n=5-11) solvation rings. The twelfth Ar atom completes the first solvation shell. A distinct drop in the binding energy for n=13 and also the appearance of an additional ν_1 peak can be convincingly associated with the beginning of a second solvation shell about an Ar₁₂-HCO⁺ icosahedral core.

One apparent anomaly concerns the filling of the first solvation ring. While the model calculations detailed in previous section suggest that this should occur at n=6, some of the cluster properties exhibit a noticeable discontinuity on going from n=5 to n=6 (figures 9.1 and 9.4). This strongly suggests that while up to six ligands can comfortably coordinate with the proton (one CO molecule, five Ar atoms: one linearly disposed, four arranged in a ring), the introduction of an additional sixth Ar atom into the first solvation ring causes some degree of strain. Thus, formation of a second ring may already begin at Ar₆-HCO⁺, with completion of the first ring occurring at a later stage. Significantly, enthalpies for the N₂+H(N₂)_{n-1}⁺, H(N₂)_n⁺ and CO+H(CO)_{n-1}⁺, H(CO)_n⁺ clustering reactions exhibit pronounced drops at the corresponding point (between n=6 and n=7) [229], an observation that has been linked to the formation of an octahedral coordination shell about a central proton for n=6.

9.3. The Ne₂-HCO⁺, He₂-HN₂⁺ and Ne_n-HN₂⁺ clusters

Figure 9.6: A vibrational predissociation spectrum of Ne₂-HCO⁺

Comparison of the vibrational photodissociation spectra of ²⁰Ne₂-HCO⁺ and ²⁰Ne-HCO⁺ in the ν₁ region (C-H stretch). In both cases the spectra are obtained by monitoring the HCO⁺ fragment current as a function of photon frequency.

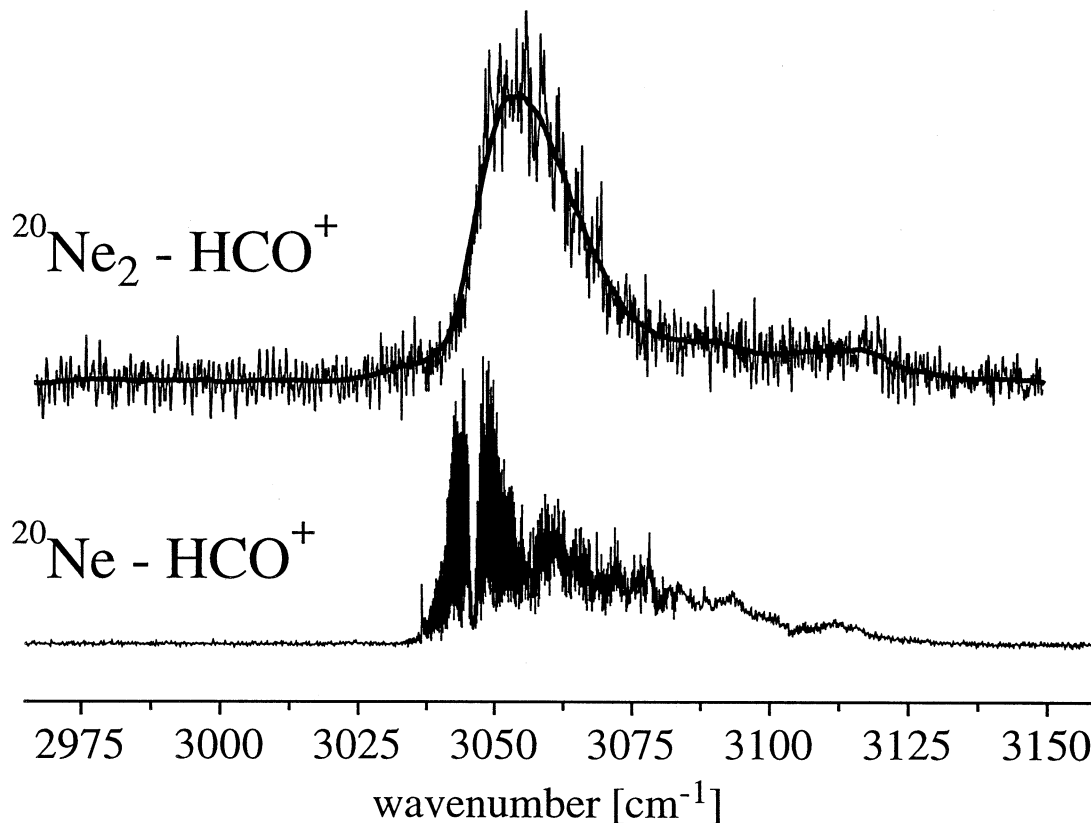
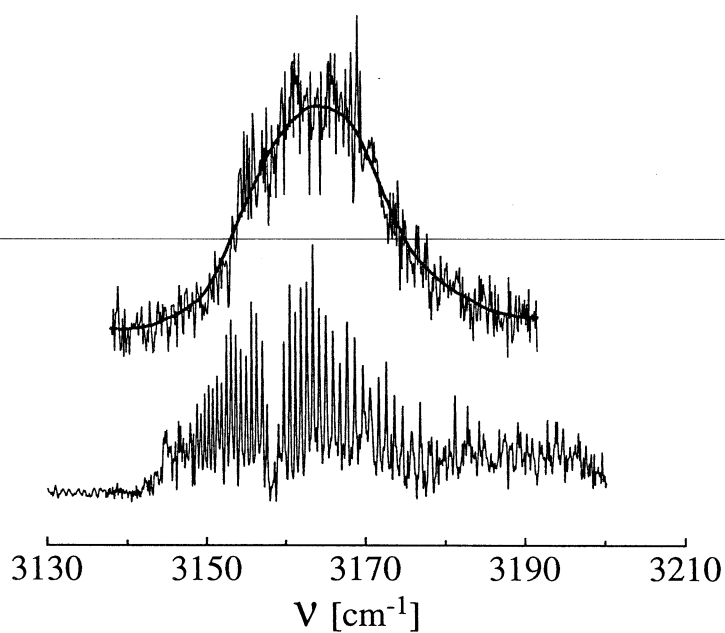


Figure 9.7: Vibrational predissociation spectra of He-HN₂⁺ and He₂-HN₂⁺

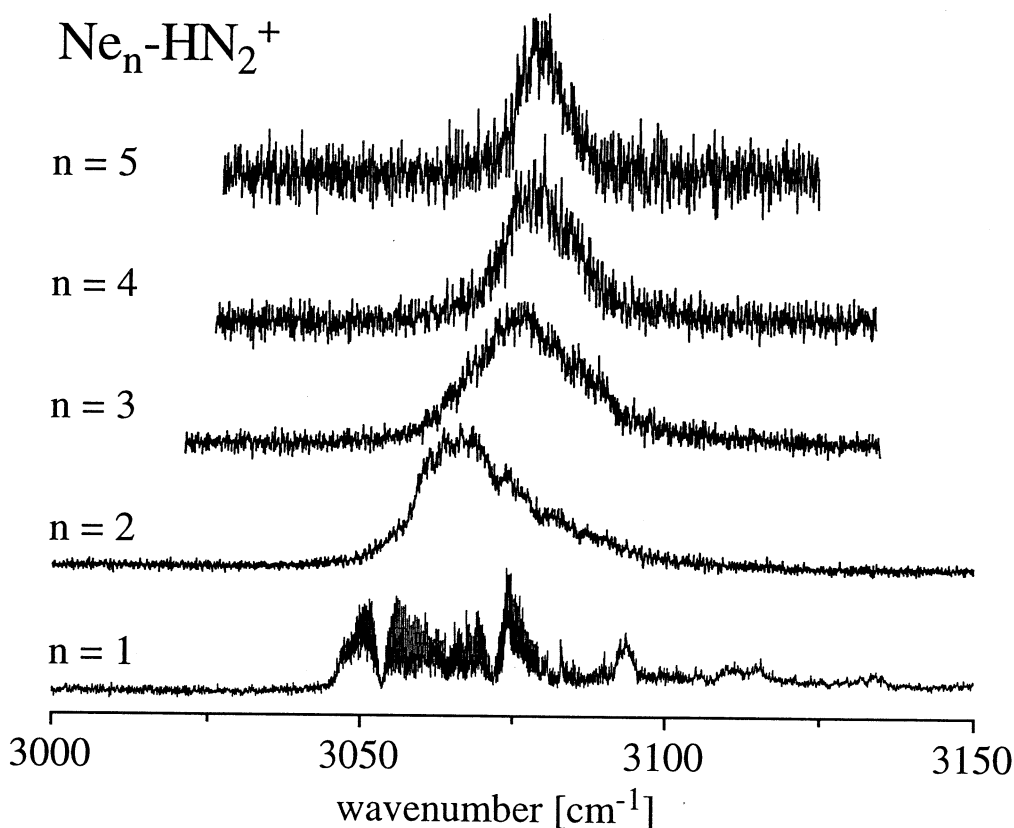
In both cases, the spectra were obtained by monitoring the HN₂⁺ photofragment intensity.



The ν_1 band of the Ne₂-HCO⁺ trimer was recorded by monitoring its photofragmentation into the HCO⁺ monomer (see figure 9.6). No Ne-HCO⁺ photofragment ions were detected, and given the S/N ratio for the measurements, the branching ratio for the two possible photofragmentation channels $n=2 \rightarrow n=0$ and $n=2 \rightarrow n=1$ is at least 10. The spectrum of the trimer exhibits a single broad peak ($\text{fwhm} \approx 20 \text{ cm}^{-1}$) without any traces of rotational resolution. The complexation-induced vibrational band-shifts for Ne-HCO⁺ and Ne₂-HCO⁺ behave in the way similar to the complexes with Ar. While the Ne-HCO⁺ ν_1 band origin is appreciably red shifted from the monomer one (by 42.5 cm^{-1}), addition of a second Ne atom shifts the transition slightly back to higher energy (by $8 \pm 3 \text{ cm}^{-1}$).

Situation with He₂-HN₂⁺ complex is very much the same. The spectrum of the trimer is depicted along with the He-HN₂⁺ one in figure 9.7 and consists of a single broadened peak centred at $3164 \pm 2 \text{ cm}^{-1}$, approximately 6 cm^{-1} to higher energy from the He-HN₂⁺ ν_1 band. Again the He₂-HN₂⁺ ν_1 band lacks discernible rotational structure and no He-HN₂⁺ photofragments are detected.

Figure 9.8: Vibrational predissociation spectra of Ne_n-HN₂⁺



For the Ne_n-HN₂⁺ series spectroscopic measurements were made for n up to 6. The spectra are displayed in figure 9.8. Once again the ν_1 transition of the Ne-HN₂⁺ dimer is characterized by a massive red shift of 180.5 cm^{-1} from the free monomer value whereas in the spectra of larger complexes much smaller incremental shifts ($\Delta\nu_{\text{inc}}(n) = \nu_1(n) - \nu_1(n-1)$) back to higher frequencies are observed. As the cluster size increases the incremental shift becomes notably smaller, with virtually no difference existing in the positions of the ν_1 maximum for $n=4$ and $n=5$. At the same time the S/N ratio in the spectra goes down which might be in part due to a drop in stepwise binding energies. The spectrum of Ne₆-HN₂⁺ has not been recorded because of a poor S/N ratio, however it has been estimated that the

complex absorbed in roughly the same spectral range as the one with n=5. The widths of the absorption features drop with cluster size in parallel with the observation for Ar_n-HCO⁺ complexes though this may also happen because the Fermi resonance between ν_1 and $\nu_2+\nu_3+\nu_b$ existing in the dimer is destroyed in the higher clusters. Positions of absorption maxima for Ne_n-HN₂⁺ are summarized in table 9.4.

Table 9.4: Absorption maxima of Ne_n-HN₂⁺ spectra

n	position [cm ⁻¹] ^a
1	3053.5 ^b
2	3066.1
3	3075.9
4	3078.3
5	3079.0
6	≈3079 ^c

^a All clusters dissociate into HN₂⁺; ^b Ne-HN₂⁺ ν_1 origin; ^c Estimated

Though the qualitative trends observed in the spectra of Ne_n-HN₂⁺ are the same as for the Ar_n-HCO⁺ series, there are subtle differences in the relative magnitudes of the incremental shifts of the ν_1 transition maximum ($\Delta\nu_{inc}$). For Ar_n-HCO⁺ complexes addition of an Ar atom in the first solvation ring results in near constant displacement of the ν_1 band from that in the (n-1) complex ($\Delta\nu_{inc} \approx 25$ cm⁻¹). This situation persists for n=2-5, and starting from n=6 a markedly different slope in the dependence of $\Delta\nu_{inc}(n)$ on cluster size is obtained signaling the start of the second solvation ring formation. For n=7-12 the values of $\Delta\nu_{inc}$ are again of the same order of magnitude (4 cm⁻¹). For the Ne_n-HN₂⁺ complexes $\Delta\nu_{inc}(2)$ and $\Delta\nu_{inc}(3)$ are indeed of similar magnitude (10-11 cm⁻¹) suggesting that the second and the third Ne atoms occupy near equivalent positions with respect to the HN₂⁺ axis. However the values $\Delta\nu_{inc}(4,5,6)$ are much smaller, of the order of 1-2 cm⁻¹, implying that some other structural sites are occupied. In the Ar_n-HCO⁺ section it was assumed that the total ν_1 frequency shift from the free monomer value is dictated in the first approximation by the strength of interaction of the axial Ar atom with central proton and that the off-axial Ar atoms influence the total shift by weakening or strengthening this interaction. In this picture Ar ligands from the second solvation ring, that are further separated from the terminal Ar atom, produce much smaller incremental shifts in the ν_1 frequency than the first solvation ring ligands. Transferring this view on the Ne_n-HN₂⁺ system it appears that the fourth and the fifth Ne ligands are structurally closer to the N end of the Ne-HN₂⁺ than are either the second or the third ones. This indicates that the mechanism of the shell closure in Ne_n-HN₂⁺ and Ar_n-HCO⁺ might be qualitatively different. From electrostatic viewpoint a satisfactory explanation for this phenomenon can be obtained from consideration of the positive charge distribution within the HN₂⁺ and HCO⁺ monomer frameworks. As can be shown from either Mulliken or distributed multipole analysis, the HN₂⁺ and HCO⁺ ions are principally different in this respect. While in the former positive charge is distributed in roughly equal proportion among all three atoms [266], in the latter the charge is concentrated predominantly on carbon and to a lesser extent on hydrogen atoms [162, 267]. This may explain why in the small Ar_n-HCO⁺ complexes a well defined ring of ligands is formed around the CH bond and why Ne_n-HN₂⁺ complexes seem to have less defined structures. Since in the first approximation the ligands place themselves such as to maximize the amount of charge - induced dipole interaction, the Ne atoms can stick anywhere to the HN₂⁺ axis without losing much in the binding energy contrary to the more space-limited case of the Ar -- HCO⁺ interaction. Besides, interaction between the ligands plays less important role in Ne_n-HN₂⁺ as compared to Ar_n-HCO⁺ clusters.

9.4. Conclusions for the Rg_n-HCO⁺/HN₂⁺ complexes

In this section connections between structures and vibrational band shifts (and other spectroscopic properties) for rare-gas containing proton-bound complexes of the type Rg_n-HCO⁺/HN₂⁺ has been discussed. In these clusters a single rare-gas atom appears to occupy a privileged linear proton-bound position, effectively forming a dimer core to which further rare-gas atoms are more loosely bonded. The extra ligands can form primary and secondary solvation rings each containing four or five rare gases as in the case of Ar_n-HCO⁺ clusters or be distributed around the dimer axis in a less regular fashion. It is the terminal, proton-bound rare-gas atom that is primarily responsible for the flattened effective proton potential and consequent decrease in the ν_1 frequency. The additional rare-gas atoms crowd about the proton, pushing the terminal rare-gas atom further away, thereby diminishing its flattening effect on the effective proton potential and leading to the small incremental blue shifts experimentally observed in the spectra. It is perhaps important to emphasize at the outset that without rotationally resolved spectra for the larger clusters, the structural conclusions presented in this section are to some extent tentative.

9.5. Complexes Ar_n-NH₄⁺

9.5.1. Preview

As different from either HCO⁺ or HN₂⁺ based ionic complexes, one NH₄⁺-X_n cluster series, NH₄⁺-(NH₃)_n, have been studied in IR range long before this work by using direct absorption and photodissociation methods. Low resolution (25 cm⁻¹) IR absorption spectra for n=0-4 [14] revealed two NH₄⁺ core vibrations between 2000 and 4000 cm⁻¹ assigned to the strong IR allowed ν_3 and $2\nu_4$ bands. Higher resolution (~ 1 cm⁻¹) spectra of mass selected clusters (n=1-10) [63, 64] obtained by IR vibrational predissociation spectroscopy confirmed the assignment of the spectral features attributed to the ionic core and showed additional absorptions associated with the NH₃ ligands. The main conclusion emerged from these two studies was that the first four ligands form the first coordination shell, supporting similar views obtained from thermochemical data [268] and *ab initio* calculations [65, 269]. Spectral features due to internal rotation of the NH₃ ligands in the first solvation shell vanish for n>7 indicating that each of the second shell ligands forms a hydrogen bond to one first shell ligand. There are a few differences between NH₄⁺-Ar_n complex presented in this chapter and NH₄⁺-(NH₃)_n complexes. Firstly, replacing the NH₃ ligands by Ar atoms avoids complications in the spectra due to the ligand absorptions. Secondly, the binding energy of NH₄⁺-Ar is much lower than that of NH₄⁺-NH₃ and consequently the complexation induced frequency shifts are expected to be significantly smaller. And finally, in contrast to NH₄⁺-NH₃, the binding energy of NH₄⁺-Ar is lower than any intramolecular frequency, i.e. the absorption of a single IR photon is sufficient to dissociate cold cluster ions.

9.5.2. *Ab initio* calculations

Ab initio calculations were of a great help in guiding the analysis of the vibrational spectra. Computations at the MP2 level have been carried out to determine the dimer geometry and the influence of the first ligand on the vibrational frequencies of the NH₄⁺ monomer. For the larger clusters (n=0-5) the calculations were performed at Hartree-Fock (HF) level. Details of the calculations are given in reference [270]. Two stable minima of the dimer were investigated at MP2 level, namely the vertex- and the face-bound structures. The vertex-bound structure is the global minimum with a binding energy of $D_e \sim 500$ cm⁻¹ while the face-bound structure lies ~ 200 cm⁻¹ higher in energy. The most striking difference between the two dimer geometries is the size of the splitting of ν_3 fundamental upon complexation (table 9.5). While the calculations predict only a small splitting (< 1 cm⁻¹) for the face-bound structure, a large splitting (68 cm⁻¹) is obtained for the vertex-bound one. Experimentally observed splitting of 43 cm⁻¹ agrees with the latter structure.

The geometry of the NH₄⁺ core is almost unaffected by Ar complexation implying that interaction within the complex is relatively weak. Larger clusters were investigated only at the HF level. Harmonic frequencies and complexation induced frequency shifts calculated for the monomer and the dimer agree qualitatively with those determined on the MP2 level. Similar to the MP2 results, the ν_3 band splitting calculated at the HF level is only significant for the vertex-bound dimer. The binding energies as well as the ν_3 band splittings calculated at both levels of theory lead to the conclusion that the face-bound minima are significantly less stable. Thus, for the larger cluster calculations as well as for the analysis of their experimental spectra, it was assumed that the first four Ar atoms bind to the vertices of the NH₄⁺ tetrahedron leading to geometries with T_d, C_{3v}, C_{2v}, C_{3v}, and T_d symmetry for n=0-4, respectively. In clusters with n>4, the additional Ar atoms probably occupy positions at the faces of the tetrahedron. The Ar...Ar separation in the computed NH₄⁺-Ar₄ structure of around 6 Å, combined with the vdW radius of Ar (~ 1.7 Å), suggests that at

least one Ar atom can fit within the triangle of three vertex-bound ligands with close contact to the respective face of NH₄⁺. It is not clear whether these additional Ar atoms are situated in the centre of the faces leading to geometries with C_{3v}, C_{2v}, C_{3v}, and T_d symmetry for n=5-8, or whether they occupy less symmetric sites in order to maximize the Ar...Ar interaction. In the present work, only the C_{3v} configuration of the n=5 complex was examined by keeping the optimized NH₄⁺-Ar₄ geometry frozen and relaxing only the three intermolecular coordinates of the fifth, i.e. the face-bound Ar atom.

Table 9.5: NH₄⁺ and NH₄⁺-Ar calculated vibrational frequencies

Unscaled calculated MP2 harmonic frequencies of NH₄⁺ and NH₄⁺-Ar. For the dimer both face- and vertex-bound minima were considered. In addition the last row gives predicted transition frequencies of NH₄⁺ from an *ab initio* quartic force field potential [193].

	ν_1	ν_2	ν_3	ν_4	$2\nu_4$	$\nu_2+\nu_4$	$2\nu_2$
NH ₄ ⁺	3424(a ₁)	1757(e)	3556(t ₂)	1504(t ₂)			
NH ₄ ⁺ -Ar (vertex)	3379(a ₁)	1760(e)	3495(a ₁) 3563(e)	1495(a ₁) 1514(e)			
NH ₄ ⁺ -Ar (face)	3432(a ₁)	1762(e)	3565(a ₁) 3565(e)	1507(a ₁) 1510(e)			
NH ₄ ⁺ force field	3237	1690	3345	1447	2860(a ₁) 2887(e) 2899(t ₂)	3121(t ₂) 3138(t ₁)	3376(a ₁) 3377(e)

9.5.3. Spectra

NH₄⁺-Ar_n complexes were produced in a pulsed and skimmed supersonic expansion of NH₃, H₂, and Ar with a ratio of about 1:5:100 at backing pressures of 3-5 bar. Photodissociation spectra were obtained in usual way by monitoring the NH₄⁺-Ar_m fragment ion intensity as a function of the laser frequency. When several fragmentation channels were observed, spectra were recorded for each of them simultaneously by switching the second quadrupole mass filter between the respective fragment masses for each laser wavelength.

Table 9.6: Branching ratios in NH₄⁺-Ar_n spectra

Branching ratios for photofragmentation of NH₄⁺-Ar_n complexes into the various NH₄⁺-Ar_m daughter channels. Only contributions larger than 0.01 are listed. The estimated accuracy is ±0.05. The complexes with n=1-3 all dissociate in NH₄⁺.

n	m=0	m=1	m=2	m=3	m=4
4	0.63	0.37			
5		0.68	0.32		
6			0.82	0.18	
7			0.02	0.94	0.04

Photodissociation spectra of NH₄⁺-Ar_n complexes recorded in the region between 3000 and 3500 cm⁻¹ are reproduced in figure 9.9 for n=1-5. Parts of the low energy region of the spectra are vertically expanded to show the weak features. Possible NH₄⁺ monomer fundamentals, overtones and combination bands which fall into the scanned region are indicated by sticks together with their symmetry labels. Their positions have been calculated from an *ab initio* force field that reproduces the experimental ν_3 and ν_4 frequencies of NH₄⁺ to within a few cm⁻¹ [193]. For n=6 and 7, spectra have been recorded only in the region of the strong bands (3250-3450 cm⁻¹). They are not presented because they are similar in appearance to the spectra for n=5, displaying only a single slightly blue shifted band.

Figure 9.9: Photofragmentation spectra of NH₄⁺-Ar_n (n=1-5)

The spectra were recorded on the respective dominant fragment channel. Possible NH₄⁺ monomer fundamentals, overtones and combination bands which fall into the scanned region are indicated by sticks.

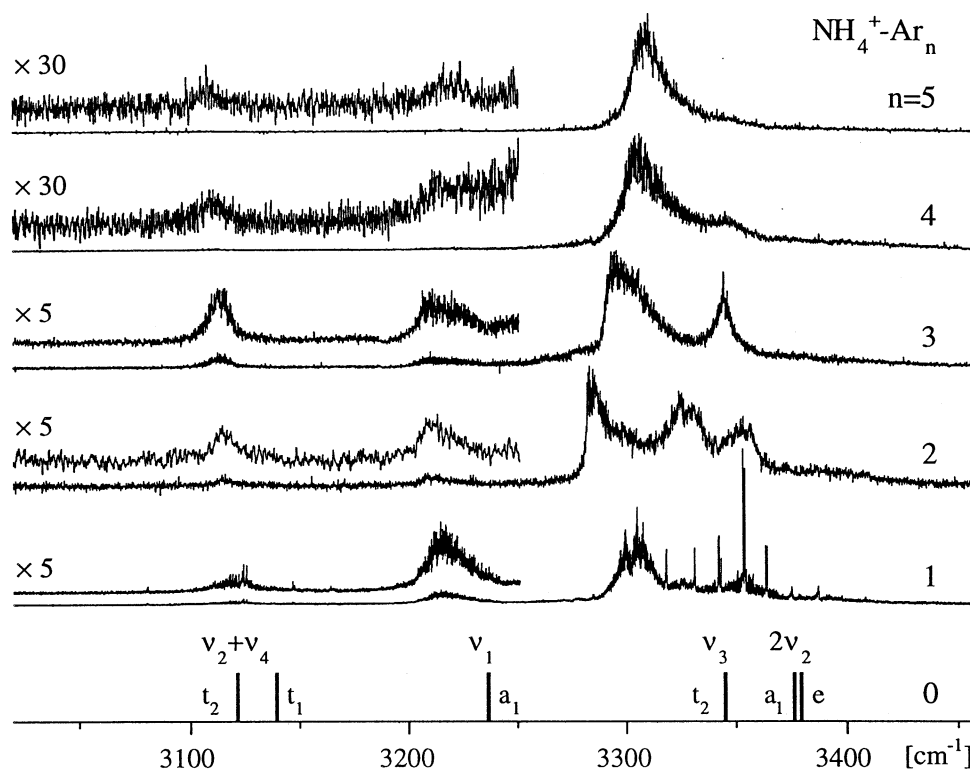
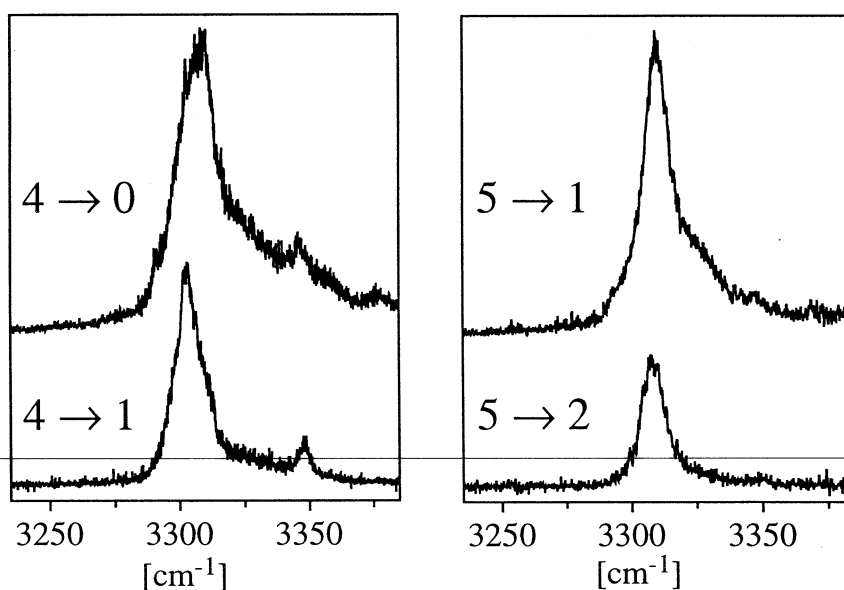


Figure 9.10: Different dissociation channels in NH₄⁺-Ar₄ and NH₄⁺-Ar₅



Photoexcitation of mass selected NH₄⁺-Ar_n complexes in the 3000-3500 cm⁻¹ spectral range resulted in narrow distributions of fragment ion sizes. Table 9.6 summarizes the fragmentation ratios measured for excitation at the respective ν_3 band maxima. For parent complexes with $n < 4$ only molecular NH₄⁺ fragment ions were observed. For larger complexes ($n = 4-7$) fragment cluster ions of the form NH₄⁺-Ar_m ($m > 0$) were also detected with significant intensity, with the channel corresponding to the loss of four Ar atoms being dominant. In a rough approximation, the averaged binding energy can be estimated by dividing the absorbed photon energy by the number of ligands lost. This simple model gives

a binding energy of $\approx 3300/4 = 825 \text{ cm}^{-1}$ per Ar atom. The discrepancy between this value and the theoretical prediction of $\sim 500 \text{ cm}^{-1}$ may arise from several effects, including the neglect of the initial internal energy of the parent cluster ion and the kinetic and internal energy of the respective fragments in the simple view described above, or inadequacy of the calculation. In cases where two significant fragment channels were observed for a given parent cluster photodissociation spectra were measured for each daughter channel. Figure 9.10 shows the respective spectra obtained for $n=4$ and 5. The spectra obtained for both daughter channels are similar in appearance. The bands in the lower mass fragmentation channel are only slightly shifted and broadened compared to the corresponding bands in the larger fragment channel. Similar effects were observed previously for other weakly proton bound systems, like e.g. the HCO⁺-Ar_n and H₃⁺-(H₂)_n [44, 45] series.

9.5.4. Vibrational analysis

First, the group of intense bands lying between 3280 and 3400 cm^{-1} is considered. The strength and proximity of these transitions to the strongly allowed fundamental ν_3 of the NH₄⁺ monomer are strongly suggestive of an assignment to the various symmetry components of this intramolecular vibration arising from complexation-induced symmetry reduction in the system. The measured band centres are summarized in table 9.7 ($n=0-7$). Note that the number of ν_3 components in the spectrum of every particular cluster with $n \leq 4$ agrees nicely with expectations from the respective molecular point groups. Three bands are observed in the Ar₂-NH₄⁺ spectrum, two for Ar-NH₄⁺ and Ar₃-NH₄⁺, and one for Ar₄-NH₄⁺. This tendency can be explained by the reduction of the triply degenerate t_2 vibration of NH₄⁺ to vibrational species a_1 and e when symmetry of the system is lowered down to C_{3v} and to respectively a_1, b_1 , and b_2 species for the case of C_{2v} group, with IR dipole transitions into all components being allowed. If the vertex bound structures favored by the *ab initio* calculations are adopted the symmetry of the Ar_n-NH₄⁺ complexes for $n=0-4$ will change in succession T_d, C_{3v}, C_{2v}, C_{3v}, T_d, giving rise to respectively 1, 2, 3, 2, 1 bands in the ν_3 spectra, as observed experimentally. Theoretical harmonic frequencies calculated at HF level for $n=0-5$ also behave in a similar fashion. The ν_3 splittings predicted from *ab initio* calculations are compared graphically with experimental ones for $n=0-5$ in figure 9.11. Symmetry labels in the respective point groups are given as well. One can see that the patterns of the splittings are in an excellent qualitative and a fair quantitative agreement giving a strong support to the vertex bound structures. Note that for the face bound configurations calculated values of the splittings are substantially smaller.

There is a weak feature slightly shifted to the blue of the $n=4$ ν_3 band, and its proximity to the $n=3$ a_1 component suggests that it may be due to another less stable isomer of Ar₄-NH₄⁺ with three Ar atoms bound to a vertex and a fourth Ar bound to a face of NH₄⁺. As mentioned above, Ar atoms located at the face have less influence on the ν_3 transition frequencies compared to vertex-bound Ar atoms. For the face-bound dimer a blue shift without a significant splitting upon complexation has been calculated. A similar behaviour is predicted for the hexamer ($n=5$) with C_{3v} geometry. This is in line with the experimental observation that only a single band is observed in the spectra of $n=5$ to 7 indicating that further splittings of the ν_3 band must be small. The various transitions arising from the overtone of ν_2 fall also in the range of the ν_3 frequency according to theoretical predictions however they are expected to have much lower intensity than the ν_3 bands. Very weak and broad features centred around 3390 cm^{-1} in the spectra of $n=2$ and 3 may possibly be due to $2\nu_2$ bands.

Now the weak band series between 3200 and 3250 cm^{-1} is considered. It is associated with the totally symmetric NH stretch mode (ν_1) of NH₄⁺ which is of a_1

symmetry in all considered symmetry groups. Thus, it is dipole forbidden for the NH₄⁺ monomer and Ar₄-NH₄⁺ (T_d), while it becomes weakly allowed for complexes with lower symmetry. This prediction is in close agreement with the experimental observation (figure 9.9), that for n=1-3 a weak, but clearly visible band is present in the expected spectral range, while for n=4 the relative intensity of the corresponding band drops drastically. The calculations predict for n=1-3 an intensity ratio of around 0.03 to 0.1 for ν₁ with respect to the ν₃ components again in qualitative agreement with the experiment. The fact that the n=4 band does not vanish completely may again be indicative of less stable isomers with lower symmetry, e.g. one with three Ar atoms bound to vertices and the fourth one bound to a face. For the n=5 complex, the symmetry is also reduced turning ν₁ again into an allowed fundamental. However, as expected, the intensity of the observed band is quite weak indicating that only vertex-bound Ar atoms appreciably distort the symmetric NH stretch mode of the monomer. This observation is supported by the calculations which predict that the ν₁ intensity for the face-bound dimer is about two orders of magnitude lower than for the vertex-bound dimer. In addition, for the Ar₅-NH₄⁺ complex of C_{3v} symmetry the ν₁ band is calculated to be about 3 orders of magnitude weaker than the respective ν₃ transitions, again in qualitative agreement with the experiment. Finally, the ν₁ frequency shifts are considered. The experimental monomer value is not known, and the probably best theoretical prediction comes from the high level force field calculation ν₁=3237 cm⁻¹[193], with an estimated error of a few wavenumbers. The experimental dimer ν₁ frequency of 3215 cm⁻¹ would then imply a red shift of around 20 cm⁻¹. In contrast to the MP2 calculation which predicts a larger shift (45 cm⁻¹), the HF level underestimates it (4 cm⁻¹) similar to the ν₃ component shifts. However, the qualitative trend of the ν₁ shift as a function of cluster size can again be reproduced by the HF computations.

Table 9.7: Vibrational positions in NH₄⁺-Ar_n spectra

Vibrational band positions (in cm⁻¹) for NH₄⁺-Ar_n in photofragmentation spectra recorded on the dominant fragment channel

n	ν ₃		ν ₁	ν ₂ +ν ₄	2ν ₂
1	3305(4)	(a ₁)	3215(4)	3120(3) ^a	
	3347.8(1)	(e)			
2	3284(3)	(b ₂)	3211(3)	3115(2)	3390(8)
	3327(3)	(a ₁)			
	3354(3)	(b ₁)			
3	3298(4)	(e)	3215(4)	3115(2)	3390(8)
	3346(1)	(a ₁)			
4	3306(3)	(t ₂)		3111(2)	
	3347(2) ^b		3217(3) ^b		
5	3310(2)		3220(3)	3107(2)	
6	3314(3)				
7	3317(2)				

^a There are also sharp Q branch like features at 3164.5(1), 3147.1(1), and 3080.4(1) cm⁻¹

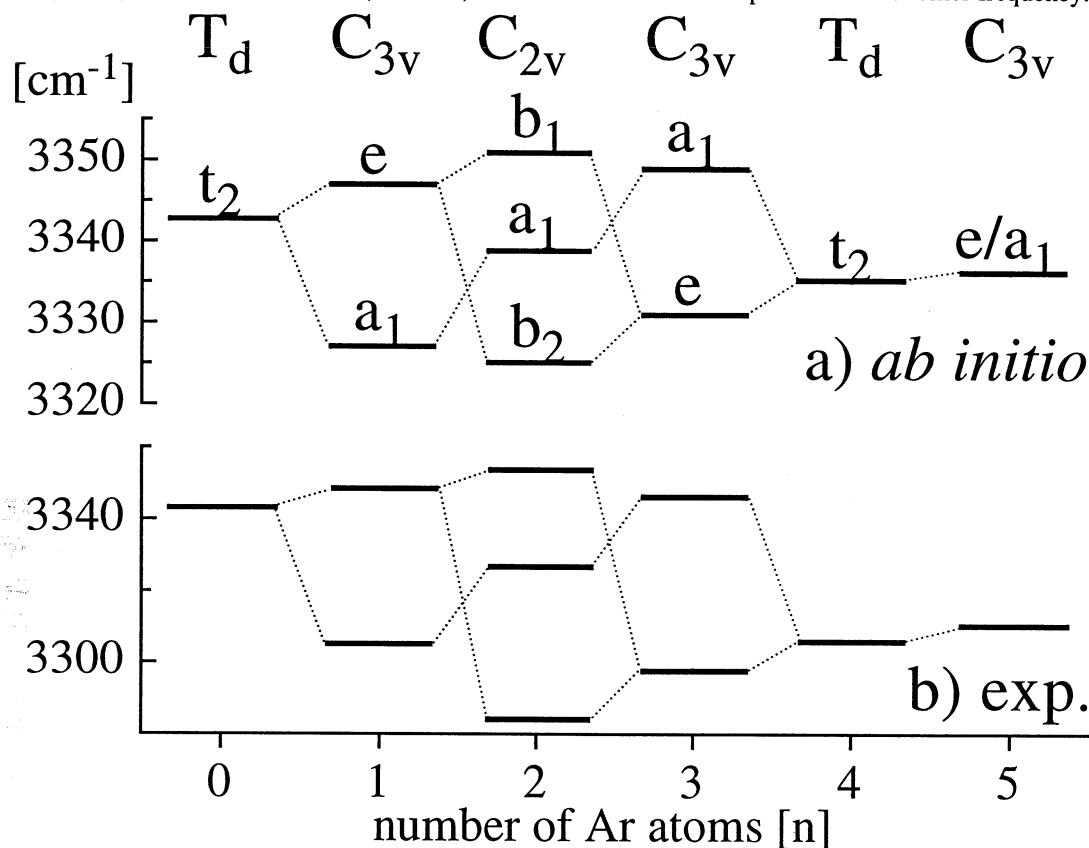
^b assigned to a less stable non-tetrahedral isomer.

The weak transitions in the 3100-3150 cm⁻¹ spectral range are attributed to the various components of the ν₂+ν₄ combination band. The two monomer transitions are calculated to be at 3120.5 (t₂) and 3138.0 (t₁) cm⁻¹. Both, the HF and the MP2 calculations predict only small complexation shifts for the ν₂ and ν₄ fundamentals. Symmetry reduction to C_{3v} or C_{2v} resolves the t₁ and t₂ components into various IR allowed symmetry species. For the dimer, a broad feature around 3120 cm⁻¹ that is probably due to one or more parallel bands is observed, in addition to several perpendicular type features which could not be definitely assigned. The spectra of the larger clusters show only single broad bands and

their positions are given in table 9.7. The components of the overtone of the strong IR active ν_4 fundamental are predicted to be near 2900 cm⁻¹, however an assignment of the discussed bands to these components can be discarded after comparison with the theoretical calculations which predict only small frequency complexation shifts for ν_4 .

Figure 9.11: Graphical representation of Ar_n-NH₄⁺ vibrations

Theoretical (a) and experimental (b) positions of the various components of the ν_3 vibration of NH₄⁺-Ar_n (n=0-5). The *ab initio* values (HF level) are scaled to match the experimental monomer frequency.



With exception of the e component of the dimer's ν_3 band and the unassigned sharp Q branch like features near the $\nu_2+\nu_4$ region, the observed bands do not show resolved rotational structure. The most likely reason for this observation is the finite laser bandwidth of 0.02 cm⁻¹, as may be seen from the dimer's ν_3 band, where the parallel band is congested due to the overlap of several $\Delta K=0$ subbands, while the perpendicular band could be rotationally resolved in respective P, Q, and R branches of separated $\Delta K=\pm 1$ subbands. In addition some homogeneous line broadening processes could conceivably contribute to the broadness of the absorption features.

9.5.5. Summary

The analysis of vibrational bands observed in infrared photofragmentation spectra of mass selected NH₄⁺-Ar_n (n=1-7) cluster ions in conjunction with *ab initio* calculations revealed a consistent picture of the microsolvation process of the ammonium ion surrounded by Ar ligands. The results are in accord with cluster ion geometries where the first four Ar atoms are located at the vertices of the tetrahedron while further Ar atoms occupy equivalent face-bound positions

10. Discussion

10.1. H₂ stretching vibrations in H₂-M⁺ complexes

From preceding theoretical and experimental work, as well as from the data presented in this thesis, it is apparent that the structures of proton bound AHB⁺ species are such that the proton is effectively shared by the stable neutral bases A and B. Generally each constituent tries to adopt the same disposition with respect to the central proton as it would do in the absence of the other. As H₃⁺ is a stable triangular ion, all of the H₂-HM⁺ complexes (at least from those studied to date) appear to be T shaped, in the sense that the H₂ ligand adopts a side approach to the central proton. Such a structure is also expected on electrostatic grounds since the T-shaped geometry is favored by charge-quadrupole forces. Electrostatic forces are also responsible for T-shaped structures of the complexes of the type H₂-M⁺ that do not belong to the proton-bound family (e.g. H₂-Na⁺). A selection of experimentally known complexes between positive ions and molecular hydrogen is presented in table 10.1.

Table 10.1: H₂ stretching vibrations in selected H₂-M⁺ complexes

Ionic complexes H₂-HM⁺ and H₂-M⁺ with experimentally known H₂ stretching frequencies. Note that only about half of them can be considered as proton-bound, for example the H₂-SiH₃⁺ complex is not such.

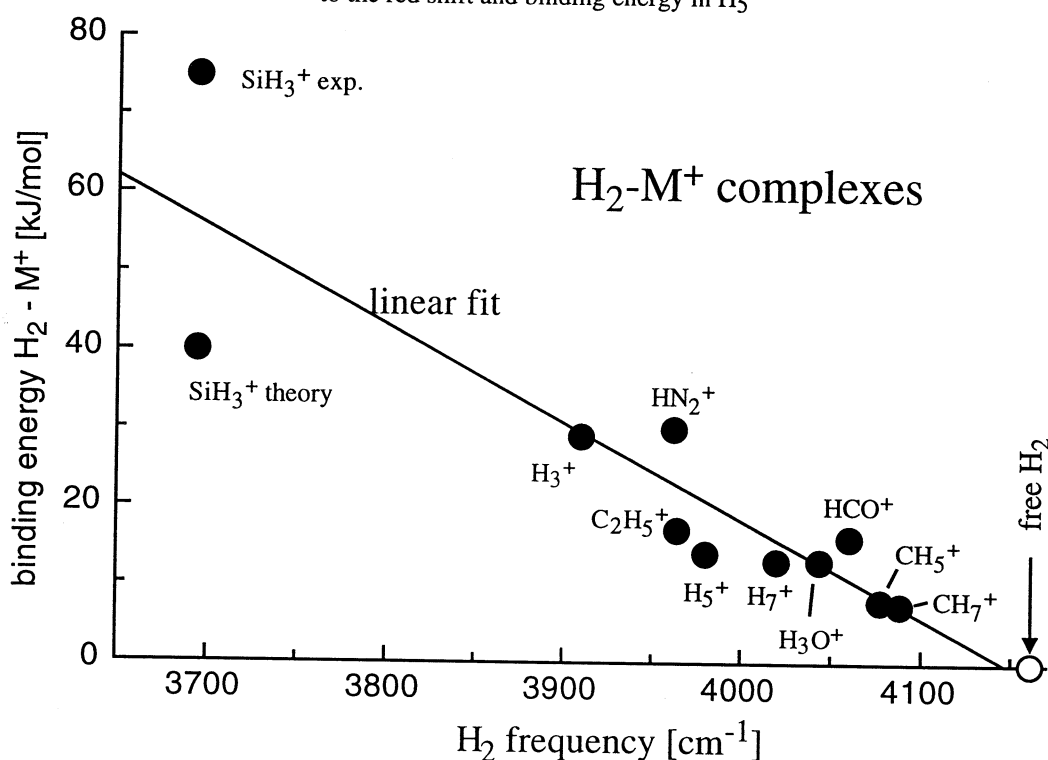
ion HM ⁺ or M ⁺	PA(M) ^a kJ/mol	-ΔH ⁰ (H ₂ -HM ⁺) kJ/mol	H ₂ freq. cm ⁻¹	spectroscopy ref.
NH ₄ ⁺	852	-	4106.4*	this work
H ₃ O ⁺	697	≈13 ^b	4043.7*	this work
H ₅ O ₂ ⁺	-	-	4105	[61]
H ₇ O ₃ ⁺	-	-	4155	[61]
H ₂ -H ₃ O ⁺	-	-	4055	[61]
(H ₂) ₂ -H ₃ O ⁺	-	-	4065	[61]
HCO ⁺	594	16 ^c	4060.3*	this work
HN ₂ ⁺	494.5	30 ^d	3962	this work
SiH ₃ ⁺	-	75 ^e ; 43 ^f	3694.3*	[81]
SiH ₅ ⁺	648	-	3866*	[82]
CH ₅ ⁺	551	7.9 ^g	4077.4*	[75]
H ₂ -CH ₅ ⁺	-	7.4 ^g	4088.2	[75]
C ₂ H ₅ ⁺	-	17 ^h	3964	[67]
H ₃ ⁺	423.4	29 ⁱ	3910	[45]
H ₅ ⁺	-	14 ⁱ	3980	[45]
H ₇ ⁺	-	13 ⁱ	4020	[45]
HXe ⁺	496	-	3890	this work
HAr ⁺	371	28 ^j	3460	this work

* Q branch position (≈ Π←Π transition origin); ^a refs. [133, 164]; ^b ref. [61] ^c ref. [212]; ^d ref. [229]; ^e ref. [271]; ^f theory, D₀ [79]; ^g ref. [78]; ^h ref. [272]; ⁱ ref. [54]; ^j ref [273]

From the inspection of the table certain trends become readily apparent. It has been suggested previously [45, 61] that the red shift in the HH stretching vibration from the free molecule value can be directly correlated with the increase in the strength of the intermolecular bond. Such a correlation can be intuitively understood on the basis of simple qualitative arguments. The formation of the complex is accompanied by partial polarization of the electron density of the H₂ molecule. The density from the H₂ σ bond shifts towards the protonated ion, which serves to establish the incipient intermolecular bond. At the same time the H₂ bond becomes weaker resulting in a vibrational red shift.

Figure 10.1: Binding energy - $\Delta\nu_1$ correlation in H₂-M⁺ complexes

Correlation between binding energies and H₂ stretching frequencies of the H₂-M⁺ ionic complexes. Data is taken from table 10.1. Ions shown near each data point correspond to M⁺, e.g. label H₃⁺ in the figure refers to the red shift and binding energy in H₅⁺



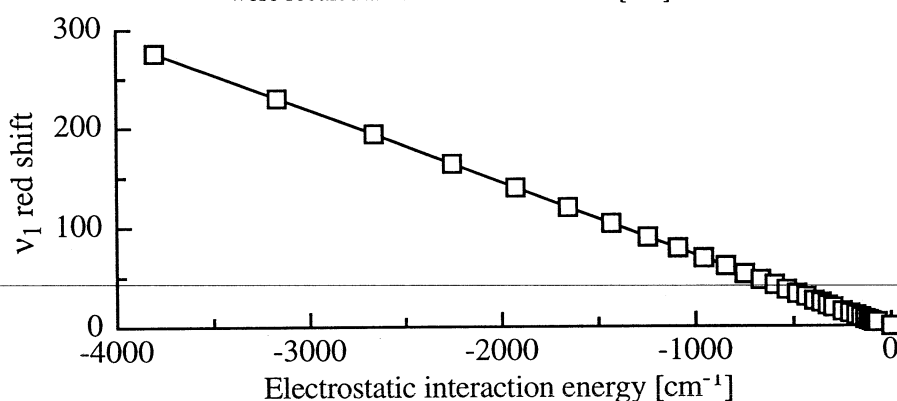
Vibrational frequencies of the complexed H₂ molecules are plotted against binding energies of the respective complexes in figure 10.1. Free H₂ molecule, which can be thought of as a part of a H₂-M⁺ complex with an infinitely small binding energy, is included as well. Though the available data is rather scarce one can see that the correlation between the two properties is generally quite good. It is highly desirable to supplement this correlation with complexes having higher binding energies and respectively lower H₂ vibrational frequencies so that it can be used to estimate the order of magnitudes of binding energies of H₂ molecules to a broad range of substrates (e.g. active sites of catalysts) from known H₂ frequencies (or *vice versa*). At the moment the predictive power of the correlation is limited to relatively weakly bound complexes. It can be noted, however, that the purely theoretical values for the frequencies [274, 275] and experimental estimations for the binding energies

[276, 277] of strongly-bound V^+-H_2 and Co^+-H_2 complexes are very close to the extrapolated linear dependence shown in figure 10.1 adding some amount of confidence in it. From the available spectroscopic data and this correlation one can predict $H_2-NH_4^+$ and XeH_3^+ to be bound by respectively ≈ 5 and ≈ 30 kJ/mol, the conclusions that would be interesting to test experimentally. If these values are correct $H_2-NH_4^+$ becomes the weakest H_2 -solvated ionic complex studied to date explaining the difficulties in producing it in the experiment.

The correlation presented above finds a theoretical support in the work of Poll and Hunt [278]. They calculated Stark-shifts of the rovibrational energy levels of an H_2 molecule perturbed by a point charge as a function of the charge- H_2 separation. If their tables are recalculated to derive the dependence of the red shift in the H_2 stretching frequency as a function of the electrostatic interaction energy between H_2 and the charge in a T-shaped arrangement, a linear correlation is obtained (figure 10.2). The fact that the experimental correlation is also roughly linear may indicate that the binding in the H_2-M^+ complexes is dominated by electrostatic interactions, with repulsive contributions being essentially similar for the considered range of complexes. Deviations from the correlation may arise from a violation of this rather loose assumption of equal repulsion or from an extensive delocalization of the charge on the chromophore unit (the charge is poorly approximated by a point one)

Figure 10.2: Electrostatic energy- $\Delta\nu_1$ correlation in a point charge- H_2 system

Dependence of the red shift of the H_2 ($\nu=1, J=1$) \leftarrow ($\nu=0, J=1$) transition on the magnitude of the electrostatic interaction energy between H_2 and a point charge. For the ($\nu=1, J=0$) \leftarrow ($\nu=0, J=0$) transition the values are nearly identical. The H_2 axis is perpendicular to the line joining H_2 center of mass and the charge. The data were recalculated from table I of ref. [278].



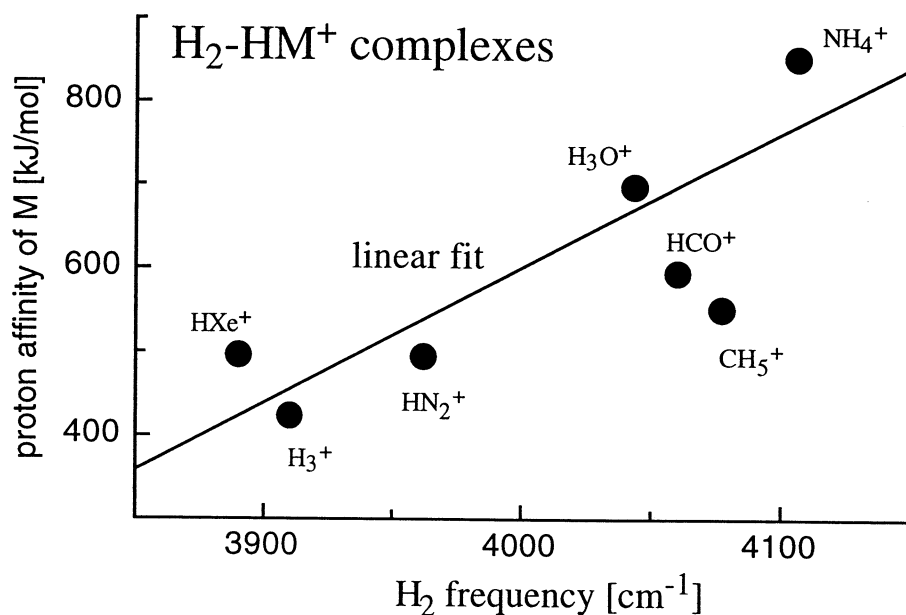
The correlation is expected to break down when the H_2 subunit of the complex loses its individuality completely and a principally different species is formed. For example certain metal cations like Sc^+ tend to form an insertion compound with hydrogen represented by formula $H-Sc-H^+$ [279]. For hydrogen bound-complexes H_2-HM^+ a possibility exists that the proton affinity of M is smaller or comparable to that of molecular hydrogen. In this case spectroscopic properties of the complex will correlate to those of H_3^+ ion. The outcome of

combining an H_2 molecule, a proton and ligands of varying proton affinities is nicely illustrated in a systematic *ab initio* study of the H_2-H^+-A complexes ($A=He, Ne, Ar, Kr$) [280]. As the size and the proton affinity of the rare gas increases, the system is transformed from one resembling an H_3^+ molecule perturbed by a rare gas atom loosely attached to one apex (e.g., $He-H_3^+$, $Ne-H_3^+$), to one consisting of an H_2 molecule bound in a T-shaped fashion to a protonated rare gas diatomic. This latter situation approximates well most of the proton-bound complexes presented in table 10.1 with the exception of ArH_3^+ .

For proton-bound complexes $A-H-B^+$ a very useful correlation between the binding energy and the difference in proton affinities of A and B is known to exist for families of related compounds [281] (e.g. when A and B represent respectively amines and alcohols). In view of the existing link in H_2-M^+ complexes between the binding energies and H_2 frequencies one can expect that the latter correlate with proton affinity of M for their proton-bound subset. Such a dependence is presented in figure 10.3. The quality of the correlation is not as good as for the binding energies-frequencies case, particularly the $H_2-CH_5^+$ complex falls out of it, but it still can be useful since proton affinities are available for a broad range of neutral molecules [133, 164] while binding energy data are sparse.

Figure 10.3: Proton affinity - $\Delta\nu_1$ correlation in proton-bound complexes

Correlation between proton affinities of M and H_2 stretching frequencies of the H_2-HM^+ proton bound complexes. The ArH_3^+ complex is not included here since representing it as H_2-HAr^+ is not quite correct.



The properties of the ionic complexes in which H_2 plays the role of a ligand can be compared to those of related van der Waals complexes. The best documented example of the neutral H_2 containing complexes is undoubtedly H_2-Ar . The most recent studies of this complex contains a number of references to the previous theoretical and experimental works [242, 282]. A high quality 3D potential energy surface is available for this complex [282]

which fully accounts for high resolution IR data, virial coefficients, and vibrational transition pressure-shifting coefficients. The complex is bound by mere 50 cm^{-1} , with more than a half of the well depth being consumed by zero point energy. The rotational constant of H_2 molecule is very much higher than any hindering terms in the potential and it is liable to almost free rotation in the complex. IR transitions observed in the spectrum correlate to the $\Delta J_{\text{H}_2}=0, 2$ and $\Delta v_{\text{H}_2}=0, 1, 2$ transitions in free H_2 (for which they are dipole forbidden), with substructure due to the overall rotation of the complex being superimposed. Similarly the hydrogen dimer complex is composed of a pair of fairly individual freely-rotating hydrogen molecules bound by just 3 cm^{-1} [283]. Certainly both Ar-H_2 and $(\text{H}_2)_2$ are by far more flexible than any of the ionic complexes with H_2 studied to date. The $\text{H}_2\text{-HF}$ complex is not that floppy and even possesses a sort of a T-shaped ordered "structure" represented by $\text{H}_2\cdots\text{HF}$. Spectroscopic studies indicate, however, that both H_2 [284, 285] and HF units [286] of the complex undergo large amplitude motions around their equilibrium positions. Though the observed spectrum could be fitted to a standard rigid asymmetric molecule hamiltonian no structure existed that would reproduce the constants obtained from the fit. The spectrum could be analyzed with more success in terms of a hamiltonian that took into account the hindered internal motion of H_2 . The anisotropy parameters V_2 derived from the analysis is substantial ($\approx 150\text{ cm}^{-1}$) but still far below the corresponding values for the $\text{H}_2\text{-HCO}^+$ and $\text{H}_2\text{-HN}_2^+$ ionic complexes ($\approx 10^3\text{ cm}^{-1}$) presented in this work. From these few examples, it seems, that the presence of the charge-induced interactions has a large impact on the stability as well as on the rigidity of H_2 containing complexes. In $\text{H}_2\text{-HCO}^+$ and $\text{H}_2\text{-HN}_2^+$ the charge-induced dipole interaction is relatively anisotropic, while the charge-quadrupole term adds anisotropy to the system sufficient to lock the complex in the T-shaped structure. The anisotropy of the considerably weaker dipole-quadrupole interaction in $\text{H}_2\text{-HF}$ is clearly not sufficient for this.

10.2. HM stretching vibrations in Rg-HM⁺ complexes

The experimental data obtained in the present work allows systematic comparison of the interaction of Rg atoms with varying size and polarizability with HN₂⁺ and HCO⁺ ions in the bonding region. Various properties of these proton bound complexes are gathered together in table 10.2. Included are the band shifts for the C-H or N-H stretch vibrations (ν_1), differences in proton affinities of rare gas atoms and CO/N₂, force constants for the intermolecular bonds, intermolecular harmonic stretching frequencies and separations calculated from formulae (4.9-4.11), and intermolecular frequencies measured in the experiment. The latter are available mainly for $\nu_1=1$ state since they can be observed in combination with strong ν_1 transition. The table additionally includes some parameters of the theoretical potential energy surfaces generated for some of the complexes by Meuwly [205] such as binding energies and intermolecular frequencies.

Several points that are worthy of note become apparent upon inspection of the table.

(1) As expected, the strength of the intermolecular bond in both HCO⁺ and HN₂⁺ containing species increases in the order He<Ne<Ar, in line with the proton affinities and polarizabilities of the attached rare gases. The strengthening of the intermolecular bond is reflected in the increase in the stretching force constants. For example from He-HCO⁺ to Ar-HCO⁺ and from He-HN₂⁺ to Ar-HN₂⁺ the force constant increases by roughly one order of magnitude. Binding energies available for He and Ar containing complexes are also much greater for the heavier ligands. The ν_1 red shifts, which reflect the influence of the rare gas on the effective proton potential, vary in the same direction. On the other hand the average intermolecular separations and stretching frequencies for a given chromophore remain on roughly the same level. The similarity is most probably due to a cancellation of two competing effects. The force constant increases parallel to the reduced mass for the intermolecular vibration and the frequency does not change very much since it is related to their ratio. As for the separation the polarization attraction is stronger for the larger rare gas atoms but their electron clouds are more extensive and overlap repulsion becomes important already at longer intermolecular distances. Optimal intermolecular separation results from the balance of these two effects.

(2) In the HCO⁺ based complexes the degree of distortion of the chromophore properties as well as the intermolecular bond strengths are systematically lower than they are for the complexes involving HN₂⁺. All attributes of the complexes appear to be affected. Intermolecular separations are on average smaller, and intermolecular frequencies, force constants, and ν_1 frequency red shifts are larger for the HN₂⁺ containing species. The latter property seems to be by far the most sensitive to the constitution of the complex. Such increase in the bond strength is in line with thermochemical studies which demonstrate that dissociation energies of proton-bound complexes are usually inversely correlated with the

- Discussion -

difference in the constituents' proton affinities [281]. As one can see from the second row of table 10.2 the proton affinity of N₂ as compared to that of CO is somewhat closer to the proton affinities of rare gas atoms. As a result the central proton is more equally shared by the bases in HN₂⁺ containing complexes and the complexes' binding energies are consequently higher. Figure 10.4 displays the correlation between $\Delta PA = PA(N_2 \text{ or } CO) - PA(Rg)$, and the respective ν_1 red shift and intermolecular stretching frequency. The origin of the apparent linearity between ν_1 red shift and ΔPA is at present unclear but the "practical" implications of this empirical observation for spectroscopic studies of Rg-HM⁺ complexes are pretty obvious.

Table 10.2: Spectroscopic and theoretical properties of Rg-HCO⁺/HN₂⁺
Compilation of spectroscopic properties of Rg-HCO⁺ and Rg-HN₂⁺ ionic complexes.

	He-HCO ⁺	Ne-HCO ⁺	Ar-HCO ⁺	He-HN ₂ ⁺	Ne-HN ₂ ⁺	Ar-HN ₂ ⁺
ΔPA [kJ/mol] ^a	416	393	223	317	294	124
k''_s [N/m] ^b	1.6±0.1	4.8±0.3	17±3	4.8±0.4	12.8±0.4	37.8±1.5
ν''_s [cm ⁻¹] Millen ^c	89±3	83±3	131±11	150±10	135±2	195±4
ν''_s [cm ⁻¹] theory	95 [*]	-	128 [¥]	152 [¥]	-	-
ν'_s [cm ⁻¹] exp. ^d	-	-	146 ^e	163	158	≥250
ν'_s [cm ⁻¹] theory	-	-	143 [¥]	165 [¥]	-	-
ν'_b [cm ⁻¹] exp. ^f	-	-	-	96	128	-
ν'_b [cm ⁻¹] theory	-	-	169 [¥]	118 [¥]	-	-
D''_0 [cm ⁻¹] theor. / exp. ^g	207 [*]	438 [*]	1593 [¥]	341 [¥]	-	2781.5
R''_{cm} [Å] ^h	3.648(2)	3.654(2)	3.797(2)	3.247(3)	3.281(1)	3.429(1)
R''_{Rg-H} [Å]	1.983(2)	1.989(2)	2.132(2)	1.724(3)	1.756(1)	1.904(1)
$\langle \Theta_{bend} \rangle''$ theor [¥]			6.5 [¥]	8.5 [¥]		
ν_1 red shift [cm ⁻¹] exp.	12.4	42.5	273.7	75.5	180.5	≈950
ν_1 red shift [cm ⁻¹] theory			322.6 [¥]	93.1 [¥]		

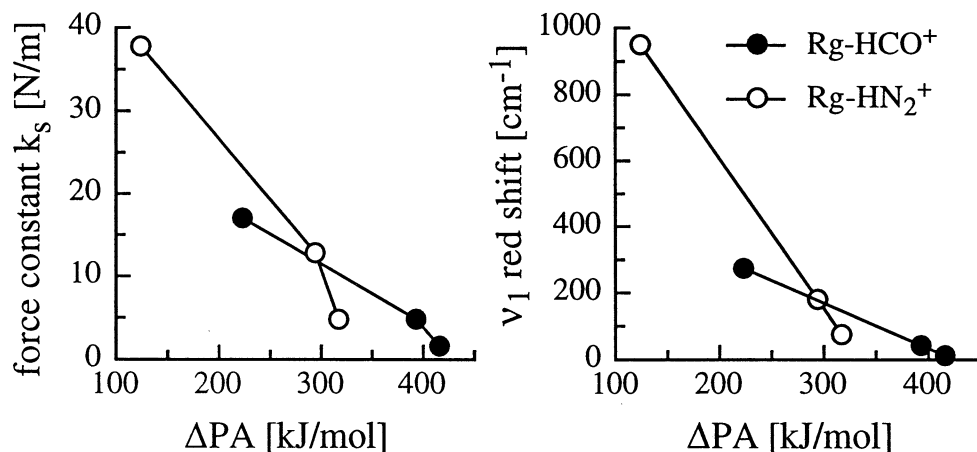
[¥] theoretical value obtained from the corrected 2D potential energy surface [205]; ^{*} theoretical value obtained from the frozen core 1D potential energy surface [205]; ^a proton affinities of He, Ne, Ar, N₂, and CO are 178, 201, 371, 495, and 594 kJ/mol [133, 164]; ^b from (4.11); ^c from (4.10); ^d ($\nu_1 + \nu_s$)- ν_1 ; ^e ν''_s of 127 cm⁻¹ is available experimentally from the $\nu_1 + \nu_s - \nu_s$ sequence band; ^f ($\nu_1 + \nu_b$)- ν_1 ; ^g experimental value obtained from rovibrational predissociation onset; ^h from (4.9);

The ionic complexes Rg-HCO⁺/HN₂⁺ can be compared to their isoelectronic neutral Rg-HCN van der Waals companions. As in the case with H₂ solvated complexes, there appear to be essential differences between ionic and neutral species. Although both ions and neutrals share a common linear minimum energy geometry, with the proton occupying an intermediate position, the ions are considerably more strongly bound and feature a somewhat stiffer intermolecular bending coordinate. In particular the *ab initio* studies of the He-HCN complex [287] indicate that around 75% of its intermolecular potential well depth (≈ 25.3 cm⁻¹) is consumed by zero point energy. Zero point level is situated above the barrier for the internal rotation of HCN making it essentially a free internal rotor. Other

known He containing van der Waals complexes are similarly characterized by fragile and floppy intermolecular bonds. Though the complexes of HCN with the larger rare gas atoms have somewhat more anisotropic potentials large zero-point angular libration is a characteristic feature of all of them. Average intermolecular angles determined from quadrupole coupling constants are 27, 31, and 47° for complexes with Kr, Ar, and Ne respectively. These values are to be compared with the average intermolecular angles predicted for He-HN₂⁺ and Ar-HCO⁺ complexes, which are both below 10°. Intermolecular bending frequencies are rather disparate too. In Ar-HCN complex it is as low as 6.1 cm⁻¹ [202] more than one order of magnitude less than the predicted value for Ar-HCO⁺. Differences between neutrals and ions extend also to the complexation induced red shifts in ν_1 . The red shift of 2.7 cm⁻¹ for Ar-HCN [203] is smaller than that for He-HCO⁺ - the weakest ionic complex studied in this work. The smaller red shift in the neutral complexes reflect their weaker influence of the properties of the chromophores and can be connected to the smaller intermolecular binding energies.

Figure 10.3: Correlation between ΔPA , k_s and $\Delta\nu_1$ for Rg-HCO⁺/HN₂⁺

Note that the red shift for the Ar-HN₂⁺ complex was estimated from combination band positions and may be in ± 50 cm⁻¹ error.



Thus it appears that the Rg-HN₂⁺/HCO⁺ ionic complexes feature more directional intermolecular bonds and larger well depths than do their isoelectronic neutral counterparts. The increase in the dissociation energy for the charged species is expected from the charge-induced polarization interaction. However, the origin of the influence of the charge on the anisotropy of the intermolecular potential is not immediately evident, since the charge-induced-dipole interaction is not anisotropic as long as the charge is localized. Moreover, distributing the charge along the HCO⁺ (HN₂⁺) axis and relying on the charge-induced-dipole interaction alone will result in a broadside approach of the Rg ligands, contrary to what is observed in the experiment. Evidently, the structure and presumably the anisotropy of the Rg-HN₂⁺/HCO⁺ complexes is substantially influenced by higher order interactions, in particular by that of the permanent dipole moment of HCO⁺/HN₂⁺ with the induced dipole on the rare gas. To this end it is interesting to note that distributed multipole analysis gives a correct prediction for the optimum geometry of these ionic complexes [205].

11. Outlook

Several directions for the high-resolution vibrational predissociation studies of ionic complexes can be proposed. This thesis is concerned with relatively simple systems, all the complexes presented in this work are small closed-shell chromophore ions solvated by the most primitive ligands one can possibly think of. Though such complexes are of interest to theoreticians as benchmarks for modeling more complicated aggregates, we feel that in future the center of attention should be shifted towards the systems of higher chemical relevance. Possible candidates include (a) intermediates of proton-transfer reactions with substrates other than rare gases such as complexes between π -systems and protonated neutrals of type HM^+ . (b) Vibrational predissociation spectroscopy of negative cluster ions. A systematic study of $\text{S}_{\text{N}}2$ reaction intermediates would be a very interesting application [288]. In addition there are many systems of fundamental importance, e.g. solvated electrons, among the negatively charged clusters. (c) Metal-hydrocarbon complexes, particularly for the metals with the pronounced catalytic activity [289]. Unfortunately all of these projects require substantial modifications to the experimental setup and are viewed as a long-term goal. In the meanwhile fundamental studies of Rg containing complexes will probably be continued though with more complicated chromophore ions (either with larger size or with electronic state other than ^1A).

12. Appendix.

Line positions of rotationally resolved bands

Table A1: He-HCO⁺ v₁ line positions

Rotational line positions for P and R branches of the v₁ band of He-HCO⁺. Due to perturbations, an extra line appears at certain J' values. Differences ($\times 10^{-3}$ cm⁻¹) between the measured line positions and those calculated using the constants given in Table 7.1 are listed in the last column.

J'	P branch [cm ⁻¹]	exp-fit [$\times 10^{-3}$ cm ⁻¹]	R branch [cm ⁻¹]	exp-fit [$\times 10^{-3}$ cm ⁻¹]
0	3075.733	0		
1	75.150	-3	3076.899	6
2	74.578	6	77.476	5
3	73.991	-1	78.044	-5
4	73.456	44	78.663	38
4	73.389	-23	78.597	-28
5	72.826	-8	79.199	-1
6	72.247	-8	79.764	-10
7	71.688	10	80.354	9
8	71.226	123	81.044	130
8	70.767	-336	80.582	-332
9	70.496	-33	81.446	-35
10	70.005	48	82.092	47
11	69.766	379	82.978	372
11	68.773	-614	81.987	-619
12	68.541	-279	82.899	-265
13	68.069	-186	83.527	-192
14	67.710	17	84.291	21
14	67.376	-317	83.947	-323
15	66.788	-345	84.472	-345

Table A2: Ne-HCO⁺ v₁ line positions

Line positions of the v₁ bands of ²⁰Ne-HCO⁺ and ²²Ne-HCO⁺ given with a 3000 cm⁻¹ offset. Differences ($\times 10^{-3}$ cm⁻¹) between the measured line positions and those calculated using the constants given in Table 7.2 are given in brackets beside each entry.

J''	P(J'') ²⁰ Ne	R(J'') ²⁰ Ne	P(J'') ²² Ne	R(J'') ²² Ne	J''	P(J'') ²⁰ Ne	R(J'') ²⁰ Ne
0		46.325 (5)			33	40.196 (5)	53.462 (5)
1	45.916 (-5)	46.528 (7)		46.385(-10)	34	40.037 (-2)	53.691 (1)
2	45.720 (-2)	46.727 (4)	45.654(17)	46.587 (0)	35	39.888 (0)	53.925 (-3)
3	45.525 (0)	46.926 (0)	45.452 (2)	46.790(10)	36	39.738 (-1)	54.167 (0)
4	45.332 (3)	47.132 (2)	45.263 (-1)	46.976 (3)	37	39.595 (2)	54.410 (4)
5	45.133 (-1)	47.336 (2)	45.072 (-7)	47.170 (2)	38	39.447 (-2)	54.651 (4)
6	44.938 (-2)	47.540 (0)	44.892 (-2)	47.362 (-2)	39	39.301 (-5)	54.897 (8)
7	44.748 (0)	47.750 (4)	44.714 (2)	47.560 (-1)	40	39.172 (5)	55.131 (-3)
8	44.554 (-1)	47.951 (-3)	44.527 (-2)	47.763 (5)	41	39.033 (3)	55.375 (-5)
9	44.365 (0)	48.164 (2)	44.345 (-4)	47.949 (-7)	42	38.892 (-5)	55.635 (6)
10	44.175 (0)	48.372 (0)	44.172 (3)	48.148 (-7)	43	38.767 (2)	
11	43.984 (-3)	48.582 (0)	43.987 (-3)	48.353 (-3)	44	38.636 (0)	56.130 (0)
12	43.799 (0)	48.795 (1)	43.813 (1)	48.555 (-1)	45	38.512 (1)	
13	43.617 (4)	49.005 (-1)	43.635 (-1)	48.761 (3)	46	38.385 (-3)	56.640 (-2)
14	43.426 (-2)	49.216 (-3)	43.462 (1)	48.963 (1)	47	38.270 (2)	56.899 (-2)
15	43.246 (1)	49.431 (-2)	43.284 (-1)	49.156 (-9)	48	38.150 (-1)	57.162 (-1)
16	43.059 (-3)	49.643 (-5)	43.112 (0)	49.373 (3)	49	38.042 (4)	57.428 (0)
17	42.880 (-2)	49.860 (-3)	42.940 (-1)	49.588(12)	50	37.931 (2)	
18	42.701 (-1)	50.080 (0)	42.766 (-3)	49.766(-16)	51	37.823 (2)	57.964 (0)
19	42.521 (-2)	50.302 (4)	42.601 (1)	49.988 (-2)	52	37.719 (0)	
20	42.346 (-1)	50.518 (2)	42.436 (5)	50.198 (0)	53	37.616 (-5)	
21	42.172 (1)	50.740 (3)	42.257 (-7)	50.412 (4)	54	37.530 (4)	
22	41.994 (-3)	50.958 (1)	42.100 (2)	50.632 (14)	55	37.435 (0)	
23	41.825 (0)	51.174 (-4)	41.940 (7)	50.822 (-8)	56	37.353 (5)	
24	41.651 (-2)	51.402 (0)	41.772 (2)	51.040 (-2)	57	37.264 (-2)	
25	41.484 (0)	51.624 (-1)	41.603 (-5)	51.256 (1)	58	37.184 (-4)	
26	41.318 (2)	51.846 (-4)		51.464 (-5)	59	37.112 (-3)	
27	41.149 (-1)	52.073 (-3)		51.697 (13)	60	37.046 (-1)	
28	40.983 (-3)	52.302 (0)		51.907 (7)	61	36.981 (-3)	
29	40.828 (5)	52.528 (-3)		52.112 (-5)			

- Appendix -

30	40.663 (0)	52.757 (-4)	52.327 (-8)	(70)*	36.678 (2)
31	40.506 (2)	52.989 (-2)		(71)*	36.678 (3)
32	40.346 (-1)	53.225 (1)		(72)*	36.678 (-3)

* head in P branch

Table A3: Ar-HCO⁺ v₁ line positions

Line positions of the v₁ bands of Ar-HCO⁺ and Ar-H¹³CO⁺. Line positions of v₁ bands of ³⁶Ar-HCO⁺ can be calculated using the constants given in the text.

J"	R(J") normal	P(J") normal	R(J") ¹³ C	P(J") ¹³ C	J"	R(J") normal	P(J") normal	R(J") ¹³ C
0	2815.201		2785.879		33	2821.607	2812.509	2792.178
1	15.343	2814.933	86.012	2785.604	34	21.851	12.482	92.424
2	15.485	14.803	86.155	85.479	35	22.103	12.458	92.666
3	15.634	14.673	86.302	85.358	36	22.352	12.436	92.920
4	15.785	14.554	86.447	85.237	37	22.603		93.176
5	15.941	14.439	86.602	85.119	38	22.858		93.455
6	16.098	14.325	86.756	85.003	39	23.118		93.801
7	16.263	14.211	86.919	84.890	40	23.377		94.092
8	16.427	14.104	87.076	84.782	41	23.641		94.363
9	16.595	14.003	87.234	84.682	42	23.918		94.628
10	16.766	13.902	87.410	84.576	43	24.161		94.910
11	16.949	13.808	87.576	84.472	44	24.425		95.177
12	17.125	13.712	87.758	84.388	45	24.687		95.460
13	17.308	13.624	87.942	84.295	46	24.980		
14	17.494	13.540	88.115	84.207	47	25.251		
15	17.686	13.459	88.307	84.123	48	25.532		
16	17.879	13.378	88.488	84.043	49	25.829		
17	18.070	13.299	88.679	83.965	50	26.115		
18	18.273	13.228	88.877	83.893	51	26.406		
19	18.474	13.158	89.073	83.827	52	26.705		
20	18.678	13.091	89.273	83.760	53	26.992		
21	18.886	13.028	89.479	83.693	54	27.294		
22	19.100	12.971	89.683	83.627	55	27.598		
23	19.314	12.909	89.898	83.567	56	27.896		
24	19.529	12.860	90.110	83.508	57	28.193		
25	19.752	12.806	90.326	83.456	58	28.502		
26	19.976	12.760	90.548	83.411	59	28.807		
27	20.197	12.714	90.770	83.366	60	29.114		
28	20.429	12.674	90.994	83.326	61	29.420		
29	20.660	12.636	91.221	83.287	62	29.719		
30	20.891	12.602	91.461		63	30.027		
31	21.129	12.569	91.690		64	30.320		
32	21.369	12.535	91.937		65	30.665		

Table A4: Ar-HCO⁺ v₁ + v₂ line positions

Line positions of the v₁ + v₂ band of Ar-HCO⁺. R branch lines coincident with stronger Q branch lines are marked with asteriks.

J"	R(J")	Q(J")	P(J")	J"	R(J")	Q(J")	P(J")
0	3696.789*			20	3700.948	3698.006	
1	96.935	3696.647		21	1.251	98.166	3695.234 [‡]
2	97.095*	96.664	3696.387	22	1.477	98.332	
3	97.258*	96.689	96.270	23	1.790	98.484	
4	97.427	96.720	96.155	24	2.082	98.645	
5	97.594	96.751	96.056	25	2.352	98.793	
6	97.761	96.789	95.963	26	2.631	98.956	
7	97.965	96.840	95.865	27	2.913	99.110	
8	98.166*	96.894	95.782	28	3.197	99.273	
9	98.368	96.954	95.709	29	3.477	99.435	
10	98.578	97.022	95.640	30	3.775	99.609	
11	98.793*	97.095	95.576	31	4.062	99.790	
12	99.003	97.176	95.517	32	4.354	99.959	
13	99.222	97.258	95.467	33	4.655	3700.124	
14	99.454	97.351	95.415	34	4.965	0.290	
15	99.687	97.445	95.374	35	5.278		
16	99.923	97.544	95.337	36	5.605		
17	3700.167	97.647	95.301	37	5.945		
18	0.411	97.758		38	6.273		

- Appendix -

44	96.142	84.166	71.870	90	9.016
45	96.373	84.137	72.095	91	9.298
			head		
			2759.557		head
					2783.903

Table A7: Ar-HCO⁺ 2955 cm⁻¹ band line positions

J''	R(J'')	P(J'')	J''	R(J'')	P(J'')	J''	R(J'')	P(J'')
0	2955.546		17	2960.309	2955.204	33	2965.101	2956.068
1	55.733	2955.242	18	60.662	55.302	34	65.319	
2	55.948	55.154	19	61.029	55.392	35	65.527	
3	56.115	55.078	20	61.393	55.487	36	65.732	
4	56.338		21	61.748	55.587	37	65.935	
5	56.566		22	62.099	55.682	38	66.150	
6	56.814		23	62.437	55.775	39	66.352	
7	57.071		24	62.755	55.852	40	66.553	
8	57.336	54.815	25	63.068	55.925	41	66.744	
9	57.600	54.815	26	63.389	55.988	42	66.950	
10	57.949	54.815	27	63.648	56.027	43	67.149	
11	58.246	54.815	28	63.906		44	67.353	
12	58.555		29	64.164	56.068	45	67.556	
13	58.894	54.921	30	64.410	56.068	46	67.763	
14	59.235	54.980	31	64.645	56.068	47	67.992	
15	59.592	55.041	32	64.877	56.068	48	68.194	
16	59.956	55.117						

Table A8: Positions of $\nu_1+\nu_8$, 3068, and 3125 cm⁻¹ bands of Ar-HCO⁺

These three transitions were grouped together because of their similar band structure. Perturbations in the upper states provoke formation of 2 extra heads in P branches of these bands (heads are marked with asterisks in the table). Besides normal P-head arising from a positive ΔB value is possible. Certain perturbed upper state J levels occur twice. Lines are labeled in terms of upper state J.

J'	2961 cm ⁻¹ band		3068 cm ⁻¹ band		3125 cm ⁻¹ band	
	R(J')	P(J')	R(J')	P(J')	R(J')	P(J')
0		2961.029		3068.034		3124.801
1	2961.286	60.890	3068.303	67.908	3125.070	24.674
2	61.428	60.764	68.449	67.789	25.208	24.553
3	61.576	60.662	68.609	67.679	25.304	24.374
4	61.748	60.543	68.771	67.572	25.478	24.281
5	61.900	60.444	68.947	67.485	25.612	24.152
					25.739	24.281
6	62.066	60.341	69.130	67.399	25.841	24.119
7	62.240	60.245	69.325	67.334	25.993	23.997
8	62.416	60.158	69.553	67.293*	26.153	23.891
			69.172	66.911*		
9	62.600	60.069	69.819	67.293*	26.338	23.812
			69.434	66.911*		
10	62.786	59.993	69.669	66.882	26.504	23.716
11	62.977	59.924	69.894	66.840	26.682	23.629
12	63.183	59.857	70.118	66.786	26.866	23.545
13	63.389	59.803	70.330	66.737	27.072	23.484
14	63.626		70.539	66.699	27.244	23.389
15	63.858		70.766	66.643	27.431	23.320
	63.458					
16	64.101	59.721*	70.989	66.609	27.646	23.267
	63.716	59.314*				
17	64.361	59.721*	71.209		27.879	23.230*
	63.961	59.314*				
18	64.220	59.314*	71.451		28.137	23.230*
19	64.471	59.314*	71.694		28.431	23.230*
20	64.744	59.314*	71.942			
21	65.035	59.314*	72.211	66.501*		
22			72.497			
23			72.787			
24			73.144			
25			73.427			
26			73.723		28.634	21.605*
27			74.023		28.930	21.605*
28			74.297		29.182	21.605*

- Appendix -

29			74.590		29.432	21.605*
30			74.886		29.662	21.573
31			75.185		29.861	21.513
32			75.506		30.078	21.465
33					30.237	21.371
					30.322	21.448
34					30.484	21.344
35					30.693	21.282
36					30.894	21.228
37					31.091	21.150
38					31.299	21.101
39					31.503	21.048
40					31.712	20.990
41					31.920	20.937
42					32.140	20.878
43					32.372	20.821
44						20.765
45						20.714

Table A9: Line positions of $\nu_1+\nu_s$ band of Ar-H¹³CO⁺

J''	P(J'')	R(J'')	J''	P(J'')	R(J'')	J''	P(J'')	R(J'')
1	2928.495	2928.905	14	2927.317	2931.240	27	2926.316	2933.645
2	28.365	29.055	15	27.241	31.425	28	26.246	33.830
3	28.248	29.210	16	27.168	31.617	29	26.164	34.018
4	28.130	29.371	17	27.095	31.809	30	26.085	34.193
5	28.026	29.646	18	27.019	32.011	31	26.012	34.379
6	27.934	29.793	19	26.950	32.132	32	25.929	34.567
7	27.934	29.963	20	26.885	32.347	33	25.855	34.747
8	27.823	30.135	21	26.742	32.538	34	25.778	34.930
9	27.729	30.317	22	26.696	32.724	35	25.701	35.123
10	27.637	30.502	23	26.627	32.909	36	25.626	35.325
11	27.553	30.684	24	26.550	33.095	37	25.556	35.501
12	27.476	30.867	25	26.476	33.271	38	25.494	35.703
13	27.394	31.048	26	26.400	33.462	39		35.936

Table A10: He-HN₂⁺ ν_1 line positions

Rotational line positions of the ν_1 band of He-HN₂⁺. Differences ($\times 10^{-2}$ cm⁻¹) between the measured and calculated line positions are given at the end of each entry

J	P(J)	R(J)	J	P(J)	R(J)
0		3159.21/01	13	3150.41/01	3169.67/01
1	3157.77/-01	59.94/01	14	49.90/01	70.54/-01
2	57.11/02	60.70/04	15	49.41/02	71.50/03
3	56.42/01	61.43/00	16	48.93/01	72.41/01
4	55.76/02	62.18/-01	17	48.49/02	73.36/01
5	55.110/01	62.94/-02	18	48.04/00	74.29/-03
6	54.45/-01	63.76/01	19	47.64/02	75.34/03
7	53.82/-01	64.54/-02	20	47.23/00	76.34/03
8	53.21/-01	65.37/00	21	46.84/-02	77.37/04
9	52.62/-01	66.20/00	22	46.56/04	78.33/-05
10	52.02/-02	67.04/00	23	46.16/-06	79.44/-01
11	51.46/-02	67.85/-04	24	45.94/01	
12	50.92/-01	68.74/-02	25	45.67/00	

Table A11: He-HN₂⁺ combination bands' line positions

Rotational line positions of the $\nu_1+\nu_s$ and $\nu_1+\nu_b$ bands of He-HN₂⁺. Differences between measured calculated wavenumbers are given in brackets.

J	$\nu_1+\nu_b^\ddagger$		$\nu_1+\nu_s^\yenmark$	
	P(J)	R(J)	P(J)	R(J)
0		3255.056 (29)		3322.23 (08)
1		55.761 (14)	3320.68 (-08)	22.80 (01)
2	3252.924 (07)	56.456 (-17)	20.08 (05)	23.46 (03)
3	52.236 (06)	57.170 (-33)	19.21 (-07)	24.01 (-01)
4	51.529 (-22)	57.985 (48)	18.51 (01)	24.55 (-05)
5	50.847 (-30)	58.611 (-60)	17.69 (-01)	25.17 (03)
6	50.251 (44)	59.432 (32)	16.90 (03)	25.64 (-02)

- Appendix -

7	49.472 (-67)	60.159 (37)	16.06 (05)	26.09 (-04)
8	48.893 (24)	60.812 (-21)	15.17 (05)	26.55 (-02)
9	48.211 (17)	61.522 (-05)	14.08 (-11)	26.95 (-02)
10			13.22 (-03)	27.36 (03)
11	46.805 (-04)		12.33 (08)	
12			11.26 (04)	
13			10.15 (-00)	
14			09.00 (-03)	

‡ Q branch maximum at 3254.388 cm⁻¹

¥ R branch head at 3328.46 cm⁻¹

Table A12: Ne-HN₂⁺ line positions I

Line positions of the ν_1 band of Ne-HN₂⁺ for three studied isotopomers. All line positions are given with 3000 cm⁻¹ offset.

J''	P(J) normal	R(J) normal	P(J) 22Ne	R(J) 22Ne	P(J) 15N	R(J) 15N	J''	P(J) normal
0		53.781		53.477		38.108	44	
1	53.295	54.045	53.026	53.737	37.592	38.330	45	46.893
2	53.043	54.298	52.798	53.993	37.376	38.592	46	46.811
3	52.830	54.554	52.578	54.241	37.158	38.846	47	46.741
4	52.585	54.826	52.364	54.494	36.932	39.110	48	46.677
5	52.365	55.097	52.151	54.753	36.720	39.370	49	46.605
6	52.142	55.380	51.940	55.015	36.508	39.653	50	46.534
7	51.927	55.654	51.740	55.281	36.310	39.931	51	46.470
8	51.723	55.939	51.541	55.552	36.112	40.214	52	46.410
9	51.509	56.228	51.345	55.826	35.915	40.498	53	46.329
10	51.307	56.524	51.146	56.110	35.731	40.794	54	46.251
11	51.114	56.824	50.968	56.395	35.547	41.100	55	46.174
12	50.923	57.125	50.783	56.684	35.368	41.400	56	46.079
13	50.732	57.435	50.604	56.975	35.199	41.712	57	45.980
14	50.549	57.742	50.430	57.272	35.027	42.025		
15	50.371	58.063	50.263	57.576	34.861	42.341		
16	50.197	58.383	50.094	57.883	34.718	42.676		
17	50.031	58.705	49.935	58.190	34.556	42.997		
18	49.863	59.035	49.782	58.506	34.409	43.336		
19	49.702	59.375	49.633	58.828	34.270	43.673		
20	49.557	59.713	49.483	59.146	34.139	44.017		
21	49.400	60.050	49.343	59.473	34.006	44.356		
22	49.250	60.398	49.207	59.802	33.888	44.713		
23	49.109	60.743	49.067	60.136	33.755	45.065		
24	48.970	61.109	48.941	60.468	33.654	45.416		
25	48.838	61.463	48.815	60.809	33.528	45.775		
26	48.712	61.819	48.694	61.160	33.432	46.137		
27	48.582	62.186	48.576	61.502		46.481		
28	48.468	62.553	48.462	61.860		46.854		
29	48.349	62.935	48.355	62.207				
30	48.239	63.302	48.254	62.567				
31	48.124	63.675	48.144	62.927				
32	48.037	64.067	48.041	63.297				
33	47.928	64.445	47.953	63.663				
34	47.831	64.832	47.862	64.025				
35	47.733	65.214	47.772	64.402				
36	47.646	65.615	47.685	64.771				
37	47.557	66.000	47.593	65.127				
38	47.474	66.399	47.519	65.482				
39	47.395	66.794	47.420	65.847				
40	47.312		47.332					
41	47.225		47.250					
42	47.131		47.169					
43	47.049		47.096					

Table A13: Ne-HN₂⁺ line positions II

Line positions of the $\nu_2+\nu_3+\nu_b$ bands of Ne-HN₂⁺ for three studied isotopomers. All line positions are given with 3000 cm⁻¹ offset.

J''	normal		22Ne		15N	
	P(J)	R(J)	P(J)	R(J)	P(J)	R(J)
0		72.098		71.909		-4.39

- Appendix -

1	71.608	72.338	71.466	72.166	-4.88	-4.15
2	71.366	72.585	71.243	72.392	-5.09	-3.92
3	71.121	72.829	71.006	72.625	-5.33	-3.68
4	70.875	73.072	70.764	72.857	-5.58	-3.45
5	70.634	73.325	70.545	73.088	-5.81	-3.21
6	70.396	73.573	70.313	73.328	-6.05	-2.97
7	70.160	73.820	70.084	73.559	-6.29	-2.73
8	69.913	74.072	69.852	73.791	-6.52	-2.51
9	69.676	74.316	69.613	74.029	-6.76	-2.25
10	69.440	74.564	69.386	74.254	-7.00	-2.02
11	69.197	74.811	69.161	74.491	-7.23	-1.79
12	68.959	75.065	68.929	74.714	-7.47	-1.56
13	68.720	75.310	68.700	74.952	-7.70	-1.33
14	68.489	75.558	68.466	75.179	-7.94	-1.09
15	68.248	75.808	68.230	75.404	-8.18	-0.85
16	68.016	76.056	68.006	75.641	-8.41	-0.61
17	67.770	76.305	67.771	75.863	-8.65	-0.38
18	67.538	76.552	67.538	76.088	-8.88	-0.15
19	67.300	76.797	67.297	76.317	-9.12	0.07
20	67.063	77.039	67.065	76.528	-9.37	0.33
21	66.821	77.285	66.825	76.753	-9.60	0.56
22	66.592	77.530	66.584	76.964	-9.83	0.75
23	66.355	77.771	66.351	77.167	-10.07	0.99
24	66.096	78.002	66.098	77.379	-10.33	1.22
25	65.865	78.244	65.847	77.567	-10.53	1.46
26	65.615	78.482	65.596	77.764	-10.79	1.69
27	65.372	78.707	65.341	77.947	-11.02	1.91
28	65.132	78.934	65.066	78.118	-11.28	2.13
29	64.883	79.156		78.276	-11.49	2.36
30	64.619	79.366	64.498	78.401	-11.75	2.61
31	64.364	79.571	64.189	78.518		2.82
32	64.102	79.768	63.866	78.626		3.02
33	63.828	79.948	63.559	78.723		3.23
34	63.549	80.118	63.202	78.802		3.44
35	63.246	80.281	62.854			3.64
36	62.936	80.415	62.454	78.959		3.85
37	62.625	80.529		79.020		4.07
38	62.265	80.638		79.088		4.27
39	61.923					
40	61.559					

Table A14: Ne-HN₂⁺ line positions III

Line positions of the $\nu_1+\nu_3$ band of Ne-HN₂⁺ and ²²Ne-HN₂⁺.

J''	P(J'')	R(J'')	P(J'')	R(J'')	J''	P(J'')	R(J'')	P(J'')	R(J'')
	normal	normal	²² Ne	²² Ne		normal	normal	²² Ne	²² Ne
0		3212.213		3208.269	22	3206.057	3216.888	3202.425	3212.732
1	3211.735	12.452	3207.810	8.489	23	5.760	17.071	2.153	12.910
2	11.474	12.685	7.568	8.720	24	5.461	17.250	1.865	13.078
3	11.232	12.923	7.335	8.941	25	5.166	17.431	1.590	13.249
4	10.981	13.155	7.098	9.160	26	4.862	17.607	1.299	13.421
5	10.722	13.382	6.854	9.377	27	4.550	17.770	1.016	13.586
6	10.478	13.613	6.610	9.589	28	4.249	17.944	0.725	13.744
7	10.216	13.834	6.365	9.812	29	3.935	18.112	0.435	13.912
8	9.952	14.056	6.118	10.015	30	3.628	18.270	0.146	14.070
9	9.688	14.274	5.869	10.226	31	3.312	18.421	3199.845	14.223
10	9.423	14.496	5.616	10.434	32	2.998	18.584	99.544	14.376
11	9.157	14.705	5.360	10.636	33	2.674	18.740	99.254	14.527
12	8.888	14.921	5.107	10.841	34	2.354	18.884	98.948	14.676
13	8.614	15.132	4.848	11.038	35	2.026	19.027	98.641	14.818
14	8.342	15.336	4.588	11.233	36	1.690	19.160	98.334	14.948
15	8.062	15.544	4.328	11.431	37	1.364	19.284	98.021	15.065
16	7.785	15.742	4.061	11.623	38	1.024	19.388	97.701	
17	7.502	15.936	3.788	11.812	39	0.669	19.455	97.376	
18	7.222	16.135	3.526	11.997	40	0.301		97.023	
19	6.937	16.326	3.253	12.182	41	3199.895		96.639	
20	6.638	16.517	2.982	12.374	42			96.300	
21	6.350	16.706	2.708	12.547					

- Appendix -

Table A15: Ne-HN₂⁺ line positions IV

Line positions of the 3289 and 3181 cm⁻¹ (P and R branches only)* bands of Ne-HN₂⁺.

J''	P(J'')	R(J'')	P(J'')	R(J'')	J''	P(J'')	R(J'')	P(J'')	R(J'')
	3289	3289	3181	3181		3289	3289	3181	3181
0		3289.608			16	85.123	93.477	77.685	85.876
1	3289.114	89.883			17	85.052	93.853	77.514	86.201
2	88.885	90.143		3181.813	18	84.960	94.219	77.343	
3	88.663	90.402		82.076	19	84.854	94.562	77.182	86.853
4	88.423	90.693	3180.102	82.332	20	84.724	94.866		87.187
5	88.210	90.971	79.861	82.604	21	84.581	95.150	76.883	87.528
6	88.006	91.279	79.651	82.903	22	84.413	95.398	76.729	87.872
7	87.802	91.592	79.442	83.138	23	84.202	95.638	76.580	88.220
8	87.620	91.926	79.224	83.452	24	83.979	95.859	76.450	88.569
9	87.445	92.296	79.026	83.735	25	83.725	96.126	76.314	88.898
10	87.292	92.668	78.809	84.021	26	83.445	96.315	76.169	89.239
11	87.181	93.082	78.614	84.331	27		96.542	76.048	89.654
12	87.067	93.542	78.421	84.623	28		96.745	75.925	90.013
13	86.989	92.238	78.220	84.930	29		96.925	75.791	
14	86.960	92.668	78.040	85.249	30			75.679	
15	85.177	93.082	77.860	85.560					

* Q branch at 3181.04 and 3180.65 cm⁻¹ for normal and ²²Ne isotopomers respectively

Table A16: Ar-HN₂⁺ line positions I

The bands are arranged in the ascending order with respect to excitation energy. Only Σ-Σ type bands are listed here.

For the first three bands transitions into low J levels are not predissociating and therefore not observed.

J''	P(J'')	R(J'')	J''	P(J'')	R(J'')	J''	P(J'')	R(J'')
2505.40 cm ⁻¹ band (A band, ν ₁ +ν _s)								
60		2518.664	65	2498.733	2520.038	70	2498.552	2521.453
61		18.934	66	98.691	20.314	71	98.517	21.748
62	2498.866	19.208	67	98.655	20.599	72		22.036
63	98.819	19.483	68	98.618	20.888	73		22.329
64	98.771	19.760	69	98.581	21.174	74		22.619
2707.34 cm ⁻¹ band (B band, ?)								
30		2711.537	39	2699.837	2712.505	47	2698.072	2713.221
31		11.644	40	99.648	12.638	48	97.827	13.302
32	2701.356	11.762	41	99.421	12.720	49	97.573	13.362
33	1.143	11.866	42	99.237	12.801	50	97.336	13.444
34	0.937	11.960	43	98.999	12.871	51	97.083	13.494
35	0.716	12.062	44	98.754	12.985	52	96.840	13.531
36	0.489	12.166	45	98.511	13.070	53	96.572	
37	0.276	12.257	46	98.304	13.146	54	96.300	
38	0.050	12.412						
2755.62 cm ⁻¹ band (C band, ν ₁ +2ν _s)								
17		2758.490	28	2750.841	2760.137	39		2761.750
18		58.639	29	50.757	60.272	40	2748.902	61.873
19	2752.513	58.818	30	50.604	60.396	41	48.679	62.089
20	52.329	58.914	31	50.404	60.531	42	48.503	62.160
21	52.187	59.049	32	50.221	60.688	43	48.350	62.298
22	51.961	59.186	33	50.044	60.794	44	48.132	62.397
23	51.764	59.346	34	49.866	60.964	45	47.924	62.496
24	51.593	59.452	35	49.668	61.082	46	47.717	62.701
25	51.420	59.599	36	49.498	61.264	47	47.552	
26	51.224	59.753	37	49.305	61.447	48	47.354	
27	51.031	59.959	38		61.656			
2839.80 cm ⁻¹ band								
0		2839.977	12	2838.090	2842.209	23	2836.947	2844.673
1	2839.639	40.134	13	37.970	42.415	24	36.868	44.969
2	39.485	40.305	14	37.841	42.629	25	36.757	45.219
3	39.332	40.481	15	37.737	42.850	26	36.743	45.472
4	39.171	40.651	16	37.629	43.061	27	36.667	45.733
5	39.037	40.845	17	37.521	43.287	28	36.604	45.980
6	38.888	41.031	18	37.404	43.518	29		46.250
7	38.746	41.229	19	37.315	43.749	30		46.523
8	38.608	41.410	20	37.229	43.981	31		46.798
9	38.471	41.612	21	37.128	44.215	32		47.072
10	38.348	41.803	22	37.041	44.459	33		47.352
11	38.219	42.007						

- Appendix -

2966.05 cm ⁻¹ band								
0		2966.210	14	2963.644	2968.292	28	2960.981	2970.084
1	2965.883	66.369	15	63.465	68.428	29	60.769	70.191
2	65.725	66.527	16	63.283	68.564	30	60.555	70.299
3	65.558	66.687	17	63.096	68.697	31	60.342	70.406
4	65.390	66.843	18	62.905	68.826	32	60.128	70.518
5	65.229	66.994	19	62.715	68.967	33	59.910	70.626
6	65.060	67.146	20	62.522	69.096	34	59.703	70.720
7	64.887	67.303	21	62.330	69.219	35	59.483	70.807
8	64.718	67.452	22	62.148	69.343	36	59.258	70.901
9	64.547	67.604	23	61.948	69.456	37	59.027	70.996
10	64.373	67.717	24	61.746	69.574	38	58.795	71.071
11	64.204	67.859	25	61.543	69.711	39	58.563	71.157
12	64.004	68.008	26	61.338	69.859	40	58.320	
13	63.820	68.149	27	61.160	69.971	41	58.085	
3070.89 cm ⁻¹ band								
0		3071.058	8	3069.642	3072.418	15	3068.631	3073.676
1	3070.735	71.220	9	69.496	72.597	16	68.485	73.858
2	70.571	71.385	10	69.349	72.780	17	68.341	74.033
3	70.409	71.559	11	69.202	72.954	18	68.199	74.205
4	70.251	71.726	12	69.056	73.132	19	68.048	74.357
5	70.100	71.892	13	68.918	73.319	20	67.899	
6	69.947	72.069	14	68.775	73.494	21	67.732	
7	69.789	72.243						
3077.96 cm ⁻¹ band								
0		3078.117	7	3076.827	3079.235	14	3075.654	3080.320
1	3077.790	78.276	8	76.660	79.385	15	75.480	80.465
2	77.632	78.448	9	76.492	79.548	16	75.307	80.613
3	77.476	78.608	10	76.319	79.702	17	75.135	80.748
4	77.312	78.771	11	76.155	79.852	18	74.954	80.889
5	77.156	78.929	12	75.986	80.013	19	74.772	
6	76.991	79.082	13	75.822	80.166	20	74.586	
3195 cm ⁻¹ band								
0		3194.707	20	3191.375	3197.987	40	3188.008	3201.067
1	3194.383	94.867	21	91.205	98.132	41	87.833	1.208
2	94.221	95.020	22	91.034	98.280	42	87.649	1.347
3	94.057	95.172	23	90.859	98.401	43	87.494	
4	93.888	95.324	24	90.684	98.559	44	87.302	1.714
5	93.715	95.471	25	90.485	98.721	45		1.860
6	93.542	96.215	26	90.316	98.884	46	87.038	2.008
6		95.608						
7	93.362	96.299	27	90.153	99.047	47	86.859	
7		95.758						
8	93.774	96.384	28	90.000	99.205	48	86.700	2.366
8	93.178	95.887						
9	93.542	96.480	29	89.831	99.362	49	86.529	
9	93.002	95.990						
10	93.312	96.583	30	89.674	99.498	50	86.410	
10	92.802	96.066						
11	93.080	96.703	31	89.509	99.630	51		2.910
11	92.586	96.128						
12	92.858	96.824	32	89.322	99.861	52		3.071
13	92.657	96.951	33	89.136	99.977	53	85.988	3.250
14	92.458	97.091	34	89.050	3200.153	54	85.827	3.425
15	92.261	97.247	35	88.827	0.312	55	85.676	3.600
16	92.083	97.388	36	88.695	0.448	56	85.526	
17	91.911	97.532	37	88.529	0.608	57	85.384	
18	91.732	97.680	38	88.351	0.762	58	85.253	
19	91.551	97.831	39	88.177	0.898			
3364.91 cm ⁻¹ band								
0		3365.080	9	3363.318	3366.328	18	3361.467	3367.321
1	3364.766	65.224	10	63.120	66.448	19	61.243	67.415
2	64.585	65.374	11	62.929	66.572	20	61.019	67.506
3	64.409	65.521	12	62.733	66.692	21	60.793	67.593
4	64.243	65.669	13	62.537	66.801	22	60.561	67.679
5	64.068	65.806	14	62.325	66.911	23	60.336	67.744
6	63.880	65.938	15	62.120	67.022	24	60.080	
7	63.698	66.085	16	61.905	67.121	25	59.825	
8	63.510	66.212	17	61.686	67.222			
3507.52 cm ⁻¹ band								

- Appendix -

0		3507.685	14	3505.193	3509.819	28	3503.026	3512.213
1	3507.371	7.851	15	5.018		29	2.853	12.377
2	7.205	8.011	16			30	2.689	12.532
3	7.046	8.167	17		10.571	31	2.525	12.706
4	6.885	8.324	18		10.694	32	2.361	12.861
5	6.714	8.487	19	4.536	10.834	33	2.207	13.027
6	6.554	8.639	20	4.399	10.971	34	2.038	13.173
7	6.387	8.793	21	4.198	11.122	35	1.874	13.332
8	6.216	8.950	22	4.028	11.286	36	1.705	13.488
9	6.046	9.107	23	3.852	11.437	37	1.546	13.666
10	5.878	9.261	24	3.687	11.592	38	1.392	13.789
11	5.711	9.409	25	3.517	11.747	39	1.235	13.942
12	5.541	9.568	26	3.352	11.915	40	1.049	
13	5.369	9.701	27	3.188	12.065	41	0.881	
3521.23 cm ⁻¹ band								
0		3521.390	9	3519.872	3523.001	18	3518.758	3524.840
1	3521.064	21.557	10	19.738	23.206	19	18.650	25.052
2	20.905	21.729	11	19.600	23.392	20	18.533	25.266
3	20.749	21.907	12	19.479	23.595	21	18.419	25.478
4	20.595	22.088	13	19.346	23.795	22	18.317	25.708
5	20.448	22.256	14	19.223	24.019	23	18.206	25.887
6	20.304	22.444	15	19.113	24.212	24	18.097	
7	20.157	22.623	16	19.001	24.421	25	17.966	
8	20.019	22.813	17	18.875	24.630			
3623.47 cm ⁻¹ band								
0		3623.634	9	3622.073	3625.180	18	3620.908	3627.010
1	3623.308	23.810	10	21.935	25.372	19	20.817	27.230
2	23.152	23.973	11	21.791	25.558	20	20.710	27.456
3	22.993	24.139	12	21.650	25.749	21	20.606	27.676
4	22.839	24.318	13	21.517	25.949	22	20.497	27.863
5	22.686	24.487	14	21.382	26.149	23	20.403	28.009
6	22.534	24.657	15	21.258	26.362	24	20.262	
7	22.383	24.842	16	21.135	26.571	25	20.099	
8	22.231	25.005	17	21.015	26.792			

Table A17: Ar-HN₂⁺ line positions II

Line positions of 2497 cm⁻¹ hot band. Low J levels are not predissociating and therefore not observed.

J"	R(J")	J"	R(J")	J"	P(J")	J"	P(J")	J"	P(J")
40	2503.898	47	2505.243	42	2490.455	52	2489.214	59	2488.389
41	4.092	48	5.439	43	90.335	52	89.268	60	88.283
42	4.285	48	5.461	44	90.207	?	89.049	61	88.168
42	4.225	49	5.658	45	90.088	53	89.096	62	88.055
43	4.483	50	5.864	46	89.964	?	89.161	63	87.940
43	4.423	51	6.063	47	89.842	54	88.932	64	87.816
44	4.622	52	6.265	48	89.717	54	88.972	65	87.704
44	4.675	53	6.475	49	89.617	55	88.823	66	87.581
45	4.875	54	6.674	49	89.585	55	88.853	67	87.466
45	4.827	55	6.881	50	89.461	56	88.738	68	87.363
46	5.076	56	7.079	50	89.496	57	88.617	69	87.248
46	5.033	57	7.276	51	89.343	58	88.497	70	87.136
47	5.269			51	89.385				

Table A18: Ar-HN₂⁺ line positions III

Line positions of the $\nu_1 + \nu_2$ band of Ar-HN₂⁺. Relative J numbering of the Q branch lines should be correct but absolute may be shifted by $\pm(1-3)$. The shift has a strong influence on q' constant. There is a perturbation centered on e parity J'=11 level.

J	P(J)	Q(J)	R(J)	J	Q(J)
1		2940.360*	2940.698	25	2941.206
2	2940.049		40.866	26	41.259
3	39.895		41.038	27	41.325
4	39.736		41.206	28	41.385
5	39.583		41.385	29	41.458
6	39.434		41.557	30	41.530
7	39.277		41.738	31	41.601
8	39.134	40.455	41.922	32	41.677
9	38.988	40.480	42.123	33	41.754
10	38.853	40.510		34	41.835
11	38.723	40.537	42.384	35	41.922

- Appendix -

12		40.565	42.589	36	41.997
13	38.344	40.598	42.782	37	42.088
14	38.222	40.629	42.977	38	42.174
15	38.095	40.678	43.174	39	42.260
16	37.968	40.719	43.376	40	42.351
17	37.837	40.767	43.573	41	42.448
18	37.706	40.815	43.771	42	42.543
19	37.583	40.866	43.985	43	42.636
20	37.470	40.908	44.188	44	42.736
21	37.353	40.959	44.408	45	42.828
22	37.232	41.013	44.635		
23	37.136				
24	37.050	41.143			

* Q branch onset

13. List of tables

Table #	Table title	Page
4.1	Spectroscopic properties of HN_2^+ , HCO^+ , and HOC^+	23
4.2	Spectroscopic properties of NH_4^+	24
5.1	Experimental conditions used for preparing ionic complexes	33
6.1	The $\text{H}_2\text{-HCO}^+$ calculated vibrations	44
6.2	Observed $\text{H}_2\text{-HCO}^+$ transitions	47
6.3	$\text{H}_2\text{-HCO}^+$ ν_1 band constants	48
6.4	Rotational constants of different isomeric forms of H_3CO^+	50
6.5	Observed $\text{H}_2\text{-HN}_2^+$ transitions	55
6.6	Band centers of the ν_1 transitions of other $\text{H}_2\text{-HM}^+$ complexes	57
7.1	The He-HCO^+ ν_1 band constants	59
7.2	The Ne-HCO^+ ν_1 band constants	63
7.3	The Ar-HCO^+ lower state constants	69
7.4	The Ar-HCO^+ ν_1 state constants	69
7.5	Ar-HCO^+ $\nu_1 + \nu_2$ band constants	71
7.6	Ar-HCO^+ 3799 cm^{-1} band constants	72
7.7	Ar-HCO^+ $\nu_1 + \nu_3 - \nu_3$ band constants	74
7.8	Ar-HCO^+ 2955 cm^{-1} band constants	78
7.9	Constants for remaining Ar-HCO^+ bands	82
7.10	He-HN_2^+ rotational constants	86
7.11	He-HN_2^+ RKR potential properties	89
7.12	Ne-HN_2^+ lower state constants	94
7.13	Ne-HN_2^+ vibrational origins and heads	96
7.14	Upper state constants for the Ne-HN_2^+ transitions	100
7.15	Ar-HN_2^+ rovibrational constants	106
8.1	Observed He-NH_4^+ transitions	116
8.2	Ar-NH_4^+ rotational constants	119
8.3	Q branch positions of the Ar-NH_4^+ $\nu_3(\text{e})$ band	120
9.1	$\text{Ar}_n\text{-HCO}^+$ absorptions	127
9.2	$\text{Ar}_n\text{-HCO}^+$ unassigned absorptions	129
9.3	$\text{Ar}_n\text{-HCO}^+$ binding energies	130
9.4	Absorption maxima of $\text{Ne}_n\text{-HN}_2^+$ spectra	134
9.5	NH_4^+ and $\text{NH}_4^+\text{-Ar}$ calculated vibrational frequencies	137
9.6	Branching ratios in $\text{NH}_4^+\text{-Ar}_n$ spectra	137
9.7	Vibrational positions in $\text{NH}_4^+\text{-Ar}_n$ spectra	140
10.1	H_2 stretching vibrations in selected $\text{H}_2\text{-M}^+$ complexes	142
10.2	Spectroscopic and theoretical properties of $\text{Rg-HCO}^+/\text{HN}_2^+$	148

- List of tables -

A1	He-HCO ⁺ ν_1 line positions	151
A2	Ne-HCO ⁺ ν_1 line positions	151
A3	Ar-HCO ⁺ ν_1 line positions	152
A4	Ar-HCO ⁺ $\nu_1 + \nu_2$ line positions	152
A5	Ar-HCO ⁺ 3799 cm ⁻¹ band line positions	153
A6	Line positions of Ar-HCO ⁺ $\nu_1 + \nu_3 - \nu_3$ band	153
A7	Ar-HCO ⁺ 2955 cm ⁻¹ band line positions	154
A8	Positions of $\nu_1 + \nu_s$, 3068, and 3125 cm ⁻¹ bands of Ar-HCO ⁺	154
A9	Line positions of $\nu_1 + \nu_s$ band of Ar-H ¹³ CO ⁺	155
A10	He-HN ₂ ⁺ ν_1 line positions	155
A11	He-HN ₂ ⁺ combination bands' line positions	155
A12	Ne-HN ₂ ⁺ line positions I	156
A13	Ne-HN ₂ ⁺ line positions II	156
A14	Ne-HN ₂ ⁺ line positions III	157
A15	Ne-HN ₂ ⁺ line positions IV	158
A16	Ar-HN ₂ ⁺ line positions I	158
A17	Ar-HN ₂ ⁺ line positions II	160
A18	Ar-HN ₂ ⁺ line positions III	160

14. List of figures

Figure #	Figure title	Page
5.1	QOQ tandem mass-spectrometer apparatus	31
5.2	Inlet gas -mixing system	31
5.3	Electron impact cluster ion source	32
5.4	Nonuniform scanning of the "Mirage 3000" OPO laser	40
6.1	Normal modes of H ₂ -HCO ⁺ from <i>ab initio</i> calculations	45
6.2	<i>Ab initio</i> H ₂ rocking potential for H ₂ -HCO ⁺	46
6.3	Vibrational predissociation spectrum of H ₂ -HCO ⁺	47
6.4	The ν_2 band of H ₂ -HCO ⁺	48
6.5	The ν_1 band of H ₂ -HCO ⁺	49
6.6	Minimum calculated energy structure for H ₂ -HN ₂ ⁺ and HN ₂ ⁺	53
6.7	Intermolecular stretching potential for H ₂ -HN ₂ ⁺	53
6.8	Vibrational predissociation spectrum of H ₂ -HN ₂ ⁺	54
6.9	The ν_1 band of H ₂ -HN ₂ ⁺	55
6.10	The ν_1 transitions of H ₂ -H ₃ O ⁺ and H ₂ -NH ₄ ⁺	57
7.1	The ν_1 band of He-HCO ⁺	58
7.2	The ν_1 band of Ne-HCO ⁺	62
7.3	Mass spectrum from an Ar/He/H ₂ /CO expansion	66
7.4	Spectra of the Ar-HCO ⁺ and Ar-H ¹³ CO ⁺ ν_1 bands	68
7.5	Results of fitting the ν_1 band of Ar-HCO ⁺	70
7.6	The $\nu_1+\nu_2$ band of Ar-HCO ⁺	71
7.7	Ar-HCO ⁺ $\nu_1+\nu_2$ fit results	72
7.8	The first overtone of the Ar-HCO ⁺ ν_1 vibration	73
7.9	Rotational distribution in Ar-HCO ⁺ from its $\nu_1+\nu_3-\nu_3$ band	76
7.10	Line positions of the 2955 cm ⁻¹ band	77
7.11	The $\nu_1+\nu_s$ and 2955 cm ⁻¹ bands of Ar-HCO ⁺	79
7.12	The 3068 cm ⁻¹ band of Ar-HCO ⁺	80
7.13	3125 cm ⁻¹ band of ar-HCO ⁺	80
7.14	Fitting the $\nu_1+\nu_s$, 3068 cm ⁻¹ , and 3125 cm ⁻¹ bands	81
7.15	Observed transition <u>origins</u> in the Ar-HCO ⁺ spectrum	84
7.16	Vibrational predissociation spectrum of He-HN ₂ ⁺	87
7.17	One dimensional radial intermolecular potential for He+HN ₂ ⁺	90
7.18	Linewidths in the He-HN ₂ ⁺ spectrum	90
7.19	Vibrational predissociation spectrum of Ne-HN ₂ ⁺	92
7.20	Observed vibrational transitions in the Ne-HN ₂ ⁺ spectra	93
7.21	An overview spectrum of Ar-HN ₂ ⁺	103
7.22	Selected bands out of the Ar-HN ₂ ⁺ spectrum	104

- List of figures -

7.23	Ar-HN ₂ ⁺ combination differences	105
7.24	J-selective predissociation in the Ar-HN ₂ ⁺ spectrum	108
7.25	Determination of the Ar-HN ₂ ⁺ binding energy	109
8.1	The ν_3 band of He-NH ₄ ⁺	115
8.2	Coordinate system for He-NH ₄ ⁺	117
8.3	A portion of the Ar-NH ₄ ⁺ photodissociation spectrum	118
8.4	Expanded view of the $\nu_3(e)$ ($1 \leftarrow 0$) subband	118
8.5	Q branch splitting in the $\nu_3(e)$ transition of Ar-NH ₄ ⁺	119
9.1	Metastable decay in the Ar _n -HCO ⁺ series	123
9.2	Predissociation spectra of Ar _n -HCO ⁺ (n=1-13) clusters	125
9.3	Different fragmentation channels in the Ar _n -HCO ⁺ spectra	126
9.4	Development of Ar _n -HCO ⁺ properties with cluster size	126
9.5	Semi-empirical structures for selected Ar _n -HCO ⁺ clusters	130
9.6	A vibrational predissociation spectrum of Ne ₂ -HCO ⁺	132
9.7	Vibrational predissociation spectra of He-HN ₂ ⁺ and He ₂ -HN ₂ ⁺	132
9.8	Vibrational predissociation spectra of Ne _n -HN ₂ ⁺	133
9.9	Photofragmentation spectra of NH ₄ ⁺ -Ar _n (n=1-5)	138
9.10	Different dissociation channels in NH ₄ ⁺ -Ar ₄ and NH ₄ ⁺ -Ar ₅	138
9.11	Graphical representation of Ar _n -NH ₄ ⁺ vibrations	141
10.1	Binding energy - $\Delta\nu_1$ correlation in H ₂ -M ⁺ complexes	143
10.2	Electrostatic energy- $\Delta\nu_1$ correlation in a point charge-H ₂ system	144
10.3	Proton affinity - $\Delta\nu_1$ correlation in proton-bound complexes	145
10.4	Correlation between Δ PA, k_s and $\Delta\nu_1$ for Rg-HCO ⁺ /HN ₂ ⁺	149

15. List of the author's publications

1. S.A. Nizkorodov, V.I. Makarov, I.V. Khmelinskii, S.A. Kotschubei, K.A. Amosov, "Time-Resolved Fluorescence of NO₂ in a Magnetic Field", Chem. Phys. Lett., **215** (1993) 662-667.
2. S.A. Nizkorodov, V.I. Makarov, I.V. Khmelinskii, S.A. Kotschubei, K.A. Amosov, "LIF Detection of NO₃ Radical after Pulsed Excitation of NO₂ Vapour at 436.45 nm", Chem. Phys. Lett., **222** (1994) 135-140.
3. A.A. Friedmann, S.A. Nizkorodov, E.J. Bieske, J.P. Maier, "Discrete UV Absorption by N₃⁺-(N₂)_n Clusters", Chem. Phys. Lett., **224** (1994) 16-20.
4. D. Lessen, S.A. Nizkorodov, P. Knupfer, T. Ruchti, E.J. Bieske, J.P. Maier, "Rotational Distribution of N₂⁺ Fragments from 355 nm Photolysis of N₄⁺", Chem. Phys. Lett., **226** (1994) 187-192.
5. A.A. Friedmann, A.M. Soliva, S.A. Nizkorodov, E.J. Bieske, J.P. Maier, "A ³Π_u ← X³Σ_g⁻ Electronic Spectrum of N₃⁺", J. Phys. Chem., **98** (1994) 8896-8902.
6. E.J. Bieske, S.A. Nizkorodov, A.A. Friedmann, J.P. Maier, "Metastable Decay of N₂⁺-He_n (v = 1) (1 < n ≤ 6) Clusters", Int. J. Mass Spectr. Ion Proc., **135** (1994) 19-30.
7. E.J. Bieske, S.A. Nizkorodov, F.R. Bennett, J.P. Maier, "The Infrared Spectrum of the H₂-HCO⁺ Complex", J. Chem. Phys., **102** (1995) 5152-5164.
8. S.A. Nizkorodov, J.P. Maier, E.J. Bieske, "The Infrared Spectrum of the N₂H⁺-He Ion-Neutral Complex", J. Chem. Phys., **102** (1995) 5570-5571.
9. E.J. Bieske, S.A. Nizkorodov, F.R. Bennett, J.P. Maier, "Combined Infrared and *ab initio* Study of the H₂-NH₂⁺ Complex", Int. J. Mass Spectr. Ion Proc., **149/150** (1995) 167-177.
10. S.A. Nizkorodov, J.P. Maier, E.J. Bieske, "The Infrared Spectrum of the He-HCO⁺", J. Chem. Phys., **103** (1995) 1297-1302.
11. S.A. Nizkorodov, O. Dopfer, T. Ruchti, M. Meuwly, J.P. Maier, E.J. Bieske, "Size Effects in Cluster Infrared Spectra: the ν₁ Band of Ar_n-HCO⁺", J. Phys. Chem., **99** (1995) 17118-17129.
12. M. Meuwly, S.A. Nizkorodov, J.P. Maier, E.J. Bieske, "Mid-infrared Spectra of He-HN₂⁺ and He₂-HN₂⁺", J. Chem. Phys., **104** (1996) 3876-3885.
13. E.J. Bieske, S.A. Nizkorodov, O. Dopfer, J.P. Maier, R. Stickland, B.J. Cotterell, B.J. Howard, "Observation of the Infrared Spectrum of the ν₃ Band of the Argon-Ammonium Ionic Complex", Chem. Phys. Lett., **250** (1996) 266-272.
14. S.A. Nizkorodov, O. Dopfer, M. Meuwly, J.P. Maier, E.J. Bieske, "Mid-Infrared Spectra of the Proton-Bound Complexes Ne_n-HCO⁺ (n=1,2)", J. Chem. Phys., **105** (1996) 1770-1777.
15. O. Dopfer, S.A. Nizkorodov, M. Meuwly, E.J. Bieske, J.P. Maier, "The ν₃ Infrared Spectrum of the He-NH₄⁺ complex", Chem. Phys. Lett., **260** (1996) 545-550.
16. S.A. Nizkorodov, Y. Spinelli, E.J. Bieske, J.P. Maier, O. Dopfer, "Dissociation energy of the Ar-HN₂⁺ complex", Chem. Phys. Lett., **265** (1997) 303-307.

16. References

1. Miller, S. and Tennyson, J., *Ab initio* investigation of the bound rovibrational states in the electronic ground state of HeN_2^+ // *J. Chem. Phys.* - 1987. - v.87. - p. 6648.
2. Miller, S., Tennyson, J., Follmeg, B., Rosmus, P., and Werner, H., *Ab initio* investigation of the bound rovibrational states in the electronic ground state of HeN_2^+ // *J. Chem. Phys.* - 1988. - v.89. - p. 2178-2184.
3. Kebarle, P., Searles, S.K., Zolla, A., Scarborough, J., and Arshadi, M., The solvation of hydrogen ion by water molecules in the gas phase. Heats and entropies of solvation of individual reactions $\text{H}^+(\text{H}_2\text{O})_{n-1} + \text{H}_2\text{O} \rightarrow \text{H}^+(\text{H}_2\text{O})_n$ // *J. Am. Chem. Soc.* - 1967. - v.89. - p. 6393-6399.
4. Crofton, M.W., Price, J.M., and Lee, Y.T., IR spectroscopy of hydrogen bonded charged clusters //, in *Clusters of Atoms and Molecules II*, H. Haberland, Editor. 1994, Springer-Verlag: Berlin. p. 44-76.
5. Keesee, R.G. and Castleman Jr., A.W., Thermochemical data on gas-phase ion-molecule association and clustering reactions // *J. Phys. Chem. Ref. Data* - 1986. - v.15. - p. 1011-1071.
6. Harris, I.A., Kidwell, R.S., and Northby, J.A., Structure of charged argon clusters formed in a free jet expansion // *Phys. Rev. Lett.* - 1984. - v.53. - p. 2390.
7. Lifshitz, C. and Louage, F., Magic numbers in kinetic energy releases for unimolecular decompositions of for $(\text{NH}_3)_n\text{H}^+$ ion clusters // *J. Phys. Chem.* - 1989. - v.93. - p. 5633-5635.
8. Castleman, A.W. and Bowen, K.H., Clusters: Structure, energetics, and dynamics of intermediate states of matter // *J. Phys. Chem.* - 1996. - v.100. - p. 12911-12944.
9. Castleman, A.W., Solvated Cluster Ions //, in *Clusters of Atoms and Molecules II*, H. Haberland, Editor. 1994, Springer-Verlag Berlin: Heidelberger Platz 3, W-1000 Berlin 33, Germany. p. 77-133.
10. Castleman, A.W. and Keesee, R.G., Ionic Clusters // *Chem. Rev.* - 1986. - v.86. - p. 589-618.
11. Castleman, A.W. and Wei, S., Cluster reactions // *Annu Rev Phys Chem.* - 1994. - v.45. - p. 685-719.
12. Elrod, M.J. and Saykally, R.J., Many-body effects in intermolecular forces // *Chem. Rev.* - 1994. - v.94. - p. 1975-1997.
13. Schwarz, H.A., Gas-phase infrared spectra of oxonium hydrate ions from 2 to 5 μ // *J. Chem. Phys.* - 1977. - v.67. - p. 5525-5534.
14. Schwarz, H.A., Gas phase infrared spectra of ammoniated ammonium ions // *J. Chem. Phys.* - 1980. - v.72. - p. 284-287.
15. Bogey, M., Bolvin, H., Demuynck, C., and Destombes, J.L., High-Resolution Spectroscopy of Weakly Bound Ionic Clusters ArH_3^+ and ArD_3^+ // *Phys. Rev. Lett.* - 1987. - v.58. - p. 988-991.
16. Bogey, M., Bolvin, H., Demuynck, C., Destombes, J.L., and Van Eijck, B.P., Tunneling Motion in ArH_3^+ and Isotopomers from the analysis of their rotational spectra // *J. Chem. Phys.* - 1988. - v.88. - p. 4120-4126.
17. Demuynck, C., Millimeter-wave spectroscopy in electric discharges: Rare molecules show themselves only if you look in the other direction! // *J Mol Spectrosc* - 1994. - v.168. - p. 215-226.
18. Ohshima, Y., Sumiyoshi, Y., and Endo, Y., Rotational spectrum of the Ar-HCO^+ complex // *J. Chem. Phys.* - 1997. - v.106. - p. 2977-2979.
19. Kennedy, R. and Miller, T.A., Spectroscopic determination of the potential surface for $\text{C}_6\text{F}_6^+ \text{He}$ // *J. Chem. Phys.* - 1986. - v.85. - p. 2326.
20. Kung, C.Y. and Miller, T.A., Inert gas clusters of C_6F_6^+ : The evolution from isolated ion to solid matrix // *J. Chem. Phys.* - 1990. - v.92. - p. 3297-3309.

- References -

21. Shy, J.-T., Farley, J.W., and Wing, F.H., Observation of the infrared spectrum of the triatomic molecular ion H_2D^+ // *Phys. Rev.* - 1981. - v.A24. - p. 1146-1149.
 22. Wing, F.H., Ruff, G.A., Lamb Jr., W.E., and Spezeski, J.J., Observation of the infrared spectrum of the hydrogen molecular ion HD^+ // *Phys. Rev. Lett* - 1976. - v.36. - p. 1488-1491.
 23. Tolliver, D.E., Kyrala, G.A., and Wing, F.H., Observation of the infrared spectrum of the helium-hydride molecular ion $^4\text{HeH}^+$ // *Phys. Rev. Lett* - 1979. - v.43. - p. 1719-1722.
 24. Bieske, E.J. and Maier, J.P., Spectroscopic Studies of Ionic Complexes and Clusters // *Chem. Rev* - 1993. - v.93. - p. 2603-2621.
 25. Richard-Viard, M., Atabek, O., Dutuit, O., and Guyon, P.M., Vibrational mode selectivity in the indirect predissociation of N_2O^+ // *J. Chem. Phys.* - 1990. - v.93. - p. 8881-8892.
 26. Larzilliere, M. and Jungen, C., Fast ion beam laser spectroscopy of N_2O^+ . Effects of orbital angular momentum and vibrational anharmonicity // *Mol. Phys.* - 1989. - v.67. - p. 807-837.
 27. Bowers, M.T., Marshall, A.G., and McLafferty, F.W., Mass spectrometry: Recent advances and future directions // *J. Phys. Chem.* - 1996. - v.100. - p. 12897-12910.
 28. Bieske, E.J., Electronic Spectroscopy of size selected ionic complexes // *Faraday Trans.* - 1995. - v.91. - p. 1.
 29. Müller-Dethlefs, K., Dopfer, O., and Wright, T.G., ZEKE spectroscopy of complexes and clusters // *Chem. Rev.* - 1994. - v.94. - p. 1845-1871.
 30. Müller-Dethlefs, K. and Schlag, E.W., High-resolution zero kinetic energy (ZEKE) photoelectron spectroscopy of molecular systems // *Ann. Rev. Phys. Chem.* - 1991. - v.42. - p. 109-136.
 31. Zhao, Y.X., Debeer, E., and Neumark, D.M., Rotationally resolved spectrum of the $\text{C}(2)\text{Pi}(u)\leftarrow\text{X}(2)\text{Pi}(g)$ electronic transition of C_4^- via resonant two-photon detachment spectroscopy // *J. Chem. Phys.* - 1996. - v.105. - p. 2575-2582.
 32. Wurz, P. and Lykke, K.R., Photodetachment from Laser-Desorbed C_2^- // *Chem. Phys.* - 1993. - v.176. - p. 185-193.
 33. Arnold, C.C. and Neumark, D.M., Study of small carbon and silicon clusters using negative ion photodetachment techniques //, in *Advances in Metal and Semiconductor Clusters*, Vol 3, 1995, M.A. Duncan, Editor. 1995, Jai Press Inc: 55 Old Post Road, No 2, Greenwich, CT 06836. p. 113-148.
 34. Arnold, C.C., Zhao, Y.X., Kitsopoulos, T.N., and Neumark, D.M., Study of C_6^- and C_6 with Threshold Photodetachment Spectroscopy and Autodetachment Spectroscopy // *J. Chem. Phys.* - 1992. - v.97. - p. 6121-6135.
 35. Novick, S.E., Structure and Dynamics of Weakly Bound Molecular Complexes [A further updated electronic version of this bibliography can be obtained from the author, snovick@wesleyan.edu, upon request] //, A. Weber, Editor. 1997, Reidel: Dordrecht. p. 201.
-
36. Simandiras, E.D., Gaw, J.F., and Handy, N.C., Ar-H_3^+ ion and its isotopomers: The structure and vibrational frequencies // *Chem. Phys. Lett.* - 1987. - v.141. - p. 166-174.
 37. Nizkorodov, S.A., Dopfer, O., Ruchti, T., Meuwly, M., Maier, J.P., and Bieske, E.J., Size effects in cluster infrared spectra: The $\nu(1)$ band of $\text{Ar}_n\text{-HCO}^+$ ($n=1-13$) // *J. Phys. Chem.* - 1995. - v.99. - p. 17118-17129.
 38. Carrington, A., Microwave spectroscopy at the dissociation limit // *Science* - 1996. - v.274. - p. 1327-1331.
 39. Carrington, A., Shaw, A.M., and Taylor, S.M., Ion-beam spectroscopy of long-range complexes // *J. Chem. Soc. Faraday. Trans.* - 1995. - v.91. - p. 3725-3740.

- References -

40. Carrington, A., Gammie, D.I., Shaw, A.M., Taylor, S.M., and Hutson, J.M., Observation of a microwave spectrum of the long-range He...H₂⁺ complex // Chem. Phys. Lett. - 1996. - v.260. - p. 395-405.
41. Ruchti, T., Speck, T., Connelly, J.P., Bieske, E.J., Linnartz, H., and Maier, J.P., Rotationally resolved infrared absorption spectrum of N₄⁺ // J Chem. Phys - 1996. - v.105. - p. 2591-2594.
42. Oka, T., Observation of the infrared spectrum of H₃⁺ // Phys. Rev. Lett. - 1980. - v.45. - p. 531-534.
43. Amano, T., High-resolution infrared spectroscopy of molecular ions // Phil. Trans. R. Soc. Lond. - 1988. - v.A324. - p. 163-178.
44. Okumura, M., Yeh, L.I., and Lee, Y.T., The vibrational predissociation spectroscopy of hydrogen cluster ions // J. Chem. Phys. - 1985. - v.83. - p. 3705-3706.
45. Okumura, M., Yeh, L.I., and Lee, Y.T., Infrared spectroscopy of the cluster ions H₃⁺ (H₂)_n // J. Chem. Phys. - 1988. - v.88. - p. 79-91.
46. Yamaguchi, Y., Gaw, J.F., and Schaefer III, H.F., Molecular Clustering about a Positive Ion. Structures, Energetics, and vibrational frequencies of the protonated hydrogen clusters H₃⁺, H₅⁺, H₇⁺ and H₉⁺. // J. Chem. Phys. - 1983. - v.78. - p. 4074-4085.
47. Wright, L.R. and Borkman, R.F., Ab Initio Studies of the stability of even and odd membered H_n⁺ clusters // J. Chem. Phys. - 1982. - v.77. - p. 1938.
48. Raynor, S. and Herschbach, D.R., Electronic structure of H_n⁺ and HeH_n⁺ Clusters // J. Phys. Chem. - 1983. - v.87. - p. 289-293.
49. Hirao, K. and Yamabe, S., Theoretical Study on the Structure and Stability of Hydrogen-Ion Clusters H_n⁺ and H_n⁻ (n=3,5,7,9,11,13) // Chem. Phys. - 1983. - v.80. - p. 237.
50. Farizon, M., Chermette, H., and Farizon-Mazuy, B., Structure and energetics of hydrogen clusters. Structures of H₁₁⁺ and H₁₃⁺. Vibrational frequencies and infrared intensities of the H_{2n+1}⁺ clusters. // J. Chem. Phys. - 1992. - v.96. - p. 1325-1332.
51. Yamaguchi, Y., Gaw, J.F., Remington, R.B., and Schaefer III, H.F., The H₅⁺ potential energy hypersurface // J. Chem. Phys. - 1987. - v.86. - p. 5072.
52. Huber, H., Near-Hartree-Fock energies and structures of even- and odd-membered H_n⁺ clusters (n≤13) obtained with floating basis sets // J. Mol. Struct. - 1985. - v.121. - p. 281-286.
53. Hiraoka, K. and Mori, T., Thermochemical Stabilities of D₃⁺(D₂)_n with n=1-10 // Chem. Phys. Lett. - 1989. - v.157. - p. 467-471.
54. Hiraoka, K., A determination of the stabilities of H₃⁺(H₂)_n with n=1-9 from measurement of the gas-phase ion equilibria H₃⁺(H₂)_{n-1} + H₂ = H₃⁺(H₂)_n // J. Chem. Phys. - 1987. - v.87. - p. 4048-4055.
55. Bae, Y.K., Observation of high-lying vibrational predissociation states of H₅⁺ // Chem. Phys. Lett. - 1991. - v.180. - p. 179-181.
56. Okumura, M., Yeh, L.I., Myers, J.D., and Lee, Y.T., Infrared Spectra of the Cluster Ions H₇O₃⁺-H₂ and H₉O₄⁺-H₂ // J. Chem. Phys. - 1986. - v.85. - p. 2328-2329.
57. Yeh, L.I., Okumura, M., Myers, J.D., Price, J.M., and Lee, Y.T., Vibrational spectroscopy of the hydrated hydronium cluster ions H₃O⁺(H₂O)_n (n=1,2,3) // J. Chem.Phys. - 1989. - v. 91. - p. 7319-7330.
58. Pudzianowski, A.T., The protonated water dimer: Extensive theoretical studies of H₅O₂⁺ // J Chem. Phys - 1995. - v.102. - p. 7761.
59. Xie, Y.M., Remington, R.B., and Schaefer III, H.F., The protonated water dimer: Extensive theoretical studies of H₅O₂⁺ // J Chem. Phys - 1994. - v.101. - p. 4878-4884.

- References -

60. Ojamae, L., Shavitt, I., and Singer, S.J., Potential energy surfaces and vibrational spectra of H_5O_2^+ and larger hydrated proton complexes // *Int J Quantum Chem.* - 1995. - p. 657-668.
61. Okumura, M., Yeh, L.I., Myers, J.D., and Lee, Y.T., Infrared spectra of the solvated hydronium ion: Vibrational predissociation spectroscopy of mass-selected $\text{H}_3\text{O}^+(\text{H}_2\text{O})_n(\text{H}_2)_m$ // *J. Phys. Chem.* - 1990. - v.94. - p. 3416-3427.
62. Yeh, L.I., Lee, Y.T., and Hougen, J.T., Vibration-rotation spectroscopy of the hydrated hydronium ions H_5O_2^+ and H_9O_4^+ // *J. Mol. Spectr.* - 1994. - v.164. - p. 473-488.
63. Price, J.M., Crofton, M.W., and Lee, Y.T., Observation of internal rotation in the $\text{NH}_4^+(\text{NH}_3)_4$ ionic cluster // *J. Chem. Phys.* - 1989. - v.91. - p. 2749-2751.
64. Price, J.M., Crofton, M.W., and Lee, Y.T., Vibrational Spectra of the Ammoniated Ammonia Ions $\text{NH}_4^+(\text{NH}_3)_n$ ($n=1-10$) // *J. Phys. Chem.* - 1991. - v.95. - p. 2182-2195.
65. Hirao, K., Fujikawa, T., Konishi, H., and Yamabe, S., A theoretical study of ammonia polymers and cluster ions // *Chem. Phys. Lett.* - 1984. - v.104. - p. 184-190.
66. Searles, S.K. and Kebarle, P., Ion-solvent-molecule interaction in the gas phase. Enthalpies and entropies for the reaction $\text{NH}_4^+(\text{NH}_3)_{n-1} + \text{NH}_3 = \text{NH}_4^+(\text{NH}_3)_n$ // *J. Phys. Chem.* - 1968. - v.72. - p. 742.
67. Yeh, L.I., Price, J.M., and Lee, Y.T., Infrared Spectroscopy of the Pentacoordinated Carbonium Ion C_2H_7^+ // *J. Am. Chem. Soc.* - 1989. - v.111. - p. 5597.
68. Cordonnier, M. and Coudert, L.H., Accounting for tunneling splittings in the rotational spectrum of C_2H_3^+ // *J Mol Spectrosc* - 1996. - v.178. - p. 59-65.
69. Bogey, M., Bolvin, H., Cordonnier, M., Demuynck, C., Escribano, R., and Gomez, P.C., Tunneling splittings in the rotational spectrum of C_2H_3^+ // *Can. J. Phys.* - 1994. - v.72. - p. 967-970.
70. Gabrys, C.M., Uy, D., Jagod, M.F., Oka, T., and Amano, T., Infrared spectroscopy of carboions
8. Hollow cathode spectroscopy of protonated acetylene, C_2H_3^+ // *J. Phys. Chem.* - 1995. - v.99. - p. 15611-15623.
71. Scuseria, G.E., The elusive signature of CH_5^+ // *Nature* - 1993. - v.366. - p. 512-513.
72. Schreiner, P.R., Kim, S.J., Schaefer, H.F., and Schleyer, P.v.R., CH_5^+ : The never-ending story or the final word? // *J. Chem. Phys.* - 1993. - v.99. - p. 3716.
73. Marx, D. and Parrinello, M., Structural quantum effects and three-centre two-electron bonding in CH_5^+ // *Nature* - 1995. - v.375. - p. 216-218.
74. Boo, D.W., Liu, Z.F., Suits, A.G., Tse, J.S., and Lee, Y.T., Dynamics of carbonium ions solvated by molecular hydrogen: $\text{CH}_5^+(\text{H}_2)_n$ ($n=1, 2, 3$) // *Science* - 1995. - v.269. - p. 57-59.
75. Boo, D.W. and Lee, Y.T., Infrared spectroscopy of the molecular hydrogen solvated carbonium ions, $\text{CH}_5^+(\text{H}_2)_n$ ($n=1-6$) // *J Chem. Phys* - 1995. - v.103. - p. 520-530.
-
76. Boo, D.W. and Lee, Y.T., Infrared Spectra of CH_5^+ core in $\text{CH}_5^+(\text{H}_2)$ // *Chem. Phys. Lett.* - 1993. - v.211. - p. 358-363.
77. Boo, D.W. and Lee, Y.T., Vibrational spectroscopy and dynamics of ionic complexes of CH_5^+ , $\text{CH}_5^+(\text{A})_x(\text{B})_y$ ($\text{A}, \text{B} = \text{Ar}, \text{N}_2, \text{CH}_4$; $x, y = 0-5$) // *Int. J. Mass. Spectrom. Ion Proc.* - 1996. - v.159. - p. 209-229.
78. Hiraoka, K., Kudaka, I., and Yamabe, S., Gas phase solvation of CH_5^+ with H_2 // *Chem. Phys. Lett.* - 1991. - v.184. - p. 271.
79. Hu, C.H., Shen, M., and Shaefer III, H.F., Toward the infrared spectroscopic observation of SiH_5^+ : The silanium ion // *Chem. Phys. Lett.* - 1992. - v.190. - p. 543.

- References -

80. Archibong, E.F., Schreiner, P.F., Leszczynski, J., Schleyer, P.V.R., Schaefer, H.F., and Sullivan, R., Ab initio prediction of the structure, harmonic vibrational frequencies, and dissociation energy of the H₂-GeH₃⁽⁺⁾-H₂ cluster ion // *J Chem. Phys.* - 1995. - v.102. - p. 3667-3673.
81. Boo, D.W. and Lee, Y.T., Infrared spectroscopy of the siliconium ion, SiH₅⁺ // *J Chem. Phys.* - 1995. - v.103. - p. 514-519.
82. Cao, Y.B., Choi, J.H., Haas, B.M., Johnson, M.S., and Okumura, M., Infrared spectrum of the silicon hydride cation SiH₇⁺ // *J. Phys. Chem.* - 1993. - v.97. - p. 5215-5217.
83. Choi, J.H., Kuwata, K.T., Haas, B.M., Cao, Y., Johnson, M.S., and Okumura, M., Vibrational spectroscopy of NO⁽⁺⁾(H₂O)_n: Evidence for the intracuster reaction NO⁽⁺⁾(H₂O)_n -> H₃O⁽⁺⁾(H₂O)_{n-2}(HONO) at n≥4 // *J. Chem. Phys.* - 1994. - v.100. - p. 7153-7165.
84. Cao, Y.B., Choi, J.H., Haas, B.M., Johnson, M.S., and Okumura, M., Intracuster rearrangement of protonated nitric acid: Infrared spectroscopic studies of H⁽⁺⁾(HNO₃)(H₂O)_n // *J Chem. Phys.* - 1993. - v.99. - p. 9307-9309.
85. Cao, Y.B., Choi, J.H., Haas, B.M., and Okumura, M., Spectroscopic studies of the intracuster hydration reaction of NO₂⁺ // *J. Phys. Chem.* - 1994. - v.98. - p. 12176-12185.
86. Lisy, J.M., Vibrational Spectroscopy of cluster ions //, in *Cluster Ions*, C.-Y. Ng, T. Baer, and I. Powis, Editor. 1993, John Wiley & Sons: New York. p. 217-241.
87. Liu, W.-L. and Lisy, J.M., Infrared spectroscopy of mass-selected Cs(CH₃OH)_n⁺ n=4-16 // *J. Chem. Phys.* - 1988. - v.89. - p. 605-606.
88. Weinheimer, C.J. and Lisy, J.M., Hydrogen bonding in metal ion solvation: vibrational spectroscopy of Cs⁽⁺⁾(CH₃OH)₁₋₆ in the 2.8 μm region // *Int. J. Mass Spectrom. Ion Proc.* - 1996. - v.159. - p. 197-208.
89. Draves, J.A., Luthey-Schulten, Z., Liu, W.-L., and Lisy, J.M., Gas-phase methanol solvation of Cs⁺: Vibrational spectroscopy and Monte Carlo simulation // *J. Chem. Phys.* - 1990. - v.93. - p. 4589-4602.
90. Selegue, T.J., Moe, N., Draves, J.A., and Lisy, J.M., Gas phase solvation of Na⁺ with methanol // *J. Chem. Phys.* - 1992. - v.96. - p. 7268-7278.
91. Selegue, T.J. and Lisy, J.M., Vibrational spectroscopy of ammoniated sodium ions Na⁽⁺⁾(NH₃)_M, M=6-12 // *J. Phys. Chem.* - 1992. - v.96. - p. 4143-4145.
92. Weinheimer, C.J. and Lisy, J.M., Gas-phase cluster ion vibrational spectroscopy of Na⁽⁺⁾(CH₃OH)₂₋₇ // *J. Phys. Chem.* - 1996. - v.100. - p. 15305-15308.
93. Weinheimer, C.J. and Lisy, J.M., Vibrational predissociation spectroscopy of Cs⁽⁺⁾(H₂O)₁₋₅ // *J Chem. Phys.* - 1996. - v.105. - p. 2938-2941.
94. Selegue, T.J., Cabarcos, O.M., and Lisy, J.M., Selective ion solvation in mixed solvents: Vibrational spectroscopy of Cs⁽⁺⁾[(CH₃)₂CO]_N(CH₃OH)_M cluster ions // *J. Chem. Phys.* - 1994. - v.100. - p. 4790.
95. Dietrich, G., Dasgupta, K., Krückberg, S., Lützenkirchen, K., Schweikhard, L., Walther, C., and Ziegler, J., Infrared photodesorption of methanol molecules adsorbed on a Ar₄⁺ cluster // *Chem. Phys. Lett.* - 1996. - v.259. - p. 397-402.
96. Winkel, J.F., Jones, A.B., Woodward, C.A., Kirkwood, D.A., and Stace, A.J., Infrared laser-induced photofragmentation of the positive and negative ions of size-selected SF₆ (NO)_n clusters // *J. Chem. Phys.* - 1994. - v.101. - p. 9436-9446.
97. Stace, A.J., Jones, A.B., Winkel, J.F., and Woodward, C.A., Infrared-Induced Charge Transfer in SF₆.Ar₃⁺ - An Alternative Route to the Ionization Energy of SF₆⁺ // *J. Phys. Chem.* - 1993. - v.97. - p. 11363-11365.

- References -

98. Winkel, J.F., Woodward, C.A., Jones, A.B., and Stace, A.J., Infrared photofragmentation spectra of size-selected SF₆ Ar_n⁺ cluster ions // *J Chem. Phys* - 1995. - v.103. - p. 5177-5193.
99. Jones, A.B., Lopezmartens, R., and Stace, A.J., Laser-induced infrared photofragmentation of SF₆(C₆H₆)_n⁺ cluster ions // *J. Phys. Chem.* - 1995. - v.99. - p. 6333-6339.
100. Mouhandes, A. and Stace, A.J., Infrared photofragmentation spectra of C₂H₄ (NO)_n⁺ cluster ions // *Int. J. Mass Spectrom. Ion Proc.* - 1996. - v.159. - p. 185-196.
101. Woodward, C.A., Winkel, J.F., Jones, A.B., and Stace, A.J., Infrared predissociation in cluster ions containing a guest chromophore. A gentle route to the dynamics and spectroscopy of heterogeneous systems // *Chem. Phys. Lett.* - 1993. - v.206. - p. 49-56.
102. Amar, F.G., Goyal, S., Levandier, D.J., Perera, L., and Scoles, G., IR Spectroscopy of Solvated Molecules //, in *Clusters of Atoms and Molecules II*, H. Haberland, Editor. 1994, Springer-Verlag Berlin: Heidelberger Platz 3, W-1000 Berlin 33, Germany. p. 19-43.
103. Goyal, S., Schutt, D.L., and Scoles, G., Noble gas clusters as matrices for infrared spectroscopy. From small clusters to the bulk-matrix limit: SF₆Ar_n, SF₆Kr_n, and SF₆Xe_n with 100 ≤ n ≤ 10000 // *J Chem. Phys* - 1995. - v.102. - p. 2302-2314.
104. Neusser, H.J. and Krause, H., Binding energy and structure of van der Waals complexes of benzene // *Chem. Rev.* - 1994. - v.94. - p. 1845-1871.
105. Strobel, A., Knoblauch, N., Agreiter, J., Smith, A.M., Niederschattburg, G., and Bondybey, V.E., Identification, structure, and vibrational assignment of the NO dimer cation // *J. Phys. Chem.* - 1995. - v.99. - p. 872-874.
106. Yeh, C.S., Pilgrim, J.S., Willey, K.F., Robbins, D.L., and Duncan, M.A., Spectroscopy of weakly-bound magnesium ion complexes // *Int. Rev. Phys. Chem.* - 1994. - v.13. - p. 231-262.
107. Pilgrim, J.S., Yeh, C.S., Berry, K.R., and Duncan, M.A., Photodissociation Spectroscopy of Mg⁺-rare gas complexes // *J. Chem. Phys.* - 1994. - v.100. - p. 7945-7956.
108. Pilgrim, J.S., Yeh, C.S., and Duncan, M.A., Photodissociation Spectroscopy of Mg⁺-Ar // *Chem. Phys Lett* - 1993. - v.210. - p. 322-326.
109. Scurlock, C.T., Pilgrim, J.S., and Duncan, M.A., Rotationally resolved photodissociation spectroscopy of Mg⁺-Ar // *J Chem. Phys* - 1995. - v.103. - p. 3293-3298.
110. Robbins, D.L., Brock, L.R., Pilgrim, J.S., and Duncan, M.A., Electronic spectroscopy of the Mg⁺-N₂ complex: Evidence for photoinduced activation of N-2 // *J Chem. Phys* - 1995. - v.102. - p. 1481-1492.
111. Yeh, C.S., Willey, K.F., Robbins, D.L., Pilgrim, J.S., and Duncan, M.A., Photodissociation Spectroscopy of the Mg⁺-CO₂ Complex and Its Isotopic Analogs // *J Chem. Phys* - 1993. - v.98. - p. 1867-1875.
112. Willey, K.F., Yeh, C.S., Robbins, D.L., Pilgrim, J.S., and Duncan, M.A., Photodissociation Spectroscopy of Mg⁺-H₂O and Mg⁺-D₂O // *J Chem. Phys* - 1992. - v.97. - p. 8886-8895.
113. Buthelezi, T., Bellert, D., Lewis, V., and Brucat, P.J., The C-X transition in CaKr⁺ and CaAr⁺ // *Chem. Phys Lett* - 1995. - v.246. - p. 145-149.
114. Pullins, S.H., Scurlock, C.T., Reddic, J.E., and Duncan, M.A., Photodissociation spectroscopy of Ca⁺-rare gas complexes // *J Chem. Phys* - 1996. - v.104. - p. 7518-7525.
115. Scurlock, C.T., Pullins, S.H., Reddic, J.E., and Duncan, M.A., Photodissociation spectroscopy of Ca⁺-H₂O and Ca⁺-D₂O // *J Chem. Phys* - 1996. - v.104. - p. 4591-4599.
116. Ding, L.N., Young, M.A., Kleiber, P.D., and Stwalley, W.C., Photofragmentation spectroscopy of Mg₂CO₂⁺ // *Chem. Phys Lett* - 1993. - v.212. - p. 499-504.

- References -

117. Ding, L.N., Kleiber, P.D., Cheng, Y.C., Young, M.A., O'Neil, S.V., and Stwalley, W.C., Photofragmentation dynamics of $\text{Mg}_2(\text{CO}_2)_{1,2}^+$ // *J. Chem. Phys.* - 1995. - v.102. - p. 5235-5245.
118. Buthelezi, T., Bellert, D., Lewis, V., and Brucat, P.J., The bond length of CoKr^+ // *Chem. Phys. Lett.* - 1995. - v.242. - p. 627-631.
119. Bieske, E.J., Soliva, A.S., Welker, M., and Maier, J.P., The $\text{B} \leftarrow \text{X}$ electronic spectrum of N_2^+He // *J. Chem. Phys.* - 1990. - v.93. - p. 4477-4478.
120. Bieske, E.J., Nizkorodov, S.A., Friedmann, A., and Maier, J.P., Metastable decay of N_2^+He_n ($n=1$) ($1 < n \leq 6$) cluster // *Int. J. Mass. Spectrom. Ion. Proc.* - 1994. - v.135. - p. 19-30.
121. Bieske, E.J., Soliva, A.S., Friedmann, A., and Maier, J.P., Vibrational predissociation lifetime of N_2^+He ($X, v=1$) // *J. Chem. Phys.* - 1992. - v.96. - p. 4035-4036.
122. Bieske, E.J., Soliva, A.S., Friedmann, A., and Maier, J.P., Electronic spectra of $\text{N}_2^+(\text{He})_n$ ($n=1,2,3$) // *J. Chem. Phys.* - 1992. - v.96. - p. 28-34.
123. Bieske, E.J., Soliva, A.M., and Maier, J.P., The $\text{B} \leftarrow \text{X}$ electronic spectrum of N_2^+Ne // *J. Chem. Phys.* - 1991. - v.94. - p. 4749-4755.
124. Bieske, E.J., Soliva, A.M., Friedmann, A., and Maier, J.P., The $\text{B} \leftarrow \text{X}$ electronic spectra of N_2^+Nen ($1 \leq n \leq 8$) // *J. Chem. Phys.* - 1994. - v.100. - p. 4156-4164.
125. Oudejans, L., Nauta, K., and Miller, R.E., Extreme metastability in $\text{Ar-HCl}(v=1)$ and $\text{Ar-DF}(v=1)$ // *J. Chem. Phys.* - 1996. - v.105. - p. 10410-10415.
126. Friedmann, A., Soliva, A.M., Nizkorodov, S., Bieske, E.J., and Maier, J.P., A ${}^3\Pi_u \leftarrow X {}^3\Sigma_g^-$ Electronic spectrum of N_3^+ // *J. Phys. Chem.* - 1994. - v.98. - p. 8896-8902.
127. Friedmann, A., Nizkorodov, S.A., Bieske, E.J., and Maier, J.P., Discrete UV absorption by $\text{N}_3^+(\text{N}_2)_n$ clusters // *Phys. Chem. Lett.* - 1994. - v.224. - p. 16-20.
128. Bieske, E.J., Photodissociation of $(\text{N})_n^+$ Clusters ($2 \leq n \leq 7$) - Branching Ratios for Formation of N_2^+ and N_4^+ , and N_2^+ Fragment Vibrational Excitation // *J. Chem. Phys.* - 1993. - v.99. - p. 8672-8679.
129. Jacox, M.E., Vibrational and electronic energy levels of polyatomic transient molecules // -1994. -v. Monograph No. 3, AIP, ACS, and NIST.
130. Hirota, E., Microwave and infrared spectra of free radicals and molecular ions // *Chem. Rev.* - 1992. - v.92. - p. 141-173.
131. Hack, W., Haubold, R., Heinrich-Sterzel, C., Keller-Rudek, H., Ohms-Bredemann, U., Sciöberg, D., and Strametz, C., The Diazenyl Cation, N_2H^+ // in *Gmelin Handbook of Inorganic and Organometallic Chemistry*, P. Merlet, Editor. 1993, Springer-Verlag: p. 5-37.
132. Botschwina, P., An ab initio calculation of the frequencies and IR intensities of the stretching vibrations of HN_2^+ // *Chem. Phys. Lett.* - 1984. - v.107. - p. 535-541.
133. Lias, S.G., Barmess, J.E., Liebman, J.F., Holmes, J.L., Levin, R.D., and Mallard, W.G., Gas-phase ion and neutral thermochemistry // *J. Phys. Chem. Ref. Data Suppl.* - 1988. - v.17. - p. 1-861.
134. Turner, B.E., U93.174: A new interstellar line with quadrupole hyperfine splitting // *Astrophys. J.* - 1974. - v.193. - p. L83-L87.
135. Green, S., Montgomery, J.A., and Thaddeus, P., Tentative identification of U93.174 as the molecular ion N_2H^+ // *Astrophys. J.* - 1974. - v.193. - p. L89-L81.
136. Sakally, R.J., Dixon, T.A., Anderson, T.G., Szanto, P.G., and Woods, R.C., Laboratory microwave spectrum and rest frequencies of the N_2H^+ ion // *Astrophys. J.* - 1976. - v.205. - p. L101.
137. Anderson, T.G., Dixon, T.A., Piltch, N.D., Sakally, R.J., Szanto, P.G., and Woods, R.C., Laboratory rest frequencies for N_2D^+ // *Astrophys. J.* - 1977. - v.216. - p. L85.

- References -

138. Sastry, K.V.L.N., Helminger, P., Herbst, E., and De Lucia, F.C., Millimeter and submillimeter spectra of HN_2^+ and DN_2^+ // Chem. Phys. Lett. - 1981. - v.84. - p. 286-287.
139. Van den Heuvel, F.C. and Dymanus, A., Observation of far-infrared transitions of HCO^+ , CO^+ and HN_2^+ // Chem. Phys. Lett. - 1982. - v.92. - p. 219-222.
140. Verhoeve, P., Zwart, E., Versluis, M., Drabbels, M., ter Meulen, J.J., Meerts, W.L., and McLay, D.B., A far infrared laser sideband spectrometer in the frequency region 550-2700 GHz // Rev. Sci. Instrum. - 1990. - v.61. - p. 1612-1625. -
141. Szanto, P.G., Anderson, T.G., Saykally, R.J., Piltch, N.d., Dixon, T.A., and Woods, R.C., A microwave substitution structure for protonated nitrogen N_2H^+ // J. Chem. Phys. - 1981. - v.75. - p. 4261-4263.
142. Woods, R.C., Microwave Spectroscopy of Molecular Ions in the Laboratory and in Space // Phil. Trans. R. Soc. Lond. - 1988. - v.A324. - p. 141-146.
143. Cazzoli, G., Corbelli, G., Degli Esposti, C., and Favero, P.G., Inner and outer nitrogen hyperfine structure in the HN_2^+ ion // Chem. Phys. Lett. - 1985. - v.118. - p. 164-166.
144. Gudeman, C.S., Begemann, M.H., Pfaff, J., and Saykally, R.J., Velocity-modulated infrared laser spectroscopy of molecular ions: The ν_1 band of HNN^+ // J. Chem. Phys. - 1983. - v.78. - p. 5837-5838.
145. Nesbitt, D.J., Petek, H., Gudeman, C.S., Moore, C.B., and Saykally, R.J., A study of the ν_1 fundamental and bend-excited hot of DNN^+ by velocity modulation absorption spectroscopy with an infrared difference frequency laser // J. Chem. Phys. - 1984. - v.81. - p. 5281-5287.
146. Nakanaga, T., Ito, F., Takeo, H., and Matsumura, C., Observation of infrared absorption spectra of molecular ions, H_3^+ and HN_2^+ , by FTIR spectroscopy // Chem. Phys. Lett. - 1990. - v.169. - p. 269-273.
147. Foster, S.C. and McKellar, A.R.W., The ν_3 fundamental bands of HN_2^+ , DN_2^+ , and DCO^+ // J. Chem. Phys. - 1984. - v.81. - p. 3424-3428.
148. Sears, T.J., Observation of the ν_2 (bending) fundamental of the HN_2^+ ion at 14.6 micrometers // J. Opt. Soc. Am. B - 1985. - v.2. - p. 786.
149. Sears, T.J., Detection of the bending fundamental band of DN_2^+ by diode laser absorption spectroscopy // J. Chem. Phys. - 1985. - v.82. - p. 5757-5758.
150. Owrutsky, J.C., Gudeman, C.S., Martner, C.C., L.M., T., Rosenbaum, N.H., and Saykally, R.J., Determination of the equilibrium structure of protonated nitrogen by high resolution infrared laser spectroscopy // J. Chem. Phys. - 1986. - v.84. - p. 605-617.
151. Sasada, H. and Amano, T., Observation of the $2\nu_1$ band of HN_2^+ with a 1.57 micron distributed feedback semiconductor laser // J. Chem. Phys. - 1990. - v.92. - p. 2248-2250.
152. Ho, W.C., Pursell, C.J., Weliky, D.P., Takagi, K., and Oka, T., Infrared-microwave double resonance spectroscopy of molecular ions: HN_2^+ // J. Chem. Phys. - 1990. - v.93. - p. 87-93.
153. Kabbadj, Y., Huet, T.R., Rehfuß, B.D., Gabrys, C.M., and Oka, T., Infrared spectroscopy of highly excited vibrational levels of protonated nitrogen, HN_2^+ // J. Mol. Spectr. - 1994. - v.163. - p. 180-205.
154. Kraemer, W.P., Komornicki, A., and Dixon, D.A., The proton affinity of N_2 and spectroscopic properties of N_2H^+ // Chem. Phys. - 1986. - v.105. - p. 87-96.
155. Pursel, C.J., Weliky, D.P., and Oka, T., Collision-induced double resonance studies of HN_2^+ and HCN // J. Chem. Phys. - 1990. - v.93. - p. 7041-7048.
156. Owrutsky, J.C., Keim, E.R., Coe, J.V., and Saykally, R.J., Absolute IR intensities of the ν_1 bands of HN_2^+ and HCO^+ determined by direct laser absorption spectroscopy in fast ion beams // J. Phys. Chem. - 1989. - v.93. - p. 5960-5963.

- References -

157. Keim, E.R., Polak, M.L., Owrutsky, J.C., Coe, J.V., and Saykally, R.J., Absolute infrared vibrational band intensities of molecular ions determined by direct laser absorption spectroscopy in fast ion beams // *J. Chem. Phys.* - 1990. - v.93. - p. 3111-3119.
158. Turner, B.E., The physics and chemistry of translucent molecular clouds .4. HCO^+ and N_2H^+ // *Astrophys J* - 1995. - v.449. - p. 635-655.
159. Xu, Y.J., Fukushima, M., and Amano, T., Infrared absorption spectroscopy of molecular ions in a corona-discharge slit expansion // *Chem. Phys Lett* - 1995. - v.242. - p. 126-131.
160. Fukushima, M., Chan, M.C., Xu, Y.J., Talebbendiab, A., and Amano, T., High-resolution infrared absorption spectroscopy of jet-cooled molecular ions // *Chem. Phys Lett* - 1994. - v.230. - p. 561-566.
161. Anderson, D.T., Davis, S., Zwier, T.S., and Nesbitt, D.J., An intense slit discharge source of jet-cooled molecular ions and radicals ($T\text{-rot}<30\text{K}$) // *Chem. Phys Lett* - 1996. - v.258. - p. 207-212.
162. Weis, B. and Yamashita, K., Theoretical potential energy functions and rovibronic spectrum of electronically excited states of HCO^+ // *J. Chem. Phys.* - 1993. - v.99. - p. 9512-9519.
163. Ma, N.L., Smith, B.J., and Radom, L., Refined calculations of the structures and stabilities of the formyl (HCO^+) and isoformyl (COH^+) cations // *Chem. Phys. Lett.* - 1992. - v.197. - p. 573-580.
164. Lias, S.G., Liebman, J.F., and Levin, R.D., Evaluated gas-phase basicities and proton affinities of molecules; heats of formation of protonated molecules // *J. Phys. Chem. Ref. Data* - 1984. - v.13. - p. 695.
165. Buhl, D. and Snyder, L.E., Unidentified interstellar microwave line // *Nature* - 1970. - v.228. - p. 267-269.
166. Klemperer, W., Carrier of the interstellar 89.190 GHz line // *Nature* - 1970. - v.227. - p. 1230.
167. Woods, R.C., Saykally, R.J., Dixon, T.A., Szanto, P.G., and Anderson, T.G., Laboratory microwave spectrum of HCO^+ // *Phys. Rev. Lett.* - 1975. - v.35. - p. 1269-1272.
168. Sastry, K.V.L.N., Herbst, E., and De Lucia, F.C., Millimeter and submillimeter spectra of HCO^+ and DCO^+ // *J. Chem. Phys.* - 1981. - v.75. - p. 4169-4170.
169. Bogey, M., Demuynck, C., and Destombes, J.L., Centrifugal distortion effects in HCO^+ from its millimeter spectrum // *Mol. Phys.* - 1981. - v.43. - p. 1043-1050.
170. Woods, R.C., Saykally, R.J., Anderson, T.G., Dixon, T.A., and Szanto, P.G., The molecular structure of HCO^+ by the microwave substitution method // *J. Chem. Phys.* - 1981. - v.75. - p. 4256-4260.
171. Gudeman, C.S., Begemann, M.H., Pfaff, J., and Saykally, R.J., Velocity-modulated infrared laser spectroscopy of molecular ions: The ν_1 band of HCO^+ // *Phys. Rev. Lett.* - 1983. - v.50. - p. 727-731.
172. Gudeman, C.S. and Saykally, R.J., Velocity modulation infrared laser spectroscopy of molecular ions // *Ann. Rev. Phys. Chem.* - 1984. - v.35. - p. 387-418.
173. Amano, T., The ν_1 fundamental band of HCO^+ by difference frequency laser spectroscopy // *J. Chem. Phys.* - 1983. - v.79. - p. 3595.
174. Kawaguchi, K., McKellar, A.R.W., and Hirota, E., Magnetic field modulated infrared laser spectroscopy of molecular ions: the ν_1 band of DCO^+ // *J. Chem. Phys.* - 1986. - v.84. - p. 1146-1148.
175. Davies, P.B., Hamilton, P.A., and Rothwell, W.J., Infrared Laser Spectroscopy of the ν_3 Fundamental of HCO^+ // *J. Chem. Phys.* - 1984. - v.84. - p. 1598-1599.
176. Foster, S.C., McKellar, A.R.W., and Sears, T.J., Observation of the ν_3 fundamental band of HCO^+ // *J. Chem. Phys.* - 1984. - v.81. - p. 578-579.
177. Davies, P.B. and Rothwell, W.J., Diode laser detection of the bending mode of HCO^+ // *J. Chem. Phys.* - 1984. - v.81. - p. 5239-5240.

- References -

178. Kawaguchi, K., Yamada, C., Saito, S., and Hirota, E., Magnetic field modulated infrared laser spectroscopy of molecular ions: the ν_2 band of HCO^+ // *J Chem. Phys* - 1985. - v.82. - p. 1750-1755.
179. Blake, G.A., Laughlin, K.B., Cohen, R.C., Busrow, K.L., and Saykally, R.J., Laboratory measurement of the pure rotational spectrum of vibrationally excited HCO^+ ($\nu_2=1$) by far-infrared laser sideband spectroscopy // *Astrophys. J.* - 1987. - v.316. - p. L45-L48.
180. Liu, D.-J., Lee, S.T., and Oka, T., The ν_3 fundamental band of HCNH^+ and the $2\nu_3 < -\nu_3$ and $\nu_2 + \nu_3 < -\nu_2$ hot bands of HCO^+ // *J. Mol. Spectr.* - 1988. - v.128. - p. 236-249.
181. Blake, G.A., Helminger, P., Herbst, E., and De Lucia, F.C., Laboratory millimeter and submillimeter spectrum of HOC^+ // *Astrophys. J.* - 1983. - v.264. - p. L69-L70.
182. Bogey, M., Demuynck, C., and Destombes, J.L., Millimeter and submillimeter wave spectrum of the deuterated isoformyl ion DOC^+ // *J. Mol. Spectr.* - 1986. - v.115. - p. 229-231.
183. Gudeman, C.S. and Woods, R.C., Experimental detection of HOC^+ by microwave spectroscopy // *Phys. Rev. Lett.* - 1982. - v.48. - p. 1344-1348.
184. Nakanaga, T. and Amano, T., Infrared detection of HOC^+ by difference frequency laser spectroscopy // *J. Mol. Spectr.* - 1987. - v.121. - p. 502-504.
185. Smith, D., The Ion Chemistry of Interstellar Clouds // *Chem. Rev* - 1992. - v.92. - p. 1473-1485.
186. Crofton, M.W. and Oka, T., Infrared studies of molecular ions. I. The ν_3 band of NH_4^+ // *J. Chem. Phys.* - 1983. - v.79. - p. 3157-3158.
187. Schäfer, E., Begemann, M.H., Gudeman, C.S., and Saykally, R.J., The ν_3 vibrational spectrum of the free ammonium ion (NH_4^+). // *J. Chem. Phys.* - 1983. - v.79. - p. 3159-3160.
188. Schäfer, E., Saykally, R.J., and Robiette, A.G., A high resolution study of the ν_3 band of ammonium ion (NH_4^+) by velocity modulation laser absorption spectroscopy. // *J. Chem. Phys.* - 1984. - v.80. - p. 3969-3977.
189. Crofton, M.W. and Oka, T., Observation of forbidden transitions of ammonium ion (NH_4^+) ν_3 band and determination of ground state rotational constants. Observation of ν_3 band allowed transitions of ND_4^+ . // *J. Chem. Phys.* - 1987. - v.86. - p. 5983-5988.
190. Park, J., Xia, C., Selby, S., and Foster, S.C., The ν_4 band of ammonium, NH_4^+ // *J. Mol. Spec.* - 1996. - v.179. - p. 150-158.
191. Polak, M., Gruebele, M., DeKock, B.W., and Saykally, R.J., Velocity-Modulated Infrared Laser Spectroscopy of Molecular Ions: The ν_4 Band of ammonium // *Mol. Phys.* - 1989. - v.66. - p. 1193-1202.
192. Nakanaga, T. and Amano, T., Difference-frequency laser spectroscopy of the ν_4 fundamental band of NH_3D^+ // *Can. J. Phys.* - 1986. - v.64. - p. 1356-1358.
-
193. Martin, J.M.L. and Lee, T.J., Accurate ab initio quartic force field and vibrational frequencies of the NH_4^+ ion and its deuterated forms // *Chem. Phys Lett* - 1996. - v.258. - p. 129-135.
194. Buckingham, A.D., Fowler, P.W., and Hutson, J.M., Theoretical Studies of van der Waals Molecules and Intermolecular Forces // *Chem. Rev.* - 1988. - v.88. - p. 963-988.
195. Hutson, J.M., Intermolecular forces from spectroscopy of vdW molecules // *Annu. Rev. Phys. Chem.* - 1990. - v.41. - p. 123-154.
196. Nesbitt, D.J., High resolution IR spectroscopy of weakly bound molecular complexes // *Chem. Rev.* - 1988. - v.88. - p. 843-870.
197. Hutson, J.M., An Introduction to the Dynamics of van der Waals Molecules //, in *Advance in Molecular Dynamics and Collision Dynamics*, . 1991, JAI Press Inc.: Greenwich, Connecticut. p. 1-45.
198. Leopold, K.R., Fraser, G.T., Novick, S.E., and Klemperer, W., Current themes in microwave and infrared spectroscopy of weakly bound complexes // *Chem. Rev.* - 1994. - v.94. - p. 1807-1827.

- References -

199. Cohen, R.C. and Saykally, R.J., Vibration-rotation-tunneling spectroscopy of the van der Waals bond; A new look at intermolecular forces // *J. Phys. Chem.* - 1992. - v.96. - p. 1024-1040.
200. Brown, J.M., Hougen, J.T., Huber, K.-P., Johns, J.W.C., Kopp, I., Lefebvre-Brion, H., Merer, A.J., Ramsay, D.A., Rostas, J., and Zare, R.N., The labeling of parity doublet levels in linear molecules // *J. Mol. Spectr.* - 1975. - v.55. - p. 500-503.
201. Millen, D.J., Determination of stretching force constants of weakly bound dimers from centrifugal distortion constants // *Can. J. Chem.* - 1985. - v.63. - p. 1477-1479.
202. Drucker, S., Cooksy, A.L., and Klemperer, W., Spectroscopic characterization of the lowest Π and Σ bending states of ArHCN // *J. Chem. Phys.* - 1993. - v.98. - p. 5158-5183.
203. Fraser, G.T. and Pine, A.S., Infrared and microwave study of angular-radial coupling effects in ArHCN // *J. Chem. Phys.* - 1989. - v.91. - p. 3319-3326.
204. Herzberg, G., *Molecular Spectra and Molecular Structure. II. Infrared and Raman Spectra of Polyatomic Molecules.* // -1991. Malabar, Florida: Krieger Publishing Company.
205. Meuwly, M., Theoretische und experimentelle Untersuchungen an Protonen-gebundenen, ionischen Komplexen, // -1997. Universität Basel, Ph.D. thesis
206. Gerlich, D., Inhomogeneous RF fields: A versatile tool for the study of processes with slow ions //, in *State-selected and state-to-state ion-molecule reaction dynamics*, part 1. Experiment, C.-Y. Ng and M. Baer, Editor. 1992, Interscience publication: New Yourk. p. 1-176.
207. Daly, N.R., Scintillation type mass spectrometer ion detector // *Rev. Sci. Instr.* - 1960. - v.31. - p. 264-267.
208. Miklos, A., Bozoki, Z., Jiang, Y., and Feher, M., Experimental and theoretical investigation of photoacoustic-signal generation by wavelength-modulated diode lasers // *Appl. Phys.* - 1994. - v.B58. - p. 483-492.
209. Guelachvili, G. and Rao, K.N., *Handbook of Infrared Standards* // -1993. -v.1 and 2, London: Academic Press Inc.
210. Herbst, E. and Klemperer, W., The formation of molecules in dense interstellar clouds // *Astrophys. J.* - 1973. - v.185. - p. 505.
211. Fehsenfeld, F.C., Dunkin, D.B., and Ferguson, E.E., On the Association of C^+ and COH^+ with H_2 // *Astrophys. J.* - 1974. - v.188. - p. 43-44.
212. Hiraoka, K. and Kebarle, P., Stability and structure of H_3CO^+ formed from $COH^+ + H_2$ at low temperature // *J. Chem. Phys.* - 1975. - v.63. - p. 1688-1690.
213. Dill, J.D., Fischer, C.I., and McLafferty, F.W., Collisional activation and theoretical studies of gaseous COH_3^+ Ions // *J. Am. Chem. Soc.* - 1979. - v.101. - p. 6531-6534.
214. Dixon, D.A., Komornicki, A., and Kraemer, W.P., Energetics of the protonation of CO: Implications for the observation of HOC^+ in dense interstellar clouds // *J. Chem. Phys.* - 1984. - v.81. - p. 3603-3611.
215. Nobes, R.H. and Radom, L., HOC^+ : An Observable Interstellar Species? A Comparison with the Isomeric and Isoelectronic HCO^+ , HCN and HNC // *Chem. Phys.* - 1981. - v.60. - p. 1-10.
216. Talbi, D. and Pauzat, F., A theoretical study of the $H_3^+ + CO$ protonation process. I. The formation of HCO^+ // *Astron. Astrophys.* - 1987. - v.181. - p. 394-397.
217. Talbi, D. and Pauzat, F., A theoretical study of the $H_3^+ + CO$ protonation process. II. The formation of HOC^+ // *Astron. Astrophys.* - 1990. - v.229. - p. 253-258.
218. Ma, L.M., Smith, B.J., Pople, J.A., and Radom, L., Rearrangement and dissociative reactions of the methanol radical cation (CH_3OH^+): A comparison of theory and experiment // *J. Am. Chem. Soc.* - 1991. - v.113. - p. 7903-7912.

- References -

219. Radom, L., The chemistry of gas phase ions: a theoretical approach // *Int. J. Mass Spectrom. Ion Proc.* - 1992. - v.118/119. - p. 339.
220. Amano, T. and Warner, H.E., Laboratory Detection of Protonated Formaldehyde (H_2COH^+) // *Astrophys. J.* - 1989. - v.342. - p. L99-L101.
221. Amano, T. and Nakanaga, T., Laboratory measurements of the abundance ratio $[\text{HCO}^+]/[\text{HOC}^+]$ and their astrophysical implications // *Astrophys. J.* - 1988. - v.328. - p. 373-379.
222. Jarrold, M.F., Bowers, M.T., DeFrees, D.J., McLean, A.D., and Herbst, E., A reanalysis of the $\text{HCO}^+/\text{HOC}^+$ abundance ratio in dense interstellar clouds // *Astrophys. J.* - 1986. - v.303. - p. 392-400.
223. Illies, A.J., Jarrold, M.F., and Bowers, M.T., On the formation of HCO^+ and HOC^+ from the reaction between H_3^+ and CO // *J. Chem. Phys.* - 1982. - v.77. - p. 5847-5848.
224. McEwan, M.J., Flow tube studies of small isomeric ions //, in *Advances in Gas Phase Ion Chemistry*, N.G. Adams and L.M. Babcock, Editor. 1992, JAI Press Inc.: p. 1-42.
225. Bieske, E.J., Nizkorodov, S.A., Bennett, F.R., and Maier, J.P., The infrared spectrum of the $\text{H}_2\text{-HCO}^+$ complex // *J. Chem. Phys.* - 1995. - v.102. - p. 5152-5164.
226. Maluendes, S.A., McLean, A.D., and Herbst, E., Calculations of ion-molecule deuterium fractionation reactions involving HD // *Astrophys. J.* - 1992. - v.397. - p. 477-481.
227. Huber, K.P. and Herzberg, G., *Molecular spectra and molecular structure IV. Constants of diatomic molecules* // -1979. New York: van Nostrand Reinhold.
228. Wolniewicz, L.M., Vibrational-rotational study of the electronic ground state of the hydrogen molecule // *J. Chem. Phys.* - 1966. - v.45. - p. 515.
229. Hiraoka, K., Saluja, P.P., and Kebarle, P., Stabilities of complexes $(\text{N}_2)_n\text{H}^+$, $(\text{CO})_n\text{H}^+$, and $(\text{O}_2)_n\text{H}^+$ for $n=1$ to 7 based on gas phase ion-equilibria measurements // *Can. J. Chem.* - 1979. - v.57. - p. 2159-2166.
230. Hack, W., Haubold, R., Heinrich-Sterzel, C., Keller-Rudek, H., Ohms-Bredemann, U., Sciöberg, D., and Strametz, C., The Hydrazyl Cation, N_2H_3^+ //, in *Gmelin Handbook of Inorganic and Organometallic Chemistry*, P. Merlet, Editor. 1993, Springer-Verlag: p. 82-85.
231. Bieske, E.J., Nizkorodov, S.A., Bennett, F.R., and Maier, J.P., Combined infrared and ab initio study of the H_2HN_2^+ complex // *Int J Mass Spectrom Ion Proc* - 1995. - v.150. - p. 167-177.
232. Hirao, K. and Yamabe, S., Theoretical study of the structure and stability of $\text{HX}^+\dots(\text{H}_2)_n$ clusters // *Chem. Phys. Lett.* - 1981. - v.79. - p. 279-283.
233. Nowek, A. and Leszczynski, J., Post-Hartree-Fock study on Ar-HCO^+ and He-HCO^+ complexes: A critical examination of experimental data // *J. Chem. Phys.* - 1996. - v.105. - p. 6388-6394.
234. Kolbuszewski, M., The structure and vibrational frequencies of the ArHN_2^+ complex // *Chem. Phys. Lett* - 1995. - v.244. - p. 39-44.
235. Nizkorodov, S.A., Dopfer, O., Meuwly, M., Maier, J.P., and Bieske, E.J., Mid-infrared spectra of the proton-bound complexes Ne_nHCO^+ ($n=1,2$) // *J Chem. Phys* - 1996. - v.105. - p. 1770-1777.
236. Martin, J.M.L. and Taylor, P.R., Accurate ab initio quartic force fields for the ions HCO^+ and HOC^+ // *J. Chem. Phys.* - 1993. - v.99. - p. 286-292.
237. Le Roy, R.J., Davies, M.R., and Lam, M.E., Rate proportional to $(\text{Frequency shift})^2$ and other "All Else Being Equal" correlations in vibrational predissociation // *J. Phys. Chem.* - 1991. - v.95. - p. 2167-2175.
238. Ewing, G.E., Selection rules for vibrational energy transfer: Vibrational predissociation of van der Waals molecules // *J. Phys. Chem.* - 1987. - v.91. - p. 4662-4671.

- References -

239. Ruchti, T., Rohrbacher, A., Speck, T., Connelly, J.P., Bieske, E.J., and Maier, J.P., An electron impact ionization slit-jet apparatus for laser absorption spectroscopy // *Chem. Phys.* - 1996. - v.209. - p. 169-175.
240. Nesbitt, D.J., High-resolution, direct infrared laser absorption spectroscopy in slit supersonic jets: Intermolecular forces and unimolecular vibrational dynamics in clusters // *Annu. Rev. Phys. Chem.* - 1994. - v.45. - p. 367-399.
241. Bieske, E.J., Rainbird, M.W., and Knight, A.E.W., The van der Waals vibrations of aniline-(argon)₂ in the S¹ electronic state // *J. Chem. Phys.* - 1991. - v.94. - p. 7019.
242. McKellar, A.R.W., High resolution infrared spectra of H-2-Ar, HD-Ar, and D-2-Ar van der Waals complexes between 160 and 8620cm(-1) // *J. Chem. Phys.* - 1996. - v.105. - p. 2628-2638.
243. Lovejoy, C.M. and Nesbitt, D.J., Rotational predissociation, vibrational mixing, and van der Waals intermolecular potential of NeDF // *J. Chem. Phys.* - 1991. - v.94. - p. 208-223.
244. Lovejoy, C.M. and Nesbitt, D.J., Mode specific internal and direct rotational predissociation in HeHF, HeDF, and HeHCl: van der Waals complexes in the weak binding limit // *J. Chem. Phys.* - 1990. - v.93. - p. 5387-5407.
245. Howard, B.J. and Pine, A.S., Rotational predissociation and libration in the infrared spectrum of Ar-HCl // *Chem. Phys. Lett.* - 1985. - v.122. - p. 1-8.
246. Fraser, G.T. and Pine, A.S., van der Waals potentials from the infrared spectra of rare gas-HF complexes // *J. Chem. Phys.* - 1986. - v.85. - p. 2502-2515.
247. Meuwly, M., Nizkorodov, S.A., Maier, J.P., and Bieske, E.J., Mid-infrared spectra of He-HN₂⁺ and He₂-HN₂⁺ // *J. Chem. Phys.* - 1996. - v.104. - p. 3876-3885.
248. McKellar, A.R.W., Long-path equilibrium IR spectra of weakly bound complexes at low temperatures // *Faraday Discuss.* - 1994. - p. 69-80.
249. Randall, R.W., Ibbotson, J.A.B., and Howard, B.J., Spectroscopy and dynamics of rare gas - spherical top van der Waals complexes. The infrared spectrum of the ν₃ band of argon-silane. // *J. Chem. Phys.* - 1994. - v.100. - p. 7051-7060.
250. Brookes, M.D., Hughes, D.J., and Howard, B.J., Spectroscopy and dynamics of rare gas-spherical top complexes .2. The infrared spectrum of the ν(3) band of Ne-SiH₄ (j=1<-0 and j=0<-1 transitions) // *J. Chem. Phys.* - 1996. - v.104. - p. 5391-5405.
251. Urban, R.D., Jörissen, L.G., Matsumoto, Y., and Takami, M., Free jet infrared spectroscopy of SiF₄-rare gas complexes // *J. Chem. Phys.* - 1995. - v.103. - p. 3960-3965.
252. Ohshima, Y. and Endo, Y., Rotational spectrum and internal rotation of a methane -HCl complex // *J. Chem. Phys.* - 1990. - v.93. - p. 6256-6265.
253. Randall, R.W., Ibbotson, J.B., and Howard, B.J., A model for the energy levels of rare gas - spherical top van der Waals complexes // *J. Chem. Phys.* - 1994. - v.100. - p. 7042-7050.
254. Hutson, J.M. and Thornley, A.E., Atom-spherical top van der Waals complexes: A theoretical study // *J. Chem. Phys.* - 1994. - v.100. - p. 2505-2521.
255. Bieske, E.J., Nizkorodov, S.A., Dopfer, O., Maier, J.P., Stickland, R.J., Cotterell, B.J., and Howard, B.J., Observation of the infrared spectrum of the ν(3) band of the argon-ammonium ionic complex // *Chem. Phys. Lett.* - 1996. - v.250. - p. 266-272.
256. Dopfer, O., Nizkorodov, S.A., Meuwly, M., Bieske, E.J., and Maier, J.P., The ν₃ infrared spectrum of the He-NH₄⁺ complex // *Chem. Phys. Lett.* - 1996. - v.260. - p. 545-550.
257. Read, J.P. and Buckingham, A.D., Comment on: "The ν₃ infrared spectrum of the He-NH₄⁺ complex" // *Chem. Phys. Lett.* - 1997. - submitted. -

- References -

258. Gutowsky, H.S., Chuang, C., Klots, T.D., Emilsson, T., Ruoff, R.S., and Krause, K.R., Rotational spectra and structures of small clusters: The Ar₄-H/DF pentamers // *J.Chem.Phys.* - 1988. - v.88. - p. 2919.
259. Gutowsky, H.S., Klots, T.D., Chuang, C., Schuttenmaer, C.A., and Emilsson, T., Rotational spectra and structures of the Ar₂-H/DF trimers // *J.Chem.Phys.* - 1987. - v.86. - p. 569.
260. McIlroy, A., Lascola, R., Lovejoy, C.M., and Nesbitt, D.J., Structural dependence of HF vibrational red shifts in Ar_nHF, n=1-4, via High-resolution Slit Jet Infrared Spectroscopy // *J. Phys. Chem.* - 1991. - v.95. - p. 2636.
261. McIlroy, A. and Nesbitt, D.J., Intermolecular HF motion in Ar_nHF micromatrices (n=1,2,3,4) - classical and quantum calculations on a pairwise additive potential surface // *J Chem. Phys* - 1992. - v.97. - p. 6044-6056.
262. Niyaz, P., Bacic, Z., Moskowitz, J.W., and Schmidt, K.E., Ar_nHF (n=1-4) van der Waals clusters: A quantum Monte Carlo study of ground state energies, structures and HF vibrational frequency shifts // *Chem. Phys Lett* - 1996. - v.252. - p. 23-32.
263. Liu, S.Y., Bacic, Z., Moskowitz, J.W., and Schmidt, K.E., Isomer dependence of HF vibrational frequency shift for Ar_nHF (n=4-14) van der Waals clusters: Quantum five-dimensional bound state calculations // *J Chem. Phys* - 1995. - v.103. - p. 1829-1841.
264. Liu, S.Y., Bacic, Z., Moskowitz, J.W., and Schmidt, K.E., Size dependence of HF vibrational frequency shift for Ar_nHF (n=1-14) van der Waals clusters via quantum five-dimensional bound state calculations // *J Chem. Phys* - 1994. - v.101. - p. 10181-10184.
265. Liu, S.Y., Bacic, Z., Moskowitz, J.W., and Schmidt, K.E., HF vibrational red shift for the icosahedral Ar₁₂HF van der Waals cluster is the same as in an Ar matrix: Quantum five-dimensional bound state calculations // *J Chem. Phys* - 1994. - v.101. - p. 6359-6361.
266. Bieske, E.J., Nizkorodov, S.A., Bennett, F., and Maier, J.P., Combined infrared and ab initio study of the H₂HN₂⁺ complex // *Int. J. Mass Spectrom. Ion Proc.* - 1995. - v.150. - p. 167-177.
267. Yamaguchi, Y., Richards, C.A., and Schaefer III, H.F., High level ab initio study on the ground state potential energy hypersurface of the HCO(+)-COH(+) system // *J Chem. Phys* - 1994. - v.101. - p. 8945-8954.
268. Lifshitz, C., Unimolecular and collision induced decomposition of selected cluster ions //, in *Cluster Ions*, C.Y. Ng, T. Baer, and I. Powis, Editor. 1993, Wiley&Sons: New York. p. 121-164.
269. Ichihashi, M., Yamabe, J., Murai, K., Nonose, S., Hirao, K., and Kondow, T., Infrared spectroscopy of NH₄⁺(NH₃)_{n-1} (n=6-9): Shell structures and collective nu 2 vibrations // *J. Phys. Chem.* - 1996. - v.100. - p. 10050-10054.
270. Dopfer, O., Nizkorodov, S.A., Meuwly, M., Bieske, E.J., and Maier, J.P., Microsolvation of the ammonium ion in Argon: Infrared spectra of NH₄⁺-Ar_n complexes (n=1-7) // *Int. J. Mass Spectrom. Ion Processes* - 1997. - submitted. -
-
271. Boo, B.H. and Armentrout, P.B., Reaction of silicon ion (²P) with silane (SiH₄, SiD₄). Heat of formation of SiH_n, SiH_n⁺ (n=1,2,3) and Si₂H_n⁺ (n=0,1,2,3). Remarkable isotope exchange reaction involving four hydrogen shifts. // *J. Am. Chem. Soc.* - 1987. - v.109. - p. 3549-3559.
272. Hiraoka, K. and Kebarle, P., Stability and energetics of pentacoordinated caboneum ions. The isomeric C₂H₇⁺ ion and some higher analogues: C₃H₉⁺ and C₄H₁₁⁺ // *J. Am. Chem. Soc.* - 1976. - v.98. - p. 6119-6125.
273. Hiraoka, K. and Mori, T., Isotope Effect and Nature of Bonding in the Cluster Ions H₃⁺(Ar)_n and D₃⁺(Ar)_n // *J. Chem. Phys.* - 1989. - v.91. - p. 4821-4826.
274. Maitre, P. and Bauschlicher, C.W., Structure of V(H₂)_n(⁺) clusters for n=1-6 // *J. Phys. Chem.* - 1995. - v.99. - p. 6836-6841.

- References -

275. Bauschlicher, C.W. and Maitre, P., Structure of $\text{Co}(\text{H}_2)_n(^+)$ clusters, for $n=1-6$ // J. Phys. Chem. - 1995. - v.99. - p. 3444-3447.
276. Bushnell, J.E., Kemper, P.R., and Bowers, M.T., Spin change induced in Vanadium(I) by low-field ligands: Binding energies of $\text{V}^+(\text{H}_2)_n$ clusters ($n=1-7$) // J. Phys. Chem. - 1993. - v.97. - p. 11628-11634.
277. Kemper, P.R., Bushnell, J.E., von Helden, G., and Bowers, M.T., $\text{Co}^+(\text{H}_2)_n$ clusters: binding energies and molecular parameters // J. Phys. Chem. - 1993. - v.97. - p. 52-58.
278. Poll, J.D. and Hunt, J.L., On the theory of the stark shifts of the rotational-vibrational levels of the hydrogen molecule and its isotopes produced by a point charge. I: H_2 , D_2 , and T_2 // Can. J. Phys. - 1985. - v.63. - p. 84.
279. Elkind, J.L. and Armentrout, P.B., State-specific reactions of atomic transition-metal ions with H_2 , HD, and D_2 : Effects of d orbitals on chemistry (and references therein) // J. Phys. Chem. - 1987. - v.91. - p. 2037-2045.
280. Hobza, P., Zahradnik, R., and Smith, D., Reactions Between H_3^+ and Rare Gas Atoms // Chem. Phys. Lett. - 1993. - v.208. - p. 497-502.
281. Meot-Ner, M., The Ionic Hydrogen Bond and Ion Solvation. 1. $\text{NH}^+ \dots \text{O}$, $\text{NH}^+ \dots \text{N}$, and $\text{OH}^+ \dots \text{O}$ Bonds. Correlations with Proton Affinity. Deviation due to Structural Effects. // J. Am. Chem. Soc. - 1984. - v.106. - p. 1257-1264.
282. Bissonnette, C., Chuaqui, C.E., Crowell, K.G., Leroy, R.J., Wheatley, R.J., and Meath, W.J., A reliable new potential energy surface for $\text{H}-2-\text{Ar}$ // J Chem. Phys - 1996. - v.105. - p. 2639-2653.
283. McKellar, A.R.W., Infrared spectra of hydrogen dimers // J. Chem. Phys. - 1990. - v.92. - p. 3261-3277.
284. Lovejoy, C.M., Nelson, D.D., and Nesbitt, D.J., The infrared spectrum of D_2HF // J. Chem. Phys. - 1988. - v.89. - p. 7180-7188.
285. Lovejoy, C.M., Nelson, D.D., and Nesbitt, D.J., Hindered internal rotation in jet cooled H_2HF complexes // J. Chem. Phys. - 1987. - v.87. - p. 5621-5628.
286. Jucks, K.W. and Miller, R.E., Infrared Stark spectroscopy of the hydrogen-HF binary complex // J. Chem. Phys. - 1987. - v.87. - p. 5629-5633.
287. Drucker, S., Tao, F.M., and Klemperer, W., Bound states of HeHCN : Ab initio calculation and high-resolution spectroscopy // J. Phys. Chem. - 1995. - v.99. - p. 2646-2655.
288. Shi, Z. and Boyd, R.J., An *ab initio* study of model $\text{S}_\text{N}2$ reactions with inclusion of electron correlation effects through second-order Möller-Plesset perturbation calculation // J. Am. Chem. Soc. - 1990. - v.112. - p. 6789-6796.
289. Armentrout, P.B. and Kickel, B.L., Gas-phase thermochemistry of transition metal ligand systems: Reassessment of values and periodic trends //, in Organometallic ion chemistry, B.S. Freiser, Editor. 1996, Kluwer Academic Publishers: p. 1-45.

17. Curriculum Vitae of the author

Personalities

Name Sergey Nizkorodov
Birth date June 13, 1971
Nationality Russian

Education

9.1978-6.1987 Primary and Secondary School, Kokchetav, Kazakhstan.
8.1987-6.1988 Physics-Mathematics School at Novosibirsk State University,
 Novosibirsk, Russia
7.1988-6.1993 Undergraduate at Novosibirsk State University, Novosibirsk, Russia
6.1993 Diploma of Higher Education in Chemistry
9.1993-9.1997 Graduate in the group of Prof. J.P. Maier, Institute of Physical
 Chemistry, University of Basle, Switzerland.
5.1997 Ph.D. thesis, Department of Natural Sciences, University of Basle

During my study in Basle I visited lectures of the following lecturers:

E. Bieske, J. Dannacher, H.P. Huber, J.P. Maier, B. Scarpellini, F.-K. Thielemann,
D. Trautmann.